

The role of the PAS-cap in the function of hEAG1 and the role of hEAG1 in cancer cell progression

Thesis submitted for the degree of Doctor of Philosophy at the University of
Leicester

Alina Finch

Molecular and Cell Biology

University of Leicester

2018

Abstract

Human ether-a-go-go 1 (hEAG1) is a voltage gated K⁺ channel that is sensitive to inhibition by Ca²⁺-calmodulin. hEAG1 is located presynaptically in brain neurons and regulates Ca²⁺ influx and neurotransmitter release. It is also ectopically expressed in >70% of human tumours. hEAG1 has been shown to increase cell proliferation. The research here aims to understand the mechanism for Ca²⁺-calmodulin regulation of gating and whether specific intracellular domains are also important for effects on proliferation. The role of hEAG1 on cell migration is studied here for the first time.

hEAG1 contains an N-terminal EAG domain consisting of a Per-Arnt-Sim (PAS) domain and a 26 amino acid PAS-cap region. On the C-terminus is a cyclic nucleotide binding homology domain (cNBHD). hEAG1 channels were mutated and channels characterised by expression in *Xenopus laevis* oocyte expression system and two electrode voltage clamp. At a membrane potential of +60mV, WT hEAG1 shows activation kinetics of 309.1 ± 16.4 ms and does not inactivate in control conditions. WT hEAG1 is inhibited $85.5 \pm 2.9\%$ when Ca²⁺ is raised. Deleting the PAS-cap (Δ 2-26) slows the activation kinetics to 801 ± 122 ms and allows the non-inactivating channel to inactivate. When Ca²⁺ is raised, the Δ 2-26 hEAG1 current increases by $1272.7 \pm 197.1\%$. In this study we address, at the amino acid level, the interactions behind the PAS-cap's role in regulating hEAG1.

We also address whether the Ca²⁺ sensitivity and intracellular domains of hEAG1 influence its effect on proliferation by using a BrdU incorporation assay. The EAG domain and the E600 residue are important for this role as mutation of either resulted in a reduction in the number of proliferating cells. Overall the results suggest that PAS-cap, EAG and cNBH domain interactions regulate current responses to Ca²⁺-calmodulin and that the EAG domain and E600 are important for increased proliferation.

Acknowledgements

For Grandma & Grandpa and Grannie & Grandad, who will not see me graduate with the first doctorate of either of the Finch-Bates family.

I'd like to first thank the University of Leicester and the MIBTP for funding my PhD and my supervisor Dr John Mitcheson for experimental guidance and support throughout my time here. Thanks also to Dr Debbie Mitcheson for emotional support. I also want to thank my secondary supervisor Dr Fred Muskett for his attention to detail and guidance through various PyMol structures and quick wit. Thanks to Dr Noel Davies for mentoring me throughout my undergraduate degree and being the one who first convinced me to do a PhD. Also thanks for your project input and guidance during the PhD.

Massive thank you to Dr Lory Francescut for coffee breaks, chats and emotional support alongside outstanding lab help and guidance – you will never know how much you've helped me. Thank you for forming such a large part of my lab supervision. Thanks also go to Dr Rich Rainbow for help in both the lab and write up stages of the PhD but also for help with grant writing and post-doc applications. Thanks also to his lab members Dr Sean Brennan and Simona Esposito for lunch time banter and general humorous comments.

Thanks go to Prof. Luis Pardo and his entire lab at the Max Planck Institute of Experimental Medicine. Thank you for all your support and supervision throughout my time there and for kindly hosting me during my experiments, as well as the additional guidance and samples sent after my return to Leicester.

Thanks also go to my fellow PhD students; Adam for being the best housemate and for being my cheerleader throughout, Kate for listening to and understanding my every emotion and being there for me at every turn, Claire for being my voice of calm and logic in times of high stress and Priya for dealing with my constant worry and getting me back on track. Thanks to Saba for experimental help and future experiments, thank you as well for all the laughter.

Thanks go to my parents for always being at the end of the phone and believing in my ability to do everything, even when I was not so convinced. Thanks to my feline friends; Wilson, Callaghan, Grissom and Hodges for occasionally showing affection. Thanks also to the canine cohort; Speedy, Artie, Judy, Vance, Louis and Bertie for always being overly excited to see me and for reminding me that life isn't just about data and graphs. Thanks to Colin and Maureen for letting me use their house as a writing up hub over the summer whilst taking care of Dawn, the pigs, the chickens and of course the dogs. Thanks also to the Lennon & Collins families for support, tea and family.

Final thanks go to my partner and best friend Matthew Lennon for being my shoulder to cry on (quite literally), for supporting my career choices no matter where it may take us and for continually pushing me to be the best scientist and person I can be.

Contents

Abstract	1
Acknowledgements	2
List of tables	9
List of figures	10
List of abbreviations	19
1. Introduction	1
1.1. Potassium channels have diverse properties and regulate a variety of cellular functions	1
1.2. Intracellular structures of hEAG1 regulate channel gating and Ca²⁺ sensitivity 3	
1.2.1. hEAG1 has unique intracellular structures shared by the EAG family	5
1.2.2. hEAG1 shows no sensitivity to cyclic nucleotides	5
1.2.3. The PAS domain is an important regulator of ERG channel function	6
1.2.4. The EAG and cNBH domains interact to regulate channel activity	7
1.3. The role of hEAG1 in the CNS and its regulation of and by other molecules and proteins	13
1.3.1. The physiological role of hEAG1 is required during repetitive neuronal activity 13	
1.3.1.1. Activity in the post-synaptic terminal is not affected by the loss of hEAG1 13	
1.3.1.2. Accurate high frequency action potential firing is dependent on hEAG1 14	
1.3.2. hEAG1 localises to the plasma membrane but is also present in the inner nuclear membrane	14
1.3.2.1. hEAG1 is transported to the INM from the plasma membrane and is functional 16	
1.3.3. hEAG1 is found in both detergent-resistant and non-detergent-resistant membrane domains	17
1.3.3.1. hEAG1 distribution is influenced by Ca²⁺-calmodulin	17
1.3.3.2. The composition of the membrane affects hEAG1 current density	18
1.3.4. hEAG1 binds to and activates calcium-calmodulin dependent kinase II (CaMKII)	18
1.3.4.1. hEAG1 and CaMKII exist in a complex in neurons	18
1.3.4.2. Ca²⁺-calmodulin is needed initially for CaMKII to interact with hEAG1 ...	19
1.3.4.3. CaMKII activity continues in the absence of Ca²⁺-calmodulin	19
1.3.5. hEAG1 interacts with and is regulated by PIP₂	20
1.3.5.1. PIP₂ inhibits hEAG1 channels	20

1.3.5.2.	PIP₂ binds directly to hEAG1	22
1.3.6.	The epidermal growth factor receptor (EGFR) regulates hEAG1	22
1.3.6.1.	hEAG1 is regulated by EGFR kinase but not PDGFR or Src kinases	23
1.3.6.2.	hERG and hEAG1 bind to and activate SHP-1 phosphatase	23
1.3.6.3.	hEAG1 is maximally phosphorylated under control conditions	24
1.4.	hEAG1 is involved in cancer as well as congenital birth defects	25
1.4.1.	hEAG1 increases cell proliferation and induces a cancerous phenotype ...	25
1.4.1.1.	hEAG1 may be acting as an oncogene	25
1.4.1.2.	hEAG1 controls cell cycle transitions	26
1.4.1.3.	K⁺ ion flux is not required for the effects of hEAG1	27
1.4.1.4.	The position of the voltage sensor is important for hEAG1 to increase cell proliferation	28
1.4.1.5.	hEAG1 impacts on survival prognosis	28
1.4.1.6.	hEAG1 has potential as a therapeutic target and early tumour biomarker 29	
1.4.2.	Mutations of hEAG1 result in congenital, neurological syndromes	30
1.4.2.1.	ZLS is caused by de novo mutations in the KCNH1 gene	30
1.4.2.2.	TBS is also caused by de novo, gain-of-function mutations	31
1.4.2.3.	ZLS and TBS could be classed as ciliopathies	31
1.5.	hEAG1 is involved in the disassembly of the primary cilium	33
1.5.1.	Defects of the primary cilium are associated with disease	33
1.5.2.	The presence of the primary cilium may be important in cancer	33
1.5.3.	hEAG1 is a regulator of ciliary physiology	34
1.5.3.1.	Changing the expression of hEAG1 affects the presence of primary cilia 34	
1.5.3.2.	hEAG1 knock-out affects the Sonic hedgehog signalling pathway in pMEF cells 35	
1.5.3.3.	hEAG1 localises to the centrosomes and primary cilium	36
1.5.3.4.	A nuclear localisation signal of hEAG1 is needed to disassemble the primary cilium	37
1.5.4.	hEAG1 interacts with the oncoprotein cortactin	37
1.5.4.1.	CTTN directly binds to hEAG1	38
1.5.4.2.	hEAG1 channel current is affected by the presence of CTTN	38
1.5.4.3.	The C-terminus of hEAG1 is necessary for its regulation by CTTN	39
1.5.4.4.	CTTN affects and stabilises the surface expression of hEAG1 but does not affect its biophysical properties	40
1.5.4.5.	The interaction of CTTN and hEAG1 is important in ciliogenesis	42

1.6. Calmodulin is a Ca²⁺ sensing protein that regulates a wide variety of ion channels	43
1.6.1. Calmodulin can bind to targets in high and low Ca ²⁺ conditions	43
1.6.2. Calmodulin regulates a variety of ion channels	43
1.6.2.1. Calmodulin binds to Ca _v 1.2 in a Ca ²⁺ dependent manner	43
1.6.2.2. Calmodulin binds to and regulates presynaptic P/Q-type Ca ²⁺ channels	44
1.6.2.3. Calmodulin acts as an auxiliary subunit of the SK1 potassium channel ..	44
1.6.2.4. Calmodulin is constitutively associated with Na _v 1.2 and Na _v 1.5 channels	44
1.7. hEAG1 has been discovered to be regulated by Ca ²⁺ -calmodulin	46
1.7.1. hEAG1 was discovered to be expressed in the rat CNS	46
1.7.2. The Ca ²⁺ sensitivity of hEAG1 is mediated by calmodulin.....	46
1.7.3. Ca ²⁺ -calmodulin binds to intracellular domains.....	47
1.8. Project aims and objectives.....	49
2. Materials and Methods	50
2.1. Reagents and Electrophysiology Solutions	50
2.1.1. Oocyte Isolation and Solutions	50
2.1.2. Recording solutions	50
2.1.3. hEAG1 reagents.....	51
2.2. Molecular Biology	51
2.2.1. Vectors and hEAG1 constructs.....	51
2.2.2. Mutagenesis Primers	51
2.2.3. Generating hEAG1 mutant DNA and RNA	52
2.3. Two-electrode voltage clamp electrophysiology	53
2.3.1. Injection and Recording Micropipettes	53
2.3.2. Oocyte RNA injection	53
2.3.3. Two-electrode voltage clamp set up and voltage protocols	54
2.4. Whole-cell patch clamp electrophysiology	55
2.4.1. Patch clamp micropipettes.....	55
2.4.2. Patch clamp rig set up	55
2.4.3. Whole-cell patch clamp voltage protocols	56
2.4.3.1. Electrophysiology data analysis	57
2.4.3.2. Ion channel simulations in Tracn3	58
2.5. Cell Culture	58
2.5.1. Mammalian cell maintenance.....	58
2.5.2. DNA transfection of CHO cells.....	59

2.5.3.	Suspension of cells for electrophysiology	59
2.6.	Proliferation assays	60
2.6.1.	CHO cell transfection and controls	60
2.6.2.	Bromodeoxyuridine (BrdU) incorporation assay	60
2.6.3.	BrdU incorporation assay imaging and analysis	62
2.7.	Single cell migration assay	62
2.7.1.	Cell counting, plating and transfection	62
2.7.2.	Live single cell imaging protocol.....	63
2.7.3.	Cell migration analysis.....	64
2.8.	Western blotting.....	64
2.8.1.	Lysis buffer	64
2.8.2.	Western blotting protocol	64
2.9.	Immunocytochemistry for imaging the primary cilia.....	67
2.9.1.	Cell culture and DNA transfections.....	67
2.9.2.	Immunocytochemistry protocol.....	67
2.9.3.	Primary cilia staining and analysis.....	68
2.10.	Ca ²⁺ imaging of CHO cells	68
2.11.	Surface expression assays	69
3.	Results & Discussion – The Role of the PAS-cap in hEAG1 function	71
3.1.	Does the PAS-cap have a role in the voltage and Ca ²⁺ -calmodulin dependent regulation of hEAG1?	71
3.1.1.	WT hEAG1 is activated by depolarisation	71
3.1.2.	WT hEAG1 is inhibited by raised intracellular calcium ([Ca ²⁺] _i)	75
3.1.3.	Deletion of the PAS-cap results in dramatic changes to hEAG1 activation kinetics and parameters.....	79
3.1.4.	Δ2-26 hEAG1 shows a potentiation of the current when exposed to 5μM I&T 81	
3.1.5.	An alanine mutagenesis scan of the PAS-cap reveals key residues of the mechanism of regulation	86
3.1.5.1.	T16A, L18A, E19A, N20A, I21A and V22A hEAG1 show similar characteristics to the WT channel	88
3.1.5.2.	N15A and F17A both bare similarity to Δ2-26 hEAG1	103
3.1.6.	The E600 residue within the cNBHD is a promising interaction partner for residues of the PAS-cap.....	116
3.1.7.	Dual mutant N15E:E600N does not recover a WT-like phenotype	128
3.1.8.	Y198 of the EAG domain is not involved in the mechanism of action of Δ2-26 hEAG1	135

3.1.9.	E279 of the S2-S3 linker is not involved in the behaviour seen in Δ 2-26 hEAG1	141
3.2.	Discussion	149
3.2.1.	The PAS-cap regulates the inhibition of WT hEAG1 under high Ca^{2+} conditions	149
3.2.2.	Residues N15 and F17 of the PAS-cap are key for its role in regulation hEAG1 function	151
3.2.3.	E600 of the cNBHD and N15 of the PAS-cap are likely part of an interaction network	154
3.2.4.	Neither Y198 of the EAG domain or E279 of the S2-S3 linker are involved in the PAS-cap's mechanism of action	155
4.	Results and Discussion - How does the PAS-cap influence hEAG1 channel behaviour in terms of N, <i>i</i> and P_{open} ?	157
4.1.	The mechanism of regulation of hEAG1 by the PAS-cap	157
4.1.1.	Expression of WT and Δ 2-26 hEAG1 yields functional currents in CHO cells	159
4.1.2.	Simulations of hEAG1 data predict possible outcomes	171
4.1.3.	Noise analysis of WT hEAG1 reveals $5\mu\text{M}$ I&T changes to N and P_{open}	178
4.1.4.	Noise analysis of Δ 2-26 hEAG1 shows that neither N or <i>i</i> are affected by $5\mu\text{M}$ I&T	180
4.1.5.	Surface expression assays show a reduction of WT hEAG1 expression but not of Δ 2-26 hEAG1 following $5\mu\text{M}$ I&T	181
4.1.6.	WT hEAG1-BBS, but not Δ 2-26 hEAG1-BBS, is expressed and functional in CHO cells	185
4.2.	Discussion	194
4.2.1.	The PAS-cap likely influences the P_{open} of the hEAG1 channel	194
4.2.2.	The large current inhibition caused by $5\mu\text{M}$ I&T can be partly explained by a reduction in surface localisation of channels	196
4.2.3.	The BBS peptide insert alters the functional properties of hEAG1 channels	197
5.	Results and Discussion - Are the intracellular domains involved in hEAG1's role in cancer?	199
5.1.	hEAG1 is well documented as an oncogenic K^+ channel	199
5.1.1.	Δ EAG hEAG1 and E600R hEAG1 reduce the proliferation of transfected CHO cells in a BrdU assay	199
5.1.2.	Δ EAG hEAG1 and E600R hEAG1 reduce the percentage of ciliated hTERT-RPE1 cells	204
5.1.3.	Ca^{2+} imaging untransfected & WT hEAG1-expressing CHO cells	211
5.1.4.	Western blots show that hEAG1 protein for all constructs except Δ cNBHD hEAG1 are expressed in CHO cells.	217

5.1.5.	All hEAG1 constructs are functional in CHO cells except ΔcNBHD hEAG1 .	218
5.1.6.	Addition of 140mM K⁺ causes rapid and consistent reduction in WT hEAG1 current	235
5.1.7.	WT hEAG1 does not affect CHO cell migration when grown in either 0.1% or 10% FBS	239
5.2.	Discussion	254
5.2.1.	Interactions between the EAG domain and the E600 residue may be behind the mechanism of increase cell proliferation but WT hEAG1 does not influence cell migration	254
5.2.2.	The EAG domain, cNBH domain and both calmodulin binding domains are important for the role of hEAG1 in cilia disassembly	255
5.2.3.	The Ca²⁺ response profile of CHO cells to 5μM I&T was different when WT hEAG1 was stably expressed	256
6.	Summary and conclusions	258
7.	References	261

List of tables

Table 1.	A table showing all measured parameters for WT hEAG1 and all studied mutants both in control and in 5 μ M I&T.	147/148
Table 2.	A table showing the measured parameters of the WT hEAG1 channel along with 4 tested mutants using whole cell patch clamp.	193
Table 3.	A table displaying the parameters measured of hTERT-RPE1 cells from immunocytochemistry experiments regarding the primary cilia.	250
Table 4.	A table showing the measured parameters of the WT hEAG1 channel along with 5 tested mutants using whole cell patch clamp.	251
Table 5.	A table showing the measured parameters of the migration assays conducted in both 0.1% and 10% FBS for pXoon and WT hEAG1 transfected CHO cells.	252

List of figures

Figure 1.1.	A cartoon diagram showing the membrane topology and intracellular domains of a monomer of hEAG1.	4
Figure 1.2.	The full cryo-EM structure of rEAG showing the interactions between the main intracellular domains (modified from Whicher and MacKinnon, 2016).	9
Figure 1.3.	A full cryo-EM structure of rEAG with calmodulin bound in place (modified from Whicher and MacKinnon, 2016).	11
Figure 1.4.	A simulation model of the PAS-cap of hEAG1.	12
Figure 3.1.	Current traces of WT hEAG1 in control alongside the I/V protocol.	73
Figure 3.2.	Graphs showing the relationship of both current and conductance against membrane potential of WT hEAG1.	74
Figure 3.3.	Current traces and graph showing the time dependent effect of 5 μ M I&T on WT hEAG1 current.	76
Figure 3.4.	Current traces of WT hEAG1 >300s after the application of 5 μ M I&T.	77
Figure 3.5.	Graphs showing the effect of 5 μ M I&T on the relationship of both current and conductance against membrane potential of WT hEAG1.	78
Figure 3.6.	Data showing the response of WT and Δ 2-26 to changes in membrane voltage.	80

Figure 3.7.	Steady pulsing current data showing how $\Delta 2-26$ hEAG1 responds to $5\mu\text{M}$ I&T over time.	82
Figure 3.8.	Data showing the response of $\Delta 2-26$ hEAG1 to changes in membrane voltage following the application of $5\mu\text{M}$ I&T.	84
Figure 3.9.	A graph showing the effect of $5\mu\text{M}$ I&T on the current amplitude of WT and $\Delta 2-26$ hEAG1 with time.	85
Figure 3.10.	A homology model showing the residue orientation of the PAS-cap's amphipathic helix between the EAG and cNBH domains of hEAG1.	87
Figure 3.11.	Current traces of 6 PAS-cap mutants in control.	89
Figure 3.12.	I/V graphs of 6 PAS-cap mutants showing their response to increasing membrane potential.	90
Figure 3.13.	G/V graphs of 6 PAS-cap mutants showing their conductance response to increasing membrane potential.	92
Figure 3.14.	Current traces showing the inhibition of 6 PAS-cap mutants in response to $5\mu\text{M}$ I&T.	93
Figure 3.15.	Steady pulsing graphs showing the inhibition of 6 PAS-cap mutants in response to $5\mu\text{M}$ I&T over time.	95
Figure 3.16.	Current traces of 6 PAS-cap mutants in $5\mu\text{M}$ I&T.	97
Figure 3.17.	I/V graphs of 6 PAS-cap mutants showing how their I/V relationship changes with $5\mu\text{M}$ I&T.	99

Figure 3.18.	G/V graphs of 6 PAS-cap mutants showing how their G/V relationship changes with 5 μ M I&T.	102
Figure 3.19.	Data showing the response of WT and N15A hEAG1 to changes in membrane voltage.	104
Figure 3.20.	Steady pulsing data showing how the N15A hEAG1 current responds to 5 μ M I&T.	106
Figure 3.21.	Data showing the response of N15A hEAG1 to changes in membrane voltage following the application of 5 μ M I&T.	108
Figure 3.22.	Data showing the response of WT and F17A hEAG1 to changes in membrane voltage.	110
Figure 3.23.	Steady pulsing data showing how the F17A hEAG1 current responds to 5 μ M I&T.	112
Figure 3.24.	Data showing the response of F17A hEAG1 to changes in membrane voltage following the application of 5 μ M I&T.	114
Figure 3.25.	Data showing the response of WT and E600A hEAG1 to changes in membrane voltage.	117
Figure 3.26.	Steady pulsing data showing how the E600A hEAG1 current amplitude responds to 5 μ M I&T.	119
Figure 3.27.	Data showing the response of E600A hEAG1 to changes in membrane voltage following the application of 5 μ M I&T.	121
Figure 3.28.	Data showing the response of WT and E600R hEAG1 to changes in membrane voltage.	123

Figure 3.29.	Steady pulsing data showing how the E600R hEAG1 current amplitude responds to 5 μ M I&T.	125
Figure 3.30.	Data showing the response of E600R hEAG1 to changes in membrane voltage following the application of 5 μ M I&T.	127
Figure 3.31.	A cryo-EM structure displaying the distance in \AA between the N15 and E600 residues of hEAG1.	128
Figure 3.32.	Data showing the response of WT and N15E:E600N hEAG1 to changes in membrane voltage.	130
Figure 3.33.	Steady pulsing data showing how the N15E:E600N current amplitude changes over time in 5 μ M I&T.	132
Figure 3.34.	Data showing the response of N15E:E600N hEAG1 to changes in membrane voltage following the application of 5 μ M I&T.	134
Figure 3.35.	A cryo-EM structure showing the interaction distances from the Y198 between F17 and E600.	135
Figure 3.36.	Data showing the response of WT and Y198F hEAG1 to changes in membrane voltage.	137
Figure 3.37.	Steady pulsing data showing how the current amplitude of Y198F hEAG1 changes over time with 5 μ M I&T.	138
Figure 3.38.	Data showing the response of Y198F hEAG1 to changes in membrane voltage following the application of 5 μ M I&T.	140
Figure 3.39.	A cryo-EM structure showing the resolved section of the unstructured region of the PAS-cap and its potential interaction with E279.	141

Figure 3.40.	Data showing the response of WT and E279A hEAG1 to changes in membrane voltage.	143
Figure 3.41.	Steady pulsing data showing how the current amplitude of E279A hEAG1 changes over time with 5 μ M I&T.	144
Figure 3.42.	Data showing the response of E279A hEAG1 to changes in membrane voltage following the application of 5 μ M I&T.	146
Figure 4.1.	A graph comparison of the effect of 5 μ M I&T on the current amplitude of WT and Δ 2-26 hEAG1.	158
Figure 4.2.	Current traces of WT hEAG1 and pXoon showing the responses to the I/V protocol in CHO cells.	160
Figure 4.3.	I/V graphs of WT hEAG1 showing how the channel responds to voltage in CHO cells and oocytes.	161
Figure 4.4.	G/V graphs of WT hEAG1 showing how the conductance responds to voltage in CHO cells and oocytes.	162
Figure 4.5.	Steady pulsing data showing the response of WT hEAG1 to 5 μ M I&T when expressed in CHO cells.	164
Figure 4.6.	Steady pulsing data showing the difference in response of WT hEAG1 to 5 μ M I&T.	165
Figure 4.7.	Current traces elicited from the I/V protocol of Δ 2-26 hEAG1 showing how the channel responds to voltage in CHO cells.	166

Figure 4.8.	I/V graphs showing how $\Delta 2-26$ hEAG1 behaves in response to voltage in both CHO cells and oocytes.	167
Figure 4.9.	G/V graphs showing how the conductance of $\Delta 2-26$ hEAG1 behaves in response to voltage in CHO cells and oocytes.	168
Figure 4.10.	Steady pulsing data showing how $\Delta 2-26$ hEAG1 responds to $5\mu\text{M}$ I&T in CHO cells.	169
Figure 4.11.	Steady pulsing data comparing $\Delta 2-26$ hEAG1 in CHO cells and oocytes.	170
Figure 4.12.	A flow chart demonstrating the closed to open state transitions of hEAG1 channels.	171
Figure 4.13.	Graphs showing how the mean current and the variance change with decreasing P_{open} .	172
Figure 4.14.	Graphs showing how the mean current and the variance change with increasing P_{open} .	173
Figure 4.15.	Graphs showing how the variance data changes when N is reduced.	174
Figure 4.16.	Graphs showing how the variance data changes when N is increased.	175
Figure 4.17.	Graphs showing how the variance and mean current change upon reducing i .	176
Figure 4.18.	Graphs showing how the variance and mean current change upon increasing i .	177
Figure 4.19.	Mean-variance graphs showing how the WT hEAG1 variance is affected by the addition of $5\mu\text{M}$ I&T.	179
Figure 4.20.	Noise analysis data of $\Delta 2-26$ hEAG1 showing how the variance changes from control to $5\mu\text{M}$ I&T.	180

Figure 4.21.	An image panel showing the change in α -BTX fluorescence following the addition of 5 μ M I&T for 100 and 300s.	182
Figure 4.22.	Data showing how the WT channel surface expression responds to 5 μ M I&T.	182
Figure 4.23.	An image panel showing how the fluorescence of α -BTX changes after application of 5 μ M I&T for 60 and 300s to Δ 2-26 hEAG1-BBS expressing CHO cells.	184
Figure 4.24.	Data showing how the Δ 2-26 hEAG1 surface expression responds to 5 μ M I&T.	184
Figure 4.25.	Data showing the response of WT hEAG1-BBS to the I/V protocol in control solution when expressed in CHO cells.	186
Figure 4.26.	Steady pulsing data showing the response of WT hEAG1-BBS to 5 μ M I&T over time.	187
Figure 4.27.	Steady pulsing data showing how some individual cells expressing WT hEAG1-BBS responded to 5 μ M I&T.	188
Figure 4.28.	Data showing the response of Δ 2-26 hEAG1-BBS to the I/V protocol.	190
Figure 4.29.	Steady pulsing data showing how Δ 2-26 hEAG1-BBS responds to the addition of 5 μ M I&T.	191
Figure 4.30.	Steady pulsing data showing how different cells expressing Δ 2-26 hEAG1-BBS responds to the addition of 5 μ M I&T.	192
Figure 5.1.	An image panel showing the BrdU incorporation, GFP expression and Hoechst staining of the nuclei of the 8 plasmid constructs used in CHO cells.	201
Figure 5.2.	A bar chart showing the percentage of proliferating CHO cells in cultures transfected with the relevant hEAG1 constructs.	203
Figure 5.3.	An image panel showing the acetylated-tubulin staining (AlexaFluor-594) and the nuclei staining of hTERT-RPE1 cells transfected with the 8 proliferation constructs.	205
Figure 5.4.	A bar chart showing how different hEAG1 constructs affect the fraction of hTERT-RPE1 cells capable of producing a primary cilium.	207

Figure 5.5.	A bar chart showing how the hEAG1 constructs affect the length and width of the primary cilium in hTERT-RPE1 cells.	208
Figure 5.6.	Bar charts showing how different hEAG1 constructs affect the cell size and circularity of hTERT-RPE1 cells.	210
Figure 5.7.	An image panel showing the changes in Ca ²⁺ signal before and after the addition of 5μM I&T.	211
Figure 5.8.	The Ca ²⁺ response of untransfected CHO cells before and after 5μM I&T.	212
Figure 5.9.	An image panel showing the changes in Ca ²⁺ signal of CHO cells stably expressing WT hEAG1 before and after the application of 5μM I&T.	213
Figure 5.10.	The Ca ²⁺ response of CHO cells stably expressing WT hEAG1 before and after 5μM I&T.	214
Figure 5.11.	The Ca ²⁺ profile of untransfected CHO cells compared to the stably transfected WT hEAG1 CHO cell line.	215
Figure 5.12.	A Western blot from CHO cells transiently transfected with the hEAG1 constructs.	216
Figure 5.13.	Data showing how ΔEAG hEAG1 responds to the I/V protocol when expressed in CHO cells.	217
Figure 5.14.	Data from ΔEAG hEAG1 expressing CHO cells showing the response of the channel to 5μM I&T.	220
Figure 5.15.	Data showing how BD-N1 hEAG1 responds to the I/V protocol when expressed in CHO cells.	222
Figure 5.16.	Data from BD-N1 hEAG1 expressing CHO cells showing the response of the channel to 5μM I&T.	224
Figure 5.17.	There is a loss of function of ΔcNBHD hEAG1 when expressed in CHO cells.	226
Figure 5.18.	Data showing how E600R hEAG1 responds to the I/V protocol when expressed in CHO cells.	227
Figure 5.19.	Data from E600R hEAG1 expressing CHO cells showing the response of the channel to 5μM I&T.	229
Figure 5.20.	Data showing how BD-C2 hEAG1 responds to the I/V protocol when expressed in CHO cells.	230

Figure 5.21.	Data from BD-C2 hEAG1 expressing CHO cells showing the response of the channel to 5 μ M I&T.	232
Figure 5.22.	Data of WT hEAG1 showing how changing the extracellular solution from control (5mM K ⁺) to 140mM K ⁺ affects hEAG1 channel function.	234
Figure 5.23.	Steady pulsing data showing the change in WT hEAG1 current amplitude following the addition of 140mM [K ⁺] _e .	236
Figure 5.24.	Images of pXoon and WT hEAG1 transfected CHO cells at 6hr intervals during the migration assay in 0.1% FBS.	238
Figure 5.25.	An image panel showing the migration of pXoon and WT hEAG1 expressing CHO cells in 10% FBS.	240
Figure 5.26.	Effects of WT hEAG1 expression in CHO cells on track displacement length, track length and track duration.	241
Figure 5.27.	Effects of WT hEAG1 expression in CHO cells on track straightness, average speed and maximum speed.	243
Figure 5.28.	Effects of 0.1% and 10% FBS media on track displacement length, track length and track duration of pXoon and WT hEAG1 expressing CHO cells.	245
Figure 5.29.	Effects of 0.1% and 10% FBS media on track straightness, average speed and maximum speed of pXoon and WT hEAG1 expressing CHO cells.	247

List of abbreviations

HTR_{2A}	5-hydroxytryptamine receptor 2A
ACh	acetylcholine
ATP	adenosine triphosphate
BK	big potassium
BD	binding domain
BLI	bilayer interferometry
BrdU	bromodeoxyuridine
BTX	bungarotoxin
BBS	bungarotoxin binding site
Ca²⁺	calcium
CDI	calcium-dependent inactivation
apo-CaM	calcium-free calmodulin
CaM	calmodulin
CaMKII	calmodulin kinase 2
CDB	cell dissociation buffer
CNS	central nervous system
CHO	chinese hamster ovary
Cl⁻	chloride
CLS	ciliary localisation signal
G/V	conductance-voltage
CTTN	cortactin
cryo-EM	cryo-electron microscopy
I/V	current-voltage
cAMP	cyclic adenosine monophosphate
cGMP	cyclic guanosine monophosphate
cNBHD	cyclic nucleotide binding homology domain
CNG	cyclic nucleotide gated

DNA	deoxyribonucleic acid
DRM	detergent-resistant membrane
DAG	diacylglycerol
DEN	diethylnitrosamine
DMSO	dimethyl sulphoxide
K_D	dissociation constant
ER	endoplasmic reticulum
EGF	epidermal growth factor
EGFR	epidermal growth factor receptor
EAG	ether-a-go-go
ERG	ether-a-go-go related gene
ELK	ether-a-go-go-like potassium
EPSC	excitatory post-synaptic potential
FAK	focal adhesion kinase
Gli1	glioma-associated oncogene 1
GST	glutathione
GFG	glycine, phenylalanine, glycine
GYG	glycine, tyrosine, glycine
GFP	green fluorescent protein
HEK	human embryonic kidney
hEAG1	human ether-a-go-go 1
hERG	human ether-a-go-go related gene
HFFs	human foreskin fibroblasts
hTERT-RPE1	human telomerase reverse transcriptase retinal pigment epithelial 1
HCN	hyperpolarisation-dependent cyclic nucleotide-gated
ITIM	immune-receptor tyrosine inhibitory motif
INM	inner nuclear membrane
IP₃	inositol 1,4,5 trisphosphate
[Ca²⁺]_i	intracellular calcium concentration

I&T	ionomycin and thapsigargin
KO	knock out
V_m	membrane potential
mRNA	messenger ribonucleic acid
MβCD	methyl-β-cyclodextrin
MAPK	mitogen-activated protein kinase
mEAG	murine ether-a-go-go
NLS	nuclear localisation signal
NMR	nuclear magnetic resonance
NPC	nuclear pore complex
ONM	outer nuclear membrane
PAS	Per-Arnt-Sim
PCC	pericentrosomal preciliary compartment
PTEN	phosphatase and tensin homologue deleted on chromosome 10
PBS	phosphate buffered saline
PBS	phosphate buffered saline
PIP₂	phosphatidylinositol 4,5-bisphosphate
PLC	phospholipase C
PTO	phosphorothioate antisense oligonucleotide
PDGFRs	platelet-derived growth factor receptors
PCR	polymerase chain reaction
K⁺	potassium
pMEFs	primary mouse embryonic fibroblasts
rEAG1	rat ether-a-go-go 1
<i>p_r</i>	release probability
pRb	retinoblastoma protein
RNA	ribonucleic acid
siRNA	short interfering ribonucleic acid
Shh	Sonic hedgehog
SHP-1	Src-homology phosphatase 1

TBS	Temple-Baraitser syndrome
TRP	transient receptor potential
TEVC	two electrode voltage clamp
VEGF	vascular endothelial growth factor
WT	wild type
ZLS	Zimmermann-Laband syndrome

1. Introduction

1.1. Potassium channels have diverse properties and regulate a variety of cellular functions

There are over 70 different genes coding for individual potassium (K^+) channel subunits with the potential for different combinations forming homomeric or heteromeric channels (Jentsch, 2000; Gutman *et al.*, 2005). K^+ channels are membrane proteins whose main physiological role is to set a negative resting membrane potential (V_m). This is crucial for controlling cellular excitability, a role which is of the utmost importance in cell types such as neurons and cardiac myocytes where abnormalities in electrical excitability can have dangerous consequences such as epilepsy and long QT syndrome (Trimmer, 2015; Schmitt *et al.*, 2014).

Aside from their role in excitable cells, K^+ channels also have well documented roles in non-excitabile cells including lymphocytes where voltage-gated $K_v1.3$ channels are involved in the production of some cytokines and lymphocyte proliferation (Koshy *et al.*, 2014). Pathologies of the immune system such as multiple sclerosis have been linked to overexpression of this channel (Vianna-Jorge and Suarez-Kurtz, 2004). Some channels such as the inward rectifier $K_{IR4.1}$, are involved in maintaining an osmotic gradient via the efflux of K^+ ions, as the ions flow down their electrochemical gradient water molecules follow causing a reduction in cell volume. $K_{IR4.1}$ is expressed in the glial cells of the brain and retina. Transient ischaemia provokes a down regulation of this channel leading to severe swelling due to intracellular accumulation of K^+ (Pannicke *et al.*, 2004).

Whilst the majority of K^+ channel activity depends upon changes in membrane potential, there are many which additionally rely on a variety of other cellular changes – which differ depending on the channel. The ATP sensitive K^+ channel (K_{ATP}) channel detects changes in intracellular adenosine triphosphate (ATP) concentration to modulate its activity. K_{ATP} allows the flow of K^+ ions in low ATP conditions but is inhibited by the binding of ATP as it is synthesised and the concentration increases. This inhibits the flow of K^+ ions and so makes the

membrane potential more positive. Dysfunction of this channel has been implicated in heart disease and diabetes (Foster and Coetzee, 2016; Koster *et al.*, 2005).

Some K⁺ channels such as the acetylcholine-activated K⁺ channel (K_{ACh}) in the heart are regulated by the βγ subunit of G-proteins. The subunit binds directly to the channel and increases its activity thus having an inhibitory effect on the excitability of cardiac myocytes (Logothetis *et al.*, 1987; Krapivinsky *et al.*, 1995). Other channels can also respond to changes in intracellular calcium ([Ca²⁺]_i) with Ca²⁺ ions binding directly to regulatory domains – such as in Big Potassium (BK) channels where ions bind to an intracellular aspartate bowl. The binding of Ca²⁺ ions activates the BK channels causing an increase in K⁺ efflux (Ledoux *et al.*, 2006).

Human ether-a-go-go 1 (hEAG1), also known as K_v10.1 or KCNH1 is the founding member of the EAG family of K⁺ channels. It is a voltage-gated, non-inactivating K⁺ channel almost exclusively and highly expressed in the central nervous system (CNS), specifically the cerebral cortex, hypothalamus, cerebellum and hippocampus but not in the corresponding glial cells (Issy *et al.*, 2014). Studies so far suggest that in the CNS, hEAG1 contributes to synaptic efficiency and transmission during long trains of action potentials (Mortensen *et al.*, 2015). Knock-down experiments in zebrafish show a severe disruption in CNS development (Stengel *et al.*, 2012). However, knock-out experiments in mice show that fetuses are viable and develop no significant CNS differences – both morphologically and electrically – compared to their WT counterparts. hEAG1 expression begins after birth and reaches a maximum in adult mice and there are no detected compensatory upregulation of other channels in the KO mice (Ufartes *et al.*, 2013). This would indicate that in higher organisms the role of hEAG1 in development is not vital and may be an example of system redundancy or that the channel is required under specific conditions. hEAG1 is another example of an ion channel regulated by [Ca²⁺]_i. Ca²⁺ ions bind to calmodulin which in turn interacts with the intracellular domains of hEAG1 leading to inhibition of the channel. This difference between the regulation of BK and hEAG1 channels by Ca²⁺ ions shows that K⁺ channels are not targeted equally by the same effector (Schönherr *et al.*, 2000).

1.2. Intracellular structures of hEAG1 regulate channel gating and Ca²⁺ sensitivity

hEAG1 belongs to the large family of voltage-gated K⁺ channels, are tetrameric, with each subunit sharing the same transmembrane structure consisting of 6 transmembrane α helices (Figure 1.1).

The voltage-sensing domain of hEAG1, as well as many K⁺ channels, is formed from S1-S4 and the K⁺ selective pore is formed by the co-assembly of the S5-S6 domains from the four channel subunits. The S1-S4 domain contains charged amino acids that sense a change in voltage across the membrane causing a conformational change in the channel as the helices move relative to the voltage. Depolarisation causes an alteration in the conformation of the voltage sensor that is linked to the opening of the channel pore and the efflux of K⁺, whilst hyperpolarisation has the opposite effect. S5 and S6 are connected via a P-loop that forms and positions the K⁺ selectivity filter, which is usually a GYG motif but is a GFG motif in the case of hEAG1, that in the tetrameric channel, creates an oxygen cage of the correct dimensions to selectively pass K⁺ ions and exclude others (Schönherr *et al.*, 2000).

S6 forms the inner helices of the pore, which bend at the flexible hinge position, allowing cytoplasmic ends of the inner helices to “splay” apart to open the pore. S6 thus forms the activation gate of the channel.

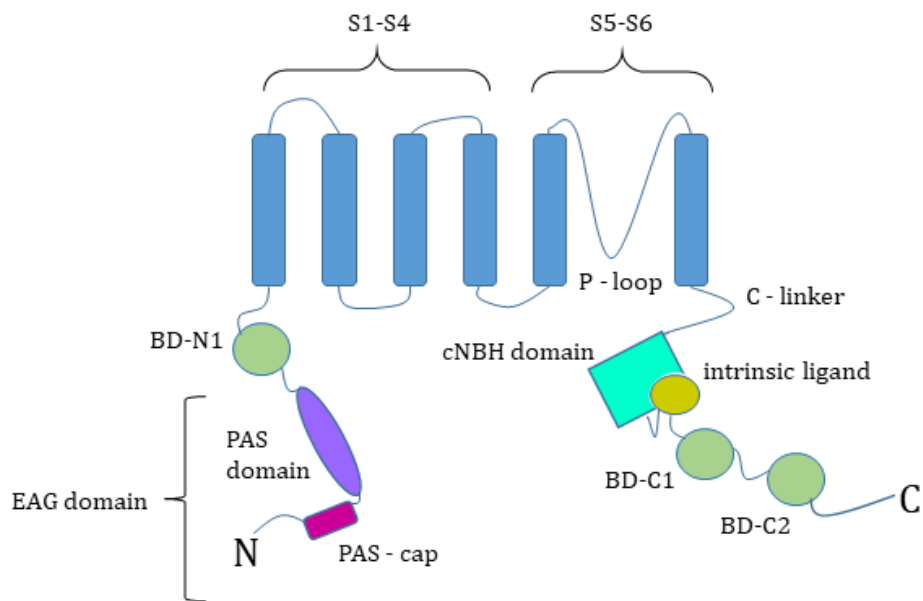


Figure 1.1. A cartoon diagram showing the membrane topology and intracellular domains of a monomer of hEAG1.

The membrane spanning region of the channel consists of 6 transmembrane domains, with S1-S4 being the voltage sensor domain containing charged amino acids and S5-S6 being the pore forming subunits.

The P-loop lines part of the pore when the channel is in its tetrameric conformation and contains the selectivity filter.

hEAG1 has a substantial intracellular structure, containing 3 calmodulin binding sites (BD-N1, BD-C1 and BD-C2) as well as a cNBHD and an EAG domain.

1.2.1. hEAG1 has unique intracellular structures shared by the EAG family

The EAG family of K⁺ channels consists of 3 subfamilies; EAG – consisting of EAG1 and EAG2 –, ether a-go-go related gene (ERG, K_v11) – ERG1 to 3 –, and EAG-like potassium (ELK, K_v12) – ELK1 to 3. This family of channels has a highly conserved subset of intracellular domains that regulate their activity including an N-terminal EAG domain and a C-terminal cyclic nucleotide binding homology domain (cNBHD). hEAG1 additionally contains 3 Ca²⁺-calmodulin binding domains, 1 in the N-terminus and 2 in the C-terminus (Morais-Cabral and Robertson, 2015) (Figure 1.1).

1.2.2. hEAG1 shows no sensitivity to cyclic nucleotides

hEAG1 is somewhat related to both cyclic nucleotide gated (CNG) and hyperpolarisation-dependent cyclic nucleotide-gated nonselective cation (HCN) channels. This is because it contains a cNBHD that has a degree of sequence homology to the cyclic nucleotide binding domain found in CNG and HCN channels (Carlson *et al.*, 2013b). The cNBD in CNG and HCN channels allows them to alter their activity based on the intracellular concentrations of cyclic nucleotides including cAMP and cGMP (Craven and Zagotta, 2006).

The cNBHD of hEAG1 has no physiologically relevant sensitivity to cyclic nucleotides, with K_D values >50μM. This lack of sensitivity is down to the loss of conservation throughout the EAG family of the residues present in CNG and HCN that are required for cyclic nucleotide binding (Marques-Carvalho *et al.*, 2012). Instead, two residues - Y672 and L674 - originate from a portion of the C-terminus and occupy the space where a cyclic nucleotide would bind. These residues are highly conserved in the EAG family. Because of the C-terminal origin of these residues, the channel is said to be “self-liganded”. This is known as the intrinsic ligand and it almost exactly conforms to the dimensions of a cyclic nucleotide (Morais-Cabral and Robertson, 2015). The combination of the intrinsic ligand and lack of conserved cyclic nucleotide binding residues is what renders hEAG1 insensitive to cyclic nucleotides.

Substituting Y672 and L674 for alanine residues displaces the intrinsic ligand and causes the voltage dependence of activation to shift to more depolarised

potentials. This points to a physiological role for the intrinsic ligand as being involved in gating kinetics (Carlson *et al.*, 2013a).

1.2.3. The PAS domain is an important regulator of ERG channel function

The EAG domain of hEAG1 comprises the first 135 residues of the protein. It is further broken down into a Per-Arnt-Sim (PAS) domain (27-135) and a PAS-cap (1-26). PAS domains are common structural domains named after the proteins in which they were discovered (Moglich *et al.*, 2009). They are found in a wide variety of different proteins, which are known for facilitating protein-protein interactions but have also been shown, in some cases to bind to small molecules and detect changes in the local chemical environment such as the redox potential (Taylor and Zhulin, 1999) and even changes in light when associated co-factors absorb blue light (Moglich *et al.*, 2009). Therefore the domain's presence in hEAG1 is interesting as it indicates the N-terminus may be able to interact with other peptides and cofactors. A crystal structure has been reported for the murine EAG (mEAG) channel PAS domain (Adaixo and Morais-Cabral, 2010) that bears similarity to the NMR derived structures of the hERG PAS domain (Morais-Cabral and Robertson, 2015). These PAS domains have no assigned small molecule to which they bind, however a cavity of varying shape and volume is present within them (Morais-Cabral and Robertson, 2015).

PAS domain stoichiometry has been documented as an important factor in ERG channel regulation. There exists an alternatively spliced isoform of ERG (ERG1b) that is missing the PAS domain. This isoform can co-assemble with the isoform containing the PAS domain (ERG1a), thereby altering the number of PAS domain present in the tetramer. Heterotetramers activate and deactivate with faster kinetics than the ERG1a homomer and loss of function of the ERG1b isoform in cardiac cells, due to mutation, has been associated with long QT syndrome (Sale *et al.*, 2008). Mutagenesis to delete the PAS-cap in hERG showed the same acceleration of deactivation kinetics (Muskett *et al.*, 2011). The close sequence homology between EAG and ERG suggests that the PAS domain in EAG has a key role in dictating channel kinetics.

1.2.4. The EAG and cNBH domains interact to regulate channel activity

Deleting the entire EAG domain and even just the PAS-cap has dramatic effects on gating kinetics in hERG and cancer-associated mutations in the EAG domain of hEAG1 also affect its gating kinetics (Gianulis *et al.*, 2013; Morais-Cabral and Robertson, 2015). Gustina and Trudeau (2011) made a hERG channel mutant that lacked the cNBHD. With this they revealed the same trend as shown by the EAG domain deletions – an acceleration of gating kinetics – which indicates that there is an EAG-cNBHD interaction that is important for channel gating. Mutations in both the EAG and cNBH domains together had no additive effect on gating, meaning that they are likely interaction partners as opposed to controlling gating via 2 distinct mechanisms.

Fluorescence anisotropy showed that purified mEAG and cNBH domains interacted with an affinity of $13.2 \pm 2.3 \mu\text{M}$. Resolution of a crystal structure to 2\AA shows 4 EAG domains and 4 cNBHDs from the mEAG channel in a 1:1 stoichiometry, and an extensive contact surface with a total buried surface area of 1440\AA^2 . This biological unit shows the 2 domains packing against one another forming an interface between them. Mutations associated with cancer and those that cause changes in channel gating cluster around this interface adding weight to the argument that they are interacting partners and that disruption of this interaction may be pathogenic (Haitin *et al.*, 2013).

The E600 residue of hEAG1 (E627 in mEAG) has been studied in the Mitcheson lab. It lies along the interface proposed by Haitin *et al.* (2013) and is in close proximity to the amphipathic helix found within the PAS-cap – which was documented in hERG using NMR (Muskett *et al.*, 2011) – indicating that this is one of the residues involved in bridging the EAG-cNBHD interaction.

Until recently there existed no structure containing the C-linker (which connects the cNBHD to the S6 domain), the distal C-terminus (in which 2 of the 3 Ca^{2+} -calmodulin binding domains reside). Whicher and MacKinnon (2016) have since published a cryo-electron microscopy (cryo-EM) structure of the entire rEAG ion channel with calmodulin bound in-place. This is a novel and exciting structure as it shows the EAG and cNBHD interaction as well as how the C-linker interacts with the

pore structure and intracellular domains (Figure 1.2). The structure clearly shows that the C-linker interacts with both the S5-S6 transmembrane region and the cNBHD, with the cNBHD sitting directly beneath the C-linker domain. The PAS domain interacts almost exclusively with the cNBHD and is situated to one side and away from the pore structure (Figure 1.2a and b).

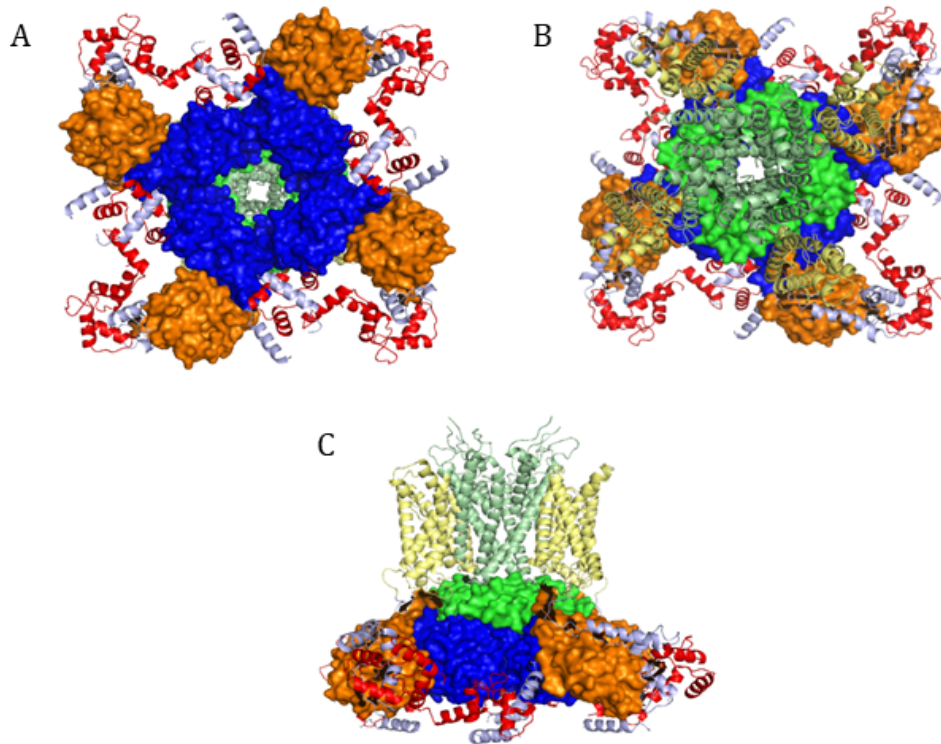


Figure.1.2. The full cryo-EM structure of rEAG showing the interactions between the main intracellular domains (modified from Whicher and MacKinnon, 2016).

A: a view of rEAG from the intracellular side looking up through the pore. The EAG domain (orange), cNBHD (blue) and the C-linker (green) are shown. Calmodulin is shown in red.

B: a 180° rotation of A to show the domains from the top view of the channel

C: a side view of the channel showing S1-S4 (pale yellow) and the S5-S6 (pale green) domains. The EAG domain (orange), cNBHD (blue) and the C-linker (green) are also shown interacting with one another: Calmodulin is shown for reference in red.

Data has shown the affinity of Ca^{2+} -calmodulin for the 3 binding domains and the Whicher and MacKinnon (2016) structure shows where calmodulin is binding to the channel (Figure 1.3). The stoichiometry of this is one calmodulin module per subunit monomer, so that 4 calmodulins in total can bind to the channel (Figure 1.3b). It appears from the structure that a single calmodulin monomer can span from the BD-N1 of one subunit to the BD-C1 and BD-C2 of an adjacent subunit (Figure 1.3a) as opposed to previous suggestions that calmodulin binds only in an intra-subunit manner. The ability of calmodulin to do this may be the reason that hEAG1 experienced such a dramatic inhibition in response to raised Ca^{2+} . The calmodulin bridges between two monomers and pulls the subunits together, potentially resulting in a much more tightly packed structure than is usually experienced in the closed state.

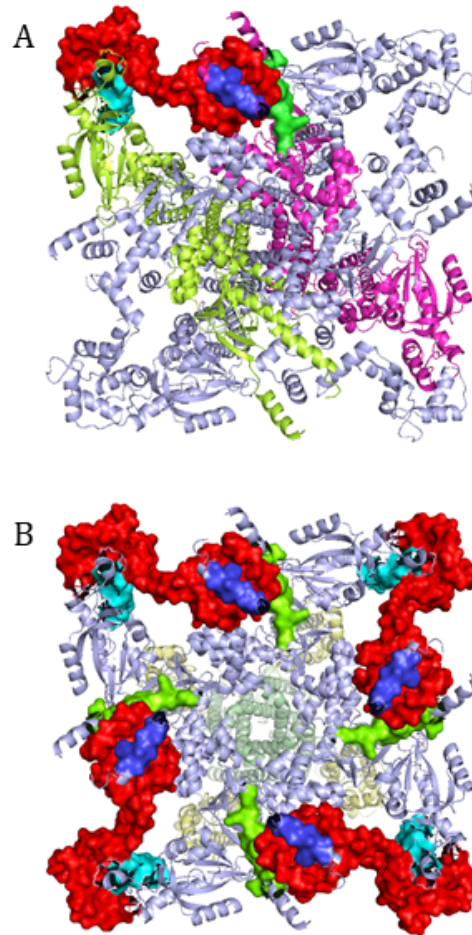


Figure.1.3. A full cryo-EM structure of rEAG with calmodulin bound in place (modified from Whicher and MacKinnon, 2016)

A: a underside view of the channel showing calmodulin (red) spanning two subunits (lime green and pink) by binding to the BD-N1 domain (cyan) of one subunit and BD-C1 and BD-C2 (green and purple respectively) of the other

B: a full underside structure of the channel showing all four calmodulin molecules bound in place and holding the channel in a closed pore conformation.

The recent cryo-EM structure from Whicher and MacKinnon (2016) has given insight into the interaction of the intracellular domains of hEAG1 but it has also, for the first time, resolved the structure of the PAS-cap in relation to the rest of the channel domains. Previous structures have relied on isolated domains or simulation modelling to provide insight (Haitin *et al.*, 2013; Lorinczi *et al.*, 2016) as shown in Figure 1.4. The PAS-cap contains an unstructured region (residues M1 to P13) and a structured amphipathic helix (residues Q14 to N26) (Figure 1.4). The cryo-EM structure shows that the PAS-cap largely sits on top of the EAG domain, with some contact surface with the cNBHD (Figure 1.4). This agrees with previous data that the PAS-cap interacts with the EAG and cNBH domains. Part of the unstructured region of the PAS-cap has also been resolved in this structure and shows it reaching up towards the transmembrane domains (Figure 1.4). The unstructured region is unfortunately not completely solved so there is still a degree of uncertainty as to its exact position relative to other channel domains.

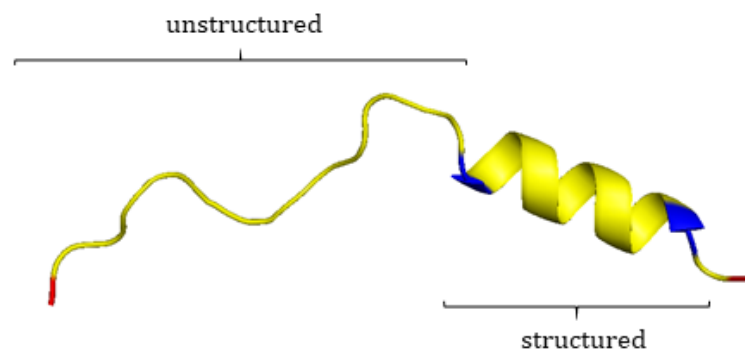


Figure.1.4. A simulation model of the PAS-cap of hEAG1.

This is a simulation model – based off of the crystal structure provided by Zagotta *et al* – showing the structured and unstructured regions of the PAS-cap. Residues M1 and N26 at the start and end of the PAS-cap respectively are indicated in red whilst residues Q14 and R24 at the start and the end of the amphipathic helix respectively are shown in blue.

1.3. The role of hEAG1 in the CNS and its regulation of and by other molecules and proteins

The exact physiological and pathophysiological roles of hEAG1 have not yet been identified. hEAG1 shows a high level of expression throughout the CNS but does not feature significantly anywhere else in the body. This has lead researchers to focus on its potential role in neurons and assess its protein-protein interactions as well as its interactions with small molecules. hEAG1 has been shown to directly interact with calmodulin as well as a wide range of other proteins (Schönherr *et al.*, 2000; Lorinczi *et al.*, 2016). These other proteins include rabaptin-5, cullin 7 and cortactin but also extends to include phospholipids (Ninkovic *et al.*, 2012; Hsu *et al.*, 2017; Herrmann *et al.*, 2012; Han *et al.*, 2016).

1.3.1. The physiological role of hEAG1 is required during repetitive neuronal activity

Mortensen *et al.* (2015) used rat cerebellum and the mAb62 anti-K_v10.1 antibody to show that there is an asymmetric distribution of hEAG1 between the soma and synaptic terminals of parallel fibres. The highest staining was seen at the synapse from the parallel fibres onto the Purkinje cell spines. hEAG1's location was further investigated biochemically using subcellular fractionation with hEAG1 being present in the synaptosomal fraction. hEAG1 along with other presynaptic markers was protected from proteolysis indicating that the primary area of hEAG1 expression is presynaptic.

1.3.1.1. Activity in the post-synaptic terminal is not affected by the loss of hEAG1

It has already been shown that K⁺ play a critical presynaptic role, K_v7 channels have been shown to set the resting membrane potential of the Calyx of Held in rat brains and were also demonstrated to decrease the synaptic release probability (p_r) of the synapse (Huang and Trussell, 2011). K_v3 channels contribute to the duration of action potentials in parallel fibres of mice and they also limit the frequency of action potential firing, thus allowing the correct encoding of information (Matsukawa *et al.*, 2003).

Mortensen *et al.* (2015) expanded on this information and tested whether WT or K_v10.1-KO mice showed differences in their synaptic transmission. They showed that the interval between synaptic events was no different in the WT

compared to the KO indicating that the basal p_r and the resting Ca^{2+} concentration were not affected by the lack of hEAG1. The amplitude of the excitatory post-synaptic current (EPSC) was also not changed between WT and KO mice meaning that the post-synaptic compartment is not affected by the loss of hEAG1.

1.3.1.2. Accurate high frequency action potential firing is dependent on hEAG1

Two-photon Ca^{2+} imaging by Mortensen *et al.* (2015) showed that single action potentials elicited by injection of current pulses lead to a transient increase in the fluorescent signal in both WT and KO mice. Increasing the number of action potentials doubled the fluorescence in both models whilst increasing the frequency from 50Hz to 100Hz did not cause any further change in the WT mouse. However increasing the frequency to 100Hz in the KO increased the peak fluorescence indicating that hEAG1 could be repolarising action potentials based on the frequency of action potentials.

Mortensen *et al.* (2015) have showed that the initial p_r is not altered between WT and KO mice which means hEAG1 is not involved in repolarising single action potentials. However, they showed increasing hEAG1 currents in HEK cells following repeated stimulations of 50Hz to mimic action potentials. This indicates that hEAG1 activates during trains of action potentials and contributes to repolarisation under these conditions. Trains of action potentials are likely to cause inactivation of other K_v channels. However, hEAG1 does not inactivate and the repeated depolarisations will accelerate activation kinetics, increasing the amount of hEAG1 current. This will allow the accurate encoding of information at high frequency firing.

1.3.2. hEAG1 localises to the plasma membrane but is also present in the inner nuclear membrane

hEAG1 has been shown to express as a plasma membrane protein from GFP-tagged proteins and patch clamp experiments (Schönherr *et al.*, 2000; Goncalves and Stuhmer, 2010). Some antibody staining experiments have also shown signals around the nuclear envelope of HEK293 cells transiently expressing hEAG1 (Goncalves and Stuhmer, 2010). This lead to the question of whether hEAG1 is functional in this location.

The nuclear envelope is a 2-layer membrane structure that encloses the nucleus, it is formed of the outer nuclear membrane (ONM), the inner nuclear membrane (INM) and the perinuclear space sits between them. Structurally the ONM is connected to the endoplasmic reticulum (ER) but shows a completely different protein composition. The perinuclear space is an extension of the lumen of the ER (Schirmer and Gerace, 2005). There is debate as to whether the nuclear pore complex (NPC), which allows the trafficking of soluble molecules <40kDa, has any permeability to ions. If not, then a potential difference will be set up across the nuclear envelope between the cytoplasm and the nucleoplasm (Chen *et al.*, 2011).

Other ion channels have been discovered to have INM expression including Cl⁻ channels and a channel able to conduct both Ca²⁺ and Zn²⁺ ions (Rousseau *et al.*, 1996; Longin *et al.*, 1997). Based on this knowledge, Chen *et al.* (2011) conducted extensive *in vitro* immunostaining for hEAG1 in neurons, transfected cells and tumour cell samples as well as monitoring hEAG1 *in vivo* using the fluorescent label DsRed in a range of different cell types. These experiments showed that depending on the cell line used there was between 20-40% showing perinuclear staining. This included cell lines that express endogenous hEAG1 meaning that its presence in the INM is not an artefact of overexpression systems. The presence of hEAG1 in the INM was confirmed by co-localisation staining for endogenous hEAG1 protein in HeLa cells, which have high endogenous expression of hEAG1, and staining of lamin A/C – proteins known to be present in the INM. hEAG1 contains a nuclear localisation signal (NLS) in its C-terminus which are present in many proteins targetted to the nucleus. In this case deletion of the NLS did not abolish the perinuclear staining of hEAG1 whilst preserving the electrophysiological properties and so the NLS is not necessary for the presence of hEAG1 in the INM.

The INM localisation was further characterised by using Triton X-100 – if the protein shows resistance to extraction it indicates an INM localisation due to changes in the lipid to protein ratio. Triton X-100 removed all hEAG1-mVenus fluorescent signals from the cytoplasm but did not affect the signal from the perinuclear region. Subcellular fractionation of isolated rat brain nuclei showed that after removal of the ONM by citraconic anhydride, the nuclear fraction showed high levels of hEAG1 as well as lamina-associate polypeptide 2 – a well-known INM

protein (Dechat *et al.*, 2000). This suggests that hEAG1 is present in the INM in physiological conditions of rat brain samples and is not just an artefact of overexpression. This indicates that hEAG1 has a physiological role at the INM in tissues that express it and may be part of the mechanism by which hEAG1 influences cancer cell proliferation.

1.3.2.1. hEAG1 is transported to the INM from the plasma membrane and is functional

Chen *et al.* (2011) went on to ask whether hEAG1 is targeted to the INM directly from the ER or whether it is first trafficked to the plasma membrane and later transported back to the INM. Surface biotinylation assays of hEAG1-expressing HEK293 cells showed that biotinylated hEAG1 was present in nuclear fractions and that it was resistant to extraction by Triton X-100 indicating that modified hEAG1 is transported back from the plasma membrane to the INM.

The presence of hEAG1 protein in the INM has been established but this does not indicate whether or not it is functional. Chen *et al.* (2011) continued their study by recording single channel currents from isolated HEK293 cell nuclei. They removed the ONM to expose the INM where hEAG1 was shown to be present and used EGTA throughout the purification process to try and remove calmodulin from hEAG1. NPC blockers were also used to uncover the smaller currents of hEAG1. Channel activity fitting that expected of hEAG1 was detected, the activation time constant was dependent on the pre-pulse potential and the current was inhibited by 5 μ M astemizole indicating that the channel responsible was hEAG1.

Whilst hEAG1 is present and functional at the INM, it is unclear what its role there may be. It has been suggested that proteins in the INM may alter gene expression by binding to and sequestering transcription activators or repressors but also by having a more direct role by binding to chromatin (Heessen and Fornerod, 2007). Plasma membrane hEAG1 has been shown to relocate to the INM and this may be important for the channel's role in cancer by altering gene expression. Reductions in intracellular K⁺ concentrations have been linked to the destabilisation of the DNA G-quadruplex structure which normally prevents the transcription of the genes around it. This destabilisation allows the affected genes to be transcribed and is therefore a potential mechanism for how hEAG1 could affect

gene expression (Tateishi-Karimata *et al.*, 2018). This would not be too dissimilar to voltage-gated Ca²⁺ channel where the C-terminal end can be cleaved and goes on to act as a transcription factor (Gomez-Ospina *et al.*, 2006).

1.3.3. hEAG1 is found in both detergent-resistant and non-detergent-resistant membrane domains

There is an increasing body of evidence that ion channels are specifically targeted to discrete locations within the plasma membrane. This separation acts to contain electrical excitability, as is the case with various neuronal K⁺ channels (O'Connell and Tamkun, 2005), but may also have a role in grouping members of a signalling cascade together. The plasma membrane can be divided into two main fractions, detergent-resistant membrane (DRM) and non-detergent-resistant membrane (non-DRM) (Jimenez-Garduno *et al.*, 2014). DRMs – also called lipid rafts – have a much higher lipid to protein ratio than other regions of the membrane (Magee and Parmryd, 2003). These regions bring together membrane components of signalling cascades so the efficiency of that cascade is improved (Simons and Toomre, 2000). Some ion channels, including BKCa, TRP1, Kv1.3 and Kv2.1 have been found to be exclusive to DRMs (Bravo-Zehnder *et al.*, 2000; Lockwich *et al.*, 2000; Bock *et al.*, 2003; Martens *et al.*, 2000) whilst others such as Kv3.2 and Kv4.2 are excluded from the DRM domains (Xia *et al.*, 2007; Martens *et al.*, 2000).

hEAG1 is found in both the DRM and non-DRM fractions of mice neurons which indicates that hEAG1 exists in at least two separate fractions (Jimenez-Garduno *et al.*, 2014). This raises the possibility that hEAG1 existing in different membrane regions and means that hEAG1 may be part of separate signalling cascades.

1.3.3.1. hEAG1 distribution is influenced by Ca²⁺-calmodulin

Jimenez-Garduno *et al.* (2014) showed that the distribution of hEAG1 between the DRM and non-DRM fractions is influenced by the interaction of Ca²⁺-calmodulin. WT hEAG1 has a DRM/non-DRM ratio of 0.79 ± 0.13 , whilst a mutant version of hEAG1 that is lacking the second C-terminal calmodulin binding domain has reduced DRM/non-DRM ratio of 0.23 ± 0.04 . This data shows that the binding of Ca²⁺-calmodulin to hEAG1 helps to sequester the channel in the DRM fraction of

the membrane, which may have consequences for signalling cascades featuring hEAG1.

1.3.3.2. The composition of the membrane affects hEAG1 current density

Cholesterol is a component of the DRM membrane fraction and has been shown to influence the kinetics of other ion channels (Levitan *et al.*, 2010). Depletion of membrane cholesterol in HEK293T cells using methyl- β -cyclodextrin (M β CD) did not affect which fraction hEAG1 was found in. However, Jimenez-Garduno *et al.* (2014) showed that the current density of hEAG1 increased 2-fold after incubation with M β CD but that the 20-80% rise time was not changed following cholesterol depletion. This is interesting as it suggests that the lipid composition of the membrane can alter the activity of hEAG1, depending on which subdomains it is sequestered in. It has already been shown that Ca²⁺-calmodulin moves hEAG1 to DRM regions (Jimenez-Garduno *et al.*, 2014) so it could be that other proteins also have this effect to modulate hEAG1 activity and cascades it is involved with.

1.3.4. hEAG1 binds to and activates calcium-calmodulin dependent kinase II (CaMKII)

CaMKII is a protein kinase targeting serine/threonine residues of its effector proteins and its activity is regulated by the binding of the Ca²⁺-calmodulin complex. CaMKII has been shown previously to regulate neuronal excitability and the activity of ion channels (Liu and Murray, 2012). EAG1 has already been shown to be an *in vivo* target of CaMKII in *Drosophila* neurons where it phosphorylates the T787 residue of dEAG1 and likely influences dEAG1's role at the neuromuscular junction (NMJ) (Wang *et al.*, 2002). In oocyte studies this phosphorylation was shown to increase the current amplitude vs a T787A mutation where CaMKII had no effect on hEAG1 current (Wang *et al.*, 2002).

1.3.4.1. hEAG1 and CaMKII exist in a complex in neurons

Sun *et al.* (2004) conducted a study in which they wanted to find out if CaMKII could locally regulate EAG function. They showed that *Drosophila* EAG and CaMKII were part of a complex existing in neurons by immunoprecipitation from WT flies. Flies that lacked expression of EAG (*eag*^{sc29}) did not precipitate CaMKII, however precipitation performed in the presence of Ca²⁺ as opposed to EGTA/EDTA,

enhanced the amount of CaMKII that co-precipitated with WT EAG. This would indicate that Ca²⁺ may improve the interaction between the two proteins.

1.3.4.2. Ca²⁺-calmodulin is needed initially for CaMKII to interact with hEAG1

Sun *et al.* (2004) was the first to show that CaMKII interacted with the C-terminal end of EAG, residues 556-1174, and this interaction relied on the presence of Ca²⁺-calmodulin because the C-terminal fragment and CaMKII could not interact in an EGTA-buffered solution (Sun *et al.*, 2004). However, when CaMKII and the C-terminal fragment were first placed in a solution containing Ca²⁺-calmodulin and then washed in EGTA, the CaMKII-C-terminus (556-1174) complex is stable even after the removal of calmodulin by EGTA washes, indicating that the EAG-CaMKII interaction may persist and be physiologically relevant even after Ca²⁺ levels return to basal levels. In light of this, it is necessary for CaMKII to be activated by Ca²⁺-calmodulin in order for it to be able to interact with EAG. Sun *et al.* (2004) showed this by using a mutant CaMKII (T306D/T307D) that cannot bind to calmodulin and was shown to be unable to bind to EAG under any Ca²⁺ or EGTA conditions. The T287D mutation leaves CaMKII constitutively active and able to bind EAG in the absence of calmodulin, indicating that calmodulin is needed to activate WT CaMKII to allow the binding to EAG.

1.3.4.3. CaMKII activity continues in the absence of Ca²⁺-calmodulin

The group also went on to monitor kinase activity once bound to EAG using radioactive phosphate groups from [$\gamma^{32}\text{P}$]-ATP. Unbound, soluble CaMKII was able to autophosphorylate in the presence – but not the absence – of Ca²⁺-calmodulin. CaMKII was then bound to the C-terminal fragment of EAG in the presence of Ca²⁺-calmodulin, the complexes were then washed with EGTA solution to removed calmodulin. The EAG-CaMKII complex without calmodulin was able to both autophosphorylate and also phosphorylate EAG indicating that Ca²⁺-calmodulin is needed to stimulate the activation of CaMKII and therefore its interaction with EAG but is not necessary once the complex has been formed.

The evidence provided here by Sun *et al.* (2004) points towards EAG being a scaffold and activator of CaMKII. CaMKII phosphorylates EAG causing an increase in

K⁺ current. The interaction tethers CaMKII at the plasma membrane and holds it close to a variety of substrates. Sun *et al.* (2004) note that this interaction with EAG changes the localisation of CaMKII to the membrane where it is in close proximity to other membrane proteins and their interacting partners – thus creating defined subcellular domains that rely less on global cellular changes and more on local changes. The ability of CaMKII to remain bound to EAG and active after the removal of calmodulin may indicate a persisting signalling pathway, which in *Drosophila* neurons could indicate neuronal plasticity.

1.3.5. hEAG1 interacts with and is regulated by PIP₂

Phosphatidylinositol 4,5-bisphosphate (PIP₂) is one of several phospholipids that consist of a negatively charged head group and two fatty acid tails. PIP₂ is found in the inner leaflet of the membrane and forms the precursor for diacylglycerol (DAG) and inositol 1,4,5 trisphosphate (IP₃), which are produced following breakdown of PIP₂ by phospholipase C (PLC) (Han *et al.*, 2016). PIP₂ is not just a precursor and has important roles of its own including the modulation of ion channels (Suh and Hille, 2008). PIP₂ increases the phosphatase activity of the membrane-associated tumour suppressor PTEN (phosphatase and tensin homologue deleted on chromosome 10) and increases its association with the membrane (Gericke *et al.*, 2013). PIP₂ is also involved in the transmission of electrical signals in the spiral ganglion neurons that relay information from the cochlear hair cells. Here, PIP₂ regulates the activity of heteromeric K_v1.1 and K_v1.2 potassium channels to fine tune the output from the cochlear nerves (Smith *et al.*, 2015).

1.3.5.1. PIP₂ inhibits hEAG1 channels

Han *et al.* (2016) provided a body of evidence that both exogenous and endogenous PIP₂ inhibits the hEAG1 current. Addition of 3 μM brain-derived PIP₂ caused a rapid and large inhibition of hEAG1 current when applied to the intracellular side of excised patches. The IC₅₀ for hEAG1 inhibition was $0.35 \pm 0.01 \mu\text{M}$. The group also tested an analogue of PIP₂, diC8-PIP₂, which also inhibited the channel but with an IC₅₀ value of $18.6 \pm 0.6 \mu\text{M}$. PIP₂ is a 12-carbon chain fatty acid whilst diC8-PIP₂ has an 8-carbon fatty acid tail. The IC₅₀ differences indicate that the length of the carbon chain is important for the role of PIP₂.

Han *et al.* (2016) also showed that hEAG1 is under tonic modulation by endogenous PIP₂. They set up a hEAG1 stable HEK293T cell line and a rapamycin-induced translocation system that uses a GFP labelled PLC enzyme (PLC-GFP) which is bound to the PIP₂ at the membrane. The rapamycin translocation system is designed as a genetic tool whereby addition of rapamycin induced the translocation of phosphoinositide 5'-phosphatase (PI 5'-phosphatase) to the membrane. Here it rapidly removes the 5' phosphate from PIP₂ thereby degrading it and removing its influence. The degradation of PIP₂ was monitored by a GFP-tagged PLC δ enzyme. 100nM rapamycin induced a translocation of the GFP signal away from the membrane – indicating that PIP₂ had been broken down by the PI 5'-phosphatase – but also showed an increase in hEAG1 current as measured by whole cell patch clamp. This data shows that hEAG1 is under tonic regulation by PIP₂ in these cell lines.

The group went on to show that hEAG1 current is increased by endogenous neurotransmitter signalling. They transfected the hEAG1-HEK293T cell line with the serotonin receptor 5-hydroxytryptamine receptor 2A (HTR_{2A}). This is a G α_q coupled GPCR that activates PLC to breakdown PIP₂ as part of its normal signalling pathway. To avoid the inhibition of hEAG1 by increased intracellular Ca²⁺ (via the IP₃ pathway), 10mM BAPTA was used to chelate the released Ca²⁺. 100 μ M serotonin induced a translocation of PLC δ -PH-GFP from the membrane and increased hEAG1 current when measured in whole cell patch clamp. This experiment shows that hEAG1 current can be modulated by PIP₂ and that receptor signalling that leads to the hydrolysis of PIP₂ has an effect on the amplitude of this current. It is also interesting to consider that in an endogenous setting, G α_q G-proteins will activate a signalling pathway that ultimately ends with an increase in intracellular Ca²⁺, which will inhibit hEAG1 in the place of the newly hydrolysed PIP₂. This indicates that hEAG1 is under tight control by more than one second messenger and that this may be important for its role in both neurons and in cancer. Whilst not much progress has been made in this area of the field, it is interesting to consider that hEAG1 may be under additional regulation by a membrane phospholipid.

1.3.5.2. PIP₂ binds directly to hEAG1

PIP₂ may bind directly to the channel, as it does to the EAG-family member hELK1 (Li *et al.*, 2015), or it may be acting indirectly via formation of distinct lipid rafts. Han *et al.* (2016) used biolayer interferometry (BLI) to show that PIP₂ binds directly to the hEAG1. BLI measures optical interference caused by binding events and it also showed that the kinetics of binding were faster with increasing concentrations of PIP₂ (Han *et al.*, 2018). The K_D value obtained from BLI was $0.35 \pm 0.04 \mu\text{M}$, which is similar to the IC₅₀, obtained from excised patch experiments (Han *et al.*, 2016).

PIP₂ binds directly to hERG1, increasing the current, by interacting with a series of positively charged residues in the distal C-terminus (Bian *et al.*, 2004). This region is conserved in hEAG1 so Han *et al.* (2016) generated a mutant in which this region was deleted. This channel showed no difference in its response to PIP₂ depletion than the WT channel indicating that this region is not required for PIP₂ binding. PIP₂ has previously been shown to interact with other ion channels, including KCNQ and TRPC channels (Delmas and Brown, 2005; Kwon *et al.*, 2007). Here the PIP₂ binding sites were found to overlap with the binding sites for calmodulin. Han *et al.* (2016) deleted each of the 3 calmodulin binding sites individually and showed that only the mutant missing the N-terminal binding site was non-responsive to changes in PIP₂ levels. There was also no BLI signal for binding for this mutant indicating that the binding site lies either partially or fully within the N-terminal calmodulin binding site. The group went on to test PIP₂ in combination with Ca²⁺-calmodulin to see if the binding of one affected the other. 0.5 μM PIP₂ was used which caused a 50% reduction in hEAG1 current, Ca²⁺-calmodulin complexes were then added which increased the hEAG1 current inhibition to almost 100%, indicating that PIP₂ and Ca²⁺-calmodulin have additive effects and may function together.

1.3.6. The epidermal growth factor receptor (EGFR) regulates hEAG1

EGFRs are monomeric, transmembrane receptor tyrosine kinases that are activated by extracellular ligands such as epidermal growth factor (EGF) among others (Downward *et al.*, 1984). Upon binding of the ligand the monomer dimerises to generate intrinsic kinase activity that autophosphorylates the dimer. This

phosphorylation of the dimer activates a variety of signalling pathways leading to cell proliferation (Oda *et al.*, 2005). Platelet-derived growth factor receptors (PDGFRs) along with EGFRs are in the family of receptor tyrosine kinases. PDGFRs share many cellular roles with EGFRs including; cell differentiation and proliferation (Heldin *et al.*, 1998). Both EGFRs and PDGFRs are heavily implicated in a range of cancers including; gliomas, ovarian and lung (Lu *et al.*, 2016; Farooqi and Siddik, 2015).

1.3.6.1. hEAG1 is regulated by EGFR kinase but not PDGFR or Src kinases

Previous data has shown that the EAG-family member hERG1 can have its activity inhibited by phosphorylation by EGFRs as well as the related protein tyrosine kinase, Src (Zhang *et al.*, 2008). The effect of protein tyrosine kinases on hEAG1 was tested with 3 specific inhibitors – AG556 for EGFRs, AG1295 for PDGFRs and PP2 for Src kinases – for their effect on whole cell hEAG1 currents. Only inhibition of EGFRs by AG556 inhibited hEAG1 currents. Inhibition of PDGFRs and Src had no effect. Inhibition of phosphatase enzymes reversed the effect caused by AG556 but did not affect hEAG1 current when used alone. This indicates that the reduction in hEAG1 current is down to inhibition of EGFRs and not direct channel block (Wu *et al.*, 2012b).

1.3.6.2. hERG and hEAG1 bind to and activate SHP-1 phosphatase

Contrastingly, more recent data showed that both hERG and hEAG1 were regulated by Src kinase by use of the Src inhibitor, PP1. 10 μ M PP1 inhibited hEAG1 current by 44% without affecting either the voltage dependence or the inactivation rate (Schlichter *et al.*, 2014). Schlichter *et al.* (2014) went on to show that hERG contains an immune-receptor tyrosine inhibitory motif (ITIM) in the C-terminus and that this motif was conserved between all members of the EAG family. ITIMs contain a tyrosine residue that is targeted by Src kinases and once phosphorylated this allows the binding of phosphotyrosine phosphatases such as Src-homology phosphatase 1 (SHP-1) that remove phosphate groups from target proteins (Barrow and Trowsdale, 2006) including hERG and hEAG1 (Schlichter *et al.*, 2014).

Schlichter *et al.* (2014) performed co-immunoprecipitation with hERG and SHP-1 as well as a mutant hERG channel in which the ITIM had been deleted (Δ ITIM-hERG). This data showed that WT hERG and not Δ ITIM-hERG co-precipitated with SHP-1. The group also showed that the tyrosine within the ITIM (Y829) had to be phosphorylated for co-precipitation with SHP-1 to occur. Using the SHP-1 substrate, *p*-nitrophenol phosphate, Schlichter *et al.* (2014) showed that only hERG with a phosphorylated ITIM could activate the phosphatase activity of SHP-1. This is the first evidence of an ion channel being able to bind to and activate the enzymatic activity of a tyrosine phosphatase. The ITIM sequence is conserved across members of EAG family, with Y666 being the conserved residue in hEAG1 (Schlichter *et al.*, 2014). This indicates that hEAG1 may also be able to activate the enzymatic activity of SHP-1 although this requires further experimentation.

1.3.6.3. hEAG1 is maximally phosphorylated under control conditions

Western blots, using an anti-phosphotyrosine antibody, showed that use of the EGFR specific inhibitor (AG556) reduced the amount of tyrosine phosphorylation of hEAG1 and that addition of EGF did not change the level of phosphorylation (Wu *et al.*, 2012b). This data suggests that under resting conditions, EGFRs have maximally phosphorylated hEAG1. The regulation of hEAG1 by EGFRs may be important for their role in cancer, as both have been implicated in cell proliferation (Oda *et al.*, 2005; Zhang *et al.*, 2012).

1.4. hEAG1 is involved in cancer as well as congenital birth defects

1.4.1. hEAG1 increases cell proliferation and induces a cancerous phenotype

Ion channels have long been linked to changes in cell proliferation and cancer, none more so than K⁺ channels (Huang *et al.*, 2012; Masi *et al.*, 2005; Pardo and Stuhmer, 2014).

The hEAG1 related K⁺ channel hERG1 is overexpressed in high-grade astrocytoma cancers but not significantly elevated in the control, healthy tissue. Inhibition of hERG1 by Way-123,398 – an anti-arrhythmic drug – caused a reduction in the levels of secreted vascular endothelial growth factor (VEGF) from the astrocytoma cells. This finding has also been supported by the use of E4031, another hERG specific blocker, and shows that hERG1 is involved in the growth of astrocytoma cancers (Masi *et al.*, 2005).

One of the K⁺ channels that has been most intensively investigated for its role in cancer is hEAG1. hEAG1 is highly expressed in >70% of different human cancer types including; glioblastoma multiforme, osteosarcoma, hepatocellular carcinoma, ovarian, head and neck, cervical and breast carcinomas where it is also almost always present in the secondary metastases of these tumours (Martinez *et al.*, 2015; Wu *et al.*, 2012a; de Guadalupe Chavez-Lopez *et al.*, 2015; Asher *et al.*, 2010; Menendez *et al.*, 2012; Hammadi *et al.*, 2012). Intriguingly, hEAG1 is not expressed in corresponding healthy tissue meaning that it may be possible to use it as a diagnostic marker and therapeutic target in cancer (Camacho, 2006).

1.4.1.1. hEAG1 may be acting as an oncogene

Gene expression is deregulated in cancer cells with many gene showing altered expression profiles. However, there is evidence that suggests hEAG1 to be an oncogene as opposed to its expression just being due to a side effect of the cancerous phenotype. Antisense oligonucleotides against hEAG1 have been shown to significantly reduce cell proliferation and also decrease DNA synthesis – as shown by a bromodeoxyuridine incorporation (BrdU) assay. This indicates that hEAG1 plays a role in the increase in DNA synthesis seen with rapidly proliferating cells. The same study also showed that hEAG1-transfected Chinese Hamster Ovary (CHO) cells implanted into immune-deficient mice grew rapidly into aggressive tumours.

These effects were specific to hEAG1 because CHO cells transfected with K_v1.4 – another voltage-gated K⁺ channel – did not proliferate nearly as fast and tumours arising from implanted cells were much less aggressive. In culture, the hEAG1 transfected cells showed many of the hallmarks of cancer; loss of contact inhibition, ability to grow in low serum media and in low-levels of growth factors, the same could not be shown for the K_v1.4 transfected cells (Pardo *et al.*, 1999).

1.4.1.2. hEAG1 controls cell cycle transitions

Cancer is often described as a loss of control of the cell cycle, meaning that cells miss vital check points that would usually induce apoptosis. Cell changes at the end of each phase of the cycle include changes in; cell volume, [Ca²⁺]_i, and V_m with ion channels potentially playing a role in each of these (Blackiston *et al.*, 2009). In HeLa cells, [Ca²⁺]_i rises gradually throughout G1 and peaks at the transition with S phase, and repeats this pattern through G2 into M phase where it remains high until the completion of mitosis (Urrego *et al.*, 2016). V_m changes throughout each stage of the cell cycle in a range of cell types due to either the change in expression or activity of different ion channels (Blackiston *et al.*, 2009). In MCF-7 cells, K⁺ channels are more highly expressed just prior to the S and M phase transitions whilst Cl⁻ channels show more activity during G2 phase (Ouadid-Ahidouch *et al.*, 2004; Pardo *et al.*, 1998; Valenzuela *et al.*, 2000). The presence of K⁺ channels causes a hyperpolarisation of the membrane producing a large inward driving force for Ca²⁺ ion entry (Ouadid-Ahidouch and Ahidouch, 2013). This depolarisation of the membrane is a factor known to drive the cell cycle forwards and is important to recognise due to the unique interplay between Ca²⁺-calmodulin and hEAG1 (Yang and Brackenbury, 2013). It is also interesting to speculate that overexpression of hEAG1 may further increase this driving force leading to sudden, uncontrolled Ca²⁺ influxes. The Ca²⁺ influxes would then lead to the inhibition of hEAG1 via calmodulin binding, thus maintaining the depolarised membrane potential characteristic of cancer cells. However, the link between hEAG1's regulation by Ca²⁺-calmodulin and its role in proliferation has yet to be tested.

Experiments conducted in synchronised HeLa cells show that the E2F1 transcription factor – which is known to have a responsive element within the promoter of hEAG1 – is under repression by retinoblastoma protein (pRb). Release

of this repression by hyperphosphorylation of pRb occurs at the G1/S transition, allowing E2F1 to reach maximal expression and increases the transcription of hEAG1 so that its peak expression occurs just prior to G2/M. This was also true in non-transformed cells, indicating that hEAG1 expression is normally stimulated during this stage of the cell cycle and perhaps that this signalling pathway is somehow mis-regulated in cancer cells (Urrego *et al.*, 2016).

1.4.1.3. K⁺ ion flux is not required for the effects of hEAG1

hEAG1 has been shown to increase cell proliferation when transfected into non-cancer cell lines and inhibition of hEAG1 current using the channel blocker astemizole reduces proliferation (Pardo *et al.*, 1999). It would be naïve to think that it is solely the K⁺ conductance that contributes to the cancer phenotype seen with hEAG1 transfection otherwise any K⁺ channel would show the same effects. Hegle *et al.* (2006) made use of a non-conducting mutant F546A hEAG1 – a highly conserved residue within the selectivity filter of the channel that when mutated causes abolition of ionic conductance. NIH 3T3 cells were transfected with WT hEAG1, hEAG1-F456A and an empty vector control. The mutant increased cell proliferation significantly compared to the vector control and to a similar extent as the WT channel. This evidence suggests that K⁺ flux cannot solely account for the increase in proliferation induced by hEAG1. They also continued on to show that Ca²⁺ influx is not an essential downstream component of hEAG1 signalling. By incubating transfected cells in EGTA-buffered solution they showed that hEAG1-induced proliferation was not significantly altered between the low and standard Ca²⁺ solutions – again this was true for the WT channel and the F456A mutant.

The mechanism by which hEAG1 acts is still not understood, Hegle *et al.* (2006) suggest that the p38 mitogen-activated protein kinase pathway (p38^{MAPK}) may be involved. They showed that WT hEAG1 and the F456A mutant doubled the phosphorylation of p38^{MAPK} compared to controls in the NIH 3T3 cell line. They also used a specific p38^{MAPK} inhibitor to test if p38^{MAPK} activity was required for proliferation. The inhibitor blocked the proliferation induced by the channel where inhibitors of other MAPKs such as p42 and p44 had no effect on proliferation, linking the p38 pathway with the hEAG1 induced proliferation. The use of the F456A mutant in this case also shows that activation of this pathway does not require K⁺

flux and suggests a non-canonical function of the channel. Whilst this is an interesting find, the specific interactions linking hEAG1 overexpression with p38^{MAPK} activation have yet to be identified.

1.4.1.4. The position of the voltage sensor is important for hEAG1 to increase cell proliferation

Hegle *et al.* (2006) also provide data regarding the voltage sensor of hEAG1 and its role in proliferation. They have shown that the conductance of hEAG1 is not crucial to increase proliferation, they then predicted that changes in extracellular K⁺ should therefore not affect hEAG1-induced proliferation. Increasing extracellular K⁺ by 10mM increased proliferation of vector controls but reduced the proliferation of cells expressing hEAG1 down to control levels. Increasing extracellular K⁺ depolarises the membrane leading to conformational changes in the voltage sensor, even in non-conducting mutants. The hEAG1 data predicts that by increasing the number of open channels, by depolarising the membrane, that the proliferation should be reduced.

Hegle *et al.* (2006) went on to test two mutants of the voltage sensor, EAG-TATSSA (T449S/K460S/T470A) and EAG-HTEE (H487E/T490E). Both mutants shifted the $V_{0.5}$ value to negative potentials compared to the WT channel. Both mutants increased the proliferation of NIH3T3 cells to the same extent as WT hEAG1 and all mutants resulted in negative resting membrane potentials in oocytes. The mutant conveying non-conductance, F456A, was introduced into the two voltage sensor mutants. This switched the resting membrane potential to more depolarised potentials since the channels can no longer pass K⁺ to repolarise the membrane. The two non-conducting voltage sensor mutants did not change the proliferation of cells over control levels. This indicates that the voltage sensor needs to be in a closed conformation in order to affect cell proliferation. Changes in surface and total expression were ruled out indicating that the proliferative ability of hEAG1 expressing cells is dependent on the conformation of hEAG1's voltage sensor.

1.4.1.5. hEAG1 impacts on survival prognosis

hEAG1 expression promotes cancerous properties and has the ability to allow transfected cells to grow into tumours when xenografted into mouse models. The effects of hEAG1 protein on human tumours has also been documented. 85.3%

of patients with brain metastases and 77.5% with glioblastoma multiforme showed hEAG1 expression. Those with low levels of expression had a median survival of 13 months compared to 6 months if expression levels were high (Martinez *et al.*, 2015). Similar results have also been obtained for ovarian cancer patients. Those with high levels of hEAG1 expression – as determined by immunohistochemistry – had a poor survival rate of 13.8 months compared to 24.1 months with low expression (Asher *et al.*, 2010). There was no hEAG1 expression in matched, healthy ovarian epithelium. High expression of hEAG1 was also associated with residual disease following surgery which in turn correlated with a much poorer outcome (Asher *et al.*, 2010). Taken together there is evidence showing that the expression of hEAG1 correlates to a poor survival rate.

1.4.1.6. hEAG1 has potential as a therapeutic target and early tumour biomarker

Asher *et al.* (2010) suggest that hEAG1 can be used as an early biomarker for cancer cells, since its presence is associated with poor survival rates. Its high level of surface expression also means that it is easily accessible to staining antibodies. Martinez *et al.* (2015) performed an extended study to include patients with low hEAG1 expression who were also treated with tri-cyclic antidepressants such as imipramine – a known blocker of hEAG1. Patients treated with antidepressants showed a significant increase in median survival of 13 months compared to 10 months for patients with the same hEAG1 expression that did not have antidepressant treatment.

Astemizole, a potent blocker of hEAG1 and previously used as an antihistamine, has been used to show how targeting hEAG1 can prevent the growth or even formation of tumours. Hepatocellular carcinoma was induced in rats using the chemical carcinogen diethylnitrosamine (DEN). Rats treated with DEN for 12 weeks showed moderate dysplastic changes to the liver accompanied by cirrhosis. However, rats given DEN and astemizole simultaneously showed livers comparable with that of healthy liver – indicating that early inhibition of hEAG1 can prevent the formation of tumours. It was also shown that rats administered DEN for 16 weeks with the last 4 weeks containing additional astemizole therapy showed better histological appearance to their livers compared to the group that was not given astemizole. These results indicate that astemizole may be able to prevent the growth

of already established tumours and therefore hEAG1 is worth further exploration as a therapeutic target (de Guadalupe Chavez-Lopez *et al.*, 2015).

1.4.2. Mutations of hEAG1 result in congenital, neurological syndromes

So far, two neurological conditions that stem directly from mutations in hEAG1 have been identified, these are Zimmermann-Laband syndrome (ZLS) and Temple-Baraitser syndrome (TBS) (Kortum *et al.*, 2015; Simons *et al.*, 2015).

1.4.2.1. ZLS is caused by de novo mutations in the KCNH1 gene

ZLS is a rare, autosomal dominant syndrome that is present from birth. Symptoms of ZLS include, but are not limited to; facial deformities, hypertrichosis, epilepsy and intellectual disability (Kortum *et al.*, 2015). Kortum *et al.* (2015) used whole exome sequencing of five subjects and their healthy parents to identify KCNH1 as being the cause of three out of five cases of ZLS. Three distinct, *de novo* mutations were identified; L352V, I467V and G469R. Genotyping of the healthy parents further proved the *de novo* origin of the mutations.

Kortum *et al.* (2015) used a homology model to predict the outcome of each of the mutations. They found that G469 resides in the S6 helix and that the four residues are close to each other in the closed state and move apart in the open state. They predicted that because the G469R mutant introduces four positive charges that the formation of the tetramer may be impaired or that the channel may favour an open state. Both the L352 and I467 residues are part of a hydrophobic cluster in the open state, mutations of both these residues to valine may affect how the channel transitions between the closed and open states.

Kortum *et al.* (2015) continued their investigation by recording from these mutant channels in CHO cells. L352V and I467V produced functional channels which did not differ in amplitude from the WT channel but did exhibit a negative shift in the activation voltage compared to WT. These two mutants showed slower deactivation and faster activation when compared to the WT channel whilst the G469R mutant did not produce functional channels in CHO cells. Co-expression of WT and G469R resulted in functional heterotetramers that had much larger conductance at negative potentials than the WT channel homotetramer. Taken together the data provided by Kortum *et al.* (2015) indicates that all ZLS-associated mutants of hEAG1 are gain-of-function.

1.4.2.2. TBS is also caused by de novo, gain-of-function mutations

TBS shares a lot of similar symptoms with ZLS including epilepsy and dysmorphic facial features. Similar to the discoveries with ZLS, Simons *et al.* (2015) utilised whole exome sequencing on six subjects diagnosed with TBS and their parents. Again a series of de novo mutations were discovered that were not present in the genes of the parents nor in any publically available genetic data.

Out of the six subjects, three all carried the I494V mutation, whilst the other three carried one of either L489F, Q603R or K217N. All these residues are highly conserved throughout the EAG family. Simons *et al.* (2015) expressed each of the mutants in both *Xenopus oocytes* and HEK293T cells and found that all four homotetramers gave functional channels. Much like the mutations identified in ZLS, all of the mutations found in TBS had a much lower threshold of activation than the WT channel. The voltage of half maximal activation ($V_{0.5}$) for the WT channel was +20.2mV, the $V_{0.5}$ value for the mutants ranged from -13.7mV to -28.9mV and they all showed slowed deactivation kinetics – again indicative of gain-of-function mutations.

1.4.2.3. ZLS and TBS could be classed as ciliopathies

It is interesting to speculate how mutations of hEAG1 cause the array of symptoms seen in ZLS and TBS. Since hEAG1-KO mice develop relatively normally, without any physical deformities and only some mild neural hyperactivity (Ufartes *et al.*, 2013), it could be said that a lack of hEAG1 current can otherwise be countered by other channel activity. However, gain-of-function mutations such as those described here by Kortum *et al.* (2015) and Simons *et al.* (2015) have more of an impact on the development of the foetus.

Both ZLS and TBS have overlapping symptoms with other diseases that have been classified as ciliopathies – diseases whose known cause lies within the dysfunction of the primary cilia (Waters and Beales, 2011). Some overlapping symptoms include mental retardation, hypoplasia as well as orofacial and digital malformations (Waters and Beales, 2011; Feather *et al.*, 1997). As discussed in section 1.5, hEAG1 has a role in disassembly of the primary cilia, Sanchez *et al.* (2016) also show that hEAG1 mutant L352V causes an even bigger reduction in the

number of ciliated cells compared to the WT channel. This indicates that disruption of primary cilia physiology may be an underlying cause of both ZLS and TBS.

1.5. hEAG1 is involved in the disassembly of the primary cilium

The primary cilium is an organelle found extending from the cell surface of quiescent cells and acts within the morphogenic and growth factor signalling pathways (Michaud and Yoder, 2006). Previously it was thought that this was just a vestigial organelle that served no cellular purpose, since then it has been suggested that the primary cilium acts a sensory organ and that it sequesters the centriole when the cell is not undergoing division. Differentiated, non-dividing cells and those in G₀ present with a single primary cilium at the surface. If cells in G₀ re-enter the cell cycle their primary cilium is disassembled to allow cell division to proceed (Satir *et al.*, 2010). The primary cilium is present on the apical surface of almost all cell types once they have entered G₀ (Whewey *et al.*, 2018).

1.5.1. Defects of the primary cilium are associated with disease

The importance of the primary cilium became clear when mice deficient in Tg737, a protein that is part of the intraflagellar transport complex and whose role is unknown (Pazour *et al.*, 2000), were examined. These mice developed polycystic kidneys as well as a range of other developmental abnormalities such as polydactyly and neural patterning problems (Satir *et al.*, 2010; Tian *et al.*, 2017). Mutations in, or the absence of, Tg737 result in polycystic kidney disease and death shortly after. The primary cilia of these mice are much shorter than is to be expected and indicates that the primary cilium is involved in important cellular functions (Pazour *et al.*, 2000).

Defects of the primary cilium are also associated with human disease. This is the case with Joubert syndrome which is characterised by brain stem and cerebellar abnormalities as well as the same polycystic kidney disease as the Tg737-deficient mice. Renal and retinal problems are often caused by defects in the cilia and there have been ~1000 cilia-specific proteins identified so far so mutation or loss of any of these may have devastating effects on human health via changes in cilia function (Waters and Beales, 2011).

1.5.2. The presence of the primary cilium may be important in cancer

It has been suggested that primary cilia act as a tumour suppressor, potentially by sequestering the centrioles used in cell division. Experiments on human glioblastoma cell lines show that they do not present with primary cilia

whereas cell lines of human astrocytes do. These glioblastoma cells could not be chemically 'tricked' into generating a primary cilia via serum starvation – a technique known to induce their presence. This indicates that the primary cilia may be acting as a tumour suppressor in these cell lines and that defects in the formation of the cilium may be a precursor to cancer (Moser *et al.*, 2009).

On the other hand there is some evidence suggesting the opposite, that the primary cilia can promote tumour development. Sarkisian *et al.* (2014) found that cilia were consistently present in human glioblastoma tumour biopsies as well as primary cell lines although they also showed that serum starvation did not increase the number of cells presenting with primary cilia. Emoto *et al.* (2014) found cilia in human pancreatic ductal carcinoma biopsies and also correlated the presence of primary cilia with a high frequency of lymph node metastasis. These data indicate that in some cases primary cilia may be involved in the development or maintenance of cancer although much more evidence is needed.

1.5.3. hEAG1 is a regulator of ciliary physiology

Signalling from the primary cilium may regulate the cell cycle. The disassembly of the primary cilium appears to signal the start of the re-entry of a cell into the cell cycle. Cells in G₀ have a basal body, which is differentiated from the centriole that acts as the site of growth of microtubules that form the primary cilium's structure. Disassembly of this is thought to occur before cell division begins (Kobayashi and Dynlacht, 2011).

hEAG1 interacts with proteins known to be involved in the regulation of cilia such as HIF α , rabaptin-5 and cortactin (Downie *et al.*, 2008; Ninkovic *et al.*, 2012; Herrmann *et al.*, 2012). It has also been shown that hEAG1 reaches peak expression just as the primary cilium would be disassembled (Urrego *et al.*, 2016).

1.5.3.1. Changing the expression of hEAG1 affects the presence of primary cilia

Sanchez *et al.* (2016) investigated the effect of hEAG1 expression on the primary cilia in NIH3T3 cells. 24hrs of serum starvation doubled the fraction of control cells showing primary cilia whereas those overexpressing hEAG1-eGFP did not present with primary cilia at all. Similar results were also shown in other cells lines and the use of hEAG2 – which shares 73% homology with hEAG1 – did not

cause the same reduction in ciliated cells seen with hEAG1. This shows that the effect seen with hEAG1 is specific and does not rely solely on the flow of K⁺ ions.

The human telomerase reverse transcriptase retinal pigment epithelial 1 (hTERT-RPE1) cell line shows high levels of endogenous hEAG1 and so was the perfect candidate for knock-down experiments with siRNA (Sanchez *et al.*, 2016). In cells with partial knock-down of hEAG1 that were serum starved there was an increase in the number of cells displaying cilia compared to hEAG1 expressing control cells. Addition of the serum back into the culture medium caused cells to rapidly disassemble their primary cilia. Overexpression of hEAG1 in this cell line did not further reduce the number of cilia nor did it affect the length of cilia. hEAG1 knock-down cells retained cilia for much longer periods of time than the control cells, which shows that hEAG1 speeds up the disassembly. Treatment of WT cells with 10 μ M astemizole also delayed the removal of the cilia indicating that the conformation adopted by the open channel of the K⁺ conductance itself is important for hEAG1's role.

Mutations in hEAG1 resulting in gain-of-function phenotypes have been implicated in the syndromes Zimmermann-Laband and Temple-Baraitser. Both diseases cause morphological changes that resemble ciliopathies and also show mental retardation and facial abnormalities (Kortum *et al.*, 2015; Simons *et al.*, 2015). Sanchez *et al.* (2016) generated L352V hEAG1, a mutant that has been associated with these diseases, and transfected it into primary mouse embryonic fibroblasts (pMEFs). The channel was active at resting membrane potentials, consistent with a gain-of-function change. WT hEAG1 caused a reduction in the number of cilia on pMEF cells and L352V hEAG1 caused a further reduction indicating an additive effect.

1.5.3.2. hEAG1 knock-out affects the Sonic hedgehog signalling pathway in pMEF cells

Sonic hedgehog (Shh) signalling is a factor in many types of cancer, and is one of the main signalling pathways confined of the primary cilium (Falcon-Urrutia *et al.*, 2015). Activation of the Shh pathway starts a cascade of signalling that changes the amount of repressor and activator forms of glioma-associated oncogene (Gli1), a transcription factor (Skoda *et al.*, 2018). Sanchez *et al.* (2016) measured the

amount of mRNA for Gli1 – indicating activation of the pathway – in pMEF cells that were either WT or knock-out hEAG1 as they were obtained from the mouse genetic hEAG1 knock-out model. These cells were starved of serum for 48hr with or without the Shh ligand present. hEAG1-KO cells showed a much more sensitivity to pathway activation as shown by the bigger fold-change in Gli1 mRNA levels compared to the WT cells (Sanchez *et al.*, 2016).

Serum-starved hEAG1-KO cells had increased basal levels of various genes associated with the Shh pathway including Gli2 and Smo, as well as in other cascades that interact with the Shh pathway such as TGF β and Wnt. Addition of the Shh ligand back into the media for 48hrs increased markers for activation of the Shh pathway in hEAG1-KO cells and less so in WT cells. This indicates that hEAG1-KO cells have a hyperactive Shh pathway compared to WT cells and that hEAG1 may influence the development of cancer via the Shh pathway.

1.5.3.3. hEAG1 localises to the centrosomes and primary cilium

Up to this point the localisation of hEAG1 has only been studied in dividing cells – those without a primary cilium. Human foreskin fibroblasts (HFFs) were used to study the localisation of hEAG1 as they have larger cilia than other cell types. 24hrs of serum starvation induced ciliogenesis and cells were then stained with an anti-hEAG1 antibody (Sanchez *et al.*, 2016). hEAG1 showed localisation along rod-like structures that also stained positively for Arl13B – a ciliary protein – which highly suggests localisation of hEAG1 to the primary cilia. Similar experiments conducted in hTERT-RPE1 cells show the anti-hEAG1 antibody stains discrete regions at the base of the cilia which lack microtubules (Sanchez *et al.*, 2016).

Sanchez *et al.* (2016) noted that the staining pattern observed could be the pericentrosomal preciliary compartment (PCC) which is a store of ciliary proteins. hEAG1 co-localised with pericentrin – a centrosome marker that interacts with calmodulin (Flory *et al.*, 2000) – in synchronised cells. To validate this co-localisation of endogenous hEAG1, centrosomes were purified and underwent density gradient centrifugation. Western blotting showed that full-length hEAG1 was found in fractions also positive for centrosome and microsome markers and was not present in the cytosolic or plasma membrane fractions – perhaps due to a

relative dilution of hEAG1 in these locations compared to the cilia (Sanchez *et al.*, 2016).

1.5.3.4. A nuclear localisation signal of hEAG1 is needed to disassemble the primary cilium

Trafficking of proteins to and from the primary cilium requires signals similar to those used in nuclear import and export. The C-terminus of hEAG1 contains a nuclear localisation signal (NLS) that Sanchez *et al.* (2016) predicted to also function as a ciliary localisation signal (CLS). They proceeded to delete the CLS (hEAG1^{ΔCLS}) and demonstrated that this did not alter the electrophysiological properties of the channel when expressed in oocytes. Immunocytochemistry experiments showed that hEAG1^{ΔCLS} did not localise at the primary cilia as the WT channel had done and when transfected into NIH3T3 or hTERT-RPE1 cells hEAG1^{ΔCLS} did not reduce the number of ciliated cells under serum starved conditions. This indicates that the CLS is necessary for the localisation and function of hEAG1 in the disassembly of the primary cilium (Sanchez *et al.*, 2016).

The authors hypothesised that the role of hEAG1 in disassembling the primary cilium could be important for its role in cancer. Pardo *et al.* (1999) had previously shown that injection of WT hEAG1 expressing CHO cells into immunodeficient mice caused the growth of large tumours. Sanchez *et al.* (2016) expanded on this by transfecting CHO cells with hEAG1^{ΔCLS} and injecting those cells into immunodeficient mice. The resulting tumours were smaller in size than those expressing WT hEAG1 indicating that the CLS is important for ciliary disassembly. The CLS provides hEAG1 with a non-canonical function as the CLS is not necessary for electrophysiological function but is needed to mediate tumour development.

1.5.4. hEAG1 interacts with the oncoprotein cortactin

Cortactin (CTTN) is a protein involved in the polymerisation of actin and controls the dynamics of the actin cytoskeleton (Oser *et al.*, 2010). CTTN is regulated by a range of kinases and so can function as part of many signalling cascades (Webb *et al.*, 2006; Meiler *et al.*, 2012). CTTN knock-down experiments, in which the lack of CTTN lead to an increased frequency of ciliated cells compared to WT cells showed that CTTN inhibits cilia production (Bershteyn *et al.*, 2010). CTTN has also been heavily implicated in the invasion of a range of cancer cells including breast

cancer, melanoma and lung squamous cell carcinoma. CTTN drives the production of invadopodia. These are structures that cause the increase in cell migration seen in cancer cells (MacGrath and Koleske, 2012).

1.5.4.1. CTTN directly binds to hEAG1

Herrmann *et al.* (2012) conducted a yeast-two hybrid screen to identify interacting partners of hEAG1 in the brain. Eight clones were positive for interaction with the full length hEAG1 and one was CTTN. This interaction was confirmed in native tissues using co-immunoprecipitation. This data indicates that an interaction is occurring *in vivo*. The authors also used glutathione (GST) pull-down assays to confirm the interaction. Purified hEAG1 was able to pull-down the CTTN-GST fusion protein but not the GST alone. In this experiment hEAG2 was also tested, this showed some pull-down ability but the signal was much weaker when compared to that of hEAG1 (Herrmann *et al.*, 2012).

To find the binding site within CTTN, four protein fragments were designed and purified as well as the full length CTTN protein. These four fragments were; the N-terminus (N-term), the N-terminus and the helical region (N-term-H), the helical region and the SH3 domain (HP) and the SH3 domain alone (SH3). These fragments were tested in a GST pull-down assay with only the HP fragment being able to interact with and pull-down hEAG1. The other fragments showed no or weak signals. This suggests that the interaction between hEAG1 and CTTN occurs via the proline-rich helical region of CTTN (Herrmann *et al.*, 2012).

1.5.4.2. hEAG1 channel current is affected by the presence of CTTN

CTTN has been shown previously to affect the current of BK channels by altering its open probability and to also alter the surface expression of Kv2.1. Herrmann *et al.* (2012) went on to ask whether CTTN could be affecting hEAG1's current. To test this they either injected oocytes with RNA encoding human CTTN to increase CTTN expression or a phosphorothioate antisense oligonucleotide (PTO) shown to deplete CTTN. Current amplitude positively correlated with the presence of CTTN, but the voltage dependence or kinetics of the channel were no different in the control or test cells. hEAG1 current depends on the membrane potential prior to activation – this property was also unaffected by an increase or decrease in CTTN.

The reduction in hEAG1 current occurred in a dose-dependent manner of CTTN depletion with an 80% reduction in current when using 5ng of PTO. A similar reduction was seen in hEAG1-expressing HEK293 cells that had been treated with an siRNA against CTTN. Increasing CTTN expression in oocytes over endogenous levels did not increase the hEAG1 current, but injection of more hEAG1 RNA did, indicating that the translation machinery was not saturated.

CTTN also has a role in rearrangement of the cytoskeleton and so may be acting indirectly via disruptions to the cytoskeleton. CK666 is a drug used to inhibit the Arp2/3 complex which regulates actin modelling. 50 μ M CK666 did not alter hEAG1 current compared to vehicle controls indicating that CTTN interacts with hEAG1 independently of its role in the cytoskeleton.

1.5.4.3. The C-terminus of hEAG1 is necessary for its regulation by CTTN

The group went on to test whether the C-terminus of hEAG1 is important for the interaction with CTTN. They tested the effect of depleting CTTN on C-terminal chimeras of hEAG1 and hEAG2, since hEAG2 did not interact strongly with CTTN in the pull-down assays and the majority of the sequence disparity between the two channels is in the C-terminus. Both channels were functionally expressed and currents from both chimeras showed similarity to the WT channels. Currents recorded from hEAG1 – now containing the C-terminus of hEAG2 – were not sensitive to the depletion of CTTN, but cells expressing hEAG2 – containing the C-terminus of hEAG1 – showed a reduction in current amplitude when CTTN was depleted. This indicates that the C-terminus of hEAG1 but not hEAG2 is responsible for the channel's interaction with CTTN.

Herrmann *et al.* (2012) generated 8 mutant versions of hEAG1 with each one missing a different section of the C-terminus going from position 685 to 962. They were expecting to reveal the location of the CTTN binding site by finding which mutant showed much less current than WT. 5 of the 8 deletions showed reduced current amplitude; Δ 758-776, Δ 777-818 and Δ 816-890 showed only moderate current reductions which could be further reduced by depletion of CTTN, indicating that these regions are not involved in the binding of CTTN. Deletions Δ 705-755 and Δ 933-962 showed current reductions over >90% with CTTN depletion only

marginally reducing the current of $\Delta 705-755$. These two deletion mutants as well as the WT were tagged with a bungarotoxin (BTX) binding site (BBS) to measure their surface expression. Staining against BBS was visible at the membrane for the WT and $\Delta 933-962$ but the $\Delta 705-755$ mutant showed reduced internal staining and minimal membrane signal.

Herrmann *et al.* (2012) went on to conduct precipitation experiments using both $\Delta 705-755$ and $\Delta 933-962$ mutants to see if either could pull down CTTN. $\Delta 933-962$ hEAG1 showed binding efficiencies similar to the WT channel. However, $\Delta 705-755$ hEAG1 showed a reduced binding efficiency and therefore this region of the C-terminus is responsible for hEAG1's interaction with CTTN.

1.5.4.4. CTTN affects and stabilises the surface expression of hEAG1 but does not affect its biophysical properties

The group continued their investigation by using non-stationary noise analysis to test whether CTTN had any effect on the components that comprise whole cell current – number of channels available (N), single channel current (i) and open probability (P_{open}). Their results gave similar i values in control and CTTN depletion as was the same for P_{open} . This would indicate that CTTN primarily affects the number of available channels at the membrane, consistent with their previous data.

Surface expression was monitored in oocytes via an extracellular BBS tag. hEAG1-BBS was pulled down using BTX-biotin. Cells that were CTTN-depleted contained much less hEAG1-BTX-biotin protein than controls indicating that less membrane expression. Total protein levels were not different between normal and CTTN-depleted cells indicating that the reduced surface expression was due to effects of CTTN on trafficking or turnover at the membrane and is not reduced protein synthesis.

Herrmann *et al.* (2012) also tested the localisation of hEAG1 in mammalian cells with either normal, raised or depleted levels of CTTN. There was good co-localisation between the Venus-hEAG1 fusion protein and the CFP-tagged CTTN in the cell and at the membrane. Co-staining for focal adhesion kinase (FAK) showed that hEAG1 localises at the same place and was seen in cells with normal levels of CTTN. This co-localisation with FAK was affected when cells were treated with an

siRNA against CTTN and staining was only present in the cell nucleus. The same experiment was also conducted on $\Delta 705-755$ hEAG1 and hEAG2. There was weak co-localisation between the CFP-CTTN and either of the channels, there was also no co-staining of the channels or FAK indicating that CTTN does not interact with the 705-755 region of hEAG1 or its homologue hEAG2.

CTTN is either affecting membrane expression of hEAG1 via a trafficking process or stably maintains the channel at the membrane once it has reached it. Herrmann *et al.* (2012) argued that if CTTN was involved in trafficking, then depletion of CTTN would reduce the amount of hEAG1 at the membrane and therefore reduce the current. They performed injections of PTO to reduce CTTN in oocytes. They found that if hEAG1 cRNA was injected 24hrs prior to PTO, the current was reduced to 51% of control, but if PTO was injected before hEAG1 there was no effect on the current compared with controls. This would indicate that CTTN was not involved in trafficking hEAG1 to the membrane but instead maintained it there. To test this they performed a BTX-biotin assay to measure internalisation of hEAG1. Whilst the amount of hEAG1 at the membrane was reduced the amount of internalised hEAG1 was not changed when CTTN was reduced. Overexpression of CTTN had the opposite effect and reduced internalisation of hEAG1 indicating that CTTN interacts with hEAG1 to stabilise it in the membrane.

Maintaining hEAG1 at the membrane longer than it would be under normal physiological conditions may alter its downstream signalling. HeLa cells naturally have high endogenous hEAG1 expression and channel knock-down reduces their proliferation. Transfection of these cells with CTTN further increased the proliferation due to hEAG1 remaining in the membrane for longer. Furthermore, cell lines with endogenously high levels of CTTN were treated with an siRNA against hEAG1, there was no change in proliferation indicating that it is the prolonged presence of hEAG1 and not CTTN that has the effect on proliferation (Herrmann *et al.*, 2012). This thorough study is the first to show that hEAG1 is regulated by CTTN, another study conducted by Sanchez *et al.* (2016) goes on to further explore the channel's regulation by CTTN but as yet there have been no other studies of this interaction.

1.5.4.5. The interaction of CTTN and hEAG1 is important in ciliogenesis

Sanchez *et al.* (2016) tested whether the interaction of CTTN and hEAG1 was important for hEAG1's role in ciliogenesis. hEAG1 knock-down increases the number of ciliated cells compared with control. Overexpression of CTTN in hEAG1 knock-down cells reversed this effect with numbers of ciliated cells almost at the same level as control. Overexpression of $\Delta 705-755$ hEAG1 which was previously shown by Herrmann *et al.* (2012) to be the only mutant not to bind CTTN, did not change the number of ciliated cells indicating that the interaction between CTTN and hEAG1 is important for ciliogenesis. Sanchez *et al.* (2016) also showed that the level of active CTTN which is phosphorylated was increased in hEAG1 knock-down pMEF cells but not in WT, suggesting that activation of CTTN can compensate for a loss of hEAG1 in terms of ciliogenesis.

Taken together, the data provided by Herrmann *et al.* (2012) shows that CTTN interacts directly with hEAG1 via its HP domain and the 705-755 fragment within hEAG1's C-terminus. This interaction alters the whole cell current by affecting the surface expression of hEAG1 but it does not affect its single channel current or open probability. CTTN appears to interact with hEAG1 after it has been trafficked to the membrane where its interaction with CTTN maintains it at the membrane, and influences ciliogenesis.

1.6. Calmodulin is a Ca²⁺ sensing protein that regulates a wide variety of ion channels

Calmodulin is a Ca²⁺ sensing protein that helps to control the [Ca²⁺]_i but also acts as a signalling molecule. It is ubiquitously expressed and its importance is underlined by the identification of 3 genes (CALM1-3) that are found at independent gene loci but encode identical proteins. Structurally, calmodulin is comprised of 2 globular regions, the N and C lobes separated by a flexible linker as shown by NMR data (Barbato *et al.*, 1992). Each lobe contains 2 EF-hand domains. The 2 lobes show a difference in Ca²⁺ affinity of 10-fold with K_D values of 10μM and 1μM for the N and C lobes respectively (Sorensen *et al.*, 2013).

Calmodulin interacts with and regulates a wide range of ion channels including; members of voltage-gated Ca²⁺, Na⁺ and K⁺ channels (Etxeberria *et al.*, 2008; Simms *et al.*, 2014; Kwon *et al.*, 2007).

1.6.1. Calmodulin can bind to targets in high and low Ca²⁺ conditions

As previously stated, calmodulin has 2 EF hand domains each being able to bind to 2 Ca²⁺ ions. The Ca²⁺ free state of calmodulin is called apo-CaM and has a much denser structure than when it's bound to Ca²⁺. Ca²⁺-calmodulin most commonly interacts with its targets in a 1:1 ratio by binding to sequence motifs on the target (Kovalevskaya *et al.*, 2013). In some cases, apo-CaM can interact with a target without the need to be bound to Ca²⁺ ions. Apo-CaM was shown to interact with Nav1.5 channels where instead of fully interacting with the target sequence it binds in a “semi open” state (Chagot and Chazin, 2011). This is made possible due to the flexible linker between lobes.

1.6.2. Calmodulin regulates a variety of ion channels

1.6.2.1. Calmodulin binds to Cav1.2 in a Ca²⁺ dependent manner

Cav1.2 is a voltage gated Ca²⁺ channel, also referred to as the L-type Ca²⁺ channel that activates at high voltages. It is important in regulating the upstroke of the cardiac action potential (Weiss *et al.*, 2013). Calmodulin binds directly to the N-terminus of the channel and causes the channel to inactivate once it has passed Ca²⁺ ions that have bound to and activated calmodulin. This is known as calcium-dependent inactivation (CDI) and is an important “brake” on the system that

prevents too much current being passed – a potentially dangerous event in cardiac tissue (Simms *et al.*, 2014; Ben-Johny and Yue, 2014).

1.6.2.2. Calmodulin binds to and regulates presynaptic P/Q-type Ca²⁺ channels

P/Q-type Ca²⁺ channels are another family of Ca²⁺ channels that are regulated by calmodulin (Lee *et al.*, 1999). P/Q-type channels – which are also referred to as Cav2.1 – are expressed in neurons at the presynaptic terminal where they contribute to the release of neurotransmitters (Nimmrich and Gross, 2012). The interaction between P/Q-type channels and calmodulin was first identified by Lee *et al.* (1999) using the yeast-2-hybrid system. This experiment showed that whilst P/Q-type channels were pulled out, the related N-type channel (Cav2.2) was not, indicating that calmodulin does not bind to all members of the Ca²⁺ channel family. Lee *et al.* (1999) went on to show that this interaction occurs via a calmodulin binding domain within the α -subunit and that this interaction is Ca²⁺ dependent.

1.6.2.3. Calmodulin acts as an auxiliary subunit of the SK1 potassium channel

Small conductance Ca²⁺-activated K⁺ channels such as SK1 (K_{Ca2}) are expressed throughout the CNS where they provide a long-lasting hyperpolarisation of the membrane following a train of action potentials. These channels are not sensitive to membrane voltage but are instead activated by an increase in intracellular Ca²⁺ (Maylie *et al.*, 2004).

Using the yeast-2-hybrid approach, calmodulin was identified as a binding partner for SK1 and that the proximal C-terminal domain could interact with calmodulin with or without the presence of Ca²⁺ ions (Xia *et al.*, 1998). Separate mutagenesis approaches found that it was the two N-terminal EF hands of calmodulin that were responsible for the Ca²⁺ sensitivity of SK1 channels (Keen *et al.*, 1999).

1.6.2.4. Calmodulin is constitutively associated with Nav1.2 and Nav1.5 channels

Na⁺ channels are widely expressed throughout the body and are responsible for the neuronal and cardiac action potential upstroke (Kim *et al.*, 2004). Mutations found in or around IQ binding motifs are associated with various diseases;

mutations such as L1825P in Nav1.5 contribute to congenital long QT syndrome – a dangerous arrhythmia of the heart (Makita *et al.*, 2002). Additionally, the R542Q mutant of Nav1.1 and R1902C of Nav1.2 have both been found in patients presenting with a familial form of autism (Weiss *et al.*, 2003). This data indicates that disruption of calmodulin binding to Nav channels may be important in their pathophysiology.

Kim *et al.* (2004) provide evidence of constitutive binding of calmodulin to two isoforms of Nav channel. They began by aligning the sequences of Nav1.2 and 1.5 with Cav1.2. They found extensive similarities between the two Na⁺ channels' C-terminal domain with the Ca²⁺ channel sequence. Purified Nav C-terminal domains co-purified with calmodulin in a 1:1 stoichiometry. These complexes were able to form in the absence of Ca²⁺ ions and the C-terminal peptides were able to bind with the calmodulin mutant CaM₁₂₃₄ which is insensitive to Ca²⁺ ions. This shows that the association of calmodulin to Nav1.2 and 1.5 is constitutive and independent of Ca²⁺ ions.

1.7. hEAG1 has been discovered to be regulated by Ca²⁺-calmodulin

1.7.1. hEAG1 was discovered to be expressed in the rat CNS

Ludwig *et al.* (1994) used Northern blots to find out which tissues expressed rat EAG (rEAG) messenger ribonucleic acid (mRNA) and it was almost exclusively located to the CNS. The group selectively recorded and characterised the channel using inside-out macropatch recordings based on its lack of inactivation following depolarisation and also characterised the channel's activation threshold to be between -40 and -30mV.

1.7.2. The Ca²⁺ sensitivity of hEAG1 is mediated by calmodulin

Meyer and Heinemann (1998) were investigating the ionic currents in SH-SY5Y cells – a human neuroblastoma cell line and discovered the sensitivity of hEAG1 to [Ca²⁺]_i. They used a patch pipette containing a 830nM Ca²⁺ solution in the very tip whilst the rest of the pipette contained an EGTA solution. The experiment showed an initial profound loss of hEAG1 current as the high Ca²⁺ dialysed with the cell contents. This was followed by a swift re-emergence of the hEAG1 current as the EGTA in the remaining pipette solution sequestered the Ca²⁺. This study showed that hEAG1 was highly sensitive to changes in [Ca²⁺]_i. The same response could also be evoked using acetylcholine to activate endogenous muscarinic M₃ receptors that couple with a G_{αq} G-protein to release Ca²⁺ from intracellular stores, indicating that hEAG1 may be regulated by Ca²⁺ released by physiological signalling pathways.

Schönherr *et al.* (2000) went on to show that the sensitivity of hEAG1 to Ca²⁺ was mediated by the Ca²⁺ binding protein, calmodulin. They did this by excising a patch of membrane and exposing it to 200nM Ca²⁺, which resulted in the loss of current that could be recovered using an EGTA wash. However, the discovery came when they perfused the same patch of membrane with the 200nM Ca²⁺ solution again, this time there was no effect on the current amplitude indicating that a cytoplasmic factor required for Ca²⁺-dependent inhibition had been removed during the wash. They placed the membrane patch back inside the cell to expose the intracellular surface to the cytoplasm again and this restored the Ca²⁺ sensitivity. The experiment was repeated using cell lysate in place of the EGTA solution and the inhibition by the high Ca²⁺ solution was preserved, adding weight to the argument that a cytoplasmic factor had a role in the process. This was found to be calmodulin

when the cell lysate was incubated with a synthetic peptide mimicking the calmodulin binding site on CaMKII. This peptide sequestered calmodulin and prevented binding to hEAG1, causing a loss of the Ca²⁺ sensitivity when the cell lysate was perfused over the membrane patch. Calmodulin protein was purified and a solution containing it and 200nM Ca²⁺ caused the characteristic loss of current. These experiments also showed that calmodulin was not constitutively bound to hEAG1 channels under low Ca²⁺ conditions.

1.7.3. Ca²⁺-calmodulin binds to intracellular domains

Ziechner *et al.* (2006) investigated the mechanism by which Ca²⁺-calmodulin inhibited the hEAG1 current. It was previously believed that Ca²⁺-calmodulin interacted with a sequence on the C-terminus. However a mutant in which the entire hEAG1 N-terminus was deleted showed a loss of Ca²⁺ sensitivity. Peptide arrays uncovered 3 intracellular binding domains (BD); BD-N1 (amino acids 151-165) of the N-terminus, BD-C1 (amino acids 674-683) and BD-C2 (amino acids 711-721) both of the distal C-terminus. The interactions with Ca²⁺-calmodulin were also confirmed using glutathione pull-down assays.

Goncalves and Stuhmer (2010) used fluorescence resonance energy transfer (FRET) microscopy to obtain binding affinity values for the 3 domains. BD-N1 and BD-C2 showed high affinities with K_D values of 45nM and 136nM respectively. BD-C1 on the other hand had a low affinity with a K_D value of >5μM. Ziechner *et al.* (2006) used mutagenesis to show that F714S and F717S in BD-C2 prevented Ca²⁺-calmodulin binding to the isolated BD-C2 peptide but did not prevent it binding to the intact channel. F151N and L154N mutations in BD-N1 also prevented Ca²⁺-calmodulin binding to the isolated peptide, but not to the intact channel. Channels containing the mutations in BD-N1 and BD-C2, but with an intact BD-C1 were unable to bind Ca²⁺-calmodulin, indicating that BD-C1 is not a main interacting partner.

The recent cryo-EM structure provided by Whicher and MacKinnon (2016) is consistent with these studies. It shows one lobe of calmodulin interacting with both BD-C1 and BD-C2 and the other lobe interacting with BD-N1 of a different channel subunit. This in combination with the mutagenesis Ziechner *et al.* (2006) performed suggests that calmodulin first binds tightly to BD-C2 and that contacts

with BD-C1 only serve to stabilise the interaction of calmodulin with the BD-C2 domain.

1.8. Project aims and objectives

This project aims to study the role of the PAS-cap in the regulation of hEAG1 and also the mechanisms of action of hEAG1 in cancer. The first aim will be studied using 2-electrode voltage clamp and site directed mutagenesis to manipulate the amino acid residues of the PAS-cap. These mutants will be tested in control for their role in regulating hEAG1 but will also be tested in high Ca^{2+} conditions to test how they regulate the channel under these conditions.

The second objective is to study how hEAG1 increases proliferation as well as looking into a role in migration and primary cilia regulation. Proliferation studies will try to understand whether the Ca^{2+} -sensitivity and intracellular domains of the channel are important, whilst whether or not hEAG1 has a role in migration will be studied. A role in primary cilia disassembly has already been shown and so we will try to understand how the intracellular domains of hEAG1 facilitate this process and whether or not this process relies on Ca^{2+} -calmodulin being able to bind either binding domain of the channel.

2. Materials and Methods

2.1. Reagents and Electrophysiology Solutions

2.1.1. Oocyte Isolation and Solutions

Xenopus laevis ovarian lobes obtained from the lab of Prof. Richard Evans were digested using crude collagenase type 1A (14mg/10ml) of OR2 isolation buffer. OR2 buffer contains (in mM): NaCl 82.5, KCl 2.5, HEPES 5, NaHPO₄ 1 and MgCl₂ 1 (pH 7.4). OR2 solution is nominally Ca²⁺-free as Ca²⁺ inhibits the activity of the collagenase and protease enzyme. The oocytes were left at room temperature on a shaker for 15-30mins to remove the follicle layer that holds them together in the lobes. Oocytes were washed using fresh OR2 buffer which was then replaced by Barth's solution which contained (in mM): NaCl 88, KCl 1, CaCl₂ 0.41, Ca(NO₃)₂ 0.33, MgSO₄ 1, NaHCO₃ 2.4 and HEPES 10 (pH 7.4). Oocytes were maintained at 16°C until ready for injection with RNA.

During RNA injection, the oocytes were transferred to a modified version of Barth's solution, Super Barth, that contained an addition of 1mM Na-pyruvate and 50µg/ml gentamycin.

2.1.2. Recording solutions

The recording solution used for oocyte experiments was a low Cl⁻ solution that contained (in mM): NaMES 96, KMES 2, CaCl₂ 2, HEPES 5 and MgSO₄ 1 (pH 7.6). This was a modified version of a chloride (Cl⁻) based solution where MES replaced the majority of the Cl⁻ ions. Extracellular Cl⁻ was maintained at 4mM to set E_{Cl} close to +60mV at room temperature. E_{Cl} was calculated using the Nernst equation and assumed an intracellular Cl⁻ concentration of 43.5mM as previously reported in oocytes (Weber, 1999). This means there should be no net flow of Cl⁻ ions at +60mV thus minimising potential Cl⁻ current contamination when pulsing to this membrane potential. In practise however, some Ca²⁺ activated Cl⁻ currents were observed in some cells as an inward current at the tail potential of -60mV. When tail currents exceeded 2µA the data was not included in the analysis.

For whole-cell patch clamp electrophysiology two solutions were made. The extracellular solution contained (in mM): NaCl 140, KCl 4, CaCl₂ 2, MgCl₂ 1, HEPES 5 and glucose 10 (pH 7.4). The intracellular solution used to fill the patch pipettes

contained (in mM): KCl 135, KOH 5, MgATP 5, HEPES 10 and EGTA 0.1 (pH 7.2). The intracellular solution was aliquoted into 1ml volumes and defrosted as needed to reduce time-dependent degradation of MgATP. Aliquots were kept on ice during experiments.

All extracellular solutions were stored at 4°C and were warmed to room temperature prior to experiments.

2.1.3. hEAG1 reagents

Ionomycin (I) and thapsigargin (T) were made up to a 5mM stock, whilst astemizole was made up to 50mM stock, both using dimethyl sulphoxide (DMSO). I&T and astemizole were diluted shortly before use to working concentrations of 5µM and 50µM respectively using the recording solution. Stocks were stored in a desiccator at -20°C and working concentrations were made fresh as needed to avoid degradation of the compounds. All reagents including those used in solutions were obtained from Sigma UK.

2.2. Molecular Biology

2.2.1. Vectors and hEAG1 constructs

The plasmid vector used is called pXoon, which contains the gene for GFP. The KCNH1 gene was cloned and is under the control of the CMV promoter. The pXoon plasmid is suitable for expression in mammalian cells as well as oocytes. The DNA construct WT hEAG1-BBS was donated to the lab from Professor Luis Pardo of the Max Planck Institute for Experimental Medicine. The plasmid donated was pcDNA3 and contained the KNCH1 gene with a bungarotoxin binding site (BBS) engineered within the extracellular S2-S3 linker. The KCNH1 gene with its BBS addition were cloned into pXoon so that transfected cells could be identified via the GFP expression.

2.2.2. Mutagenesis Primers

Mutagenesis primers were designed to be between 18-24 base pairs in length and the codon mutation made to be the fewest number of bases different from the WT sequence to increase efficiency of the reaction. All primers were ordered through Sigma UK and re-suspended in sterile distilled water to a concentration of

100 μ M. Primers were further diluted to a concentration of 10 μ M prior to use in PCR experiments.

Some plasmids required the design of sequencing primers. These were made to be between 15-20 base pairs long. These were also re-suspended to a concentration of 100 μ M and were diluted to a final concentration of 1 μ M for use in the sequencing reactions.

2.2.3. Generating hEAG1 mutant DNA and RNA

PCR was conducted using the Phusion 2x master mix (NEB), 1.5 μ l of each primer and 30ng/ μ l of WT hEAG1 template DNA. The total volume was made up to 50 μ l using dH₂O. Both primers were added to the same reaction because this saves having to run the programme twice, once with each primer. PCR samples were centrifuged to mix and run according to the following PCR programme; 98 $^{\circ}$ C for 2mins to denature the DNA, 95 $^{\circ}$ C for 50s to split the double helix, 65-72 $^{\circ}$ C for 50s for primer annealing, 68 $^{\circ}$ C for 15mins to allow for elongation of the DNA, 68 $^{\circ}$ C for 10mins for the final extension of the DNA and held at 4 $^{\circ}$ C until sample were retrieved. This cycle continued for 25-30 cycles and the annealing temperature was calculated for each set of primers to optimise the experiment using the NEB calculator.

PCR products were run on a 1% agarose gel to confirm the molecular weight of hEAG1 (~9.8kB). PCR products of the correct molecular weight were then transformed into gold efficiency DH5 α cells (Bioline), plated onto kanamycin agar plates and grown overnight at 37 $^{\circ}$ C. Swabs taken of single colonies were grown overnight in 5ml kanamycin LB medium and the Isolate 2 Plasmid Mini Kit (Bioline) was used to extract the DNA via mini-preps. Maxi-preps were used to generate purer DNA in large quantities using the Plasmid Maxi Kit (Qiagen). DNA was quantified using a Nanodrop and samples were sent for sequencing at the PNAFL facility at the University of Leicester. Mutants were verified by comparing the PNAFL sequence with the WT using the NCBI BLAST tool.

RNA was generated by linearising the template DNA using the XbaI restriction enzyme in a reaction mix containing 20 μ l template DNA, 5 μ l of the NEB CutSmart buffer and 1 μ l of XbaI. The reaction mix was made up to 50 μ l using dH₂O and was left for 4-5hrs at 37 $^{\circ}$ C. The RNA was generated by using the linearised DNA

by in vitro transcription in the Ambion mMessage mMachine T7 kit (Life Technologies). This kit contains the four ribonucleotides as well as a unique 7-methyl guanosine cap analogue that is incorporated in the first (5') guanosine position to closely mimic in vivo RNA from eukaryotes. An RNase inhibitor prevents the breakdown of the RNA product increasing the yield. RNA was quantified using both the Nanodrop and a 1% agarose gel containing formaldehyde which provides denaturing conditions to prevent the single stranded RNA from forming secondary structures. RNA was suspended in nuclease-free water (Ambion) and stored at -80°C.

2.3. Two-electrode voltage clamp electrophysiology

2.3.1. Injection and Recording Micropipettes

Prior to cRNA injection, micropipettes were pulled using a Flaming/Brown micropipette puller (Sutter Instrument Novato, USA. Model P-97) from glass capillaries with a 0.53mm internal diameter and 1mm outer diameter (WPI, UK). The tips of the micropipettes were broken using fine tweezers to widen the tip to 6-8 subdivisions on an eye piece graticule of a microscope with a 100x objective. The micropipettes were stored in a specially made container to prevent them from damage and accumulating dust.

Recording micropipettes for two electrode voltage clamp in oocytes were pulled from thin wall capillaries with a filament and a 1mm external diameter (model TW100F-4 WPI, UK). These were stored in the same way as the injection micropipettes but with the addition of being filled with 3M KCl at least 3-5days prior to use. This was done to ensure that trapped air bubbles within the sharp tip had been removed before recordings were made.

2.3.2. Oocyte RNA injection

Injection micropipettes were filled with mineral oil just prior to injections and mounted on the injector (Nanoliter 2000, WPI UK). The micropipette was emptied of about 80% of the mineral oil to ensure an even flow out of the tip. Volumes of RNA between 1 and 1.5µl were taken up into the electrode. The injection volume (usually 60nl) and speed were pre-set on the equipment. Oocytes were placed in a mesh-lined dish filled with Super Barth's and injected with the RNA. They

were transferred into fresh Super Barth's solution and incubated at 16°C for up to 48hrs depending on the level of expression required.

2.3.3. Two-electrode voltage clamp set up and voltage protocols

Just before an experiment, the two recording micropipettes were broken using fine tweezers to a resistance between 0.5 and 2M Ω . This ensured large ionic currents could still be accurately compensated for in voltage clamp recordings, to maintain the chosen step potential. The recording chamber and the perfusion system were cleaned thoroughly with 70% ethanol followed by distilled water before the recording solution was added to the bath.

An oocyte was placed in the recording chamber and impaled by both electrodes allowing the resting membrane potential to be measured. The recording mode was switched to voltage clamp and the gain of the feedback amplifier was increased to the maximum level or until oscillations in the membrane potential steps of voltage were observed to allow the recording of hEAG1 currents.

The voltage clamp amplifier was a GeneClamp 500 (Molecular Devices) and was connected to a Digidata 1322A (Molecular Devices) analogue to digital converter. Current and voltage signals digitised and sampled at a frequency of 1kHz and recorded on a PC for off-line analysis. Different voltage protocols were used depending on the type of experiment being conducted. A current – voltage (I/V) protocol was used to assess the current's relationship with membrane potential. The I/V protocol consisted of a holding potential of -90mV which was then stepped up to a test potential for 2s starting at -70mV and increased in 10mV increments with each sweep of the protocol up to +70mV. It was not stepped any higher than +70mV because further depolarisations risk activating endogenous currents that can contaminate the hEAG1 current traces. The voltage was returned to a tail potential of -60mV for 500ms and then stepped back to the holding potential. The start to start interval was 10s. A short pre-pulse test was applied at the beginning of each trace, this was a step to -70mV for 100ms and serves to monitor the amount of leak throughout the recording. The current resulting from this -70mV step should be equal to that of the -90mV holding potential and should remain this way through the duration of the I/V protocol. An increasing amount of current during the pre-pulse

step indicates that the cell is leaky and that the data being collected may not be good quality as a result of this leak current.

A steady pulsing protocol was used to monitor the time-dependent changes of hEAG1 currents in response to I&T. Instead of stepping to a range of membrane potentials, this protocol continually stepped to +60mV for a designated number of sweeps returning to the holding potential of -90mV before the next sweep. In some experiments, voltage was stepped to +20mV as this was the voltage where current was at its maximum due to the reduction in current at more depolarised potentials. The start to start interval was also 10s.

2.4. Whole-cell patch clamp electrophysiology

2.4.1. Patch clamp micropipettes

Patch clamp micropipettes were pulled to resistances between 3 and 5M Ω using the same micropipette puller as in 2.3.1. The glass used was a filamented borosilicate capillary glass (1.5mm outer diameter and 0.86mm internal diameter, model GC150F-10 WPI, UK). Electrodes were pulled using a pre-set programme that heats a filament to slowly melt the glass until the two micropipettes are pulled apart. Dry air is pumped on and the cycle repeats. This results in a blunt rather than sharp micropipettes.

Patch micropipettes were pulled on the day of use and used no longer than 24hrs after being pulled. Micropipettes were stored in a specialist holder that holds 16 micropipettes and was covered by a glass beaker to prevent dust from getting on the tip, which would block seal formation with cell membranes. Patch micropipettes were filled with filtered intracellular solution just prior to use.

2.4.2. Patch clamp rig set up

The perfusion pump and the gravity perfusion lines were all cleaned with 70% ethanol and then flushed with distilled water before an experiment. The pre-warmed extracellular solution was run through the perfusion lines to fill the bath. The bath was half-filled with extracellular solution and then 3-4 drops of suspended CHO cells were added to the bath and left for 10-15mins to adhere. There is a silver-chloride (AgCl) coated silver wire in the recording bath which, once the electrode is lowered into the bath solution, completes the electrical circuit by which electrons

can flow and is a low resistance pathway to ground the bath. The wire in the bath and the one inside the electrode are regularly bathed in bleach to ensure there is a sufficient layer of AgCl available for electron transfer.

After cells had attached, the pump perfusion was used briefly to remove any cells still in suspension in the bath. A micropipette was filled with the intracellular recording solution and mounted onto a holder containing the silver coated wire (electrode) that contacts the intracellular solution. The electrode was lowered into the bath solution using a micromanipulator, creating the electrical circuit, and was positioned close to a cell that was expressing the hEAG1 channel as determined by eGFP expression (see 2.2.1.).

The Clampex10.4 software (PClamp, Molecular Devices) was used to record currents and calculate the resistance of the micropipette. As the micropipette was moved onto the cell the resistance increased. A small amount of suction was applied to the micropipette via a syringe and suction line to encourage seal formation. As a 1G Ω seal was forming the command potential was gradually dropped to the desired negative holding potential as this further encourages seal formation. The 'fast capacitance' was increased to compensate for the capacitance of the electrode. The membrane under the micropipette was then ruptured by applying further suction to gain whole-cell access into the cell. The 'whole-cell capacitance' and 'series resistance' compensations were increased to compensate for the membrane capacitance, voltage, whilst the percentage compensation was increased to minimize any voltage drop or loss of voltage control. The scaled output gain was adjusted to a maximum level without exceeding the limits of the amplifier and analogue to digital converter. Series compensations were >70% and series resistances were considered acceptable if less than 10M Ω . The voltage clamp amplifier was an Axon 200B (Molecular Devices) connected to a Digidata 1322A. Signals were sampled at 5kHz, no leak subtraction was applied.

2.4.3. Whole-cell patch clamp voltage protocols

The current-voltage relationship needs to be assessed in mammalian cells to ensure that there is no significant differences in how the channel functions compared to its expression in the amphibian cells. An I/V protocol similar to that used in the oocytes (1.3.3.) was used, it begins at a holding potential of -80mV and

increases in 10mV steps up to a final potential of +70mV. This protocol also includes a step to -30mV after the main voltage pulse so the tail currents of hEAG1 can be effectively measured, the protocol then steps back to the holding potential ready to start another sweep.

Since the single channel current of hEAG1 is reported to be small, this information has to be obtained via non-stationary noise analysis. This approach relies on the stochastic nature of ion channel opening and the fact that the probability of channel opening (P_{open}) changes with voltage. The protocol used to obtain the necessary data is similar to the steady pulsing protocol (2.3.3.) in the sense that it only steps up to +20mV from the holding potential of -80mV. It then steps down to -30mV before stepping back to the holding potential.

In order for there to be enough variance to analyse, the noise analysis protocol requires a lot of data points so there is only 1.5seconds between the start of each sweep. This will allow the time-dependent changes in channel behaviour in I&T to be closely followed and to ascertain whether N , i or P_{open} is responsible for the change in current behaviour.

2.4.3.1. Electrophysiology data analysis

After electrophysiology experiments, data files were opened and data extracted using the ClampFit 10.4 software (P Clamp10, Molecular Devices, USA). Capacitance transients were removed during analysis. End pulse current data was extracted from the current traces was normalised straightaway or was converted to conductance before being normalised using Excel 2013. Mean current and conductance \pm SEM was plotted against membrane potential to give I/V and G/V relationships respectively. G/V data was fitted with a Boltzmann function which outputs values for $V_{0.5}$ and k (the slope of the curve). The k value denotes the slope of the data and the “steepness” with a small value indicating a steeper curve. The value of k is positive for channels that activate with depolarisation of the membrane.

I/V current traces were also loaded into an in-house written software called Tracan3, this software analyses the rise time of activation from 10-80% of the maximum current and is used to represent the activation kinetics. Tracan3 was also used to conduct the noise analysis of whole-cell patch clamp data where mean current and variance were fit using function 1 (see relevant results chapter).

Graphs and representative current traces were generated using the GraphPad Prism software. The statistical significance of the effect of I&T on either the WT or mutant channels was analysed in Prism.7 using a two-tailed paired Student's t-test. The effect of the mutation on the WT channel was analysed using a one-way ANOVA with the Holm-Šídák post-hoc test. Significance was recognised at $p < 0.05$.

2.4.3.2. Ion channel simulations in Tracan3

Tracan3 was used to analyse the noise analysis data collected from whole cell patch clamp but it was also used to conduct simulation experiments. These simulations rely on a Markov model for ion channel behaviour and are designed to produce outward, non-inactivating K^+ currents. It is based on a system comprising 5 closed states and 1 open state. The rate at which the ion channel moves in or out of each closed state is the same whilst the rate at which it moves into the open state can be changed to mimic changes in open probability.

The number of channels was set to 500 for all experiments and only changed when simulating changes in the number of available channels. The single channel current was set to 0.5pA except when simulating changes in the single channel current. The rate at which channels enter the open state was maintained at 0.12ms^{-1} except when testing for changes in open probability. The rate of movement into the open state is not the same as open probability but correlates with it, a faster rate of movement would correlate as a higher open probability. Simulations were run 200 times per condition tested and this data was used to calculate the mean variance. The mean variance was plotted against mean current in Tracan3 and the data was fit using Function 1 (see 3.3.2.). Graphs were exported from Tracan3 and their presentation finalised in Graph Pad Prism7.

2.5. Cell Culture

2.5.1. Mammalian cell maintenance

Chinese Hamster Ovary (CHO) cells for transient transfection with plasmid DNA were revived from -80°C at passage 4 and kept in DMEM/F-12 growth medium (Fischer Scientific) supplemented with 10% FBS and 5% pen-strep antibiotic (5000 U/ml penicillin and 5000 $\mu\text{g}/\text{ml}$ streptomycin). In some experiments a CHO cell line stably expressing hEAG1 (CHO-hEAG1) was kindly provided by Prof. L. A Pardo (Max

Planck Institute for Experimental Medicine, Gottingen) was cultured in DMEM/F-12 medium with 10% FBS and 500µg/ml Zeocin antibiotic. All cells were incubated at 37°C in a humidified chamber at 5% CO₂.

Cells were grown to 70-85% confluency, washed in PBS (no Ca²⁺ or Mg²⁺) (Fischer Scientific, UK) and were split using cell dissociation buffer (Fischer Scientific, UK). Cells were suspended in 10ml medium and centrifuged at 1000rpm for 5minutes. The pellet was suspended in 10ml of fresh medium and either plated into T75 growth flasks at 1:20 dilution or seeded into petri dishes ready for transfection. All media and reagents were warmed to 37°C prior to cell culture.

2.5.2. DNA transfection of CHO cells

Cells were seeded at 50% confluency in 36.8mm diameter 6 well plates (Sigma) and left overnight to attach to the base. 100µl medium lacking serum and antibiotic was used to mix DNA between 0.5 - 2µg with XtremeGENE9 transfection reagent (Sigma) in a ratio of 3µl to 1µg DNA. This mixture was left for 20minutes at room temperature before being added directly to the CHO cells in the petri dish containing serum. The dish was rocked back and forth to mix the DNA over the cells. There was no need to remove the transfection reagent or change the medium. CHO cells were left to express the DNA for between 18 and 48 hours at 37°C.

The plasmid containing the KCNH1 gene also contains the gene coding for enhanced green fluorescent protein (GFP). This was done so that cells transfected with the plasmid will express GFP and appear green when illuminated by fluorescent light, thus identifying them as cells that have taken up the plasmid and so should be expressing hEAG1. This is more efficient than co-transfecting GFP and hEAG1 separately as this does not guarantee that green cells will also be expressing hEAG1. The KCNH1 gene was preceded by a strong CMV promoter, whereas the GFP gene was preceded by a weaker promoter which means that green cells are more likely to be overexpressing hEAG1 and so are suitable for patching. Transfection efficiencies using XtremeGENE9 were between 50-75% as quantified by eye using the fluorescence microscope.

2.5.3. Suspension of cells for electrophysiology

Enzyme free cell dissociation buffer (CDB) (Fischer Scientific, UK) and extracellular recording solution were warmed to 37°C prior to cell culture. The cell

medium was removed from the petri dish and discarded along with any cells still in suspension. 2-3ml CDB was added to the dish and incubated at 37°C for between 2 and 5mins. The CDB was pipetted gently up and down to help re-suspend the cells. Once all the cells had dissociated from the bottom of the petri dish they were added to 5ml of extracellular recording solution. The cell suspension was kept at room temperature and in the dark and were discarded and replaced by fresh cells after a few hours.

2.6. Proliferation assays

2.6.1. CHO cell transfection and controls

Prior to starting the series of proliferation experiments, each DNA plasmid being used was purified using a midi-prep kit to obtain fresh DNA and to ensure a high enough yield for transfections. The DNA was also sequenced to ensure no random mutations had been introduced. The chosen DNAs were run on a gel to verify the concentrations were accurate and that the band intensity was consistent between the DNA types. This means that each well would contain the same concentration of plasmid DNA. To remove experimental bias, the experiments were done as a blind study. The DNA samples were coded by a third party so that the identity of the DNA constructs was unknown during the experiment and the analysis.

CHO cells were split 24-48hrs prior to experiments and seeded onto 25mm diameter glass coverslips (Scientific Lab Suppliers Ltd) in 6 well plates (see 2.5.1.) so that their confluency was ~80% on the day of the assay. Cells were transfected using 1µg of each DNA construct using the same protocol from 2.5.2. Transfected cells were incubated at 37°C and checked for adequate GFP expression. Only 6-well plates that had >50% transfection efficiency were used for the assay to ensure there would be enough GFP positive cells to analyse.

2.6.2. Bromodeoxyuridine (BrdU) incorporation assay

BrdU is a synthetic analogue of the nucleoside thymidine. Proliferating cells must replicate their DNA prior to division and so the BrdU takes the place of thymidine in the DNA structure. BrdU can then be stained for using an anti-BrdU antibody. Cells positive for the antibody are said to be proliferating as they incorporated BrdU into their DNA.

BrdU was stored at -20°C at a stock concentration of 2mM and was diluted 1:2000 in 4ml of fresh medium to a working concentration of 1µM. Cells were washed using PBS (no Ca²⁺ or Mg²⁺) and 2ml of fresh medium was added to each well. 400µl of the BrdU dilution was added to each well and the cells were incubated at 37°C for 30 minutes.

The medium was removed and the cells washed again in PBS. Cells were then fixed using 2ml 100% cold methanol stored at -20°C and were incubated at -20°C for 5minutes. The methanol was removed and the cells washed in PBS three times to remove any residual methanol. A solution of PBS was made up with 5M HCl to a working concentration of 2M HCl. The cells were then lysed using the 2M HCl solution at room temperature for 15 minutes. The HCl solution was removed and the cells were washed three times in PBS. A 5% BSA blocking solution was made using powdered BSA dissolved in PBS and stored on ice. 5% BSA solution was added to each well and was incubated at room temperature for 1 hour.

A mouse-anti-BrdU primary antibody (ThermoFischer, UK) was diluted 1:100 and a rabbit-anti-GFP primary antibody (Invitrogen) was diluted 1:1000 into BSA blocking solution together. The blocking solution was removed from the wells and 100µl of the primary antibody mix was added directly onto the coverslips, and left at room temperature for 1 hour. The wells were then washed three times in PBS to remove any unbound antibody from the coverslips. A goat-anti-mouse secondary antibody conjugated to Alexa Fluor 594 (Abcam) and the goat-anti-rabbit secondary antibody conjugated to Alexa Fluor 488 (Abcam) were both made up as a 1:1000 dilution into BSA blocking solution and 100µl was added straight onto each of the coverslips. The cells were left at room temperature for 1 hour in the dark to protect the secondary antibodies' fluorescence from bleaching in the light. The cells were then washed again with PBS three times.

Cell nuclei were stained using Hoechst (ThermoFischer, UK) in 20ml of PBS from a stock concentration of 20mM to a working concentration of 2µM. Hoechst stain solution was added to each well and incubated at room temperature for a strict time limit of 5 minutes. The wells were washed three times with PBS.

Mounting slides were labelled and a few drops of mounting medium were added to each slide. Each coverslip was carefully removed from the well and briefly immersed in distilled water to remove any excess PBS solution, the coverslips were blotted onto tissue. Coverslips were mounted cell-side down onto the mounting medium and the edges were sealed using clear nail varnish. Slides were stored in a wooden holder wrapped in foil at 4°C until ready for imaging and analysis.

2.6.3. BrdU incorporation assay imaging and analysis

Slides were analysed using a Nikon TE300 semi-automatic microscope (Nikon) with a Hamamatsu ORCA-R2 digital camera (Hamamatsu). The X-cite120 fluorescence illumination system (Excelitas) provided the fluorescent filters. This system uses high intensity LEDs across a wide spectrum to provide uniform illumination of samples. The Velocity software was used to capture and colour the images taken. A drop of microscope oil was added to the slide and cells were counted and imaged using a x40 objective. Between 150-300 green fluorescing cells, indicating GFP expression, were counted and then the same cells were counted again for Alexa Fluor 594 fluorescence to determine the percentage of transfected cells also showing BrdU incorporation, indicating proliferation. The criteria for BrdU incorporation was to identify nuclei of cells by using the Hoechst blue stain and then seeing which of those nuclei also contained red fluorescence from the Alexa Fluor 594 secondary antibody.

The number of GFP positive cells and the number of those that were also positive for BrdU incorporation were inputted into Excel 2013 and the percentage of proliferating cells was calculated for each of the 8 constructs used. The mean percentage and standard error (SEM) of proliferating cells was calculated. Statistical significance between populations was done using a one-way ANOVA followed by the Holm-Šídák post-hoc test as this has more statistical power.

2.7. Single cell migration assay

2.7.1. Cell counting, plating and transfection

Single cell migration is an assay used to track individual cells over a period of time and can be used to find out the directionality and speed of movement of the cells. The single cell assay was used here to determine whether hEAG1 can influence the speed or distance of migration of transiently transfected CHO cells.

CHO cells were grown to 80-90% confluency before being lifted, centrifuged and re-suspended in medium. 10 μ l of suspended cells were loaded onto a haemocytometer and counted. Approximately 5.52 x10³ cells were loaded into each well of a 24-well plate in 500 μ l of 0.1% FBS medium as opposed to the usual 10%. This serum reduction reduces cell proliferation allowing single cells to be track over longer periods of time with less risk of them dividing. Preliminary experiments had shown that cells grown in 10% FBS grew in dividing clumps with minimal single cell migration. Cells were transfected with 1 μ g of DNA using the XtremeGENE9 transfection reagent and left for 24-36hrs at 37°C to express.

2.7.2. Live single cell imaging protocol

Single live cell imaging was done by using a semi-automatic microscope, the Nikon eclipse Ti microscope (Nikon). The 24-well plate was mounted inside a temperature and CO₂ controlled chamber and secured in place. Cells were manually focussed on using a x20 objective and the Nikon instruments software (NIS) elements software. Cell coordinates were also set using the NIS programme, the system has a built in “perfect focus” whereby the coordinates also monitor the distance between the bottom of the plate and the field of focus. This is particularly useful during long experiments as it is not always possible to completely secure the plate prior to running and so the cells may gradually drift out of focus over time.

The microscope temperature control was switched on the evening before the experiment to ensure the microscope was up to 37°C. Cells were checked prior to experiments to make sure there was an adequate level of fluorescence and that single cells were present. The 24-well plate was placed into the chamber and secured. Water was added to the outer reservoir to maintain the humidity. The CO₂ was turned on and maintained at 5%. The NIS elements programme was loaded and the ANDOR EM-CCD camera was selected (Andor Technologies). The settings within NIS elements were set as follows: 20x objective, 500 μ s exposure length, GFP filter, 15 minute cycles lasting 24hrs.

Cells were centred and the coordinates set for the location. 5-10 coordinates were set per well depending on the number of green, single cells available. Cells were selected based on their shape, completely circular cells were ignored as these have likely died, and their proximity to other cells. Cells that were touching one

another were not imaged. Once all the coordinates were selected the programme was run to collect images every 15mins over the course of 24hrs. Files were transferred to the university directory for analysis.

2.7.3. Cell migration analysis

Analysis was performed using Imaris9.1 software (Bitplane) and images were visually examined to check cells remained viable during the experiment. Image stacks were loaded and the software located cells based off of parameters given by the user. Cell diameter was set at 10µm and the GFP filter was turned on so that only cells expressing GFP would be tracked. The distance radius was another setting to consider and it depends on the number of cells. The distance radius is the area the software scans in the next image to track where the current cell has gone. Fewer cells allowed for a larger distance radius to be used as it is less likely that another cell will entire the radius and cause the programme to potentially lose track of the original cell. Once these settings were applied and the software run, the resulting “tracks” were inspected. These tracks are the locations of the cell at each time point.. Any tracks that became separated but belonged to the same cell, perhaps due to a distance radius that was too small, were manually reconnected. Track lengths less than 20 data points were excluded and not analysed. Experiments were conducted 3 times each time with at least 10 cells being analysed. Parameters chosen for analysis were exported to be analysed in Excel. Unpaired t tests were performed and significance was recognised at $p < 0.05$.

2.8. Western blotting

2.8.1. Lysis buffer

The stock lysis buffer contained (in mM): Tris-HCl (pH7.4) 50, NaCl 300, EDTA 5 and 1% v/v Triton X100. The stock was stored at room temperature but just prior to cell lysis 1 protease inhibitor tablet (Roche) was added to 10ml of lysis buffer. This was stored in the fridge or on ice at all times.

2.8.2. Western blotting protocol

Western blotting was used to compare WT hEAG1 and mutant hEAG1 protein expression in transfected cells. Cell lysates were run on SDS-PAGE gels to separate proteins by size then transferred to nitrocellulose membranes. Antibodies were then used to detect specific proteins.

Transfected CHO cells were grown in 6-well plates until confluent. Cells were washed in ice cold PBS. Plates were kept on ice and cells were scraped off and the suspension was stored on ice in labelled Eppendorf tubes. Samples were centrifuged at 4°C for 10mins at 5000rpm to pellet the cells. The supernatant was discarded and 30µl of cold lysis buffer was added to each sample to re-suspend the pellet and incubated at room temperature for 30mins. Lysed samples were centrifuged again at 4°C for 15mins at 14,000rpm and the supernatant containing the protein was transferred to new tubes. Protein samples were stored at -20°C.

Samples were quantified using a bicinchoninic acid assay (BCA) protein assay kit (ThermoScientific) that uses known concentrations of BSA to quantify unknown protein samples. 96-well plates were analysed at 550nm in a Wallac Victor² spectrophotometer using the programme Perkin Elmer2030 that calculates absorbance of light by the colorimetric reagent of the BCA kit. Higher values mean a higher concentration of protein. Protein concentrations were calculated and the volume needed for 60µg of total protein was also calculated. Samples were kept on ice and mixed with 10x NuPage reducing buffer and 4x NuPage loading buffer (both Invitrogen). Final volumes were made up to 30µl using lysis buffer. Samples were denatured at 70°C for 10mins prior to loading. A 1x running buffer was prepared from a 20x stock of Tris-Acetate SDS (Invitrogen) and NuPage 3-8% Tris-Acetate gels (Invitrogen) we set up in the gel tank. Anti-oxidant was added to the 1x running buffer 1:400 (Invitrogen) and this was used to fill the centre of the tank only, normal 1x running buffer was used to fill the rest of the tank. 5µl of Blue Prestained Protein ladder (NEB) was added to the wells just prior to and after the protein samples, a maximum of 30µl of sample was added to each well. The gel was run at 130V for 1 hour.

The transfer buffer was prepared using 10mM NaHCO₃, 3mM Na₂CO₃, 1ml of 10% SDS, 200ml 100% methanol and topped up to 1 litre with dH₂O. Nitrocellulose membranes (GE Healthcare Life Sciences) were soaked in dH₂O and then soaked in 1x transfer buffer for at least 10 minutes. The gel was removed from the cast and trimmed, it was placed into transfer buffer along with filter papers prior to assembly of the transfer sandwich. The transfer sandwich was set up and placed in the tank filled with 1x transfer buffer. To allow efficient transfer of all proteins, the gel was

transferred in a voltage gradient, 10V for 10 minutes, 20V for 10 minutes, 30V for 10 minutes, 40V for 10 minutes and 50V for 45 minutes.

Membranes were removed and dried at 37°C for 20 minutes to fix transferred proteins, the membrane was rehydrated in dH₂O and trimmed. Membranes were incubated in enhancing reagent 1 of the Western Blot Signal Enhancer kit (ThermoScientific) for 2 minutes, washed 5 times in dH₂O and then incubated in reagent 2 (ThermoScientific) for 10 minutes before being washed 5 times in dH₂O again. Membranes were blocked with 0.1% casein-TBST (Tris buffered saline Tween20) (Invitrogen) for 2 hours and then incubated in a monoclonal rabbit anti-hEAG1 1^o antibody made in-house (1:1500 in 0.1% casein-TBST) overnight at 4°C.

The solution containing 1^o antibody was removed and stored at 4°C, the membrane was washed 5 times in dH₂O and then in TBST for 5 minutes. The secondary antibody was donkey anti-rabbit conjugated to horseradish peroxidase (HRP) (GE Life Science), and was prepared in 0.1% casein-TBST solution and diluted 1:8000. The membrane was incubated at room temperature in the secondary for 45 minutes. The membrane was again washed 7 times in dH₂O and then in TBST for 5 minutes. The reagents from the chemiluminescence kit (Millipore Imobilon Western Chem.HRP) were mixed 50% each and kept in the dark. The TBST was removed from the membrane and it was then incubated for 5 minutes in the chemiluminescence solution in the dark to develop. Blots were imaged using the BioRad camera and the QuantifyOne programme that expose the HRP conjugate.

The membrane was also probed for a housekeeping protein to ensure even loading of the wells, in this case β -actin as it is ubiquitously expressed. The membrane needed to be stripped of the current antibodies. 3-4ml of Western Blot Stripping Buffer (ThermoScientific) was used after rinsing out the chemiluminescence with dH₂O. The membrane was incubated at room temperature for 30 minutes before being rinsed again in dH₂O. The process of blocking in 0.1% casein-TBST was repeated before incubation in the primary antibody – monoclonal mouse β -actin (Santa Cruz) 1:1000 in 0.1% casein-TBST – for 1 hour. The membrane was washed 3 times in dH₂O and then in TBST for 5 minutes. The secondary antibody – sheep anti-mouse HRP (GE Life Science) – was prepared 1:8000 in 0.1%

casein-TBST and incubated at room temperature for 45 minutes. After removal of the secondary antibody the washing and chemiluminescence steps were followed as before.

2.9. Immunocytochemistry for imaging the primary cilia

2.9.1. Cell culture and DNA transfections

hTERT-RPE1 cells were grown in DMEM/F-12 medium and 10% FBS with no antibiotics, they were seeded onto fibronectin-coated coverslips in a 6-well plate at 100,000 cells per well. Cells were left to attach overnight before being transfected with 1 μ g DNA per well using Lipofectamine 3000 (Invitrogen). Transfected cells were incubated at 37°C for 24hrs before being serum starved for 48hrs. Under these conditions, untransfected cells stop dividing and produce primary cilia.

2.9.2. Immunocytochemistry protocol

To image primary cilia, immunocytochemistry techniques were used with an antibody that recognises acetylated α -tubulin. hTERT-RPE1 cells were washed 3 times in PBS and fixed using 1ml Accustain (Sigma) for 8 minutes at 4°C. The Accustain was removed and the cells washed 3 times in PBS. Cells were then permeabilised in 0.5% Triton X-100 PBS (Sigma) for 10 minutes at room temperature. Cells were washed 3 times in PBS before blocking for 30 minutes in 10% BSA in PBS (Sigma) at room temperature.

The primary antibody – mouse monoclonal anti-acetylated α tubulin (Santa Cruz) – was diluted in 10% BSA 1:3000 and incubated at room temperature for 1 hour. Cells were washed 3 times in PBS-Tween20 (1%) before incubation goat anti-mouse AlexaFluor 594 (Life Technologies) with the 2^o antibody, diluted 1:1000 in 10% BSA for 30 minutes in the dark. The cells were again washed 3 times in PBS and the nucleus was stained with Draq5 (BioStatus) diluted 1:1000 in PBS and incubated for 10 minutes in the dark. Draq5 was washed out with dH₂O to remove any excess salts. Coverslips were mounted on glass slides (ThermoScientific) using the ProLong Gold anti-fade kit (Life Technologies). The slides were stored in the dark at 4°C prior to imaging.

2.9.3. Primary cilia staining and analysis

Slides were mounted onto an inverted epifluorescence imaging microscope (Nikon TE300) for imaging. Images were obtained using the NIS elements programme. Filters for Draq5, excited at 647nm and emitted at 681nm, and Alexa Fluor 594, excited at 590nm and emitted at 617nm. Images were taken on an ANDOR EM-CCD camera (Andor Technologies). A single wide field view containing between 1000 and 3000 cells was imaged for each fluorochrome. Experiments were repeated 4 times. Images were loaded into Fiji where the blobs analysis was conducted that counts the number of cells in the Alexa Fluor 594 panel. The primary cilia were analysed by manually setting the threshold for brightness and Fiji counts objects within the size parameter chosen, in this case the range for object size was 0.4 to 3 μm^2 . Values for number of cells and cilia were analysed in Excel 2013 to obtain mean \pm SEM for the percentage of cells presenting with cilia. A one-way ANOVA test was applied to calculate statistics, the Holm-Šídák post-hoc test was used afterwards as this has more statistical power. Significance was recognised at $p < 0.05$.

2.10. Ca²⁺ imaging of CHO cells

Ca²⁺ imaging of CHO cells was done to see how the addition of 5 μM I&T affects the intracellular Ca²⁺. Two cell lines were used, untransfected CHO cells and a stable CHO cell line expressing WT hEAG1. The use of the stable cell line was to test whether the presence of WT hEAG1 affected the Ca²⁺ response of the cells.

Cells from either cell line were seeded onto 30mm coverslips (Fischer Scientific) and grown to 60% confluency. Coverslips were transferred to a bespoke made microscope adaptor where they were loaded with 2 μM Fluo-3 (Life Technologies) for 35mins in the dark at room temperature. The Fluo-3 was removed and the cells were washed twice in room temperature extracellular recording solution. The adapter was mounted on the confocal Olympus IX81 microscope and was imaged in both bright field and fluorescent channels simultaneously using the Olympus Fluoview 4.2 filter box. Cells were recorded in the dark using a x60 objective and were imaged every 5 seconds. Cells were recorded in control extracellular solution for 2mins before 5 μM I&T was added.

Image stacks were analysed in Fiji where regions of interest were manually drawn around cells. The Fluo-3 intensity was measured for each frame and data values were transferred to Excel 2013. The data for each cell was normalised to its Fluo-3 signal in control. Data was averaged and presented as mean \pm SEM and was plotted against time to produce a graph of the Ca²⁺ response. Paired t tests were conducted on the data and significance was recognised at $p < 0.05$.

2.11. Surface expression assays

CHO cells were grown on glass coverslips (Scientific Lab Suppliers Ltd) in a 6-well plate to 70% confluence before being transfected with plasmid DNA for WT hEAG1-BBS or Δ 2-26 hEAG1-BBS (see 2.5.2). 3 wells of cells were transfected per construct, one for a control study and the other two for different time points following 5 μ M I&T. Cells were checked under a fluorescent microscope for GFP signal to ensure the transfection efficiency was >50%.

Cells were washed twice in room temperature PBS to remove any contaminating medium. 1ml of room temperature extracellular solution, which was used previously for whole cell patch clamp (see 2.1.2), was added to each well. Wells to be stimulated with I&T had an additional 1ml of extracellular solution containing 10 μ M I&T added so that the final concentration of the 2ml was 5 μ M I&T. The I&T stimulation was ended at either 100s or 300s for WT hEAG1 or 60s and 300s for Δ 2-26 hEAG1 as these were the times the current amplitude was at its peak change from control (100s or 60s) or the end of the recording period in oocytes (300s) respectively. After the stimulation time, the cells were placed on ice to reduce the rate of endo/exocytosis. Cells were washed 3 times in PBS to remove the I&T from the wells.

A final concentration of 0.3 μ M BTX-594 (Thermo Scientific) was made up in 1ml of extracellular solution. The BTX-594 solution was added to the cells and left at 4°C for 60mins to allow binding of BTX to the surface expressed channels. Cells used as controls were not exposed to 5 μ M I&T and were incubated directly with 0.3 μ M BTX-594 to assess control levels of surface expression. The BTX-594 containing solution was removed from the wells and the cells were gently washed 3 times with PBS. Coverslips were rinsed in dH₂O before being mounted on glass slides (ThermoScientific) using DAPI-containing mounting medium (Vector Labs).

Slides were analysed on the same Nikon TE300 semi-automatic microscope (Nikon) with a Hamamatsu ORCA-R2 digital camera (Hamamatsu) as described in 2.6.3. The X-cite120 fluorescence illumination system (Excelitas) provided the fluorescent filters and the Velocity software was used to capture the images which we subsequently coloured using the same software. 10-20 cells per coverslip were analysed and the experiment was repeated 3 times. Images were analysed for fluorescent intensity in the Fiji software and data obtained were analysed in Excel 2013. Unpaired t tests were used to statistically analyse the data and all data was compared to the data from control cells that had not been exposed to 5 μ M I&T. Significance was recognised at $p < 0.05$.

3. Results & Discussion – The Role of the PAS-cap in hEAG1 function

3.1. Does the PAS-cap have a role in the voltage and Ca²⁺-calmodulin dependent regulation of hEAG1?

The PAS-cap comprises the first 26 amino acids of hEAG1 which are split into a structured amphipathic helix (Q14 to R24) and an unstructured region (M1 to P13). Deletion of the PAS-cap from hERG1 has shown that it's important in the gating kinetics of the channel (Muskett *et al.*, 2011) and since hEAG1 and hERG1 are closely related a similar role may exist for hEAG1.

The aim of these electrophysiology experiments was to characterise the response of the WT channel to voltage and raised [Ca²⁺]_i which was achieved by using 5µM I&T. The response of a mutant channel in which the PAS-cap was deleted (Δ 2-26 hEAG1) was also tested to see how the PAS-cap regulates the behaviour of hEAG1 in terms of its voltage and Ca²⁺ sensitivity. The aim was then to investigate further which residues of the PAS-cap were important for its function. To study this an alanine scan of the amphipathic helix was conducted to identify exact residues that contribute to the effect of the PAS-cap.

3.1.1. WT hEAG1 is activated by depolarisation

The two-electrode voltage clamp (TEVC) technique was used to study the WT channel and all its mutants as it is a robust system that allows for fast acquisition of data. The expression of channel can be controlled by altering the volume and concentration of cRNA injected. The system allows for the study of large currents which makes it a good candidate for studying the inhibition of the WT channel.

WT hEAG1 is a voltage dependent potassium channel and so its activity depends on the membrane potential (V_m). Using the TEVC technique, a series of depolarising voltage steps (the I/V protocol) (Figure 3.1b) were applied to WT hEAG1-injected oocytes and whole cell responses were measured. The pre-pulse step to -70mV shown in Figure 3.1b was there to assess the amount of leak in the cell. The current produced by this step should be consistent throughout the entire recording and should not increase with voltage, this would indicate a leaky cell and these were excluded from analysis. The tail potential step to -70mV following the main pulse step was to produce tail currents of hEAG1, this allows the deactivation

kinetics to be studied (although this was not an aim of the experiments) but also acts to decipher between hEAG1 and endogenous current within the cell.

WT hEAG1 produced outward, non-rectifying currents that increased in amplitude with each successive depolarisation from -70mV to +70mV, representative currents are shown in Figure 3.1a. The currents in the control solution are fast to activate and do not rectify at positive potentials or during the voltage steps themselves. These mean current amplitudes \pm SEM are plotted against their respective membrane potentials to show the I/V relationship (Figure 3.2a) which shows the relationship between the current and the voltage. WT hEAG1 currents in control conditions activated with a time course from 10-80% total current of 309.1 ± 16.4 ms at +60mV in control conditions (n=6). Channel conductance (G) can also be calculated and plotted against the membrane potentials to produce G/V graphs. G is calculated using the following equation:

$$G = \frac{I}{(V_m - E_K)}$$

This equation takes into account the whole cell current (I) in amps, the membrane potential (V_m) in volts and the K^+ equilibrium potential (E_K) in volts. E_K is the membrane potential at which there is no net movement of K^+ ions. Using the K^+ concentrations stated for the extracellular solution and the estimated intracellular K^+ concentration of oocytes (Weber, 1999) the E_K value was calculated to be -102.62mV. This E_K value was used throughout the TEVC experiments.

Conductance values are plotted against membrane potential and fitted with a Boltzmann function to obtain values of $V_{0.5}$ and k (Figure 3.2b). The half-maximal ($V_{0.5}$) activation voltage is the membrane potential at which the conductance is at 50% of its maximum, the k value is the slope of the conductance curve and is an indication of the channel's dependence on the voltage. The $V_{0.5}$ and k values for the WT in control conditions were 16.0 ± 2 mV and 21.4 ± 2.4 mV respectively (Figure 3.2b and Table 1.) (n=6). A Boltzmann fit provides a good estimate of a channel's $V_{0.5}$ and k values but does not take into consideration channel inactivation during the voltage pulse. Data that has not reached a maximum or channels that are slow to activate are more difficult to fit accurately using this function. The GHK equation

would potentially offer more accuracy in these cases as it takes into account the reversal potential of the ion the channel conducts.

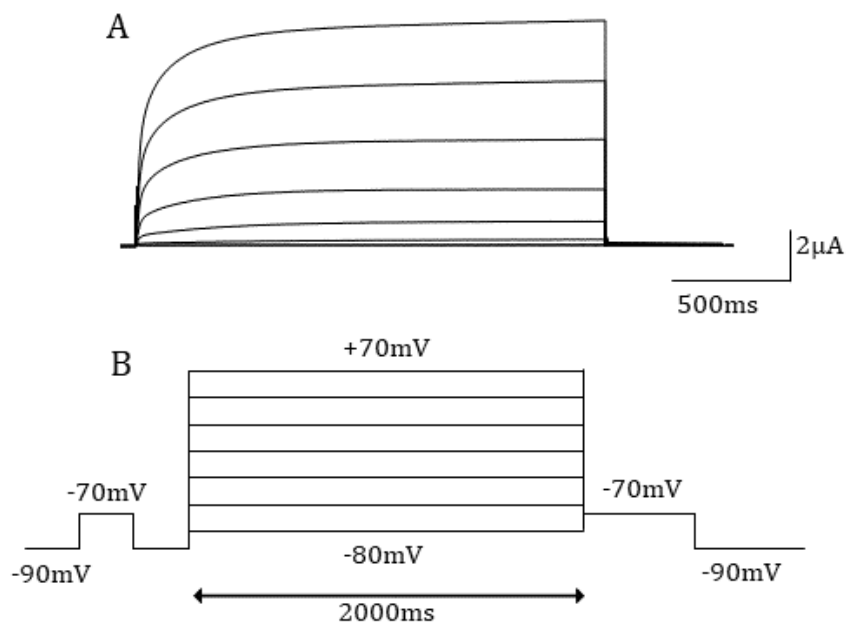


Figure 3.1. Current traces of WT hEAG1 alongside the I/V protocol.

A: currents elicited from WT hEAG1 in control solution using the protocol shown in B. These currents reach a steady state plateau and increase in amplitude with each successive depolarisation.

B: a representation of the I/V protocol used in oocyte electrophysiology to elicit the outward currents of hEAG1 across a range of voltages. Note, not all tested potentials are shown in the diagram but includes steps to -70mV through to $+70\text{mV}$ in 10mV increments.

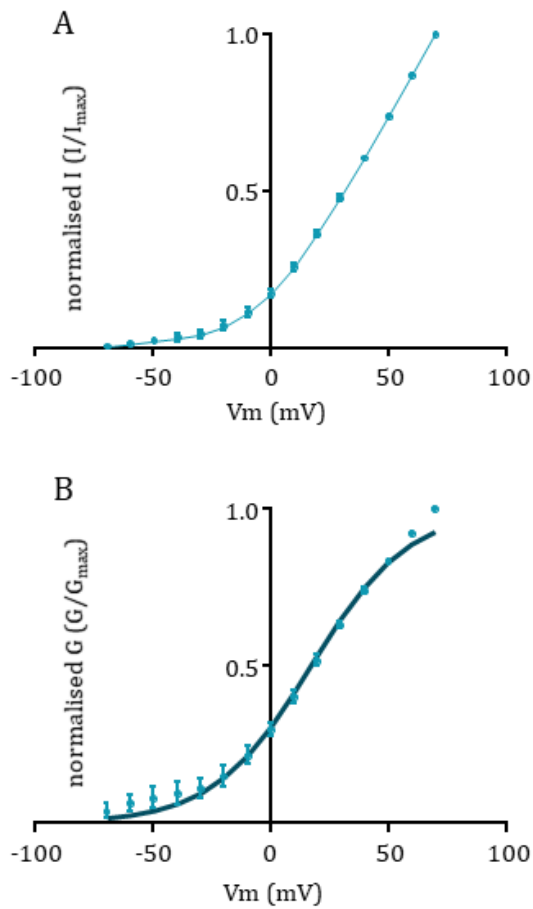


Figure.3.2. Graphs showing the relationship of both current and conductance against membrane potential of WT hEAG1.

A: mean \pm SEM current – end pulse current minus instantaneous current – plotted against voltage for WT hEAG1 in control (n=6). Current amplitudes were normalised to the highest current value in control.

B: mean \pm SEM conductance normalised to the highest control value and plotted against voltage for WT hEAG1 in control (n=6). The data is fitted with a Boltzmann function, shown in dark blue.

3.1.2. WT hEAG1 is inhibited by raised intracellular calcium ([Ca²⁺]_i)

WT hEAG1 is highly sensitive to inhibition by Ca²⁺-calmodulin with a reported IC₅₀ of ~100nM Ca²⁺ in currents recorded in excised inside-out macropatches (Schönherr *et al.*, 2000). To investigate the effect of elevated intracellular Ca²⁺ on WT hEAG1 currents recorded in *Xenopus* oocytes two compounds were used to raise intracellular Ca²⁺; ionomycin (I) – a Ca²⁺ ionophore – and thapsigargin (T) – a non-competitive inhibitor of the sarco-endoplasmic reticulum calcium ATPase (SERCA) pump. Both compounds were used at a concentration of 5μM.

Currents were stimulated using a voltage pulse to +60mV (Figure 3.3b) that was repetitively applied once every 10s. Extracellular solution containing 5μM I&T was perfused over the oocytes. WT hEAG1 currents in control solution activated quickly whilst currents elicited during the application of 5μM I&T activated much more slowly and had a reduced end pulse current amplitude compared to control traces (Figure 3.3a). WT hEAG1 currents showed a mean maximal inhibition of 85.5 ± 2.9% (p<0.0001, n=10, Figure 3.3a, Figure 3.3c and Table 1.). Following this inhibition was a phase where the current amplitude began increasing again whilst still in the presence of 5μM I&T. The amplitude increased to roughly 50% of its value in control solution (Figure 3.3c).

The I/V protocol was run again after 5μM I&T had been applied for 300s meaning the channels had some time to further recover their end pulse current amplitude. The current traces elicited this time showed slowed activation kinetics compared to the control traces but still increased in amplitude with each voltage step (Figure 3.4). The activation kinetics are much slower following exposure to 5μM I&T (Figure 3.4.) with a time course from 10-80% of 1040 ± 39ms (p<0.0001, n=6, Table 1.).

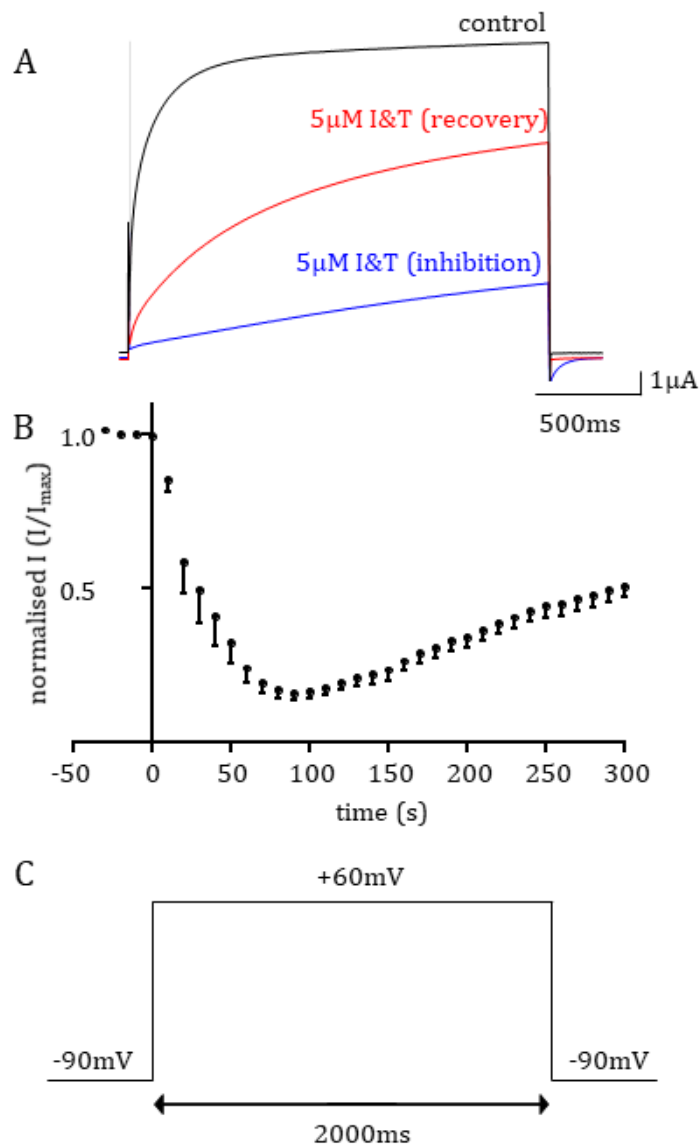


Figure.3.3. Current traces and graph showing the time-dependent effect of 5 μ M I&T on WT hEAG1 current.

A: traces showing current in control (black) and in the two states measured in 5 μ M I&T, inhibited and recovering (blue and red respectively).

B: normalised end pulse current plotted against time showing the initial inhibition of the current followed by a recovery phase back up towards control level.

C: the protocol used to elicit current for the WT channel. It continually pulses up to +60mV to activate the channel with 10s between each pulse.

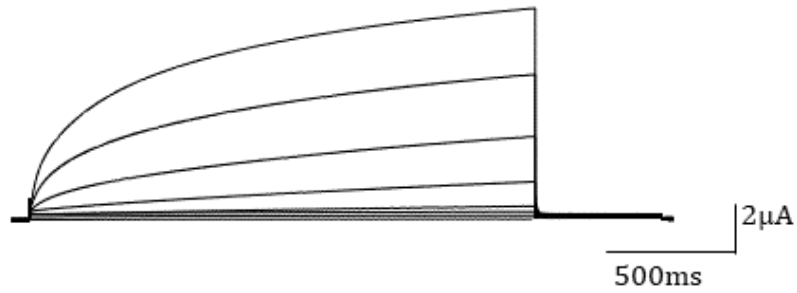


Figure 3.4. Current traces of WT hEAG1 >300s after the application of 5µM I&T.

Representative currents elicited from the same cell as Figure 3.1 >300s after the 5µM I&T was added. The channels are much slower to activate than in control solution and do not reach a steady state plateau even after the 2s voltage stimulus.

As shown by the I/V curve, for each voltage current was measured at there is a reduction in the amount of current passed at every voltage measured after the channel was exposed to 5µM I&T for >300s (Figure 3.5a). The data in control solution is also shown for comparison (Figure 3.5a). The Boltzmann fit of the conductance in 5µM I&T is shifted to the right of the control fit, this indicates that the effect of 5µM I&T causes the channel to be activated at more positive membrane potentials, the control data are again shown for comparison (Figure 3.5b).

The $V_{0.5}$ and k values measured in 5µM I&T are $28.5 \pm 2.7\text{mV}$ and $15.4 \pm 0.7\text{mV}$ respectively (Table 1, $n=6$). The $V_{0.5}$ value increased to more a more positive membrane potential from control levels ($p<0.01$) whilst the k value did not change significantly ($p>0.05$).

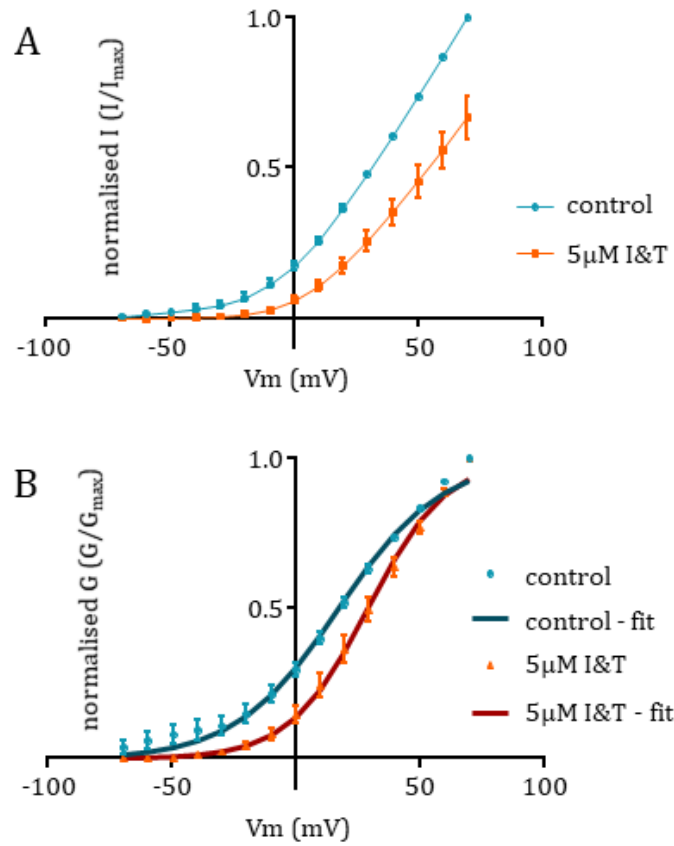


Figure.3.5. Graphs showing the effect of 5 μ M I&T on the relationship of both current and conductance against membrane potential of WT hEAG1.

A: mean \pm SEM current – end pulse current minus instantaneous current – plotted against voltage for WT hEAG1 in control (blue) and 5 μ M I&T (orange) after >300s of application (n=6). Current amplitudes were normalised to the highest current value in control.

B: mean \pm SEM conductance normalised to the highest control value and plotted against voltage for WT hEAG1 in control (blue) and 5 μ M I&T (orange) after >300s of application (n=6). The data is fitted with a Boltzmann function, shown in dark blue (control) and dark red (5 μ M I&T).

3.1.3. Deletion of the PAS-cap results in dramatic changes to hEAG1 activation kinetics and parameters

The PAS-cap of WT hEAG1 was deleted so that its role in voltage and Ca^{2+} dependence could be measured and the resulting mutant will be referred to as Δ 2-26 hEAG1. Under control conditions Δ 2-26 hEAG1 appear to activate more slowly (Figure 3.6b) than the WT channel which is shown in Figure 3.6a for comparison. Δ 2-26 hEAG1 currents also show a process called rectification whereby past a certain membrane potential the channels begin to reduce the amount of current they pass leading to a decrease in the end pulse current amplitude. The activation time course of Δ 2-26 hEAG1 was measured to be $692 \pm 27.5\text{ms}$ which is slowed when compared to the WT channel (Table 1, $p < 0.0001$, $n=4$).

When Δ 2-26 hEAG1 end pulse current is plotted against voltage (Figure 3.6c) it behaves differently to the WT channel which is shown for comparison in Figure 3.6c. Whilst the WT channel shows increasing current amplitude with the membrane potential, increasing successively with each positive increase in membrane potential, Δ 2-26 hEAG1 exhibits a process called rectification. Initially the current increases with voltage. However at +20mV the current then begins reducing with each increase in voltage ($n=4$). This would indicate that the PAS-cap has a role in voltage response of the hEAG1 channel.

The ascending component of the conductance curve was also calculated and plotted for Δ 2-26 hEAG1 to obtain values for $V_{0.5}$ and k . Under control conditions, Δ 2-26 hEAG1 has a $V_{0.5}$ value of $-22.3 \pm 1.3\text{mV}$ which is negatively (leftwards) shifted compared to the WT channel ($p < 0.0001$, $n=4$, Figure 3.6d, Table 1.). The k value for Δ 2-26 hEAG1 in control solution is $9.8 \pm 0.2\text{mV}$ which is a decrease compared to the WT channel in control solution ($p < 0.0001$, Table 1.). This reduction in the k value indicates that by the removing the PAS-cap, the channel becomes less dependent on voltage than its WT counterpart.

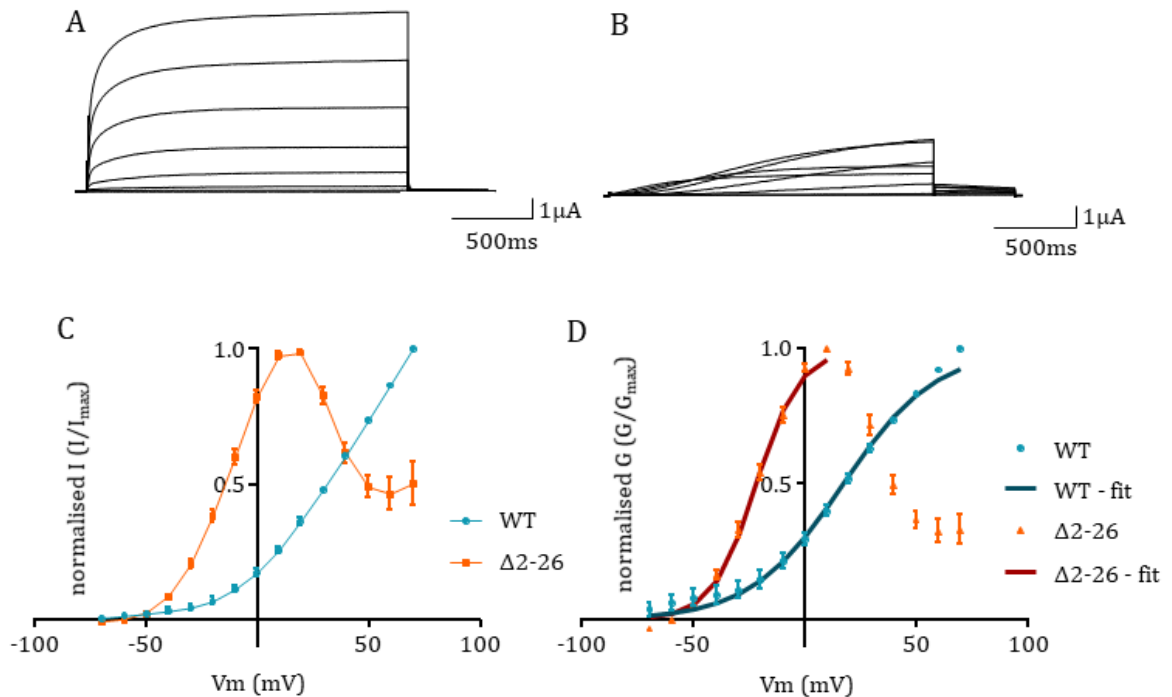


Figure 3.6. Data showing the response of WT and $\Delta 2-26$ hEAG1 to changes in membrane voltage.

A: current traces from WT hEAG1 (previously shown in Figure 3.1a) in control solution. The WT current increases in amplitude with each successive depolarisation (also shown in C, blue data).

B: current traces from $\Delta 2-26$ hEAG1 in control solution. These channels activate with a slower time course than the WT channel and do not reach a steady state plateau during the voltage pulses. Currents initially increase in amplitude with membrane depolarisation but reduce in amplitude at voltages more depolarised than +20mV (shown in C, orange data).

C: an I/V graph showing the relationship of each channel's current with voltage. WT hEAG1 is shown in blue whilst $\Delta 2-26$ hEAG1 is shown in orange. WT hEAG1 shows an continued increase in current amplitude with depolarisation whilst $\Delta 2-26$ hEAG1 increases in amplitude initially but then reduces in amplitude past +20mV.

D: a G/V graph show how the conductance of each channel relates to voltage. WT hEAG1 is shown in blue whilst $\Delta 2-26$ hEAG1 is shown in orange. WT hEAG1 shows an increase in conductance as the membrane potential depolarises, this is in line with the I/V curve shown in C. $\Delta 2-26$ hEAG1 shows an initial increase in conductance with depolarising membrane potential but this reverses at +10mV. The reduction in conductance may be down to channel inactivation or rectification.

3.1.4. Δ 2-26 hEAG1 shows a potentiation of the current when exposed to 5 μ M I&T

Δ 2-26 hEAG1 was exposed to 5 μ M I&T to find out how the PAS-cap may affect the Ca²⁺ sensitivity of the channel. The steady pulsing data to +20mV (lowered due to the maximal current being passed at +20mV) shows a large increase in current from control levels which also resulted in a large component of instantaneous current (Figure 3.7a). The current amplitude then reduced again back towards control amplitudes (Figure 3.7a). When plotted against time the data showed a ~15 fold increase in the current amplitude (Figure 3.7b). This rapidly reduces again in amplitude back towards control levels (Figure 3.7b, n=3). This is an interesting find since the WT showed a similar biphasic response to 5 μ M I&T albeit in the opposite manner – first being inhibited followed by a recovery back towards control phase (Figure 3.3c). Δ 2-26 hEAG1 has a percentage increase of $1272.7 \pm 197.1\%$ ($p < 0.01$, n=3, Table 1.) in its current when exposed to 5 μ M I&T which indicates that the PAS-cap also has a role in controlling the amount of current passed by the channel under high Ca²⁺ conditions. The responses of WT and Δ 2-26 hEAG1 are almost mirror images of one another when plotted together (Figure 3.9).

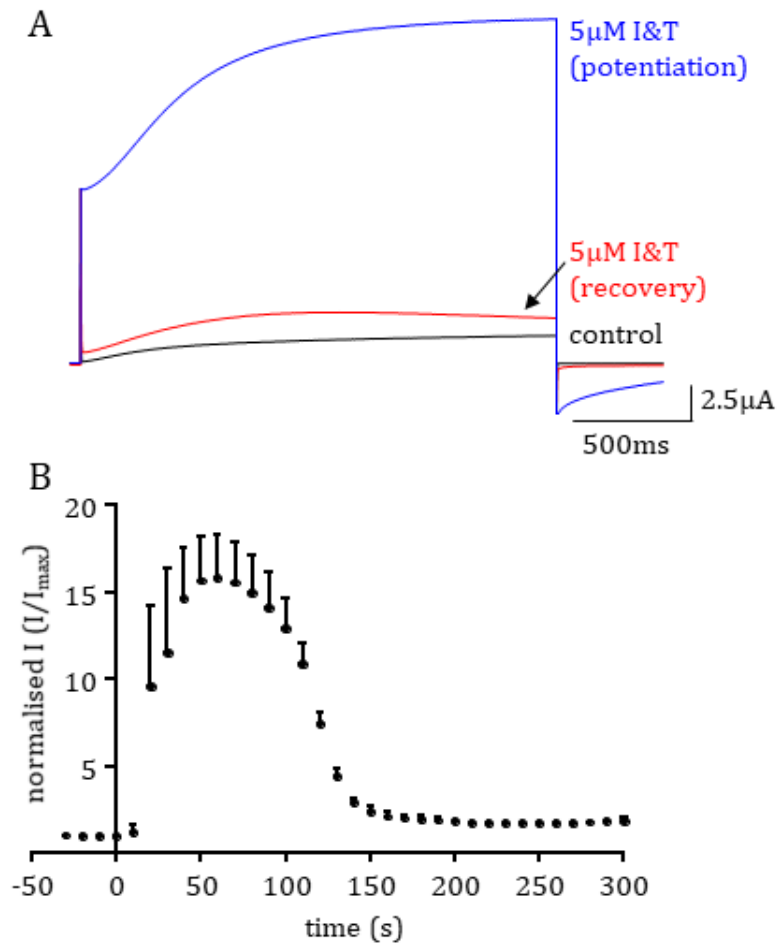


Figure 3.7. Steady pulsing current data showing how $\Delta 2-26$ hEAG1 responds to $5\mu\text{M}$ I&T over time.

A: current traces showing the $\Delta 2-26$ hEAG1 channel in control (black), the large potentiation seen with $5\mu\text{M}$ I&T (blue) and the recovery of the current amplitude back down to near control levels (red).

B: a graph showing how the current amplitude changes over time. $5\mu\text{M}$ I&T is added at $t=0$ and goes on to cause a large potentiation which then rapidly returns towards control values.

The current traces elicited from the I/V protocol (which was shown in Figure 3.1b) are shown in Figure 3.8. They show a large increase in the end pulse current compared to control conditions as well as instantaneous current at the start of the pulse. Instantaneous current indicates that $\Delta 2-26$ channels remain open from the previous voltage step, throughout the 10s gap between pulses and are still open at the start of the next voltage step and thus pass current immediately. This indicates that the PAS-cap plays a role in the deactivation kinetics of the hEAG1 channel.

When compared to the WT channel, $\Delta 2-26$ hEAG1 has slowed kinetics of activation. However, when exposed to $5\mu\text{M}$ I&T the activation kinetics slow further compared to control values, taking $867.5 \pm 85.7\text{ms}$ to activate from 10-80% of the maximal current (Table 1.). This deceleration however is not statistically significant ($p>0.05$).

The increase in current compared to control can also be seen on the I/V curve where, for each voltage, there is an increase in the amount of current passed by the channel (Figure 3.8c). The voltage at which the current begins rectifying is also shifted to more positive potentials, from +20mV to +40mV (Figure 3.8c). The control data are also shown for comparison (Figure 3.8c).

The G/V curves for $5\mu\text{M}$ I&T also show that at negative voltages the channels are open and passing more current than they were under control conditions (Figure 3.8d). The shape of the curve of the data in $5\mu\text{M}$ I&T is broader than in control conditions and means that more current is passed at more positive potentials as well as negative, despite the rectification still being present (Figure 3.8d). The $V_{0.5}$ for $\Delta 2-26$ hEAG1 in $5\mu\text{M}$ I&T was measured to be $-36.3 \pm 2.9\text{mV}$, becoming more negative than in control conditions ($p<0.05$, $n=4$, Table 1.). The negative shift in $V_{0.5}$ value indicates that the PAS-cap plays a role in the voltage of activation of hEAG1 channels. The k value for $\Delta 2-26$ hEAG1 following $5\mu\text{M}$ I&T increased from the control value to $21.0 \pm 2.7\text{mV}$ ($p<0.05$, $n=4$, Table 1.) indicating that by removing the PAS-cap the channel becomes less dependent on the voltage under increased $[\text{Ca}^{2+}]_i$.

These experiments showed that the PAS-cap has an important role in both the voltage and Ca^{2+} dependence of the hEAG1 channel and that removal of the PAS-

cap has a profound effect on the response of the channel to Ca^{2+} in which the responses mirror each other (Figure 3.9).

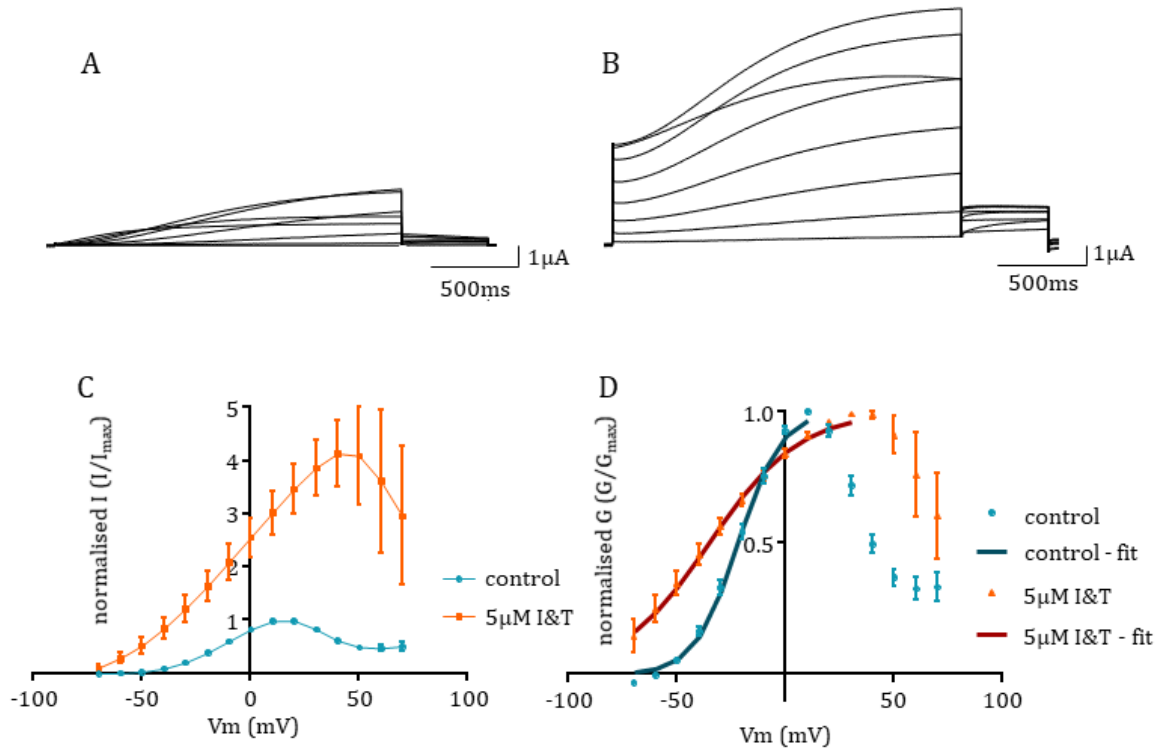


Figure 3.8. Data showing the response of $\Delta 2-26$ hEAG1 to changes in membrane voltage following the application of $5 \mu\text{M}$ I&T.

A: current traces from $\Delta 2-26$ hEAG1 (previously shown in Figure 3.6b) in control solution. The current increases in amplitude with each successive depolarisation up to $+20$ mV when it then begins reducing in amplitude (also shown in C, blue data).

B: current traces from $\Delta 2-26$ hEAG1 in $5 \mu\text{M}$ I&T solution. These channels still activate with a slow time course and do not reach a steady state plateau during the voltage pulses. Currents increase in amplitude with membrane depolarisation but now reduce in amplitude at voltages more depolarised than $+40$ mV (shown in C, orange data).

C: an I/V graph showing the relationship of $\Delta 2-26$ hEAG1 current with voltage both in control and $5 \mu\text{M}$ I&T solution. Currents in control are shown in blue whilst currents in $5 \mu\text{M}$ I&T solution are shown in orange. Currents in $5 \mu\text{M}$ I&T solution are greater in amplitude across all voltages compared to currents in control solution. Currents in $5 \mu\text{M}$ I&T solution reduce in amplitude at more positive voltages than currents in control.

D: a G/V graph show how the conductance $\Delta 2-26$ hEAG1 channel changes between control and $5 \mu\text{M}$ I&T. Control is shown in blue whilst $5 \mu\text{M}$ I&T is shown in orange. Channels are active at -70 mV in $5 \mu\text{M}$ I&T and conductance continues to increase with voltage up to $+40$ mV. Channels in control solution do not activate until -50 mV and the conductance begins reducing at $+10$ mV. Control and $5 \mu\text{M}$ I&T data are fit with Boltzmann functions (dark blue and dark red respectively).

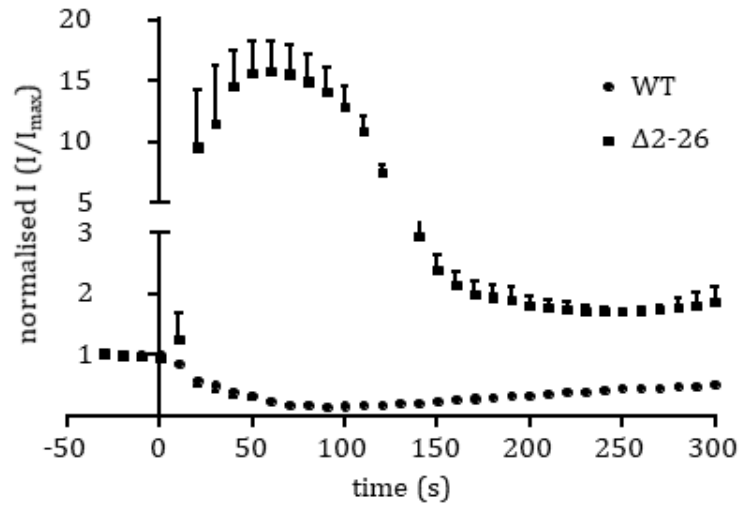


Figure 3.9. A graph showing the effect of 5µM I&T on the current amplitude of WT and Δ2-26 hEAG1 with time.

This graph shows the large potentiation of the Δ2-26 hEAG1 current (squares) against the inhibition of the WT channel (circles). 5µM I&T was added at t=0. Note that the two responses appear, to some extent, to be mirror images of each other.

3.1.5. An alanine mutagenesis scan of the PAS-cap reveals key residues of the mechanism of regulation

The PAS-cap contains an amphipathic helix spanning residues Q14 through to R24, this structured portion of the PAS-cap has potential to be interacting with its surrounding environment.

From studying the homology model generated by Dr Stansfeld based off of the available X-ray crystallography data (Haitin *et al.*, 2013), residues within the amphipathic helix are in close proximity to both the EAG and cNBH domains (Figure 3.10a). Side chains of these residues are directed towards the cNBH domain (Figure 3.10c), some towards the EAG domain (Figure 3.10d) and others are directed towards neither domain (Figure 3.10b). To begin to understand the mechanism of action of the PAS-cap, an alanine mutagenesis scan was conducted from positions N15 to V22 and resulting mutants were studied in the oocyte system using the TEVC technique.

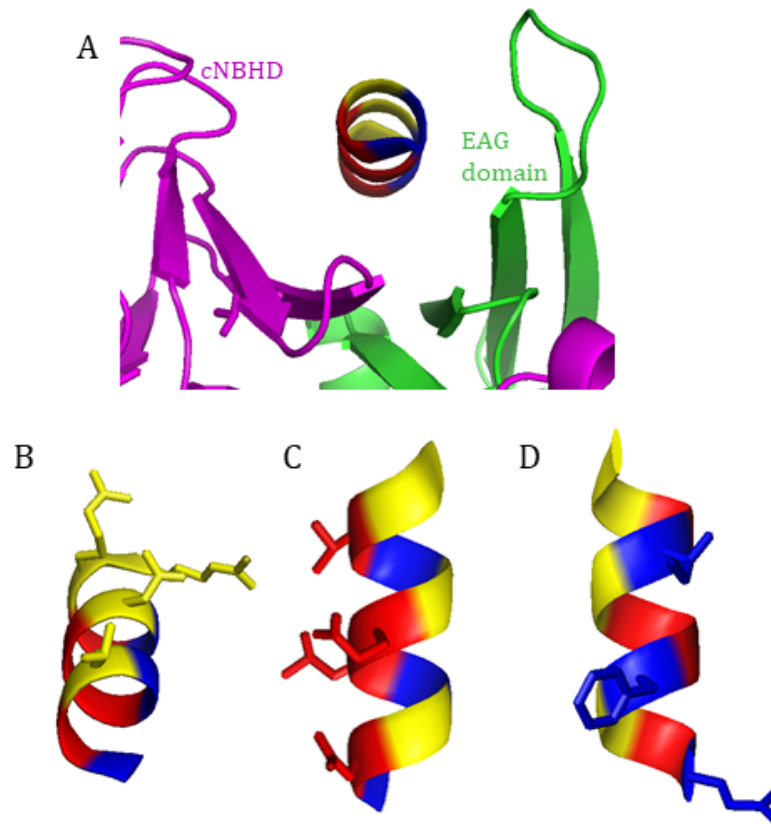


Figure 3.10. A homology model showing the residue orientation of the PAS-cap's amphipathic helix between the EAG and cNBH domains of hEAG1.

A: the amphipathic helix of the PAS-cap is shown between the EAG domain (green) and the cNBH domain (magenta). Residue positions highlighted in red point towards the cNBHD whilst those highlighted in blue point towards the EAG domain. Residues highlighted in yellow do not point at either domain.

B: stick representation of the yellow amino acid side chains, from bottom to top (N to C terminus): T16, N20, R23 and R24.

C: stick representation of the red amino acid side chains, from bottom to top (N to C terminus): N15, L18, E19 and V22.

D: stick representation of the blue amino acid side chains, from bottom to top (N to C terminus): Q14, F17 and I21.

3.1.5.1. T16A, L18A, E19A, N20A, I21A and V22A hEAG1 show similar characteristics to the WT channel

When expressed in the oocyte system 6 of the 8 mutants T16A, L18A, E19A, N20A, I21A and V22A hEAG1 all gave quickly activating, non-inactivating currents, similar to the WT channel (Figure 3.11). All of these mutant channels produce a maximal current at +70mV and the voltage at which they first pass a measurable current is indicated in Figure 3.11.

None of these mutations, with the exception of L18A, produced significant changes to the 10-80% activation time course under control conditions. T16A hEAG1 currents activated with a time course of 240.3 ± 17.9 ms ($p > 0.05$, $n=11$, Table 1.). E19A hEAG1 activates with a 10-80% time course of 175 ± 40.5 ms ($p > 0.05$, $n=11$, Table 1.). N20A hEAG1 has an activation time course of 294.6 ± 18.8 ms ($p > 0.05$, $n=5$, Table 1.). I21A hEAG1 has a time course of activation from 10-80% of 141.8 ± 31.7 ms ($p > 0.05$, $n=8$, Table 1.). V22A hEAG1 has a time course of activation from 10-80% of 419.6 ± 114.5 ms ($p > 0.05$, $n=7$, Table 1.). L18A hEAG1 has an activation time course from 10-80% of 55.5 ± 6.2 ms, a time course that is faster than the WT channel ($p < 0.01$, $n=10$, Table 1.).

The time course data gathered in control conditions indicates that only residue L18 of the PAS-cap has a role in determining the activation kinetics.

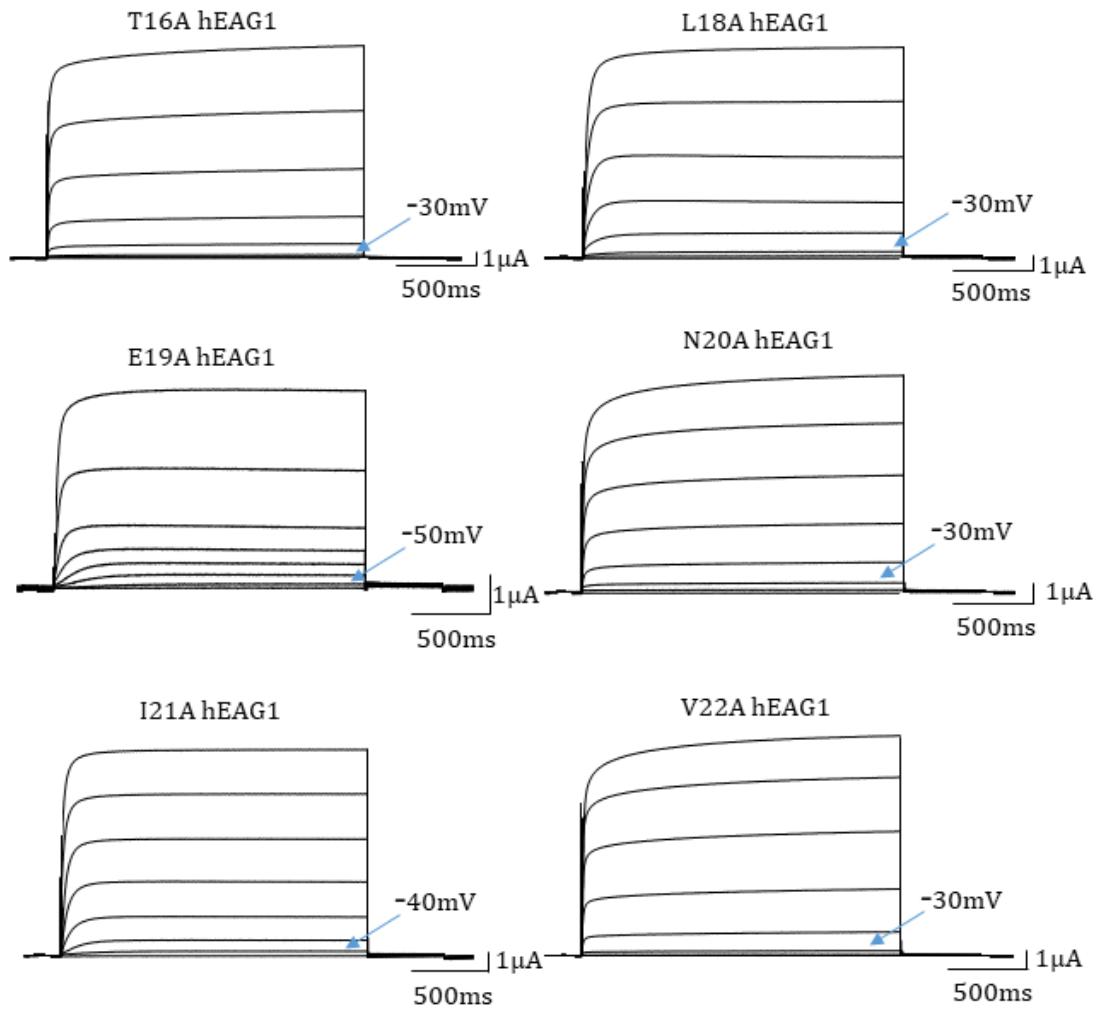


Figure 3.11. Current traces of 6 PAS-cap mutants in control solution.

Representative current traces of T16A, L18A, E19A, N20A, I21A and V22A recorded in response to the I/V protocol (Figure 3.1b). Voltage labels indicate the first voltage at which the channels pass current. All of these channels increase their current amplitude with each successive membrane depolarisation, behaviour which is similar to that of the WT channel. Maximal current is achieved at +70mV.

Similarly to the WT channel these 6 hEAG1 mutants all show increasing current amplitudes with membrane depolarisation under control conditions (Figure 3.12). L18A hEAG1 has an interesting relationship with voltage, it gradually increases in amplitude with increasing voltage but at +20mV the increases in current amplitude get much larger between voltage increases indicating some form of biphasic response to voltage (Figure 3.12, top right corner).

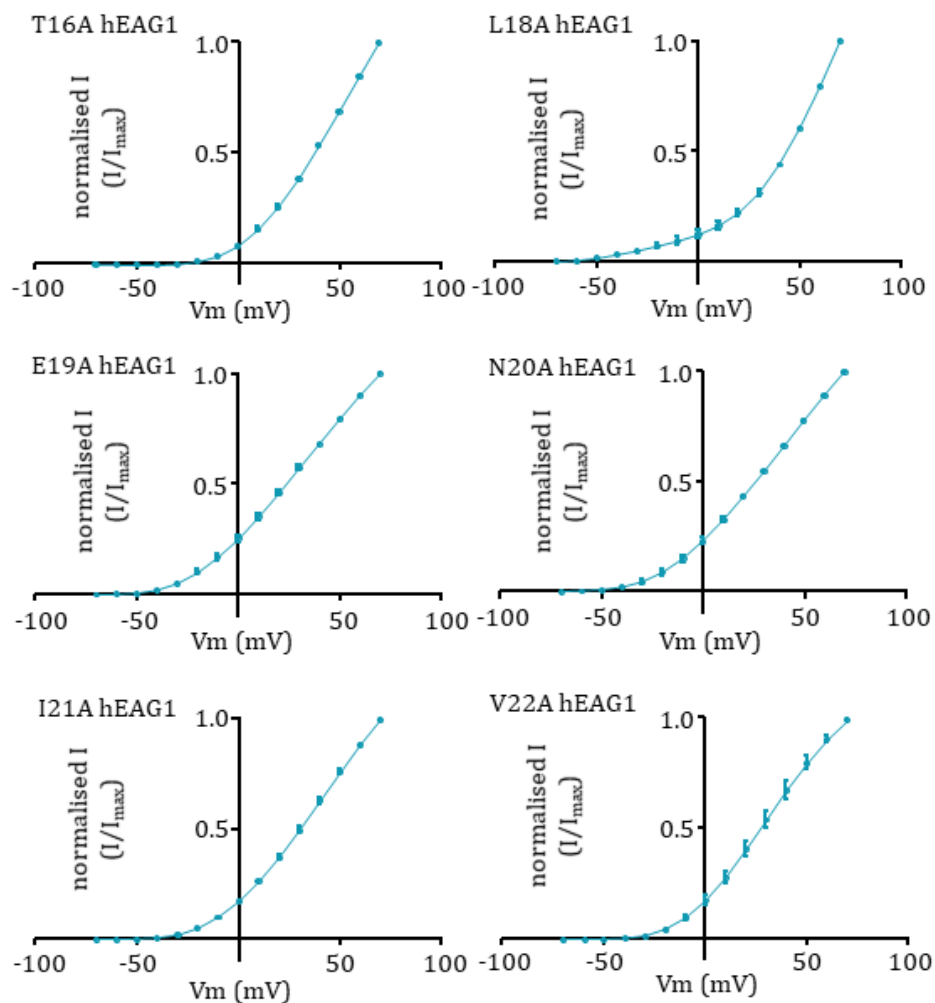


Figure 3.12. I/V graphs of 6 PAS-cap mutants showing their response to increasing membrane potential.

I/V relationships of T16A (n=11), L18A (n=10), E19A (n=11), N20A (n=5), I21A (n=8) and V22A (n=7) recorded in response to the I/V protocol. Data was normalised to the highest value in control. All channels pass increasing amounts of current at each depolarised potential.

The G/V curves for these 6 hEAG1 mutants also show a similar relationship as the WT channel. Only mutations T16A and L18A changed the $V_{0.5}$ value significantly from that of the WT channel. T16A hEAG1 yields a $V_{0.5}$ value of $28.7 \pm 0.8\text{mV}$ which is more positively shifted than the $V_{0.5}$ of the WT channel under control conditions ($p < 0.05$, $n = 11$, Table 1, Figure 3.13.). L18A hEAG1 gives rise to a $V_{0.5}$ value of $47.0 \pm 1.0\text{mV}$ which is much more positive than the WT channel ($p < 0.0001$, $n = 10$, Figure 3.13, Table 1.). E19A hEAG1 has a $V_{0.5}$ value of $6.7 \pm 2.0\text{mV}$ ($p > 0.05$, $n = 11$, Figure 3.13, Table 1.). N20A hEAG1 gave a $V_{0.5}$ value of $9.5 \pm 1.7\text{mV}$ ($p > 0.05$, $n = 5$, Figure 3.13, Table 1.). The $V_{0.5}$ value for I21A hEAG1 is $17.5 \pm 1.3\text{mV}$ ($p > 0.05$, $n = 8$, Figure 3.13, Table 1.). The $V_{0.5}$ value of V22A hEAG1 is $16.2 \pm 2.5\text{mV}$ ($p > 0.05$, $n = 7$, Figure 3.13, Table 1.).

The data from the $V_{0.5}$ values indicates that residues T16 and L18 are involved in the role of the PAS-cap to determine the voltage dependence of the channel in control conditions. The slope of the G/V curve (k value) is also an indicator of voltage dependence and was also measured.

3 mutants caused a change in the k value of the channel under control condition; T16A, L18A and V22A. T16A hEAG1 provides a k value of $14.7 \pm 0.5\text{mV}$ which is reduced compared to the WT channel ($p < 0.01$, $n = 11$, Figure 3.13, Table 1.). The k value for L18A hEAG1 is $9.2 \pm 0.4\text{mV}$ which is lower than the value for the WT channel ($p < 0.0001$, $n = 10$, Figure 3.13, Table 1.). The k value for V22A hEAG1 is $15.6 \pm 1.1\text{mV}$ which is also reduced compared to the WT channel ($p < 0.05$, $n = 7$, Figure 3.13, Table 1.). The k value for E19A hEAG1 was $18.7 \pm 0.5\text{mV}$ ($p > 0.05$, $n = 11$, Figure 3.13, Table 1.). N20A hEAG1 gave a k value of $19.6 \pm 1.1\text{mV}$ ($p > 0.05$, $n = 5$, Figure 3.13, Table 1.). The k value of I21A hEAG1 was measured to be $17.4 \pm 0.3\text{mV}$ ($p > 0.05$, $n = 8$, Figure 3.13, Table 1.).

The data shows that residues T16, L18 and V22 cause a significant reduction in the k value compared to the WT channel. This together with the $V_{0.5}$ data shows that T16 and L18 are important for two components of voltage dependence whilst V22 is responsible for the k value only.

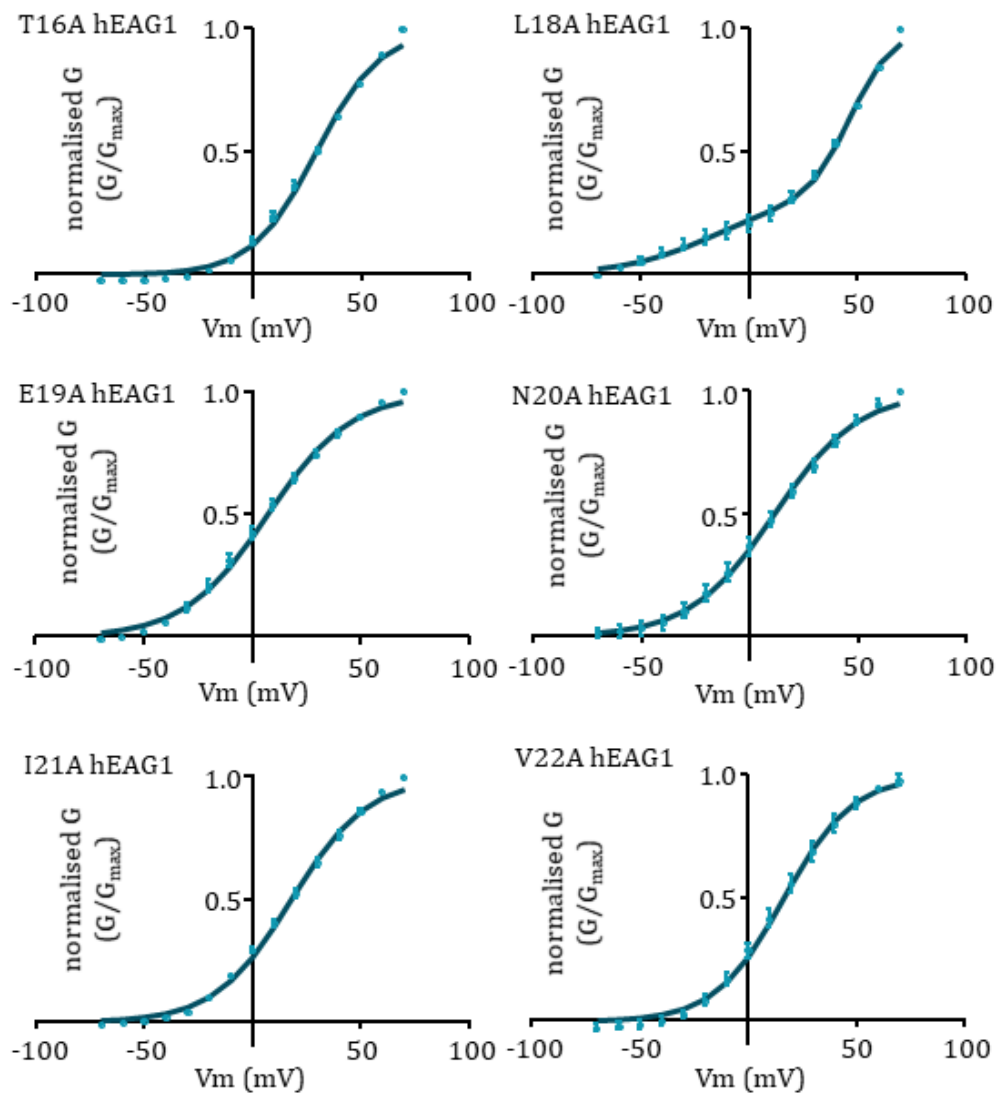


Figure 3.13. G/V graphs of 6 PAS-cap mutants showing their conductance response to increasing membrane potential.

G/V relationships of T16A, L18A, E19A, N20A, I21A and V22A recorded in response to the I/V protocol. Data was normalised to the highest value in control. Boltzmann fits for each mutant are shown in dark blue. Similarly to the I/V curves, the channels all have higher conductance at increasingly positive voltages.

These 6 mutants were also exposed to 5 μ M I&T to measure the effects on the channels during high Ca^{2+} conditions. All 6 mutants were inhibited by 5 μ M I&T and they all showed the same biphasic response as the WT channel did, recovering their current amplitude to varying degrees following the initial inhibition (Figure 3.14). During the recovery phase the channels appear to activate with much slower kinetics than in control conditions (Figure 3.14 – red traces).

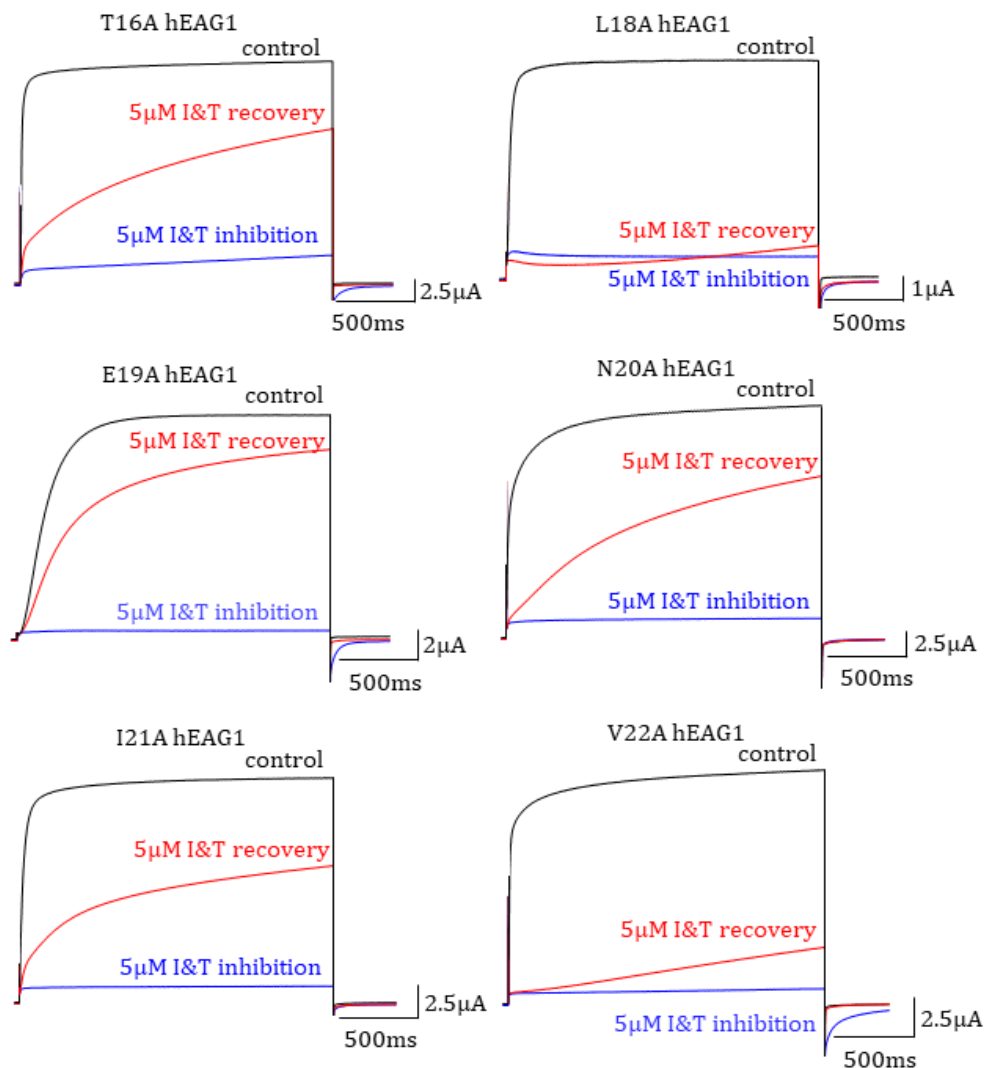


Figure 3.14. Current traces showing the inhibition of 6 PAS-cap mutants in response to 5 μ M I&T.

5 μ M I&T inhibits T16A, L18A, E19A, N20A, I21A and V22A mutants of hEAG1. Control current is shown in black whilst the maximal inhibition for each mutant is shown in blue. The red trace indicates the recovery of the current amplitude 300s after the addition of 5 μ M I&T.

All 6 mutants were significantly inhibited following the application of 5 μ M I&T. T16A hEAG1 was inhibited by $91.9 \pm 1.9\%$ from control levels ($p < 0.0001$, $n = 5$, Figure 3.15, Table 1.). L18A hEAG1 showed an inhibition of $90.4 \pm 4.6\%$ when exposed to 5 μ M I&T ($p < 0.0001$, $n = 11$, Figure 3.15, Table 1.). E19A hEAG1 was inhibited by $77.1 \pm 5.1\%$ ($p < 0.0001$, $n = 12$, Figure 3.15, Table 1.). N20A hEAG1 was inhibited by $92.4 \pm 3.0\%$ following exposure to 5 μ M I&T ($p < 0.0001$, $n = 5$, Figure 3.15, Table 1.). I21A hEAG1 shows an inhibition $93.3 \pm 1.0\%$ ($p < 0.0001$, $n = 7$, Figure 3.15, Table 1.). Finally, V22A hEAG1 was inhibited by $92.1 \pm 1.8\%$ ($p < 0.0001$, $n = 11$, Figure 3.15, Table 1.).

This data indicates that all 6 of these PAS-cap mutants were significantly inhibited by the application of 5 μ M I&T. This means that these 6 residues are likely not directly involved in the ability of the PAS-cap to regulate the response to 5 μ M I&T.

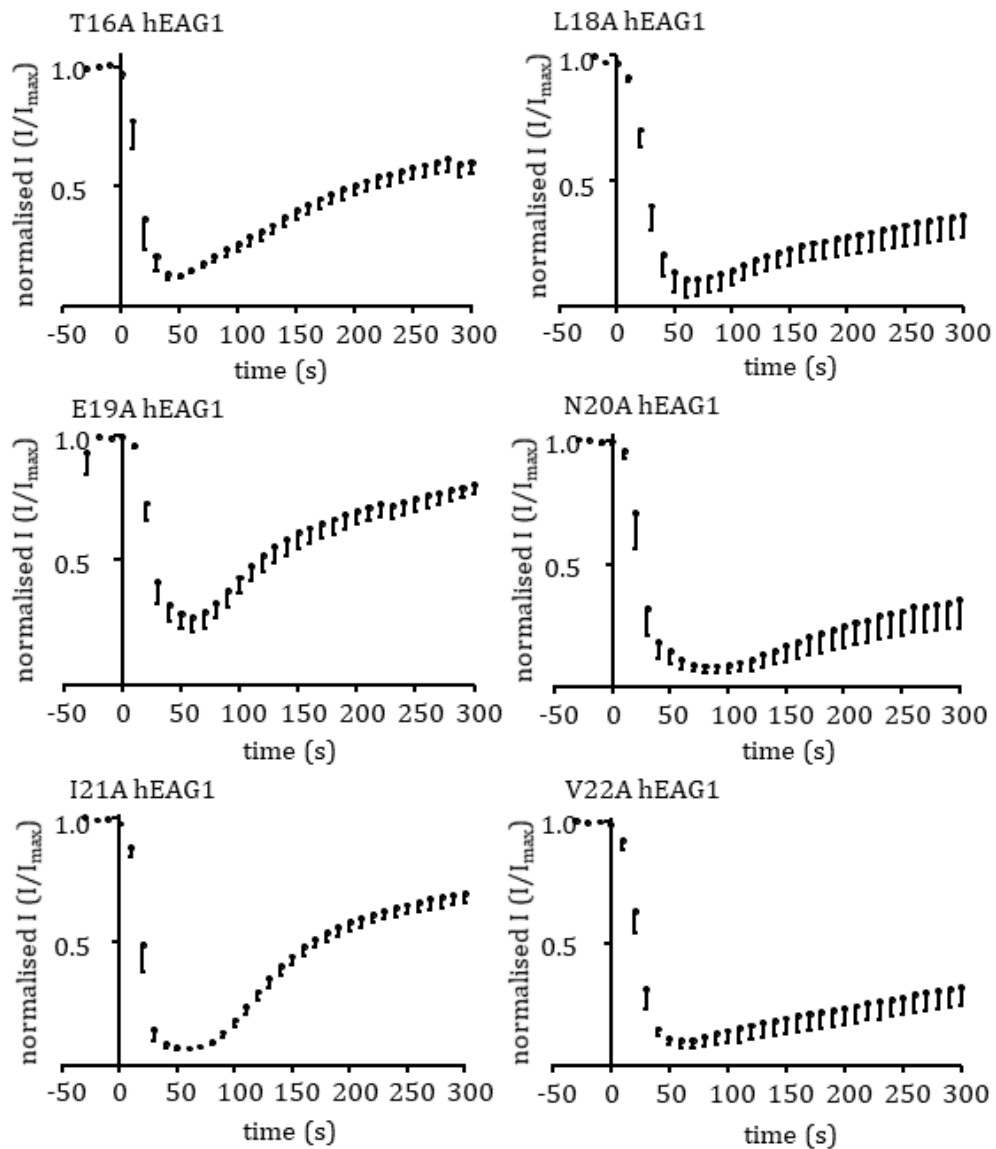


Figure 3.15. Steady pulsing graphs showing the inhibition of 6 PAS-cap mutants in response to 5 μ M I&T over time.

5 μ M I&T was added at t=0 and causes inhibition to varying degrees of T16A (n=5), L18A (n=11), E19A (n=12), N20A (n=5), I21A (n=7) and V22A (n=11) mutants of hEAG1. All mutants show a biphasic response with varying degrees of amplitude recovery after the initial inhibition.

The mutant channels were tested under the I/V protocol again >300s after the application of 5 μ M I&T. The protocol was run whilst still in the presence of 5 μ M I&T to test how the channels responded to successive depolarisations of the membrane. From the I/V traces, each mutant is maximally activated at +70mV and none show rectification behaviour similar to that of Δ 2-26 hEAG1 (Figure 3.16).

The activation kinetics of T16A hEAG1 were slowed compared to T16A in control with a 10-80% time course of 1278.3 ± 78.3 ms ($p < 0.0001$, $n = 11$, Figure 3.16, Table 1.). L18A hEAG1 had an activation time course of 1220.5 ± 144.1 ms which significantly slowed compared with L18A hEAG1 in control conditions ($p < 0.0001$, $n = 10$, Figure 3.16, Table 1.). For E19A hEAG1, the kinetics of activation from 10-80% were 537.9 ± 57.7 ms which is slower than was previously measured in control conditions ($p < 0.01$, $n = 11$, Figure 3.16, Table 1.). The time course for activation from 10-80% for N20A hEAG1 was 1156.6 ± 154.9 ms which is significantly slower than control conditions ($p < 0.01$, $n = 5$, Figure 3.16, Table 1.). For I21A hEAG1 the time course of activation from 10-80% was 808.6 ± 75.9 ms which is significantly slower than in control conditions ($p < 0.001$, $n = 8$, Figure 3.16, Table 1.). The time course of activation from 10-80% for V22A hEAG1 was 1316.9 ± 69.6 ms which is slowed compared to control conditions ($p < 0.01$, $n = 7$, Figure 3.16, Table 1.).

This data indicates that all of these 6 mutants have a role in the activation kinetics of the channel. This would also indicate that the structured region of the PAS-cap in its entirety has a role in maintaining the rate of activation of the channel and that any deviation from its structure affects the activation kinetics of hEAG1.

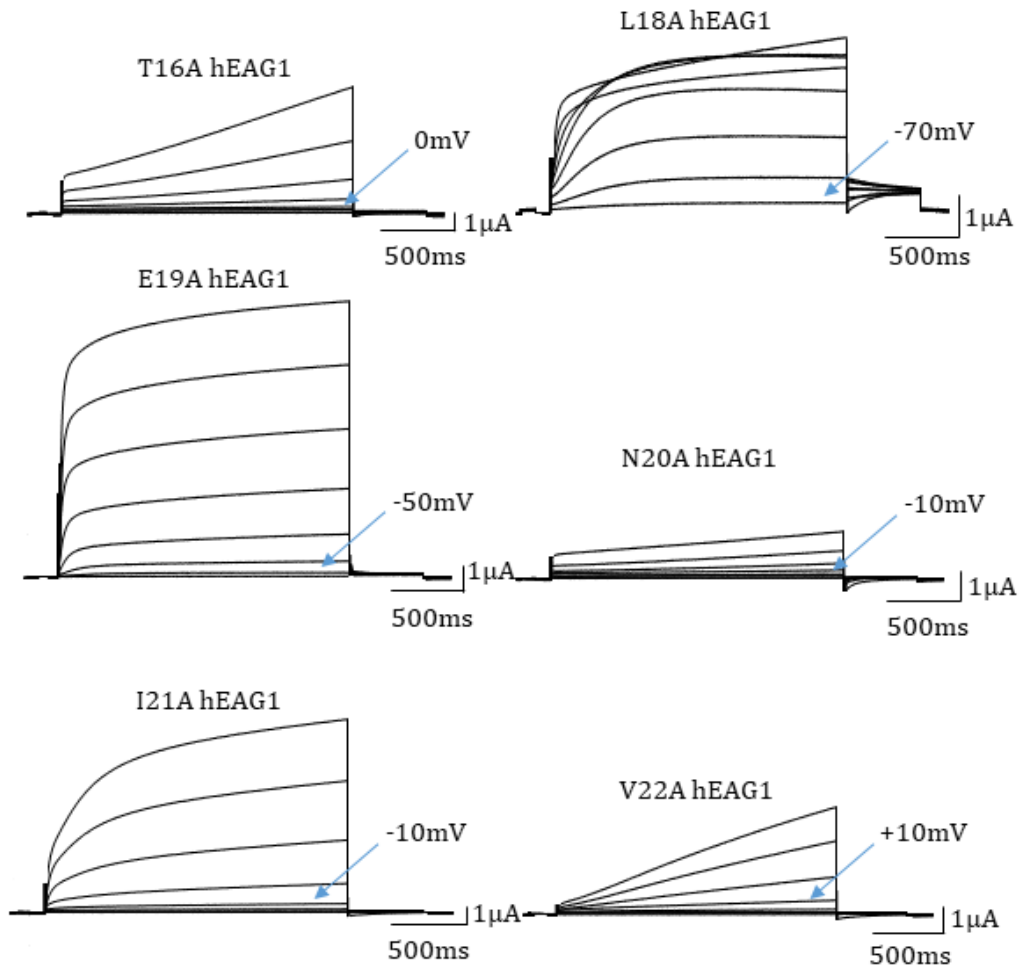


Figure 3.16. Current traces of 6 PAS-cap mutants in 5 μ M I&T.

Representative current traces of 6 mutants of the PAS-cap showing how they respond to the I/V protocol following the application of 5 μ M I&T. Voltage labels indicate the voltage at which the channels first pass current. All channels pass maximal current at +70mV.

The currents elicited from these 6 mutants were normalised against the highest control value and plotted alongside its control data to show the amount of inhibition each mutant experienced in 5 μ M I&T (Figure 3.17).

Mutants T16A, N20A, I21A and V22A all passed less current than their control counterparts across every measured voltage (Figure 3.17). L18A hEAG1 is unique among these mutants as it shows a biphasic response to voltage, at negative membrane potentials it is capable of passing more current than it was in control conditions. However, the current amplitude plateaus across the mid-range of voltages before then increasing again from $\sim +50$ mV where it passes less current than it did in control conditions (Figure 3.17 – top right corner). This is an interesting find as it is the only alanine mutation among the “inhibited mutants” that behaves like this following 5 μ M I&T. E19A hEAG1 was inhibited during the steady pulsing experiments but has practically fully recovered its current amplitude by the time of recording the I/V data (Figure 3.17 – middle left).

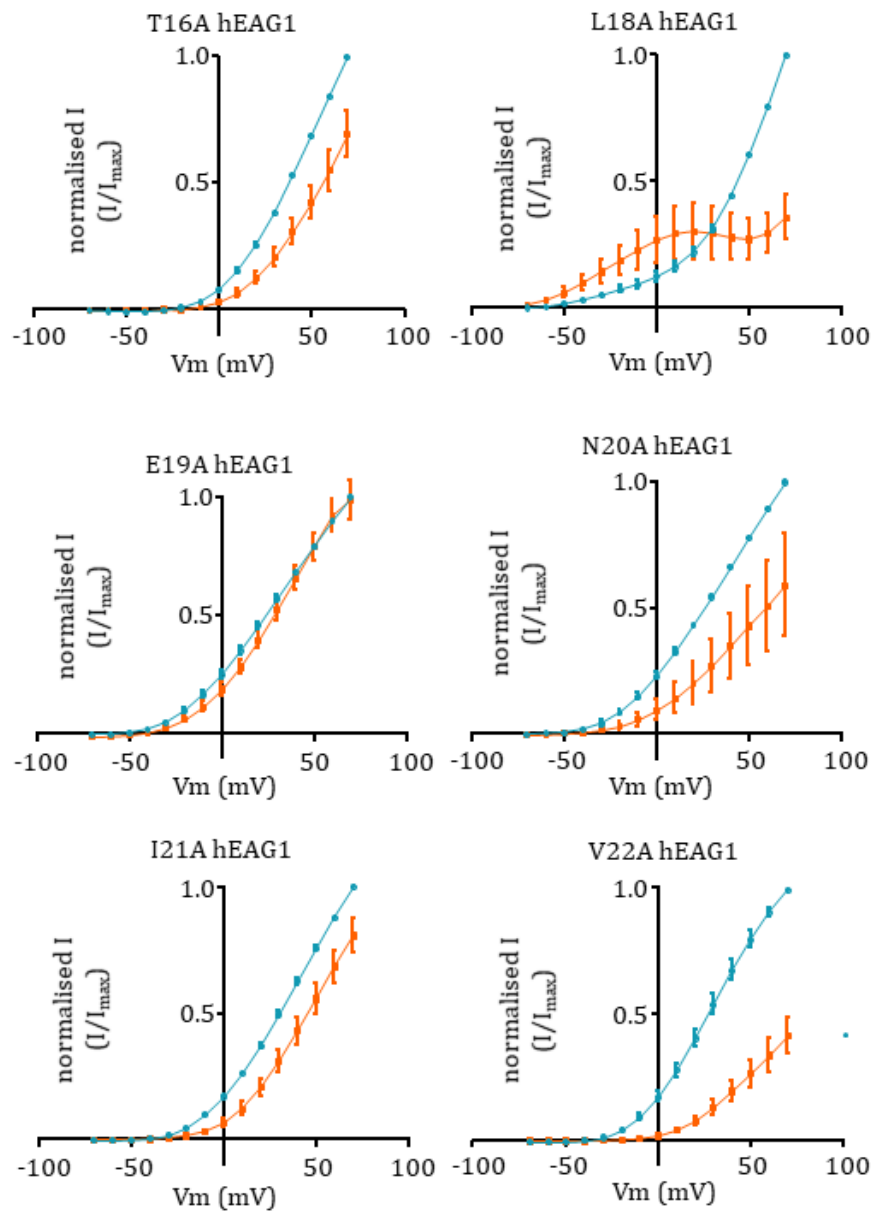


Figure 3.17. I/V graphs of 6 PAS-cap mutants showing how their I/V relationship changes with 5 μ M I&T.

I/V graphs show that >300s after the application of 5 μ M I&T most of these mutants are inhibited at all voltages compared to their control counterparts. L18A hEAG1 initially passes more current than in control before plateauing for the duration of the I/V protocol. E19A hEAG1 has practically fully recovered the amplitude it had in control.

Following the application of 5 μ M I&T, the conductance at each voltage was calculated for the 6 mutants. All mutants with the exception of L18A hEAG1 showed a rightwards shift in the position of the curve. This indicates that the mutant channels require a higher voltage to activate than they did in control conditions. Control data are also plotted alongside the 5 μ M I&T data for comparison (Figure 3.18).

The $V_{0.5}$ values for all 6 mutants were significantly changed following the application of 5 μ M I&T. T16A hEAG1's $V_{0.5}$ after the application of 5 μ M I&T was 37.2 ± 1.6 mV which is more positive than in control conditions ($p < 0.001$, $n = 11$, Figure 3.18, Table 1.). For L18A hEAG1, the $V_{0.5}$ value obtained in 5 μ M I&T was -51.1 ± 3.0 mV which is approximately 98mV of difference between control conditions ($p < 0.0001$, $n = 10$, Figure 3.18, Table 1.). The $V_{0.5}$ value for E19A hEAG1 in 5 μ M I&T was 15.8 ± 2.1 mV which is more positive than control conditions ($p < 0.0001$, $n = 11$, Figure 3.18, Table 1.). The $V_{0.5}$ value for N20A hEAG1 was 25.9 ± 3.4 mV which is more positive than in control conditions ($p < 0.01$, $n = 5$, Figure 3.18, Table 1.). The $V_{0.5}$ value for I21A hEAG1 in 5 μ M I&T was 29.8 ± 2.2 mV which is more positive than under control conditions ($p < 0.0001$, $n = 8$, Figure 3.18, Table 1.). Finally, V22A hEAG1 had a $V_{0.5}$ value of 37.1 ± 2.4 mV which is more positive than the value under control conditions ($p < 0.01$, $n = 7$, Figure 3.18, Table 1.).

This data indicates that all 6 residues show significant positive shifts in the $V_{0.5}$ values in 5 μ M I&T compared to in control conditions. L18A hEAG1 is the only mutant that has a negative shift in the $V_{0.5}$ value.

Out of the 6 mutants, only N20A and V22A did not significantly affect the k value following the application of 5 μ M I&T. The k value for T16A hEAG1 decreased from control to 13.4 ± 0.3 mV ($p < 0.01$, $n = 11$, Figure 3.18, Table 1.). The k value of L18A hEAG1 in 5 μ M I&T was 11.6 ± 0.8 mV which was a significant increase from control ($p < 0.05$, $n = 10$, Figure 3.18, Table 1.). For E19A hEAG1 the k value was 17.6 ± 0.7 mV which is a significant decrease from control ($p < 0.01$, $n = 11$, Figure 3.18, Table 1.). I21A hEAG1 had a k value of 14.6 ± 0.4 mV which is lower than in control conditions ($p < 0.001$, $n = 8$, Figure 3.18, Table 1.). The k value for N20A hEAG1 in 5 μ M I&T is 18.2 ± 2.1 mV which was not a significant change from control conditions

($p > 0.05$, $n = 5$, Figure 3.18, Table 1.). Finally, V22A hEAG1 had a k value $13.1 \pm 0.2 \text{ mV}$ which was not a statistically significant change ($p > 0.05$, $n = 7$, Figure 3.18, Table 1.).

This data suggests that all residues are involved in determining the $V_{0.5}$ values and that T16, L18, E19 and I21 are also involved in determining the k value of the channel under high Ca^{2+} conditions. L18A hEAG1 is a stand out mutant as it is the only one of these 6 that had both a negative shift in $V_{0.5}$, an increase in k value and showed a biphasic response on the I/V and G/V graphs (Figure 3.17 and 3.20). This indicates that the L18 residue is an important residue in determining the voltage dependence of the channel and the rate of ion movement through the channels.

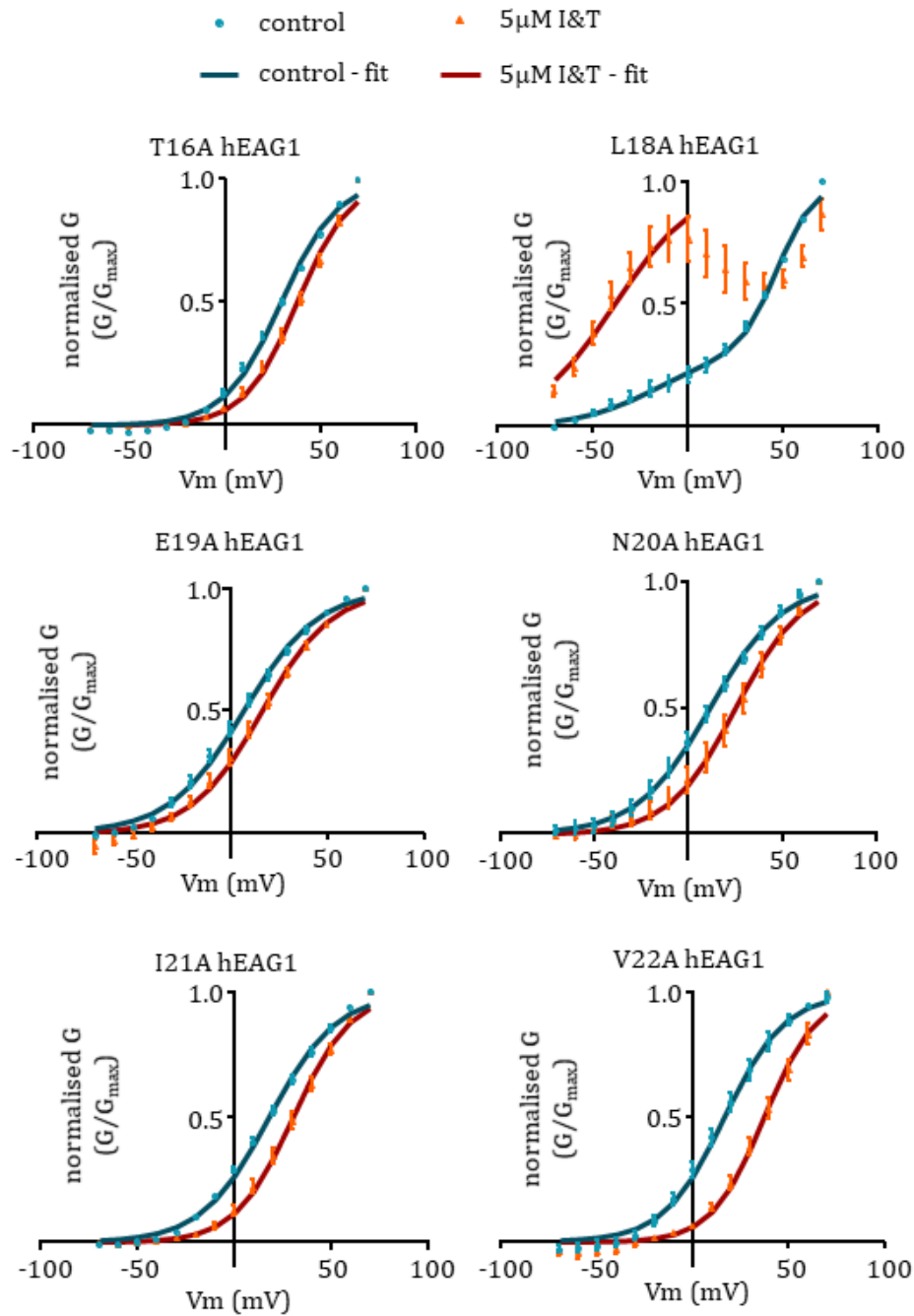


Figure 3.18. G/V graphs of 6 PAS-cap mutants showing how their G/V relationship changes with 5µM I&T.

G/V graphs show that >300s after the application of 5µM I&T most of these mutants are shifted to the right compared to their control counterparts. L18A hEAG1 is unique in that it is conducting at the lowest membrane potential used.

3.1.5.2. N15A and F17A both bare similarity to Δ 2-26 hEAG1

Mutants of the PAS-cap have revealed a number of interesting roles including, roles in voltage dependence, activation kinetics and alterations in the amount of conductance but none of them have provided an insight into how the Δ 2-26 mutant has such different behaviour to the WT channel both in control conditions and 5 μ M I&T.

N15A hEAG1 produces outward currents that slowly increase in their amplitude during each voltage pulse. These currents also show rectification at more positive potentials (Figure 3.19b). This behaviour is comparable to that of the Δ 2-26 hEAG1 channels. N15A hEAG1 currents appear to activate slowly in response to voltage initially but at the measured voltage of +60mV the channels have an activation time course from 10-80% of 264.3 ± 17.9 ms which is not significantly different to WT ($p > 0.05$, $n=8$, Table 1.). However, the I/V graph for N15A hEAG1 in control conditions does show that the channels rectify at positive potentials (Figure 3.19c) which is not a characteristic of the WT channels (Figure 3.2a) but rather one of the Δ 2-26 channels (Figure 3.6c).

N15A hEAG1 also has different conductance properties to the WT channel, the G/V curve shows that N15A hEAG1 in control conditions is conducting at the most negative voltage tested indicating that the N15A channels can be activated at negative membrane potentials (Figure 3.19d). The $V_{0.5}$ value measured for N15A hEAG1 is -35.8 ± 3.8 mV which is much more negative than the WT channel ($p < 0.0001$, $n=8$, Table 1.). The k value is 11.0 ± 1.1 mV which is lower than WT hEAG1 ($p < 0.0001$, $n=8$, Table 1.) which indicates that the N15A channels are less dependent on voltage compared to the WT channel.

This data shows that the N15 residue does not regulate the activation kinetics in control conditions but that it does have a role in the voltage dependence of the channel under control conditions. N15 also controls the rate of ion movement at more positive membrane potentials since the N15A mutant results in channels that begin slowing in their rate of conductance at potentials over +10mV (Figure 3.19d).

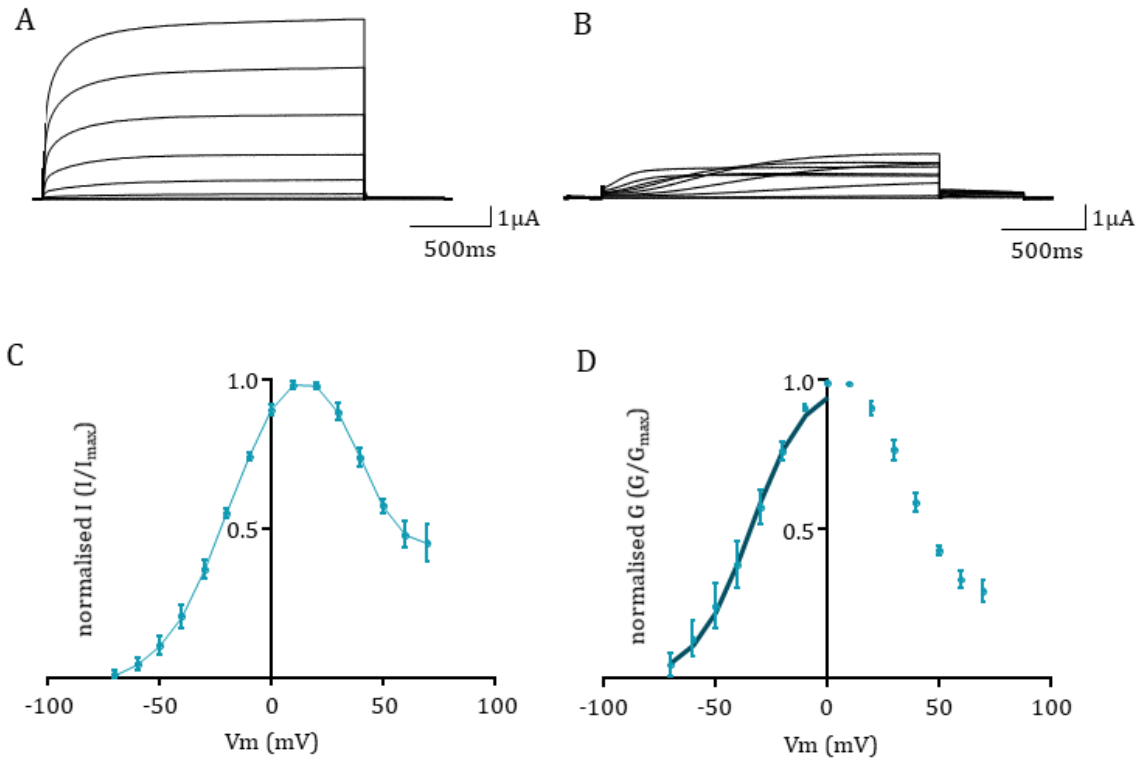


Figure 3.19. Data showing the response of WT and N15A hEAG1 to changes in membrane voltage.

A: current traces from WT hEAG1 (previously shown in Figure 3.1a) in control solution. The WT current increases in amplitude with each successive depolarisation.

B: current traces from N15A hEAG1 in control solution. These channels activate with a slower time course than the WT channel. Currents initially increase in amplitude with membrane depolarisation but reduce in amplitude at voltages more depolarised than +10mV (shown in C, blue data).

C: an I/V graph showing the relationship of N15A hEAG1's current with voltage. N15A hEAG1 increases in amplitude initially but then reduces in amplitude past +10mV. This bears great similarity to the I/V curve of $\Delta 2-26$ hEAG1 (Figure 3.6c)

D: a G/V graph show how the conductance of N15A hEAG1 relates to voltage. N15A hEAG1 shows an initial increase in conductance with depolarising membrane potential but this reverses at +10mV. The reduction in conductance may be down to channel inactivation or rectification.

N15A hEAG1 was exposed to 5 μ M I&T to see whether or not the mutation would affect the channel's response to high Ca²⁺. N15A hEAG1 was potentiated by ~4 fold over control by the 5 μ M I&T in a similar manner to the Δ 2-26 channels (Figure 3.20a). N15A hEAG1 did not show a recovery phase where the current amplitude begins returning towards control levels and instead remained at the potentiated level throughout the time course recorded for (Figure 3.20b). N15A hEAG1 showed a large component of instantaneous current during application of 5 μ M I&T which is similar to Δ 2-26 hEAG1 (Figure 3.20a). The current was potentiated by $306.0 \pm 44.9\%$ over control ($p < 0.001$, $n = 7$) which is not as much as when the entire PAS-cap was deleted but still follows a similar trend (Table 1.).

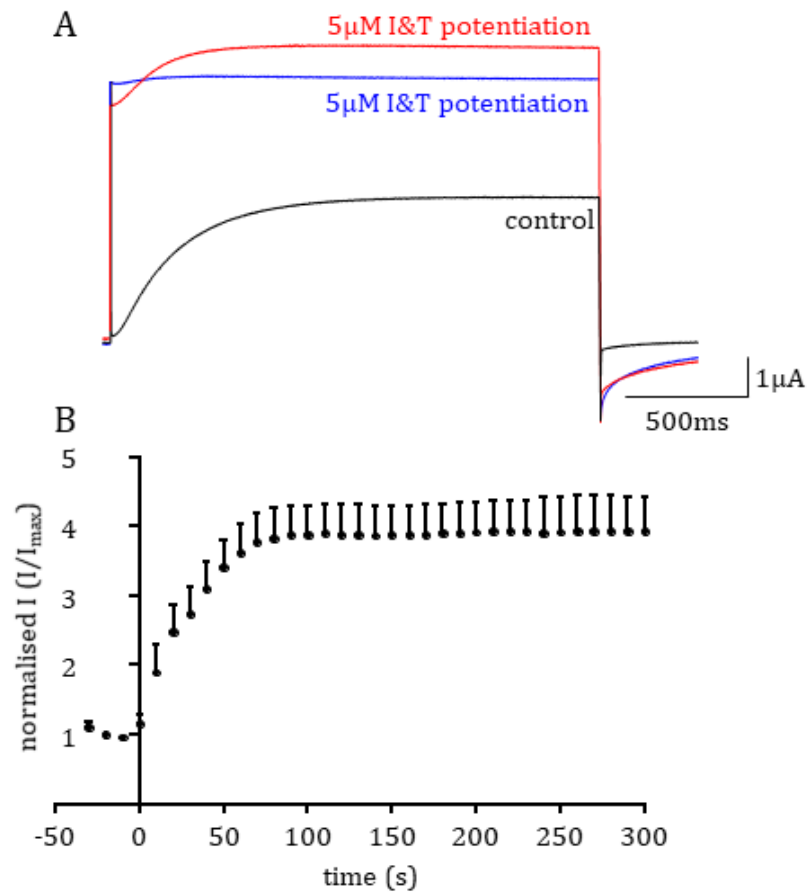


Figure 3.20. Steady pulsing data showing how the N15A hEAG1 current responds to 5µM I&T.

A: these current traces show how the channel responds to the same voltage in control (black) and in 5µM I&T - initial potentiation shown in blue and continued potentiation shown in red. There is a large component of instantaneous current following the application of 5µM I&T.

B: this graph shows how the current amplitude changes over time when 5µM I&T was added at $t=0$. The current increases before plateauing. This is different from $\Delta 2-26$ hEAG1 which reduces in amplitude again following the potentiation.

The currents elicited from N15A hEAG1 following the application of 5 μ M I&T are shown in Figure 3.21. The current amplitude is increased and there is a component of instantaneous current at the start of each voltage step (Figure 3.21). The activation kinetics of N15A hEAG1 are significantly slowed following application of 5 μ M I&T with a time course of 615.4 ± 91.8 ms ($p < 0.01$, $n = 8$, Figure 3.21, Table 1.). The channels can pass current at the most negative membrane potential recorded from and begin rectifying $\sim +30$ mV (Figure 3.21d).

The I/V curve shows that for each voltage there is more current passed by N15A channels in high Ca^{2+} conditions (Figure 3.21c). It also shows that the rectification process is still present after 5 μ M I&T and that the rectification process is shifted to more positive potentials.

The G/V curve is leftwards shifted compared to control meaning that the channels can activate at more negative voltages after addition of 5 μ M I&T. The $V_{0.5}$ value was found to be -42.2 ± 3.9 mV which is more negative than in control conditions ($p < 0.05$, $n = 8$, Figure 3.21d, Table 1.). The k value was 15.7 ± 2.5 mV which was not found to be statistically significant ($p > 0.05$, $n = 8$, Figure 3.21d, Table 1.).

This data shows that N15 is a key residue in the mechanism by which the PAS-cap regulate hEAG1 function. When mutated, N15A hEAG1 behaves in a similar manner to the $\Delta 2$ -26 channels. N15A is potentiated by an increase in $[Ca^{2+}]_i$ and shifts the $V_{0.5}$ to negative membrane potentials. N15A also shows rectification behaviour at positive membrane potentials which is only seen in $\Delta 2$ -26 hEAG1 and not the WT channel.

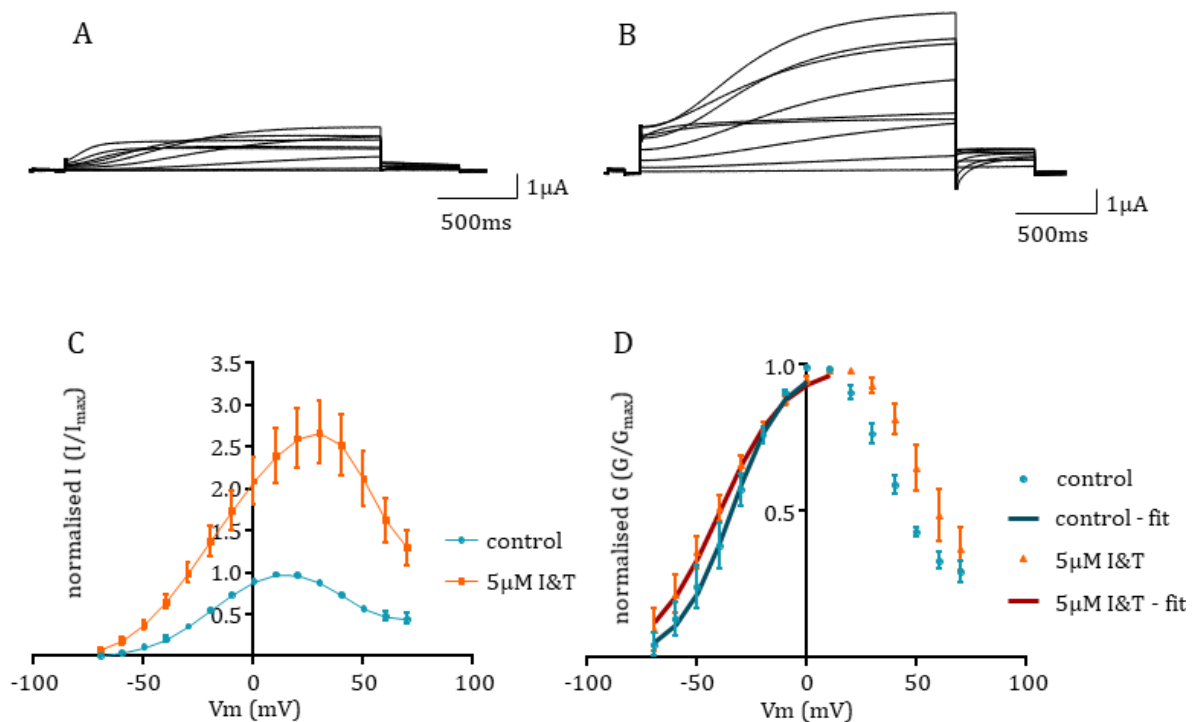


Figure 3.21. Data showing the response of N15A hEAG1 to changes in membrane voltage following the application of $5\mu\text{M}$ I&T.

A: current traces from N15A hEAG1 (previously shown in Figure 3.6b) in control solution. The current increases in amplitude with each successive depolarisation up to $+10\text{mV}$ when it then begins reducing in amplitude (also shown in C, blue data).

B: current traces from N15A hEAG1 in $5\mu\text{M}$ I&T solution. These channels still activate with a slow time course and do not reach a steady state plateau during the voltage pulses. Currents increase in amplitude with membrane depolarisation but now reduce in amplitude at voltages more depolarised than $+30\text{mV}$ (shown in C, orange data).

C: an I/V graph showing the relationship of N15A hEAG1 current with voltage both in control and $5\mu\text{M}$ I&T solution. Currents in control are shown in blue whilst currents in $5\mu\text{M}$ I&T solution are shown in orange. Currents in $5\mu\text{M}$ I&T solution are greater in amplitude across all voltages compared to currents in control solution. Currents in $5\mu\text{M}$ I&T solution reduce in amplitude at more positive voltages than currents in control.

D: a G/V graph show how the conductance N15A hEAG1 channel changes between control and $5\mu\text{M}$ I&T. Control is shown in blue whilst $5\mu\text{M}$ I&T is shown in orange. Channels are active at -70mV in $5\mu\text{M}$ I&T and conductance continues to increase with voltage up to $+20\text{mV}$. Channels in control solution are less active at -70mV and the conductance begins reducing at $+10\text{mV}$. Control and $5\mu\text{M}$ I&T data are fit with Boltzmann functions (dark blue and dark red respectively).

F17A hEAG1 is another residue mutation that, like N15A, does not bare much similarity to WT hEAG1. The currents elicited by the I/V protocol appear slower to activate than WT hEAG1 and also rectify at positive potentials (Figure 3.22). F17A hEAG1 has an activation time course of 533.2 ± 85.5 ms which is slower than the WT channel ($p < 0.05$, $n=7$, Figure 3.22, Table 1.). This behaviour is in line with the behaviour of the $\Delta 2-26$ mutation.

F17A hEAG1 has an I/V profile which is similar to $\Delta 2-26$ and N15A hEAG1. The current passed increases with voltage before rectifying at positive potentials past +10mV (Figure 3.22c). This is a further indication that F17 may also be a key residue of the PAS-cap and its ability to regulate hEAG1.

The G/V curve shows that F17A begins conducting ions at -60mV (Figure 3.22d), not a behaviour characteristic of the WT channel but more so of $\Delta 2-26$ hEAG1. The rate of ion movement reduces past +10mV which, again, is similar to $\Delta 2-26$ and N15A hEAG1. The $V_{0.5}$ value of F17A in control conditions is -30.2 ± 4.5 mV which is much more negative than the WT ($p < 0.0001$, $n=7$) and close in value to $\Delta 2-26$ and N15A hEAG1 (Table 1.). The k value is 10.5 ± 0.8 mV which is lower than the k value of WT hEAG1 ($p < 0.0001$, $n=7$, Table 1.).

This data shows that the F17 residue is involved in regulating the activation kinetics of hEAG1 in control conditions and is also involved in the voltage dependence of the channel. F17A hEAG1 displays rectification behaviour at positive potentials (Figure 3.22) indicating that the residue also plays a role in controlling the conductance of the channel at positive potentials.

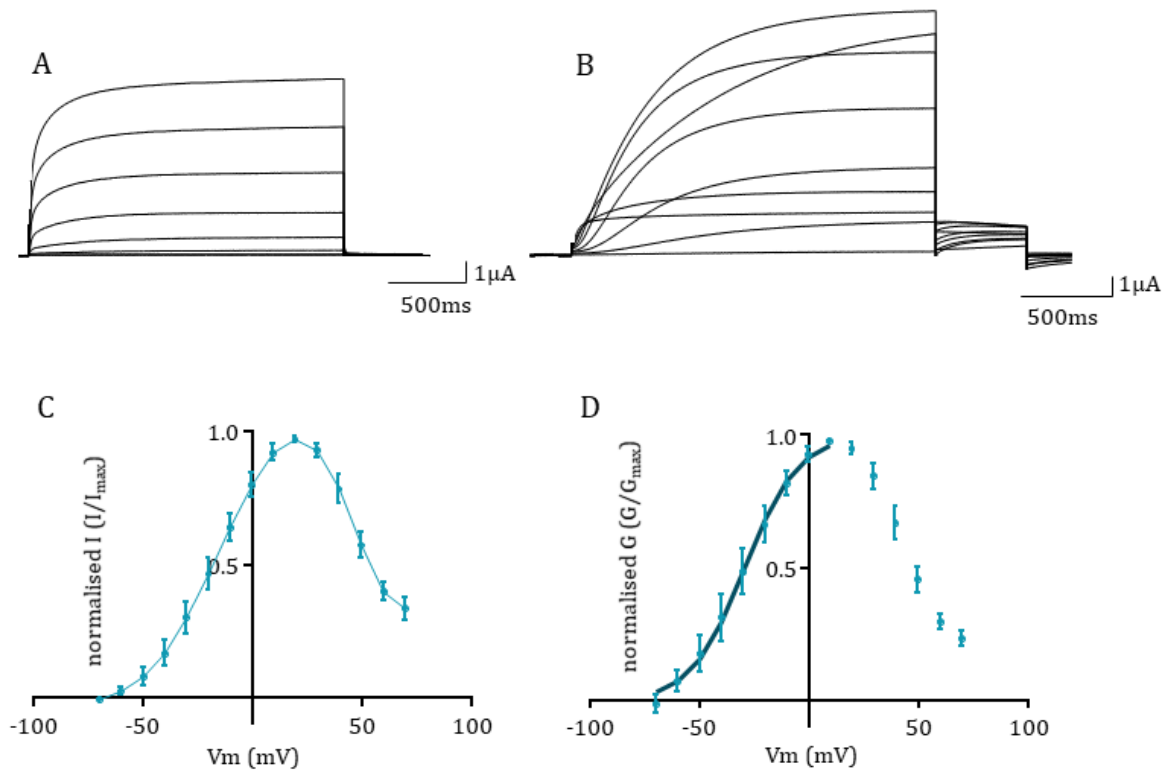


Figure 3.22. Data showing the response of WT and F17A hEAG1 to changes in membrane voltage.

A: current traces from WT hEAG1 (previously shown in Figure 3.1a) in control solution. The WT current increases in amplitude with each successive depolarisation.

B: current traces from F17A hEAG1 in control solution. These channels activate with a slower time course than the WT channel. Currents initially increase in amplitude with membrane depolarisation but reduce in amplitude at voltages more depolarised than +20mV (shown in C, blue data).

C: an I/V graph showing the relationship of F17A hEAG1's current with voltage. F17A hEAG1 increases in amplitude initially but then reduces in amplitude past +20mV. This bears great similarity to the I/V curve of $\Delta 2-26$ hEAG1 (Figure 3.6c)

D: a G/V graph show how the conductance of F17A hEAG1 relates to voltage. F17A hEAG1 shows an initial increase in conductance with depolarising membrane potential but this reverses at +10mV. The reduction in conductance may be down to channel inactivation or rectification.

Addition of 5 μ M I&T resulted in a potentiation of the F17A hEAG1 current by \sim 3 fold over control (Figure 3.23a). The potentiated current then gradually began recovering back towards control (Figure 3.23b). During the potentiation phase, there is a clear component of instantaneous current which is not attributed to leak as shown by the flat zero line (Figure 3.23a).

The current was potentiated by $242.4 \pm 60.7\%$ which, similarly to N15A hEAG1, is not as extensive as Δ 2-26 hEAG1 but still falls in line with the trend of potentiation ($p < 0.01$, $n = 12$, Table 1.). This indicates that F17 is involved in the channel's response to high Ca^{2+} conditions and is a crucial residue within the PAS-cap.

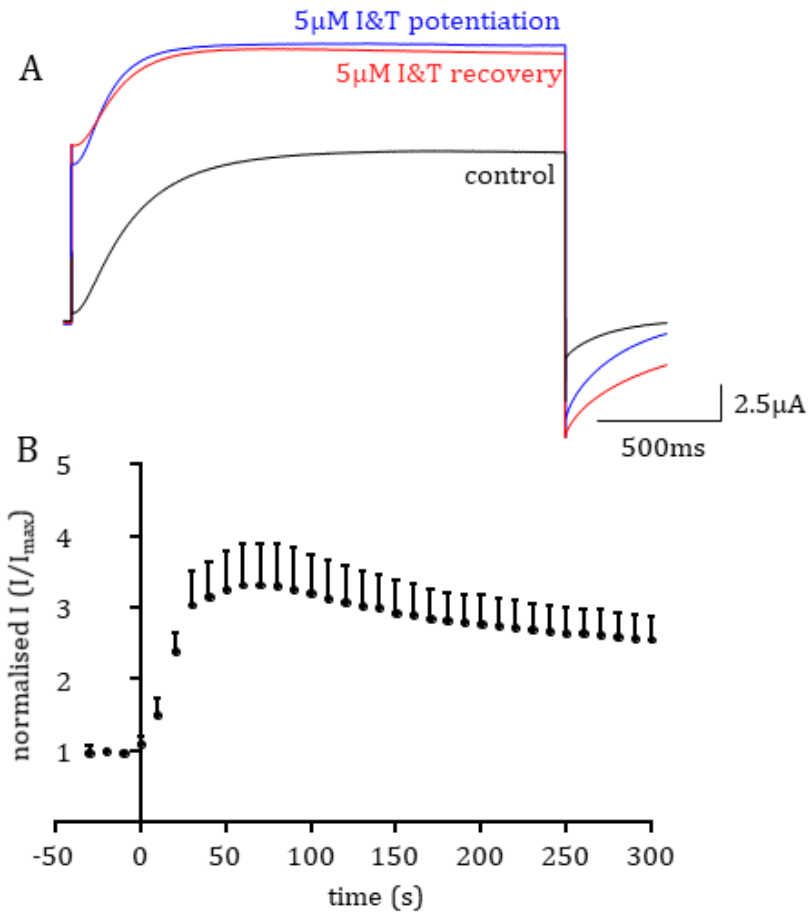


Figure 3.23. Steady pulsing data showing how F17A hEAG1 responds to 5µM I&T over time.

A: these current traces show the response of F17A hEAG1 under control (black) and the potentiation under 5µM I&T (blue) followed by a slight recovery of current amplitude (red). After the application of 5µM I&T there is a component of instantaneous current which is not present on the I/V traces conducted in 5µM I&T.

B: this graph shows how the F17A hEAG1 current amplitude changes over time following addition of 5µM I&T at t=0. The current initially increases before very slowly reducing.

The current traces elicited by the I/V protocol do not appear different to control traces (Figure 3.24). In 5 μ M I&T, F17A currents activated with a time course of 587.8 ± 43.2 ms which is not a significant change over control ($p > 0.05$, $n = 7$, Table 1.). The instantaneous current that was present during the steady pulsing experiments is not now longer seen, indicating that F17 may also have a role in the deactivation kinetics, although they were not a subject of experiment.

The I/V curve shows how the current relates to voltage under high Ca²⁺ conditions (Figure 3.24c). At each voltage tested the F17A channels pass more current than in control conditions. The channels also rectify at more positive potentials albeit still passing more current than in control conditions (Figure 3.24c). The G/V curve shows that there is no shift in the voltage dependence of activation in 5 μ M I&T compared with control (Figure 3.24d). The $V_{0.5}$ value is -29.2 ± 5.7 mV which is not statistically significant over control ($p > 0.05$, $n = 7$, Figure 3.24d, Table 1.). The k value was found to increase to 14.0 ± 1.3 mV from control ($p < 0.05$, $n = 7$, Figure 3.24d, Table 1.) which indicates that the channel has become more dependent on the voltage compared to control. This shows that under high Ca²⁺ conditions, F17 is involved in the regulation of the voltage sensitivity of the channel but not the activation kinetics.

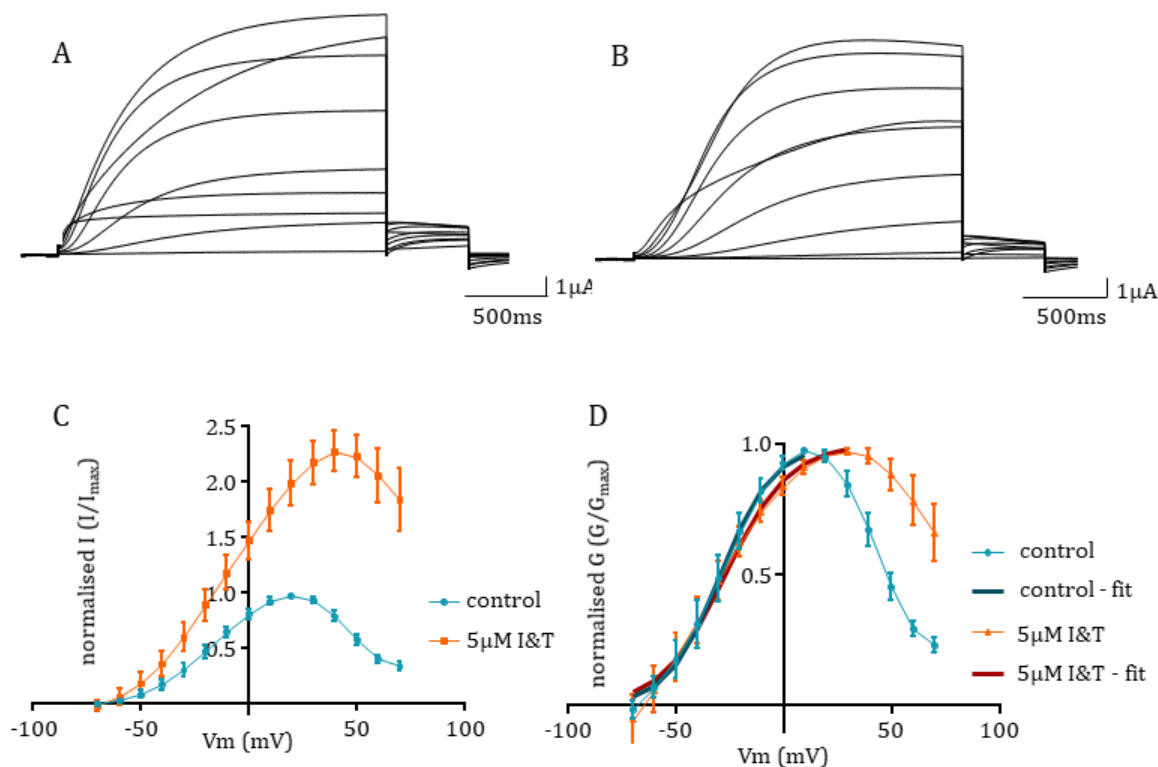


Figure 3.24. Data showing the response of F17A hEAG1 to changes in membrane voltage following the application of $5\mu\text{M}$ I&T.

A: current traces from F17A hEAG1 in control solution. The current increases in amplitude with each successive depolarisation up to $+20\text{mV}$ when it then begins reducing in amplitude (also shown in C, blue data).

B: current traces from F17A hEAG1 in $5\mu\text{M}$ I&T solution. These channels still activate with a slow time course and do not reach a steady state plateau during the voltage pulses. Currents increase in amplitude with membrane depolarisation but now reduce in amplitude at voltages more depolarised than $+40\text{mV}$ (shown in C, orange data).

C: an I/V graph showing the relationship of F17A hEAG1 current with voltage both in control and $5\mu\text{M}$ I&T solution. Currents in control are shown in blue whilst currents in $5\mu\text{M}$ I&T solution are shown in orange. Currents in $5\mu\text{M}$ I&T solution are greater in amplitude across all voltages compared to currents in control solution. Currents in $5\mu\text{M}$ I&T solution reduce in amplitude at more positive voltages than currents in control.

D: a G/V graph showing how the conductance of F17A hEAG1 channels changes between control and $5\mu\text{M}$ I&T. Control is shown in blue whilst $5\mu\text{M}$ I&T is shown in orange. Channels are active at -60mV in $5\mu\text{M}$ I&T and conductance continues to increase with voltage up to $+30\text{mV}$. Channels in control solution are active at -60mV and the conductance begins reducing at $+10\text{mV}$. Control and $5\mu\text{M}$ I&T data are fit with Boltzmann functions (dark blue and dark red respectively).

This data shows that the F17 residue of the PAS-cap is also another likely component of its role in regulating the activity of hEAG1. From the homology model available at the time this shows that the N15 side chain points towards the cNBH domain whilst the F17 side chain points towards the EAG domain (Figure 3.10).

3.1.6. The E600 residue within the cNBHD is a promising interaction partner for residues of the PAS-cap

The X-ray crystallography data of mEAG1 obtained by Haitin *et al.* (2013) pointed towards a binding surface between the cNBHD and the PAS-cap. There was an extensive number of cancer-associated mutants mapped to this binding surface which added weight to the argument that this interaction is important for the role of the PAS-cap in regulating hEAG1 function. One of the residues of interest is E600, a series of mutants were developed and tested in the Mitcheson lab including; E600A, E600R, E600L, E600I and E600Q (Lorinczi *et al.*, 2016).

E600A hEAG1, a charge neutralisation mutant, produces outward, non-inactivating currents in response to voltage in a similar manner to the WT channel (Figure 3.25). The current amplitudes increase with voltage and are maximally activated at +70mV (Figure 3.25c). E600A hEAG1 activates with a time course of 459.7 ± 56.9 ms which is not significantly different from WT hEAG1 ($p > 0.05$, $n=9$, Figure 3.25, Table 1.). The current response to the I/V protocol increases gradually with each positive increase in the membrane potential (Figure 3.25c).

The G/V curve for E600A hEAG1 in control conditions is also comparable to the WT channel, the conductance increases with voltage indicating that the rate of ion movement steadily increases with voltage (Figure 3.25d). The $V_{0.5}$ value obtained for E600A hEAG1 in control conditions is 11.1 ± 5.7 mV which is not significantly different from the WT channel ($p > 0.05$, $n=9$, Figure 3.25d, Table 1.). The k value was also measured and was found to be 20.5 ± 1.0 mV, this was also shown to not be significant ($p > 0.05$, $n=9$, Figure 3.25d, Table 1.) This data suggests that under control conditions, E600 does not have a role in the activation kinetics or the voltage dependence of hEAG1.

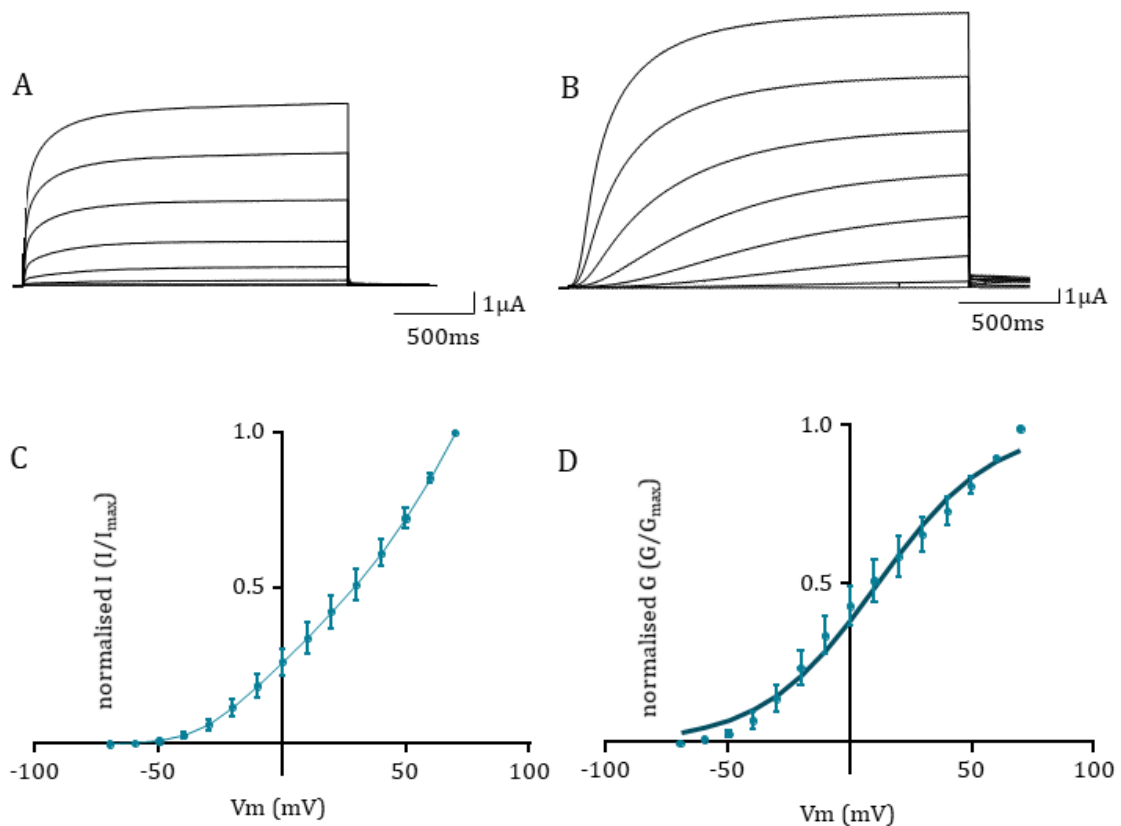


Figure 3.25. Data showing the response of WT and E600A hEAG1 to changes in membrane voltage.

A: current traces from WT hEAG1 (previously shown in Figure 3.1a) in control solution. The WT current increases in amplitude with each successive depolarisation.

B: current traces from E600A hEAG1 in control solution. Currents increase in amplitude with membrane depolarisation (shown in C, blue data).

C: an I/V graph showing the relationship of E600A hEAG1's current with voltage. E600A hEAG1 increases in amplitude which is similar to the I/V curve of WT hEAG1.

D: a G/V graph show how the conductance of E600A hEAG1 relates to voltage. E600A hEAG1 shows increasing conductance with depolarising membrane potential. Data are fitted with a Boltzmann function (dark blue line).

E600A hEAG1 was exposed to 5 μ M I&T to test how the mutant responds to an increase in [Ca²⁺]_i. It showed an initial inhibition which was then followed by a recovery phase back towards control, a similar response as seen in the WT (Figure 3.26a). The activation kinetics of the current during the recovery phase appear slowed compared to the control current (Figure 3.26a). The current showed a moderate inhibition from control levels of $62.8 \pm 8.9\%$ ($p < 0.0001$, $n=9$) which is not as much of an inhibition as the WT channel (Table 1.). The current amplitude then began to recover slowly towards control levels (Figure 3.26b).

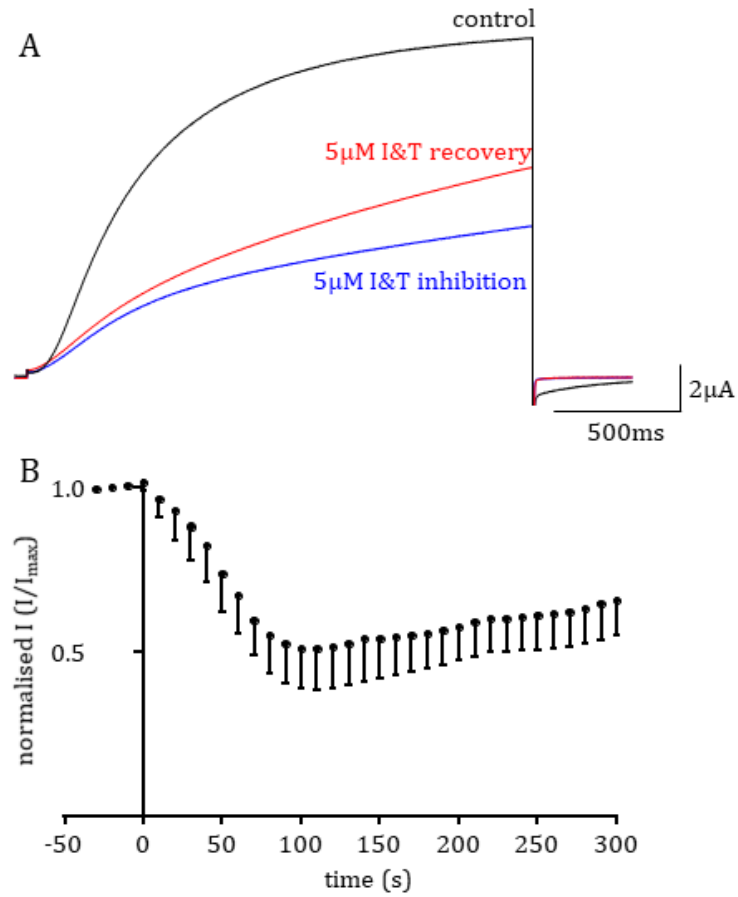


Figure 3.26. Steady pulsing data showing how E600A hEAG1* current amplitude responds to 5µM I&T.

A: these current traces show the current in control (black), the inhibited current (blue) and the current during the recovery phase (red).

B: this graph shows the response to the addition of 5µM I&T at t=0. The current amplitude is inhibited gradually and then begins to recover in amplitude towards control levels.

*raw data obtained by Dr E. Lőrinczi and re-analysed for the purpose of display here.

E600A hEAG1 was run under the I/V protocol whilst still in the presence of 5 μ M I&T. The current amplitude increased with voltage and was maximally activated at +70mV (Figure 3.27). The current had a time course of 893.4 ± 66.2 ms in 5 μ M I&T, a significant slowing of the kinetics ($p < 0.0001$, $n=9$, Figure 3.27, Table 1.).

The currents were inhibited compared to control following the application of 5 μ M I&T but had recovered the majority of their current amplitude during the follow-up I/V protocol (Figure 3.27c). The I/V curve for 5 μ M I&T shows that at some mid-range voltages the channels actually pass more current than in control conditions (Figure 3.27c) despite being inhibited initially (Figure 3.26).

The G/V curve shows that there is a leftwards shift in the G/V relationship indicating that the channels can activate at lower membrane potentials compared to control (Figure 3.27d). The $V_{0.5}$ value following 5 μ M I&T is -15.2 ± 3.2 mV which is a significant decrease compared to control ($p < 0.0001$, $n=9$, Figure 3.27d, Table 1.). The k value was measured as being 17.2 ± 1.4 mV which is less than in control conditions ($p < 0.05$, $n=9$) which indicates that the channel has become less dependent on the membrane potential than in control conditions (Figure 3.27) (Table 1.).

This data indicates that the E600 residue is not necessarily involved with the regulation of hEAG1 under control conditions but that under high Ca^{2+} conditions it has a role in maintaining the activation kinetics as well as the voltage dependence of the channel.

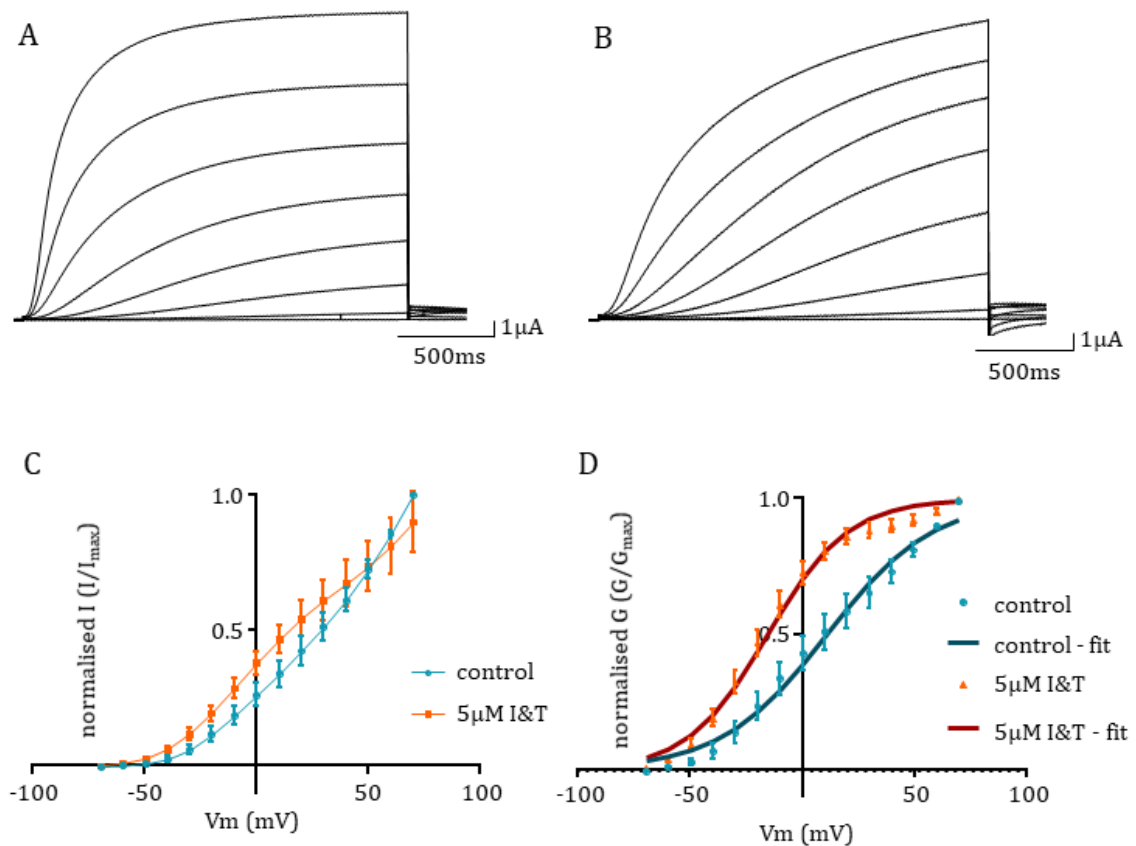


Figure 3.27. Data showing the response of E600A hEAG1 to changes in membrane voltage following the application of 5μM I&T.

A: current traces from E600A hEAG1 in control solution. The current increases in amplitude with each successive depolarisation (also shown in C, blue data).

B: current traces from E600A hEAG1 in 5μM I&T solution. These channels activate with a slow time course and do not reach a steady state plateau during the voltage pulses. Currents increase in amplitude with membrane depolarisation (shown in C, orange data).

C: an I/V graph showing the relationship of E600A hEAG1 current with voltage both in control and 5μM I&T solution. Currents in control are shown in blue whilst currents in 5μM I&T solution are shown in orange. Currents in 5μM I&T solution are slightly greater in amplitude compared to currents in control solution.

D: a G/V graph show how the conductance E600A hEAG1 channel changes between control and 5μM I&T. Control is shown in blue whilst 5μM I&T is shown in orange. Channels are active at -50mV in 5μM I&T and conductance continues to increase with voltage. Channels in control solution are active at -40mV. Control and 5μM I&T data are fit with Boltzmann functions (dark blue and dark red respectively).

Shortening the side chain and removing the charge did not have a dramatic effect on the behaviour of hEAG1 in the same way as deleting the PAS-cap did (Δ 2-26 hEAG1). However, removing one side chain from a suspected interaction surface may not be enough to disrupt an interaction. A charge reversal mutation was made producing E600R hEAG1.

E600R hEAG1 produced currents that were slow to activate and rectified at positive membrane potentials (Figure 3.28), which is similar behaviour to that produced by Δ 2-26 hEAG1. The channels activate at -50mV and are maximally activated at +70mV (Figure 3.28). The time course of activation for E600R hEAG1 is 724.9 ± 118.2 ms which is considerably slower than those of the WT channel ($p < 0.0001$, $n=7$, Table 1.).

The I/V curve shows that E600R hEAG1 activates around -50mV and increases in amplitude before plateauing around 0 to +20mV. From here the current begins increasing again (Figure 3.28c) – a response previously seen with L18A hEAG1 following application of 5 μ M I&T.

The G/V curve shows a similar trend as the I/V curve, the conductance increases initially with membrane potential before reducing across the voltage range 0 to +40mV. At +40mV the conductance increases again with voltage (Figure 3.28d) indicating that the addition of the positive charge to side chain affects the rate of ion movement across the mid-range of voltages. This also indicates that the PAS-cap / cNBH domain surface has been disrupted by the mutation and that E600 is a key regulator of this interaction.

A Boltzmann function was fitted to the ascending phase of the G/V data to obtain $V_{0.5}$ and k values. The $V_{0.5}$ value for E600R hEAG1 is 8.7 ± 16.4 mV which is more negative than the WT channel ($p < 0.0001$, $n=7$, Figure 3.28d, Table 1.). The k value was found to be 11.0 ± 4.0 mV which is also more negative than WT hEAG1 ($p < 0.0001$, $n=7$, Figure 3.28d, Table 1.) which shows that E600R channels are less dependent on voltage than the WT channel.

This data indicates that E600 is in fact involved in the activation kinetics as well as the voltage dependence of the channel under control conditions. Since the E600A mutation did not produce such a distinct I/V response, the E600 residue may

be part of larger interaction network that becomes disrupted by the addition of a positive charge.

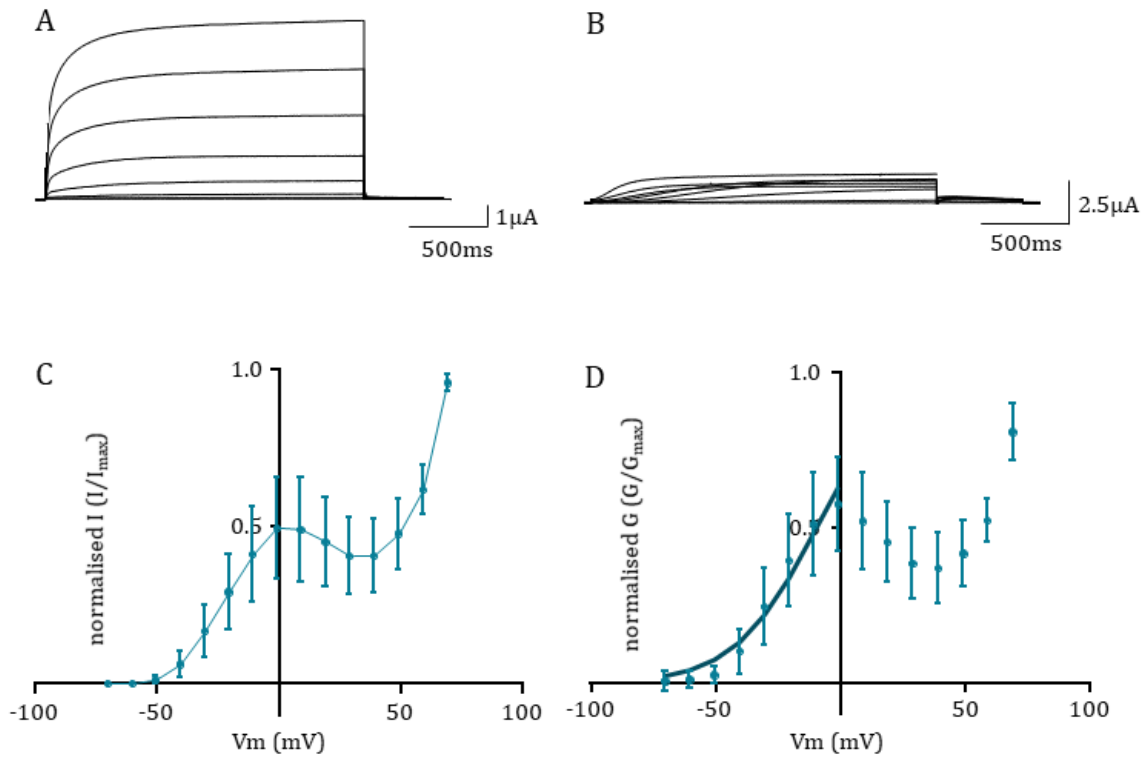


Figure 3.28. Data showing the response of WT and E600R hEAG1 to changes in membrane voltage.

A: current traces from WT hEAG1 (previously shown in Figure 3.1a) in control solution. The WT current increases in amplitude with each successive depolarisation.

B: current traces from E600R hEAG1 in control solution. These channels activate with a slower time course than the WT channel. (shown in C, blue data).

C: an I/V graph showing the relationship of E600R hEAG1's current with voltage. Currents have a biphasic relationship with voltage, initially increase in amplitude with membrane depolarisation but reduce in amplitude at voltages more depolarised than 0mV. At voltages more depolarised than +40mV the current amplitude then begins increasing again.

D: a G/V graph show how the conductance of E600R hEAG1 relates to voltage. E600R hEAG1 shows an initial increase in conductance with depolarising membrane potential but this reverses at 0mV. The reduction in conductance may be down to channel inactivation or rectification. Data are fit with a Boltzmann function (dark blue line).

Upon application of 5 μ M I&T, E600R hEAG1 currents underwent a potentiation of \sim 15 fold compared to control (Figure 3.29a). Once potentiated, the current amplitude stays at the same level throughout the recording (Figure 3.29b) – unlike the Δ 2-26 hEAG1 which recovers back down to control. This continuation of the potentiated current is similar to that of the N15A hEAG1 mutant. During the application of 5 μ M I&T, there was a small component of instantaneous current which can be seen at the beginning of the voltage pulse (Figure 3.29a).

The current increased by $865.6 \pm 296.6\%$ compared to control ($p < 0.05$, $n = 3$, Table 1.). This increase in current amplitude is similar in behaviour to the Δ 2-26 hEAG1 and further indicates the involvement of E600 as a potential interacting partner.

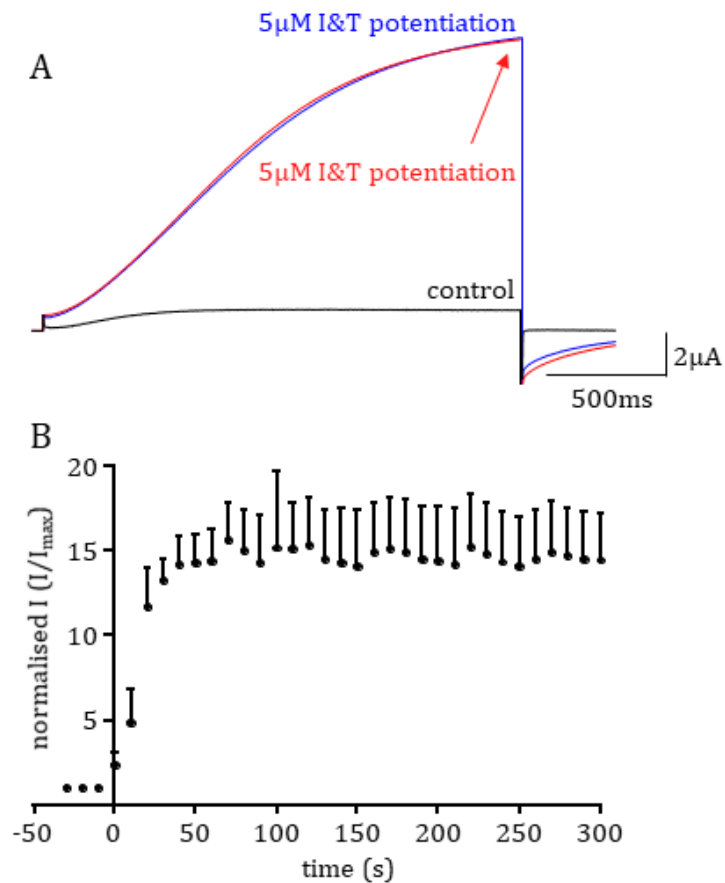


Figure 3.29. Steady pulsing data shows how E600R hEAG1* current amplitude responds to 5µM I&T.

A: these current traces show how E600R hEAG1 responds in control (black), current potentiation (blue) and continued potentiation (red). There is a large potentiation but no large component of instantaneous current as seen with other potentiating mutants.

B: this graph shows how the current amplitude responds over time following addition of 5µM I&T at t=0. The amplitude increases rapidly by a large amount and remains at this level for the duration of the recording.

*raw data obtained by Dr. E. Lőrinczi and re-analysed for display here

The current traces elicited under the I/V protocol whilst still in 5 μ M I&T are shown in Figure 3.30. The channels are slow to open and there is a noticeable increase in the end pulse current compared to control traces. The channels begin to pass current at \sim -50mV and are maximally activated at +40mV, showing a component of rectification (Figure 3.30). The traces were recorded >300s after the application of 5 μ M I&T and yet there is still a component of instantaneous current present at the start of each current trace (Figure 3.30), indicating that E600 also has a role in the deactivation kinetics of the channel.

The kinetics of activation have slowed compared to control down to 844.4 ± 87.3 ms but this is not a significant change ($p>0.05$, $n=7$, Figure 3.30, Table 1.).

The I/V curve shows that at every tested voltage, the channels pass more current than in control conditions (Figure 3.30c). The current also begins to rectify at positive potentials which is also a characteristic of the Δ 2-26 mutant. Even when rectified, the channels in 5 μ M I&T pass more current for the same voltage than they did in control conditions (Figure 3.30c).

The G/V curve shows a leftwards shift indicating that the channel can activate at more negative voltages compared to control (Figure 3.30d). There is also a change in the shape of the curve, in control conditions the channel's conductance slowed down during the mid-range voltages before increasing again thereafter. However, in 5 μ M I&T the conductance does reduce but at more positive potentials than control and it does not go on to increase again (Figure 3.30d) indicating that under high Ca²⁺ conditions this residue plays a role in the rate of ion movement at positive potentials.

The $V_{0.5}$ value is -22.5 ± 1.5 mV which is more negative than control but is not statistically significant ($p>0.05$, $n=7$, Figure 3.30d, Table 1.). The k value is 11.8 ± 1.7 mV which is no different to that in control conditions ($p>0.05$, $n=7$, Figure 3.30d, Table 1.). This data indicates that under high Ca²⁺ conditions the E600 residue is not involved in the voltage dependence or the activation kinetics of the channel but that it is involved in the response to raised [Ca²⁺]_i in a manner similar to that of the N15A mutant previously described.

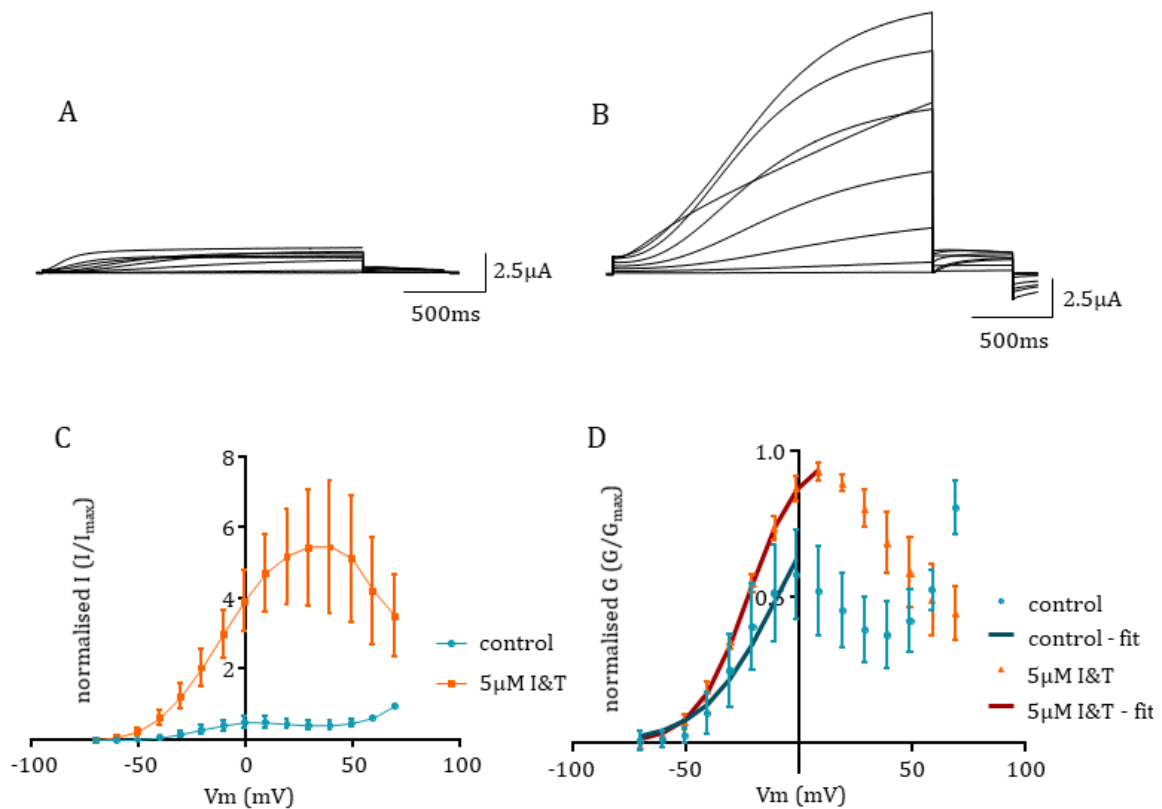


Figure 3.30. Data showing the response of E600R hEAG1 to changes in membrane voltage following the application of 5µM I&T.

A: current traces from E600R hEAG1 in control solution. The current increases in amplitude with each successive depolarisation up to +10mV when it then begins reducing in amplitude (also shown in C, blue data).

B: current traces from E600R hEAG1 in 5µM I&T solution. These channels activate with a slow time course and do not reach a steady state plateau during the voltage pulses. Currents increase in amplitude with membrane depolarisation but now reduce in amplitude at voltages more depolarised than +40mV (shown in C, orange data).

C: an I/V graph showing the relationship of E600R hEAG1 current with voltage both in control and 5µM I&T solution. Currents in control are shown in blue whilst currents in 5µM I&T solution are shown in orange. Currents in 5µM I&T solution are greater in amplitude across all voltages compared to currents in control solution. Currents in 5µM I&T solution reduce in amplitude at more positive voltages than currents in control.

D: a G/V graph show how the conductance E600R hEAG1 channel changes between control and 5µM I&T. Control is shown in blue whilst 5µM I&T is shown in orange. Channels are active at -60mV in 5µM I&T and conductance continues to increase with voltage up to +10mV. Channels in control solution are active at -50mV and the conductance begins reducing at 0mV. Control and 5µM I&T data are fit with Boltzmann functions (dark blue and dark red respectively).

3.1.7. Dual mutant N15E:E600N does not recover a WT-like phenotype

Data so far has shown that N15A and E600R have similar responses to 5 μ M I&T. Their current amplitudes are both potentiated and stay at the potentiated amplitude for the duration of the recording (Figure 3.20b and Figure 3.29b). Following the publication of the cryo-EM structure of hEAG1, (Whicher and MacKinnon, 2016) the locations of the PAS-cap residues can be more accurately determined. N15 and E600 are shown to be 5.4 \AA away from each other in the structure (Figure 3.31) which is close enough for polar interactions to be playing a role. N15 may be the binding partner within the PAS-cap for E600 and may be one of many interaction partners that form the binding surface.

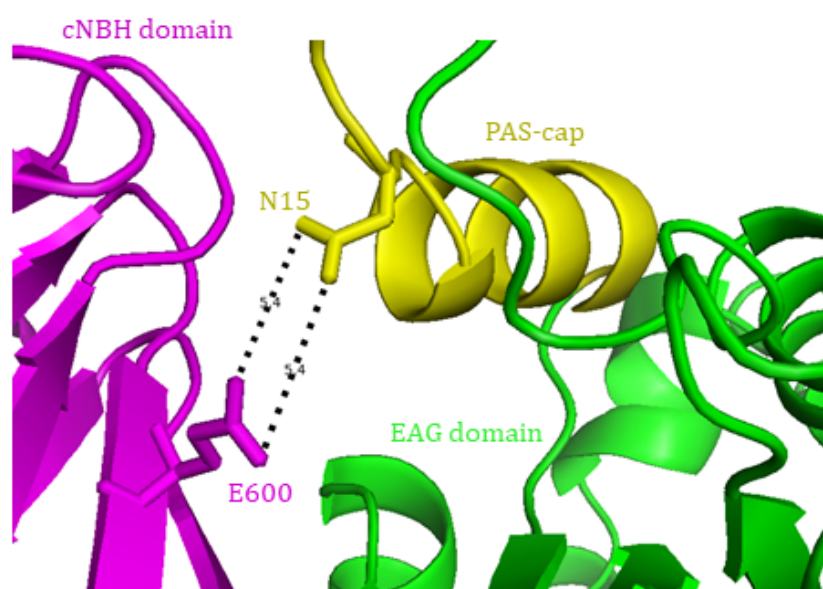


Figure 3.31. A cryo-EM structure* displaying the distance in \AA between the N15 and E600 residues of hEAG1.

The PAS-cap is shown in yellow, the EAG domain in green and the cNBH domain in magenta. In this cryo-EM structure, the N15 side chain (yellow sticks) is 5.4 \AA away from the E600 side chain (magenta sticks) which is an indicator that they are close enough for polar interactions to occur.

*structure adapted from Whicher & MacKinnon, 2016.

To test this, residues N15 and E600 were swapped to create N15E:E600N. If these residues are binding partners then the interaction should persist despite the residues being swapped thus rescuing a WT-like behaviour.

Under control conditions, N15E:E600N hEAG1 produced small currents that rectified at positive potentials (Figure 3.32) which is a characteristic of Δ 2-26 hEAG1 and not of the WT channel. These currents begin to pass current \sim -50mV and are maximally activated at +10mV before rectifying (Figure 3.32). The currents activate with a time course from 10-80% of 214.4 ± 28.3 ms which is not significantly different from the WT channel ($p > 0.05$, $n=9$, Figure 3.32, Table 1.).

The I/V curve shows that the current initially increases with voltage up to +10mV where it begins rectifying (Figure 3.32c). Again this is behaviour more seen with the Δ 2-26 hEAG1 than it is with WT hEAG1.

The G/V curve shows that N15E:E600N hEAG1 begins conducting at negative potentials and increases in conductance to 0mV (Figure 3.32d). From here the conductance begins reducing again, producing a bell shaped curve (Figure 3.32d) – more rectification than seen in any of the rectifying mutants.

The $V_{0.5}$ value is -37.5 ± 1.9 mV which is much more negative than the WT channel ($p < 0.0001$, $n=9$, Figure 3.32d, Table 1.). The k value was found to be 10.4 ± 0.4 mV which is lower than WT hEAG1 meaning that by swapping N15 and E600 the channel becomes less dependent on the voltage ($p < 0.0001$, $n=9$, Figure 3.32d, Table 1.).

This data indicates that swapping N15 and E600 does not rescue a WT-like phenotype in control conditions. Instead it behaves more like Δ 2-26 hEAG1. Swapping N15 and E600 does not affect the activation kinetics of the channel but it does affect the voltage dependence of the channel.

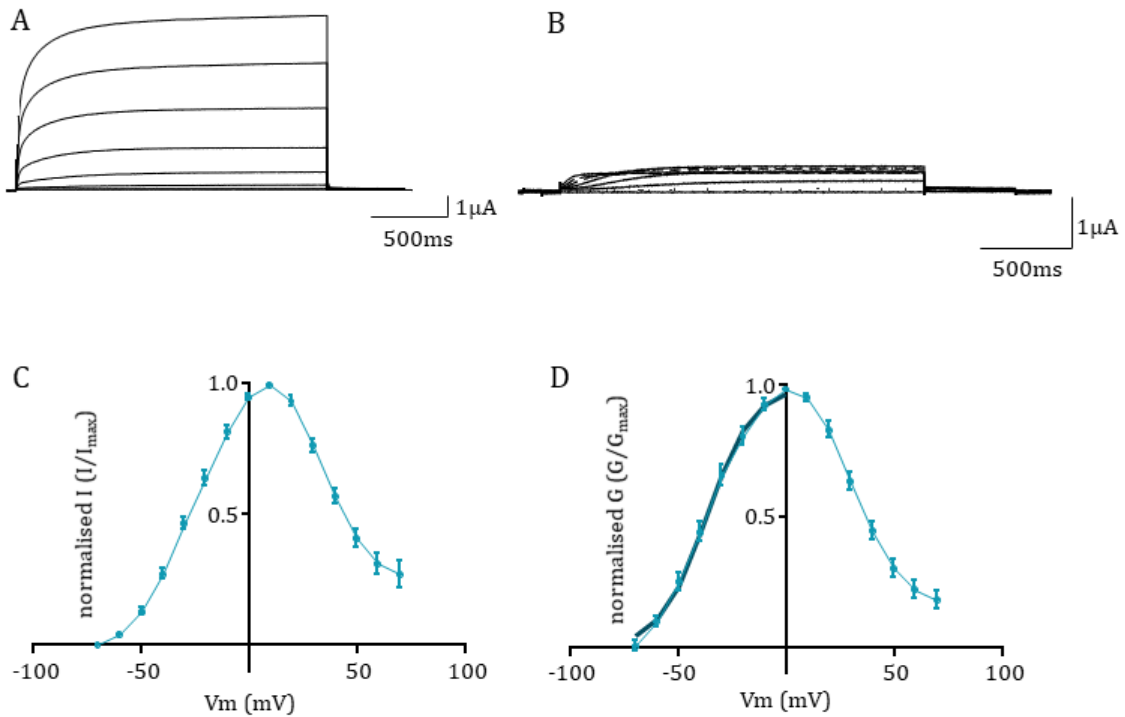


Figure 3.32. Data showing the response of WT and N15E:E600N hEAG1 to changes in membrane voltage.

A: current traces from WT hEAG1 (previously shown in Figure 3.1a) in control solution. The WT current increases in amplitude with each successive depolarisation.

B: current traces from N15E:E600N hEAG1 in control solution. These channels activate more slowly than the WT channel. Currents initially increase in amplitude with membrane depolarisation but reduce in amplitude at voltages more depolarised than +10mV (shown in C, blue data).

C: an I/V graph showing the relationship of N15E:E600N hEAG1's current with voltage. N15E:E600N hEAG1 current increases in amplitude initially but then reduces in amplitude past +10mV. This bears great similarity to the I/V curve of $\Delta 2-26$ hEAG1 (Figure 3.6c)

D: a G/V graph show how the conductance of N15E:E600N hEAG1 relates to voltage. N15E:E600N hEAG1 shows an initial increase in conductance with depolarising membrane potential but this reverses at 0mV. The reduction in conductance may be down to channel inactivation or rectification. Data are fit with a Boltzmann function (dark blue line).

When N15E:E600N hEAG1 is exposed to 5 μ M I&T it potentiates its current by $2137.1 \pm 388.7\%$ ($p < 0.001$, $n = 9$, Figure 3.33a) which is approximately 20 fold over control (Figure 3.33b). This is a considerably bigger response than the $\Delta 2-26$ mutant (Table 1.), the current amplitude begins to reduce towards control levels following the potentiation (Figure 3.33b).

The currents appear slowed in their activation compared to those in control conditions (Figure 3.33a) and during the potentiation phase there is a component of instantaneous current (Figure 3.33a) which indicates that the residue swap has affected the deactivation kinetics of the channel. There is also a consistent, delay in the response to 5 μ M I&T (Figure 3.33b). The 5 μ M I&T is added at $t = 0$ but the current amplitude does not begin increasing for ~ 30 s after the application. This may indicate that the rate of binding of Ca^{2+} -calmodulin has been reduced due to this residue swap.

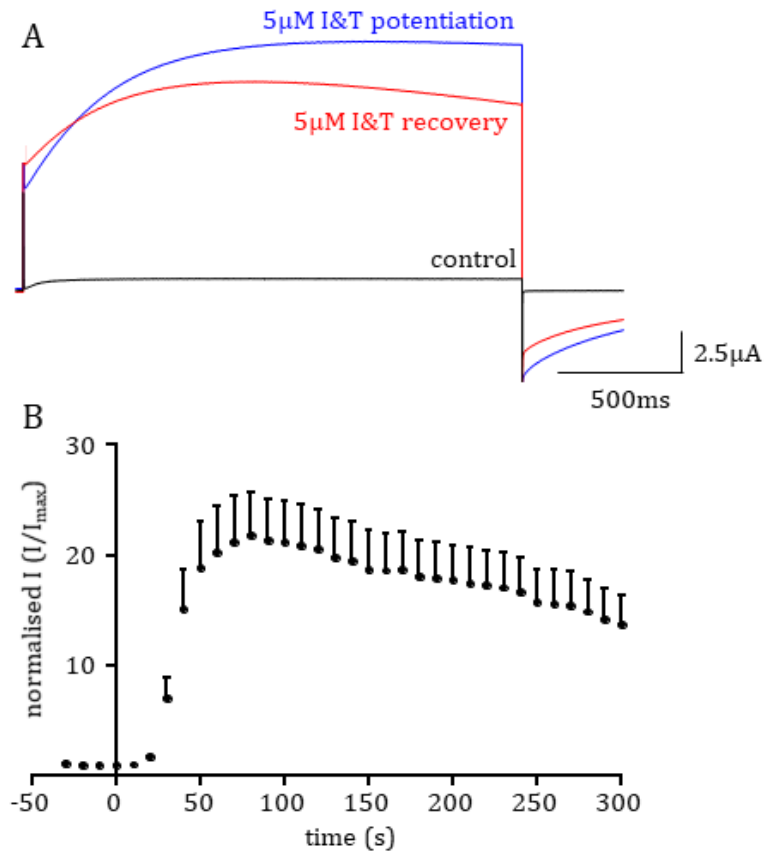


Figure 3.33. Steady pulsing data showing how the N15E:E600N current amplitude changes over time in 5µM I&T.

A: these current traces show the current's response over time in control (black), 5µM I&T potentiation (blue) and the recovery of the current (red). Note that the current amplitude during the recovery begins declining during the pulse indicating that channels are inactivating whilst the membrane potential is still at a positive value.

B: this graph shows how the current amplitude changes over time following the addition of 5µM I&T at t=0. The amplitude initially increases almost 20 times over control values before gradually reducing back towards control levels.

The I/V protocol was run again whilst still in 5 μ M I&T, after >300s of exposure. The currents increase in amplitude before rectifying past +40mV where the current is at its maximum (Figure 3.34). N15E:E600N hEAG1 has a time course of activation of 550.3 ± 61.2 ms which is slow compared to the time course in control conditions ($p < 0.001$, $n=9$, Figure 3.34, Table 1.).

The current traces also show a component of instantaneous current at the start of each trace. This shows that by swapping N15 and E600, the deactivation kinetics of the channel have been considerably slowed (Figure 3.34).

The I/V protocol shows that for each voltage tested the channel passes more current following the application of 5 μ M I&T (Figure 3.34c). The channels are capable of activating at -70mV indicating that the activation threshold has been shifted to negative potentials (Figure 3.34c). The voltage at which the current begins rectifying has also shifted from 0mV in control conditions to +40mV in 5 μ M I&T (Figure 3.34c).

The G/V curve confirms that the channels are activating at more negative voltages as they are already conducting at -70mV (Figure 3.34d). The ascending phase is leftwards shifted compared to control but at more positive potentials it is more rightwards shifted indicating that the conductance curve has broadened (Figure 3.34d). The $V_{0.5}$ value is -50.6 ± 2.2 mV which is more negative than in control conditions ($p < 0.001$, $n=9$, Figure 3.34d, Table 1.). The k value is 19.5 ± 1.2 mV which is higher than in control conditions ($p < 0.0001$, $n=9$, Figure 3.34d, Table 1.) indicating that under high Ca^{2+} conditions N15E:E600N hEAG1 becomes more dependent on voltage. This data indicates that following the application of 5 μ M I&T, the residue swap results in slower activation kinetics and a change in voltage dependence. The channel is also potentiated by 5 μ M I&T ~20 fold over control which is a more severe phenotype than the deletion of the PAS-cap which was ~15 fold potentiated over control.

Taken together, the residue swap of N15 and E600 did not result in a rescuing of the WT characteristics. This does not rule out the two residues as interacting but may have been caused by a change in the microenvironment of each amino acid

which may have caused a re-arrangement of the surrounding residues and structures.

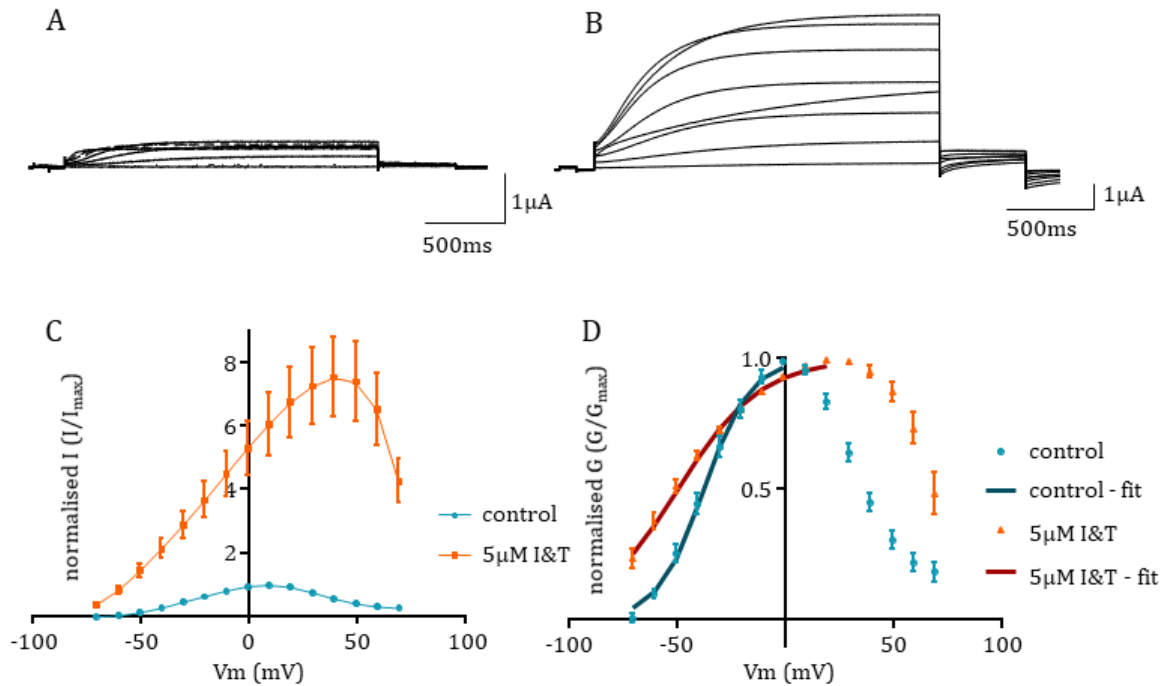


Figure 3.34. Data showing the response of N15E:E600N hEAG1 to changes in membrane voltage following the application of 5µM I&T.

A: current traces from N15E:E600N hEAG1 in control solution. The current increases in amplitude with each successive depolarisation up to +10mV when it then begins reducing in amplitude (also shown in C, blue data).

B: current traces from N15E:E600N hEAG1 in 5µM I&T solution. These channels still activate with a slow time course. Currents increase in amplitude with membrane depolarisation but now reduce in amplitude at voltages more depolarised than +40mV (shown in C, orange data).

C: an I/V graph showing the relationship of N15E:E600N hEAG1 current with voltage both in control and 5µM I&T solution. Currents in control are shown in blue whilst currents in 5µM I&T solution are shown in orange. Currents in 5µM I&T solution are greater in amplitude across all voltages compared to currents in control solution. Currents in 5µM I&T solution reduce in amplitude at more positive voltages than currents in control.

D: a G/V graph show how the conductance N15E:E600N hEAG1 channel changes between control and 5µM I&T. Control is shown in blue whilst 5µM I&T is shown in orange. Channels are active at -70mV in 5µM I&T and conductance continues to increase with voltage up to +30mV. Channels in control solution are active at -60mV and the conductance begins reducing at 0mV. Control and 5µM I&T data are fit with Boltzmann functions (dark blue and dark red respectively).

3.1.8. Y198 of the EAG domain is not involved in the mechanism of action of Δ 2-26 hEAG1

From examination of the cryo-EM structure of hEAG1 (Whicher and MacKinnon, 2016) it seems as though residue Y198 in the EAG domain is within interaction distance of both F17 and E600 (Figure 3.35). The hydroxyl group of Y198 is 2.5Å away from the side chain of E600 whilst the benzene ring of Y198 is close enough to that of F17 that they may be π -stacking with each other (4.2 – 5.0Å). By mutating Y198 to Y198F and removing the hydroxyl group there may be a disruption of the proposed E600 residue interaction.

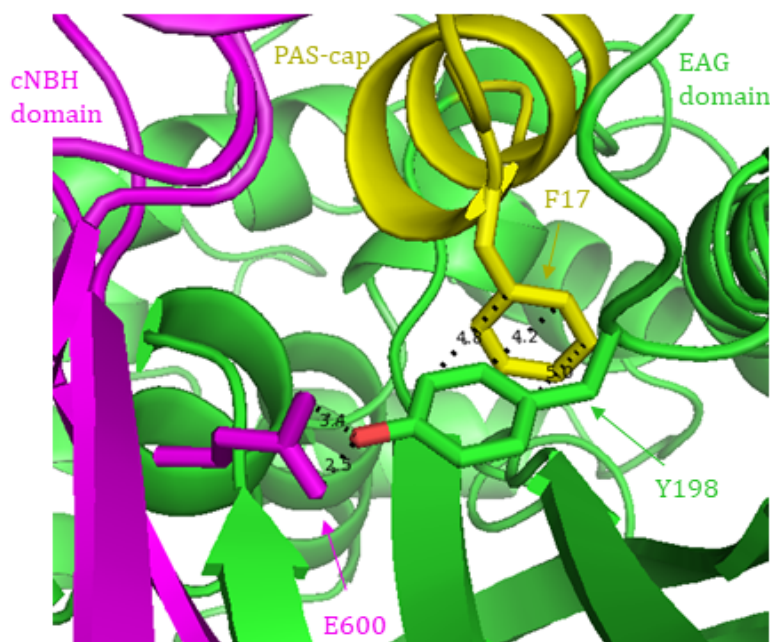


Figure 3.35. A cryo-EM structure* showing the interaction distances from the Y198 between F17 and E600.

The cryo-EM structure shows that the hydroxyl group of Y198 – which is in the EAG domain (green) – is within hydrogen bonding distance of the two electronegative oxygen atoms of E600 of the cNBH domain (magenta) (2.5 and 3.4Å respectively).

The benzene ring of Y198 may also be able to form a π -stack with F17 of the PAS-cap (yellow) as it is between 4.2 and 5.0Å away.

*structure adapted from Whicher & MacKinnon, 2016.

Y198F hEAG1 produces rapidly activating, non-inactivating currents that increase in amplitude with increasing membrane potential (Figure 3.36). The current is at a maximum at +70mV and begins activating at -30mV (Figure 3.36). Under control conditions, these channels activate with a time course of 141.8 ± 37.9 ms, this is faster than the WT channel but not significantly ($p > 0.05$, $n = 10$, Figure 3.36, Table 1.).

The I/V curve shows how the current amplitude changes with voltage, the Y198F channels begins activating around -30mV (Figure 3.36c) which is more positive than -50mV which is seen for the WT channels. Y198F hEAG1 shows a similar relationship with voltage as the WT channel, increasing in amplitude with each step in membrane potential (Figure 3.36c).

The G/V curve for Y198F hEAG1 again shows a similar relationship as the WT channel (Figure 3.36d). The conductance increases with voltage meaning that the rate of ion movement is increasing as the membrane potential becomes more positive (Figure 3.36d). The $V_{0.5}$ value for Y198F hEAG1 is 21.6 ± 2.1 mV which is more positive than the WT channel however this is not a significant find ($p > 0.05$, $n = 10$, Figure 3.36d, Table 1.). The slope of the G/V curve in control conditions appears steeper for Y198F hEAG1 than it is for WT hEAG1 (Figure 3.36d), the k value for Y198F hEAG1 is 15.8 ± 0.4 mV which is lower than that of the WT channel ($p < 0.05$, $n = 10$) indicating that Y198F hEAG1 is less dependent on the voltage than the WT channel (Figure 3.36d, Table 1.).

The data in control conditions has shown that Y198 is involved in the voltage dependence of the channel but not the voltage of activation or the activation kinetics. There is no evidence yet that Y198F hEAG1 shares the behaviour that E600R hEAG1 does which may indicate that in control conditions these residues do not interact with one another.

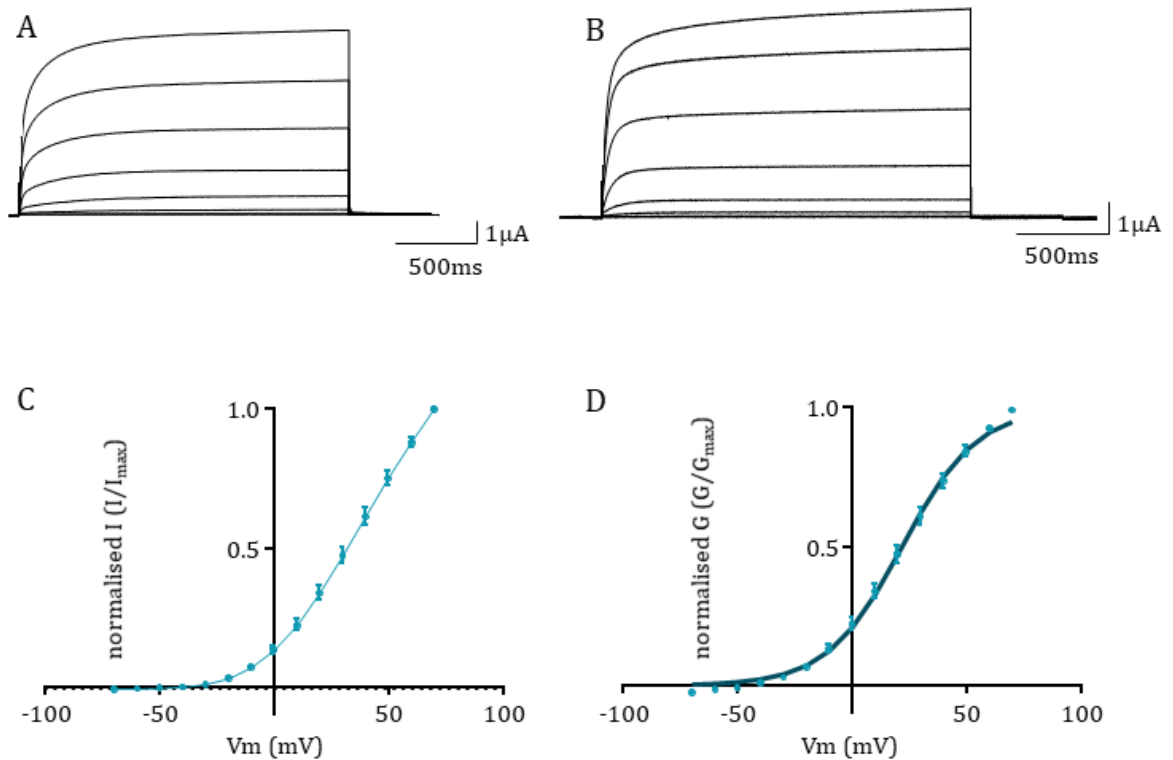


Figure 3.36. Data showing the response of WT and Y198F hEAG1 to changes in membrane voltage.

A: current traces from WT hEAG1 (previously shown in Figure 3.1a) in control solution. The WT current increases in amplitude with each successive depolarisation.

B: current traces from Y198F hEAG1 in control solution. Currents increase in amplitude with membrane depolarisation (shown in C, blue data).

C: an I/V graph showing the relationship of Y198F hEAG1's current with voltage. Y198F hEAG1 increases in amplitude which is similar to the I/V curve of WT hEAG1.

D: a G/V graph show how the conductance of Y198F hEAG1 relates to voltage. Y198F hEAG1 shows increasing conductance with depolarising membrane potential. Data are fitted with a Boltzmann function (dark blue line).

Y198F hEAG1 was exposed to 5 μ M I&T and showed a large inhibition of the current by $95.4 \pm 2.0\%$ ($p < 0.0001$, $n = 10$, Figure 3.37a). The activation kinetics of the channel during the recovery phase are slowed compared to the current in control conditions (Figure 3.37a). The current follows a similar trend as the WT channel, with an initial inhibition followed by a recovery phase. In the case of Y198F hEAG1 the recovery phase is much more gradual than the WT channel (Figure 3.37b).

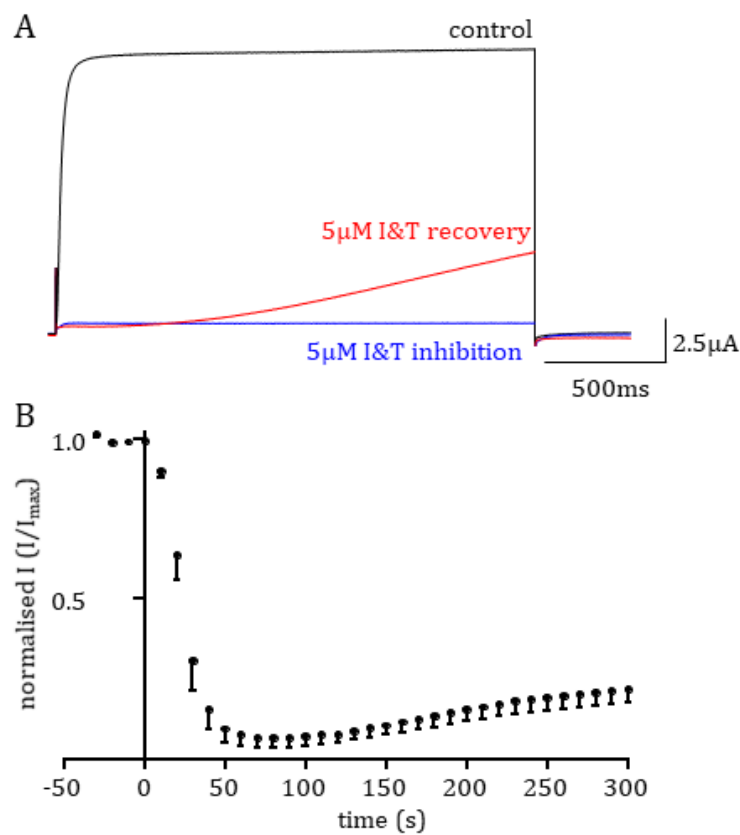


Figure 3.37. Steady pulsing data showing how the current amplitude of Y198F hEAG1 changes over time with 5 μ M I&T.

A: these current traces show the current of Y198F hEAG1 in control (black), 5 μ M I&T inhibition (blue) and the recovery phase (red). The activation kinetics of the channel appear greatly slowed in the recovery phase compared to the control.

B: this graph shows how the current amplitude changes over time following the application of 5 μ M I&T at $t = 0$. The current initially reduces close to 0 but begins to recover in amplitude towards the end of the recording.

The current elicited from the I/V protocol in 5 μ M I&T are much smaller in amplitude compared to the control traces and increase with increasing membrane potential (Figure 3.38). The currents activate with a time course of 1410.9 ± 34.8 ms – almost ten times slower than in control conditions ($p < 0.0001$, $n = 10$, Table 1.). The channels begin to pass current at 0mV and are maximally activated at +70mV (Figure 3.38).

The I/V curve shows that for every voltage, the Y198F channels pass less current than in control conditions (Figure 3.38c) which is similar to the WT channels. The channels also begin to pass current at more positive membrane potentials compared to control (Figure 3.38c). The G/V curve shows a rightwards shift compared to control indicating that a higher voltage is required to activate the channel (Figure 3.38d).

The $V_{0.5}$ value is 36.0 ± 2.3 mV which is more positive than in control conditions and is similar in trend to the WT channel ($p < 0.001$, $n = 10$, Figure 3.38d, Table 1.). The k value for Y198F hEAG1 following 5 μ M I&T is 16.0 ± 0.7 mV which is not statistically different from the value in control conditions ($p > 0.05$, $n = 10$, Figure 3.38, Table 1.).

The data shows that under high Ca^{2+} conditions, Y198 is involved in the activation kinetics of the channel as well as the voltage dependence of the channel. The mutation did not behave in the same manner as E600R indicating that any interaction between these two residues is not key to the regulation of hEAG1.

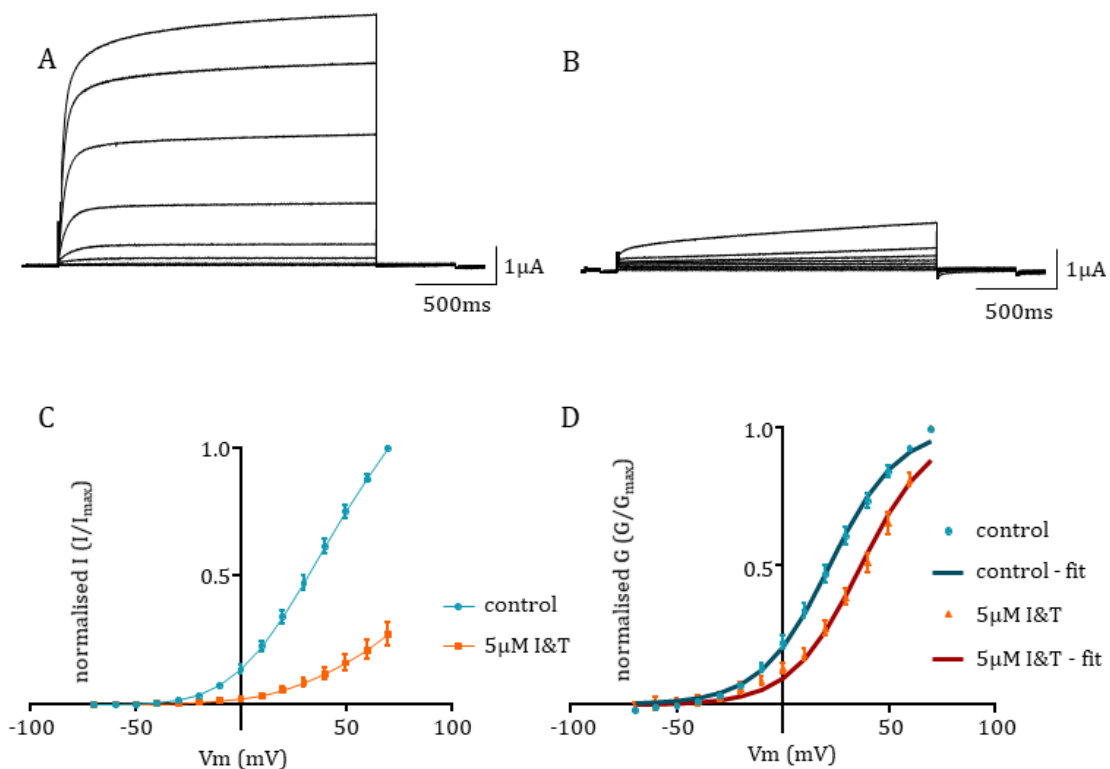


Figure 3.38. Data showing the response of Y198F hEAG1 to changes in membrane voltage following the application of 5µM I&T.

A: current traces from Y198F hEAG1 in control solution. The current increases in amplitude with each successive depolarisation (also shown in C, blue data).

B: current traces from Y198F hEAG1 in 5µM I&T solution. These channels activate with a slow time course and do not reach a steady state plateau during the voltage pulses. Currents increase in amplitude with membrane depolarisation (shown in C, orange data).

C: an I/V graph showing the relationship of Y198F hEAG1 current with voltage both in control and 5µM I&T solution. Currents in control are shown in blue whilst currents in 5µM I&T solution are shown in orange. Currents in 5µM I&T solution are smaller in amplitude compared to currents in control solution at every voltage tested.

D: a G/V graph show how the conductance Y198F hEAG1 channel changes between control and 5µM I&T. Control is shown in blue whilst 5µM I&T is shown in orange. Channels are active at -30mV in 5µM I&T and conductance continues to increase with voltage. Channels in control solution are active at -30mV. Control and 5µM I&T data are fit with Boltzmann functions (dark blue and dark red respectively).

3.1.9. E279 of the S2-S3 linker is not involved in the behaviour seen in Δ 2-26 hEAG1

Intracellular linker regions of hEAG1 may be involved in the gating kinetics and Ca^{2+} -calmodulin regulation of the channel. In light of the new cryo-EM structure, (Whicher and MacKinnon, 2016) it appears as though the unstructured region of the PAS-cap may reach up towards the transmembrane helices. The resolved structure begins at residue L10 and does not include residues 1-9, however taking into account the flexible nature of the unstructured region it may be that E279 of the S2-S3 linker interacts with R7 and R8 of the PAS-cap (Figure 3.39).

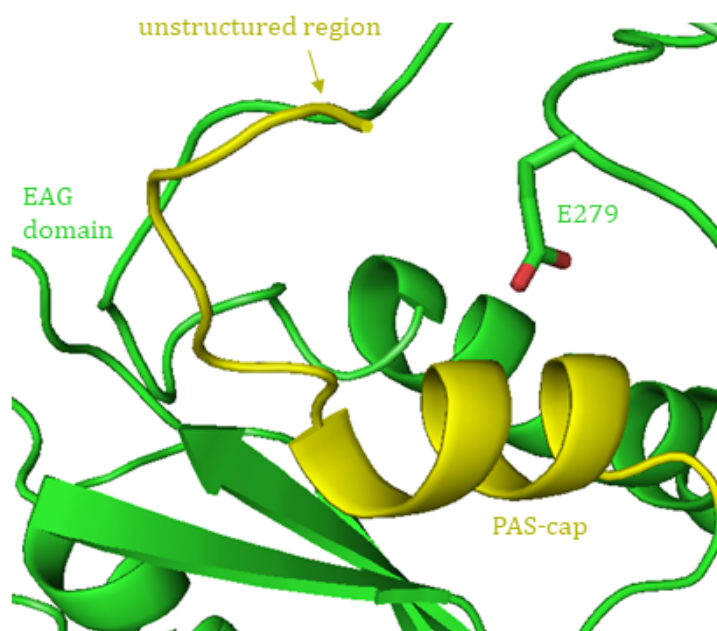


Figure 3.39. A cryo-EM structure* showing the resolved section of the unstructured region of the PAS-cap and its potential interaction with E279.

E279 is a residue of the S2-S3 linker and, due to the flexible nature of the unstructured region, may be able to interact with the double arginine residues R7 and R8. These two residues have not been resolved in the cryo-EM structure but the unstructured region is believed to extend up towards the transmembrane domains.

*structure adapted from Whicher & MacKinnon, 2016.

Disrupting the potential electrostatic interaction between R7, R8 and E279 a charge neutralisation of E279A was tested to see if this interaction was part of the mechanism of regulation of hEAG1 by the PAS-cap.

E279A hEAG1 produced currents that activated quickly and were non-inactivating under the I/V protocol (Figure 3.40). At positive potentials the current amplitude does begin slowing in their rate of increase but do not rectify (Figure 3.40). The channels begin activating at -30mV and are at a maximum at +70mV. Currents in control conditions activated with a time course of 278.8 ± 34.8 ms which is not different statistically from the WT channel ($p > 0.05$, $n = 12$, Figure 3.40, Table 1.).

The I/V protocol shows that E279A hEAG1 has a positive relationship with the membrane potential (Figure 3.40c). As shown by the current traces in Figure 3.40, the channels begin to pass current at -30mV (Figure 3.40c). At positive membrane potentials (+50 to +70mV), the current begins to plateau but not to the point of rectification as seen in the $\Delta 2-26$ hEAG1 mutant (Figure 3.40c).

The G/V curve shows that the conductance increases with voltage (Figure 3.40d). The $V_{0.5}$ value in control conditions is 10.1 ± 2.2 mV which is more negative than the WT channel, however this is not a significant change ($p > 0.05$, $n = 12$, Figure 3.40d, Table 1.). The k value found for E279A hEAG1 is 13.3 ± 0.9 mV which is less than WT hEAG1 indicating that the channel has become less voltage dependent than the WT channel ($p < 0.0001$, $n = 9$, Table 1.).

This data indicates that in control conditions, E279 is involved in the voltage dependence of the channel but not the kinetics of activation. The lack of $\Delta 2-26$ hEAG1-like behaviour initially indicates that the proposed interaction between E279 and R7, R8 is not vital for the PAS-cap's role in the regulation of hEAG1. It may also be the case that the R7 and R8 values are not within interaction distance of E279 but since this section of the PAS-cap was not resolved in the structure it cannot be known for sure at this stage.

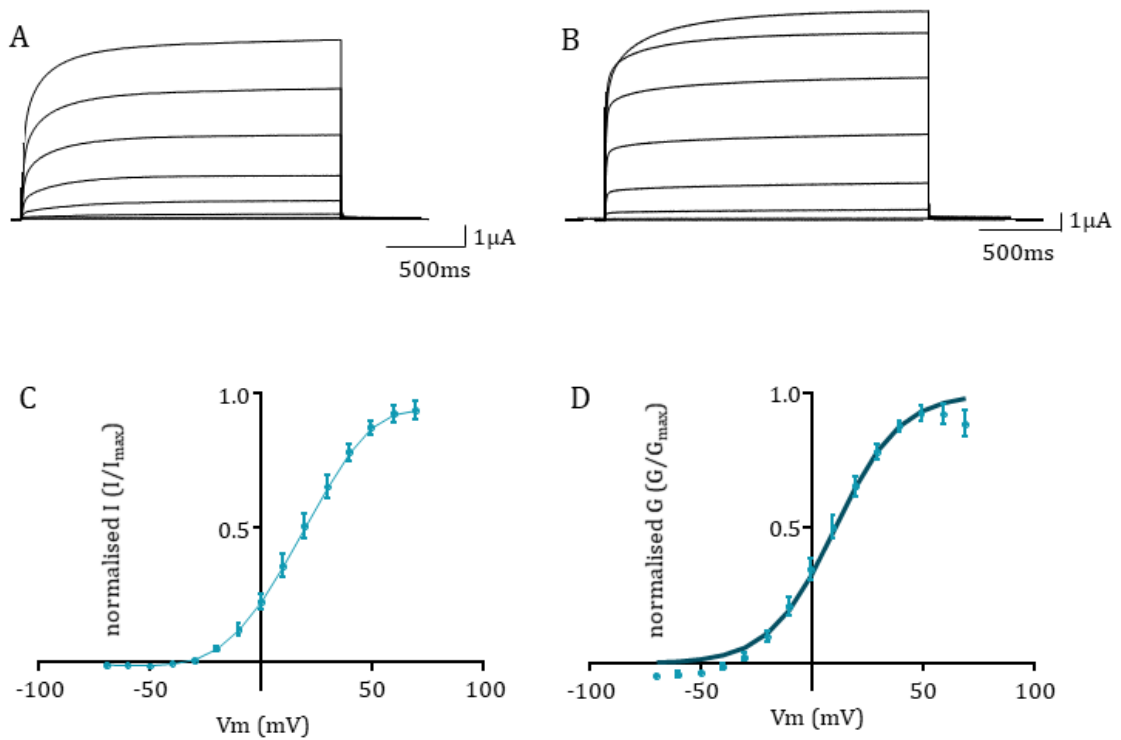


Figure 3.40. Data showing the response of WT and E279A hEAG1 to changes in membrane voltage.

A: current traces from WT hEAG1 (previously shown in Figure 3.1a) in control solution. The WT current increases in amplitude with each successive depolarisation.

B: current traces from E279A hEAG1 in control solution. Currents increase in amplitude with membrane depolarisation (shown in C, blue data).

C: an I/V graph showing the relationship of E279A hEAG1's current with voltage. E279A hEAG1 increases in amplitude which is similar to the I/V curve of WT hEAG1.

D: a G/V graph show how the conductance of E279A hEAG1 relates to voltage. E279A hEAG1 shows increasing conductance with depolarising membrane potential. Data are fitted with a Boltzmann function (dark blue line).

Following the application of 5 μ M I&T, E279A hEAG1 current was inhibited by $82.4 \pm 4.8\%$ compared to control ($p < 0.0001$, $n = 8$, Figure 3.41a, Table 1.). Following the inhibition, the current showed a recovery phase of the current amplitude in a similar manner to the WT channel (Figure 3.41b). The current in recovery displays a slowing of the activation kinetics compared to the control current (Figure 3.41a).

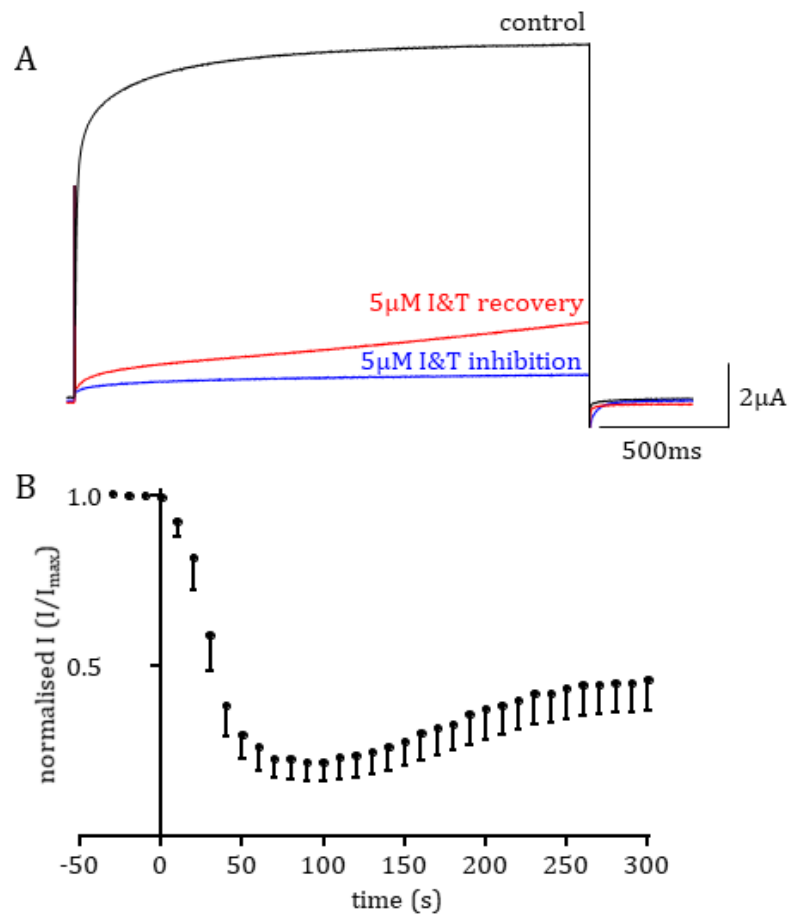


Figure 3.41. Steady pulsing data showing how the current amplitude of E279A hEAG1 changes over time following addition of 5 μ M I&T.

A: these current traces show how the current responds in control (black) and to 5 μ M I&T which comprises of an inhibition phase (blue) and a recovery phase (red).

B: this graph shows how the current amplitude changes with time following the application of 5 μ M I&T at $t = 0$. The amplitude initially decreases before gradually recovering in amplitude.

The channels were measured in 5 μ M I&T under the I/V protocol (Figure 3.42). The current amplitude increases as the membrane potential becomes more positive with the current at a maximum at +70mV. The channels begin to pass current at +10mV (Figure 3.42). The activation time course of E279A hEAG1 is slowed to 1364.6 ± 28.9 ms from control ($p < 0.0001$, $n = 12$, Figure 3.42, Table 1.).

The I/V curve shows that for each voltage the amount of current passed was reduced compared to the control (Figure 3.42c). The G/V curve shows a rightward shift in the curve compared to control which indicates that the channels require higher voltages to activate (Figure 3.42d) which is a similar response as the WT hEAG1 G/V graph. The $V_{0.5}$ value in 5 μ M I&T is 33.7 ± 1.5 mV which is more positive than in control conditions ($p < 0.0001$, $n = 12$, Figure 3.42d, Table 1.). The k value of the same curve is 15.1 ± 0.6 mV which is not a significant increase from control ($p > 0.05$, $n = 12$, Figure 3.42d, Table 1.).

This data indicates that under high Ca²⁺ conditions the E279 residue is involved in the activation kinetics of the channel as well as the voltage dependence. However, the residue mutant E279A hEAG1 did not influence the channel's behaviour in the same way as $\Delta 2-26$ nor the two residue mutants within the PAS-cap, N15 and F17 which means E279 is not a vital part of the PAS-cap's influence over the behaviour of hEAG1.

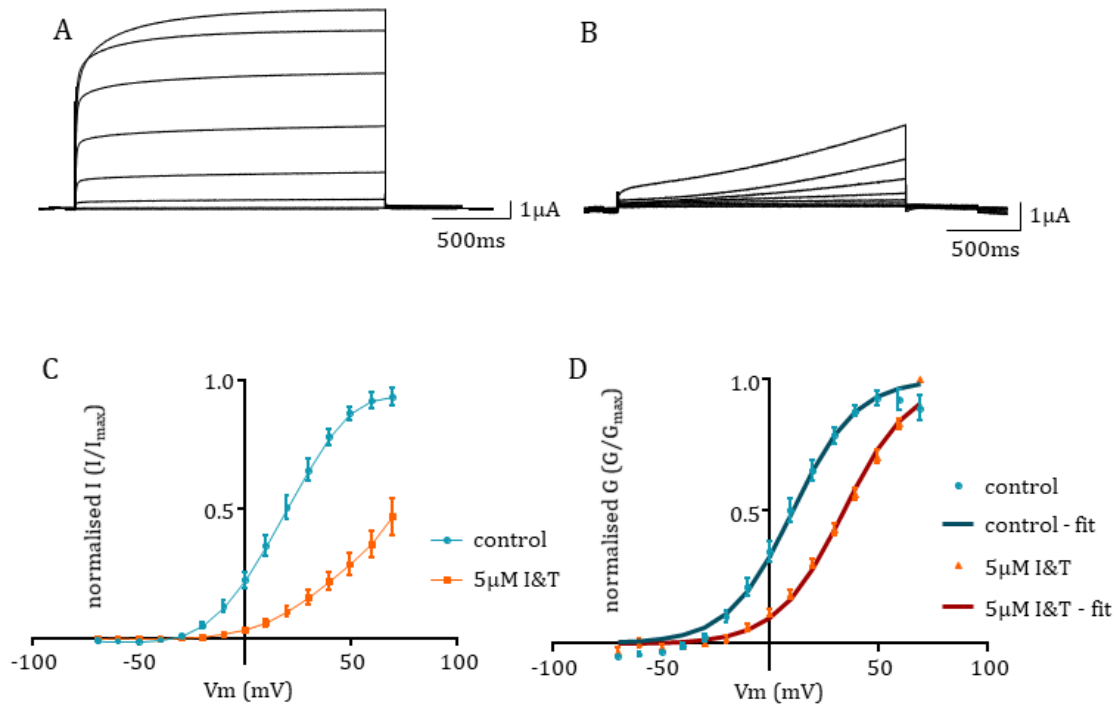


Figure 3.42. Data showing the response of E279A hEAG1 to changes in membrane voltage following the application of 5µM I&T.

A: current traces from E279A hEAG1 in control solution. The current increases in amplitude with each successive depolarisation (also shown in C, blue data).

B: current traces from E279A hEAG1 in 5µM I&T solution. These channels activate with a slow time course and do not reach a steady state plateau during the voltage pulses. Currents increase in amplitude with membrane depolarisation (shown in C, orange data).

C: an I/V graph showing the relationship of E279A hEAG1 current with voltage both in control and 5µM I&T solution. Currents in control are shown in blue whilst currents in 5µM I&T solution are shown in orange. Currents in 5µM I&T solution are smaller in amplitude compared to currents in control solution at every voltage tested.

D: a G/V graph show how the conductance E279A hEAG1 channel changes between control and 5µM I&T. Control is shown in blue whilst 5µM I&T is shown in orange. Channels are active at -20mV in 5µM I&T and conductance continues to increase with voltage. Channels in control solution are active at -20mV. Control and 5µM I&T data are fit with Boltzmann functions (dark blue and dark red respectively).

hEAG1 construct	% change in I&T	V _{0.5} (mV)		k value		10-80% activation time (ms)	
		control	I&T	control	I&T	control	I&T
WT	85.5 ± 2.9 ****	16.0 ± 2.0	28.5 ± 2.7 **	21.4 ± 2.4	15.4 ± 0.7	309.1 ± 16.4	1040 ± 39.0 ****
Δ2-26	1272.7 ± 197.1 **	-22.3 ± 1.3	-36.3 ± 2.9 *	9.8 ± 0.2	21.0 ± 2.7 *	692 ± 27.5	867.5 ± 85.7
N15A	306.0 ± 44.9 ***	-35.8 ± 3.8	-42.2 ± 3.9 *	11.0 ± 1.1	15.7 ± 2.5	264.3 ± 17.9	615.4 ± 91.8 **
T16A	91.9 ± 1.9 ****	28.7 ± 0.8	37.2 ± 1.6 ***	14.7 ± 0.5	13.4 ± 0.3 **	240.3 ± 55.6	1278.3 ± 78.3 ****
F17A	242.4 ± 60.7 **	-30.2 ± 4.5	-29.2 ± 5.7	10.5 ± 0.8	14.0 ± 1.3 *	533.2 ± 85.5	587.8 ± 43.2
L18A	90.4 ± 4.6 ****	47.0 ± 1.0	-51.1 ± 3.0 ****	9.2 ± 0.4	11.6 ± 0.8 *	55.5 ± 6.2	1220.5 ± 144.1 ****
E19A	77.1 ± 5.1 ****	6.7 ± 2.0	15.8 ± 2.1 ****	18.7 ± 0.5	17.6 ± 0.7 **	175 ± 40.5	537.9 ± 57.7 **
N20A	92.4 ± 3.0 ****	9.5 ± 1.7	25.9 ± 3.4 **	19.6 ± 1.1	18.2 ± 2.1	294.6 ± 18.8	1156.6 ± 154.9 **
I21A	93.3 ± 1.0 ****	17.5 ± 1.3	29.8 ± 2.2 ****	17.4 ± 0.3	14.6 ± 0.4 ***	141.8 ± 31.7	808.6 ± 75.9 ***
V22A	92.1 ± 1.8 ****	16.2 ± 2.5	37.1 ± 2.4 **	15.6 ± 1.1	13.1 ± 0.2	419.6 ± 114.5	1316.9 ± 69.6 **
N15E:E600N	2137.1 ± 388.7 ***	-37.5 ± 1.9	-50.6 ± 2.2 ***	10.4 ± 0.4	19.5 ± 1.2 ****	214.4 ± 28.3	550.3 ± 61.2 ***
Y198F	95.4 ± 2.0 ****	21.6 ± 2.1	36.0 ± 2.3 ***	15.8 ± 0.4	16.0 ± 0.7	141.8 ± 37.9	1410.9 ± 34.8 ****
E279A	82.4 ± 4.8 ****	10.1 ± 2.2	33.7 ± 1.5 ****	13.3 ± 0.9	15.1 ± 0.6	278.8 ± 34.8	1364.6 ± 28.9 ****
E600A	62.8 ± 8.9 ****	11.1 ± 5.7	-15.2 ± 3.2 ****	20.5 ± 1.0	17.2 ± 1.4 *	459.7 ± 56.9	893.4 ± 66.2 ****
E600R	865.6 ± 296.6 *	8.7 ± 16.4	-22.5 ± 1.5	11.0 ± 4.0	11.8 ± 1.7	724.9 ± 118.2	844.4 ± 87.3

Table. 1. A table showing all measured parameters for WT hEAG1 and all studied mutants both in control and in 5 μ M I&T.

The first parameter measured was the % change in current following application of 5 μ M I&T, values highlighted in red represent mutants that resulted in an increase (potentiation) of the current. The next parameter, $V_{0.5}$, is the membrane potential that elicits the half-maximal current. It is measured by fitting the conductance curve with a Boltzmann function. The k value is also a product of a fitted Boltzmann function and represents the slope of the curve (mV) that fits the data. An increase in k value indicates that the channel is less dependent on voltage whilst a decrease in the k value indicates an increase in voltage dependence. Lastly, the activation time course measures the time taken for the current to increase from 10 to 80% of its maximum. All values are presented as mean \pm SEM and significance is indicated by the asterisks (* is <0.05, ** is <0.01, *** is <0.001, **** is <0.0001).

3.2. Discussion

3.2.1. The PAS-cap regulates the inhibition of WT hEAG1 under high Ca^{2+} conditions

The aim of these experiments was to understand the role of the PAS-cap in hEAG1 regulation and also to dissect out the roles of each residue of the amphipathic helix. This gives us greater understanding of the role the PAS-cap plays in regulating hEAG1 and how different intracellular domains may be interacting with one another in the functional channel.

The experiments began by characterising the response of the WT channel to successive depolarisations in membrane potential. It has previously been documented that the WT channel increases its current amplitude with voltage (Lorinczi *et al.*, 2015). Our data agrees with this as we show WT hEAG1 currents to increase in amplitude as the membrane potential becomes more positive. The conductance-voltage relationship was also studied to obtain values for $V_{0.5}$ and k , our data agrees with the data presented by Lorinczi *et al.* (2015) who also used a Boltzmann function to fit their data producing $V_{0.5}$ values of $16.0 \pm 2\text{mV}$ and $16.3 \pm 0.58\text{mV}$ respectively, although we obtained a higher k value.

The Ca^{2+} -calmodulin inhibition of the channel has been shown many times (Schönherr *et al.*, 2000; Ziechner *et al.*, 2006) and has also been shown to be a physiologically controlled mechanism by the addition of muscarine to a stably-expressing cell line (Stansfeld *et al.*, 1996). Data provided by Bijlenga *et al.* (1998) partially agrees with our data in that the application of $0.5\mu\text{M}$ ionomycin – 10-fold diluted compared to our experiments – causes a reduction in the hEAG1 current. No recovery phase was documented in this case as reported by us as Bijlenga *et al.* (1998) removed the ionomycin from their solution and kept recording. Our experiment was designed with two factors in mind, first to provide a robust increase $[\text{Ca}^{2+}]_i$ and second that the Ca^{2+} level is maintained throughout the experiment. This is why $5\mu\text{M}$ ionomycin, to rapidly increase Ca^{2+} , and thapsigargin, to block the reuptake of Ca^{2+} by the SERCA pump, were used. Thus the recovery phase documented by us is a novel discovery of WT hEAG1 in oocytes.

The behaviour of the WT channel following current inhibition and recovery was altered. The channel opened with slowed activation kinetics compared to in control conditions (Table 1.) which indicates that the binding of Ca²⁺-calmodulin to the channel causes a conformational change that influences the activation gate of the channel. Other studies have suggested that the N-terminal intracellular domain of EAG1 are involved in the activation kinetics (Terlau *et al.*, 1997). The cryo-EM structure described by Whicher and MacKinnon (2016) suggests that the distal N-terminus of the PAS domain, residues 1 to 13, may be interacting up with the voltage sensor and that this interaction determines the activation kinetics. With calmodulin bound in place, as shown by the cryo-EM structure, the cNBHDs of each subunit sit directly under the pore and are connected to it by the C-linker which may be a factor in the slow opening of the pore as the structure is more tightly packed following the application of 5µM I&T and the binding of calmodulin (Whicher and MacKinnon, 2016).

The PAS-cap is a 26 amino acid α helix that is at the N-terminus of the PAS domain and is a structure shared between the KCNH family (Whicher and MacKinnon, 2016; Harley *et al.*, 2016; Brelidze *et al.*, 2012). Deletion of the PAS-cap in hERG1 channels was shown to accelerate the rate of deactivation equivalent to deleting the entire PAS domain (Muskett *et al.*, 2011). This indicates that the PAS-cap is important in the kinetics of hERG1 and due to the high sequence homology between hERG1 and hEAG1 the PAS-cap may also have an important role in hEAG1.

The PAS-cap was deleted from the hEAG1 gene resulting in the mutant referred to as Δ 2-26 hEAG1. This mutant under control conditions resulted in slowed activation kinetics compared to the WT channel (Table 1.) and also resulted in rectification during the I/V protocol, when the conductance becomes reduced at more positive membrane potentials rather than increasing progressively with voltage. Our data for WT hEAG1 shows that it maintains this positive relationship whereas the Δ 2-26 mutant does not and begins reducing in current amplitude from +20mV. This is an interesting discovery. Not only does the loss of the PAS-cap cause slowed activation kinetics but it also affects the conductance of the channel. Lorinczi *et al.* (2009) state that WT hEAG1 does actually show rectification at high membrane potentials and that this can be attributed to block by intracellular Na⁺ ions (Pardo *et*

al., 1998). Deletion of the PAS-cap causes a leftwards shift in the activation threshold compared to WT hEAG1, as shown by the I/V curve, and in doing so may bring the process of rectification to more negative potentials and into the range of potentials examined in these experiments. However we cannot rule out the possibility that the PAS-cap has a direct effect on the conductance of hEAG1 and cause the rectification at +20mV in an independent manner.

Δ 2-26 hEAG1 produces a large potentiation of the current following the addition of 5 μ M I&T. Current potentiation has been noted in K_v1.2 channels where the channels increase their current with trains of repetitive action potentials. This was attributed to changes in the gating mode that allowed the channel to pass more current under certain circumstances (Baronas *et al.*, 2017). Potentiation of hEAG1 current has not yet been described and we provide evidence that the current potentiation of Δ 2-26 hEAG1 was $1272.7 \pm 197.1\%$ of the current in control conditions. This data suggests that the PAS-cap may be acting a molecular “brake” on the hEAG1 current and when it is present acts to reduce hEAG1 current when [Ca²⁺]_i increases but that when it is absent there is reduced control over the regulation of the current. Experiments conducted on pentameric ligand-gated ion channels showed that a point mutation within the second transmembrane domain caused compounds that inhibited the current to become potentiators (Bromstrup *et al.*, 2013). Whilst this was shown for ligand-gated ion channels and not voltage-gated ion channels the idea still stands that inhibitors of the current can become potentiators when there are structural rearrangements of the channel. This may be a potential mechanism by which the PAS-cap regulates WT hEAG1.

3.2.2. Residues N15 and F17 of the PAS-cap are key for its role in regulation hEAG1 function

Our main experiment involving the PAS-cap was an alanine scan of the amphipathic helix. At the time of experimentation, only the homology model developed from the X-ray crystal structure of the EAG and cNBH domains generated by Haitin *et al.* (2013) was available (Lorinczi *et al.*, 2016). The homology model of the PAS-cap was used to inform our decisions when designing the mutagenesis which began at Q14 which was at the N-terminal end of the amphipathic helix through to V22 which was at the C-terminal end of the helix. An individual alanine

mutation was generated for each position and the constructs were tested for two things; their response to the voltage protocol to find out the role of the residue under resting Ca^{2+} conditions and also the response to raised Ca^{2+} to test whether the residue had a role in how the channel responds to Ca^{2+} .

The first point to note is that the alanine mutants of T16, L18, E19, N20, I21 and V22 all shared behaviour that was similar to the WT channel. They all activated with fast kinetics and produced currents that gained in amplitude with each successive depolarisation of the membrane. These mutant channels were also inhibited by $5\mu\text{M}$ I&T in a similar biphasic manner as the WT channel. However, the mutation did sometimes affect the $V_{0.5}$ and k values of the channel meaning that they are still involved in how the channel responds to voltage. Of the mutants that causes a statistically significant change in $V_{0.5}$ for activation – T16A and L18A only – they shifted $V_{0.5}$ to more positive membrane potentials indicating that under control conditions these residues of the PAS-cap act to anchor the threshold of activation at more negative potentials. The mutants that significantly changed the k value were T16A, L18A and V22A, all of which reduced the k value indicating that the mutant channels are more sensitive to voltage. All other alanine mutants did not significantly affect either the $V_{0.5}$ or k values of their respective channels. From analysis of the cryo-EM structure it appears as though both T16 and L18 lie between the EAG and cNBH domains of the channel and that the ability of the PAS-cap to bridge between the two domains may be a mechanism of action for these residues (Whicher and MacKinnon, 2016).

These residues were also tested under $5\mu\text{M}$ I&T to see how the channels responded to high Ca^{2+} conditions. All the constructs, except for L18A, shifted the $V_{0.5}$ for activation of the channel to positive potentials compared to control. The same applies for the k value where all except N20A (which had no effect) and L18A caused a reduction in the k value. The significant data includes residues that lie between the EAG and cNBH domains and indicates that the interaction of the PAS-cap to both domains is important for its role in maintaining the voltage dependence of the channel under high Ca^{2+} conditions (Whicher and MacKinnon, 2016).

L18 is a residue of particular interest, it behaves as a “hybrid” between the WT and $\Delta 2-26$ hEAG1 channels. On the one hand it has fast activation kinetics in

control conditions and shows the same biphasic response to 5 μ M I&T as the WT channel. But following the application of 5 μ M I&T it begins showing tendencies of the Δ 2-26 channel such as slow activation kinetics and a large negative shift in the $V_{0.5}$ value and an increase in the k value. It is the only alanine mutant of the PAS-cap that behaves this way after addition of 5 μ M I&T and points towards L18 being an important residue in maintaining the WT functionality of the channel under high Ca^{2+} conditions. L18 lies directly between the EAG and cNBH domains in the cryo-EM structure and provides more evidence that the interaction of the PAS-cap with both the N and C-terminal domains is critical for it to regulate hEAG1 in both control and high Ca^{2+} conditions.

Two residues of the PAS-cap, N15 and F17, stood out as being important for maintaining the WT phenotype as when they were mutated to alanine they both behaved in a manner similar to that of the Δ 2-26 hEAG1 channel. Both mutants show rectifying behaviour at depolarised membrane potentials. Both mutants in their own right behave in a similar manner to Δ 2-26 hEAG1, they both have negatively shifted $V_{0.5}$ values in control conditions meaning that both residues are involved in the voltage dependence of activation of the channel. They both also have reduced k values compared to the WT channel meaning that they become more dependent on the voltage. This data indicate that the N15 and F17 residues are key within the PAS-cap in order for it to maintain a WT-like phenotype.

The most important comparison comes when the mutants are exposed to 5 μ M I&T. N15A shows a \sim 4 fold potentiation of the current whilst F17A is \sim 3 fold. Neither mutant has quite the same potentiation as the Δ 2-26 mutant, indicating that whilst these residues are clearly involved in this process, the effect is constrained by the rest of the PAS-cap structure being present. The cryo-EM provided by Whicher and MacKinnon (2016) shows that the N15 and F17 residues are on opposite sides of the amphipathic helix. N15 points towards the cNBHD whilst the F17 residue points towards the EAG domain. This indicates that the two residues act to stabilise the helix between the two domains and position it in such a way that allows the rest of interactions. Hence mutating either of them could result in a destabilisation of the PAS-cap and a disruption of other residue interactions.

An interesting point of the Δ 2-26 channel was the component of instantaneous current observed during the I/V protocol in 5 μ M I&T. It is caused by channels from the previous voltage stimulus still being open, 8 seconds later, when the next voltage stimulus occurs. The channels being open removes the part of the time-dependent current because time is not spent opening the channel pore so that current can be passed immediately following the change in membrane potential. This indicates a severe slowing of the deactivation kinetics, something that has not been outright measured in this experiment but is still worth noting as data gathered from hERG1 channels missing the PAS-cap shows the opposite effect since the role of the PAS-cap in hERG1 is to slow deactivation (Morais Cabral *et al.*, 1998; Muskett *et al.*, 2011; Wang *et al.*, 2000). Following the addition of 5 μ M I&T, N15A hEAG1 also showed a component of instantaneous current albeit to a lesser extent than Δ 2-26 hEAG1 which indicates that the N15 residue is at least partly involved in the deactivation kinetics but is not acting alone. The F17A mutant doesn't show any instantaneous current after being exposed to 5 μ M I&T which shows that this residue is likely not involved in the deactivation kinetics – at least not to the extent that it can be seen as an instantaneous current.

3.2.3. E600 of the cNBHD and N15 of the PAS-cap are likely part of an interaction network

The X-ray crystal structure produced by Haitin *et al.* (2013) showed that there was an interaction surface between the cNBHD and the EAG domains of mEAG. Haitin *et al.* (2013) mapped a series of cancer associated mutants (at homologous positions in hEAG1) and long QT syndrome mutants (at homologous positions in hERG1) to this interaction surface. One of the residues that mapped to this interface was homologous to E788 in hERG1, this residue, when mutated, is associated with long QT syndrome (Lorinczi *et al.*, 2016). The equivalent position in hEAG1 is E600 which we tested using both an alanine and an arginine mutant, i.e a charge neutralisation and reversal. The charge neutralisation, E600A, behaved in many respects at the WT channel. It was inhibited by 5 μ M I&T and recovered in current amplitude as the WT channel does. The E600R mutant behaved much more like the Δ 2-26 mutant, including slow activation kinetics, potentiation of the current following 5 μ M I&T and a component of instantaneous current. Interestingly, when

exposed to 5 μ M I&T the E600R mutant increased its current but did not show a recovery phase back towards control giving a time dependence graph with the same profile as the N15A mutant.

Since the E600R and N15A mutants both have similar responses to 5 μ M I&T we examined their positions using the cryo-EM structure which had not long been published (Whicher and MacKinnon, 2016). The structure revealed that the two residues were \sim 5.4 \AA apart which is within the range for polar interactions to occur. With this in mind, we produced a residue swapped channel, N15E:E600N which was designed to test whether or not these residues were interacting. If they were important interaction partners we expected to see a WT-like phenotype from the mutant. However, this mutant behaved much more like Δ 2-26 hEAG1 except with an exaggerated effect from 5 μ M I&T. The Δ 2-26 hEAG1 channel potentiated its current \sim 15 fold whilst N15E:E600N hEAG1 potentiated \sim 20 fold indicating that by swapping the residues we have allowed the channel to pass even more current during high Ca²⁺ conditions. The data from this mutant indicates that if these residues are interacting, it is likely to be part of a larger interaction network and not a direct interaction of the two residues. Swapping a negatively charged amino acid into the place of a polar residue may have also caused a disruption of the structure of the PAS-cap which could have exacerbated the phenotype seen.

3.2.4. Neither Y198 of the EAG domain or E279 of the S2-S3 linker are involved in the PAS-cap's mechanism of action

We still wanted to understand how the F17 residue interacts with its environment and how this could influence its control of hEAG1. The cryo-EM structure shows that Y198 of the EAG domain is between 4.2 and 5.0 \AA away from F17 (Whicher and MacKinnon, 2016). Both residues contain a benzene ring which can π -stack with each other in a non-covalent interaction (Akher *et al.*, 2017). From the cryo-EM structure it appears as though the two benzene rings are offset from each other in a "T" configuration. This configuration of the rings has actually been shown to be more energetically favourable when compared to direct stack on top of each other (Akher *et al.*, 2017; McGaughey *et al.*, 1998).

The hydroxyl group is 2.5Å from the side chain of E600 which may also provide hydrogen bonding. The mutant Y198F was generated as this maintained the structure of the benzene ring but lost the hydroxyl group from the side chain, thus separating the effects of E600 from F17. Y198F hEAG1 behaved in the same way as the WT channel by showing an inhibited current following 5µM I&T with only a reduction in voltage dependence in control conditions. In 5µM I&T the $V_{0.5}$ value was positively shifted from control – as was the WT channel – thus there was no evidence that Y198 interacted with E600 as it did not share any aspects of the E600R phenotype. The next logical step would be to generate the Y198A mutant to remove the benzene ring and test whether a potential π -stacking interaction between F17 is important. This will allow us to further understand how F17 interacts with its surrounding residues and decipher which ones are important to anchor F17 and maintain the stability of the PAS-cap.

Another aspect of the cryo-EM structure was that it was the first structure to fully resolve the amphipathic helix of the PAS-cap bound in place with the rest of the channel. It also resolved a small portion of the unstructured region – although residues 1-10 were missing. This gives us an idea as to which other parts of the channel the PAS-cap interacts with. A negatively charged residue, E279, of the S2-S3 linker is close to where the resolution of the PAS-cap ends. Residues R7 and R8 are not shown in the structure but due to the position of the PAS-cap, they may be close enough for a charged interaction with E279. A charge neutralisation of E279A was generated and showed behaviour similar to that of the WT channel. It showed fast activation kinetics in control conditions and was inhibited by 5µM I&T which then caused a positive shift in $V_{0.5}$ just as seen in the WT channel. This indicates that the R7 and R8 residues are not close enough to E279. It could be due to the flexibility of the unstructured region, especially given the proline residue at position 13, that Whicher and MacKinnon (2016) have captured the unstructured region in one of potentially many conformations thus meaning that the R7 and R8 residues are in an entirely different position.

4. Results and Discussion – How does the PAS-cap influence hEAG1 channel behaviour in terms of N, *i* and P_{open}?

4.1. The mechanism of regulation of hEAG1 by the PAS-cap.

The deletion of the PAS-cap of hEAG1 ($\Delta 2-26$ hEAG1) has been shown to alter the channel's behaviour. The most intriguing property of $\Delta 2-26$ hEAG1 is that following the application of 5 μ M I&T the current amplitude increases by $1272.7 \pm 197.1\%$ over control whilst the WT channel is inhibited by $85.5 \pm 2.9\%$ (Table 1, Figure 4.1). It is highly unusual for an ion channel to show such a large potentiation of the current amplitude so it was important to investigate this behaviour further.

Whole cell current – such as that measured in the oocyte two-electrode system – is comprised of 3 variables as shown by the equation:

$$I = NiP_{open}$$

Where I = whole cell current, N = number of channels available to open, *i* = single channel current and P_{open} = the open probability for the channel. Deleting the PAS-cap and exposing the channel to raised [Ca²⁺]_i changes one or more of these properties yielding the large potentiation seen with $\Delta 2-26$ hEAG1 in oocytes.

To decipher the mechanism of action of the PAS-cap on hEAG1 behaviour, WT and $\Delta 2-26$ hEAG1 were expressed in CHO cells and whole cell patch clamp data recorded. Steady pulsing voltage protocols, similar to those used in the oocytes, were applied to obtain voltage and time-dependent currents and their responses to 5 μ M I&T. This data was then analysed using noise analysis to obtain values for N and *i* but also show whether or not P_{open} was affected. Noise analysis was used because single channel amplitudes are reported to be too small (Bruggemann *et al.*, 1993). In preliminary experiments it was not possible to detect single channel events in the Mitcheson lab.

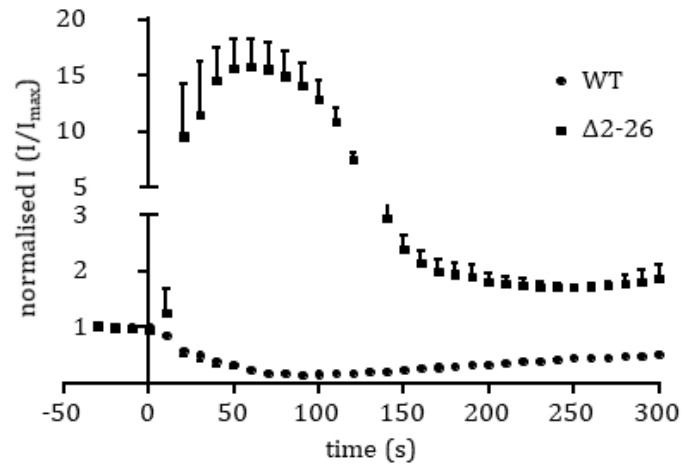


Figure 4.1. A graph comparison of the effect of 5 μ M I&T on the current amplitude of WT and Δ 2-26 hEAG1.

This graph shows the large potentiation of the Δ 2-26 hEAG1 current (squares, n=3) against the inhibition of the WT channel (circles, n=10). 5 μ M I&T was added at t=0. Current amplitudes are normalised to the current amplitude in control.

4.1.1. Expression of WT and Δ 2-26 hEAG1 yields functional currents in CHO cells

To conduct noise analysis experiments, WT hEAG1 was expressed in CHO cells and whole cell patch clamp recordings were made. Before this WT hEAG1 currents were first characterised using an I/V protocol similar to that used in the oocytes with a voltage range of -50mV to +70mV increasing in 10mV increments (Figure 4.2c).

When expressed in CHO cells, WT hEAG1 produced outward, fast activating currents that increased in amplitude with successive increases in membrane potential above 0mV (Figure 4.2a and Figure 4.3a). This was similar behaviour to that seen in the oocyte system under the two-electrode recording technique although the voltage threshold was more positive in the CHO cells compared to the oocytes (Figure 4.3). The currents yielded in the CHO cells activated with a 10-80% time course of 158.5 ± 40.6 ms at +60mV which is faster than the time course measured in oocytes which was 309.1 ± 16.4 ms at the same voltage ($p < 0.05$, $n = 20$, Table 2.). CHO cells were also transfected with the empty vector control, pXoon, which gave no significant current when tested with the I/V protocol (Figure 4.2b), indicating the low expression of endogenous channel in CHO cells.

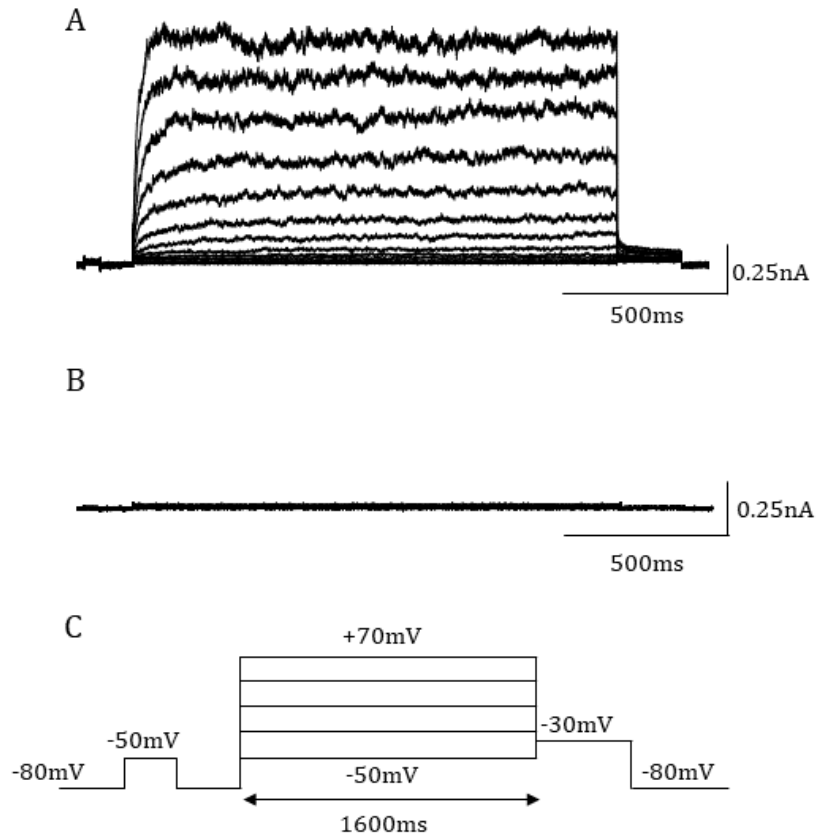


Figure 4.2. Current traces of WT hEAG1 and pXoon showing the responses to the I/V protocol in CHO cells.

A: these current traces show how the WT channel responds to the I/V protocol shown in C in CHO cells. The current increases with each successive depolarisation in the same way the channel does in the oocytes system.

B: these traces show how pXoon-expressing cells respond to voltage. pXoon is the empty vector control so the lack of current is expected.

C: the I/V protocol used in the CHO cell system, the main pulses start at -50mV and end at +70mV, each lasting 1.6s, with a tail potential of -30mV. The holding potential was maintained at -80mV and a test potential of -50mV was used before each voltage step to monitor leak. There was a 5 second gap between the start of each pulse.

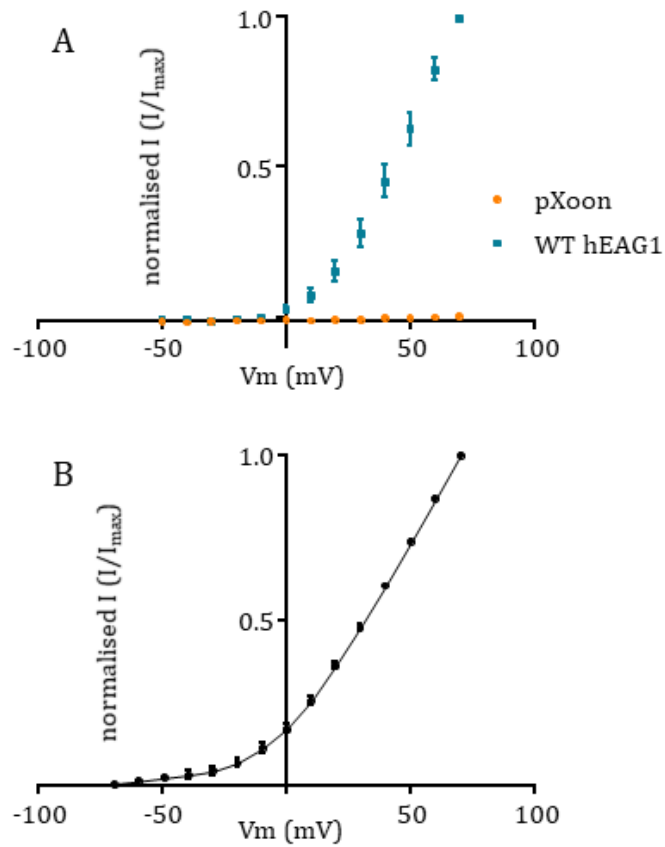


Figure 4.3. I/V graphs of WT hEAG1 showing how the channel responds to voltage in CHO cells and oocytes.

A: this data is taken from CHO cells and shows WT hEAG1 current (blue) increasing with each voltage step. The empty vector, pXoon is shown for comparison (orange). The response of WT hEAG1 in CHO cells is similar to that seen in the oocytes.

B: this data is from the oocytes expressing WT hEAG1 and is shown for comparison - data described in Figure 3.2.

The G/V curve of the CHO cell data shows that the WT channel activates at potentials more positive than in the oocytes (Figure 4.4). The $V_{0.5}$ value for WT hEAG1 in the CHO cells was $37.2 \pm 3.0\text{mV}$ which was significantly more positive than the value obtained from the oocytes which was $16.0 \pm 2.0\text{mV}$ ($p < 0.001$, $n = 20$, Figure 4.4, Table 2.). The slope factor (k value) for the CHO cell system was $10.3 \pm 0.6\text{mV}$ which is significantly lower than in the oocytes where it was $21.4 \pm 2.4\text{mV}$ ($p < 0.0001$, $n = 20$, Figure 4.4, Table 2.). This indicates that in the mammalian system the channel has altered voltage dependence compared to the oocytes.

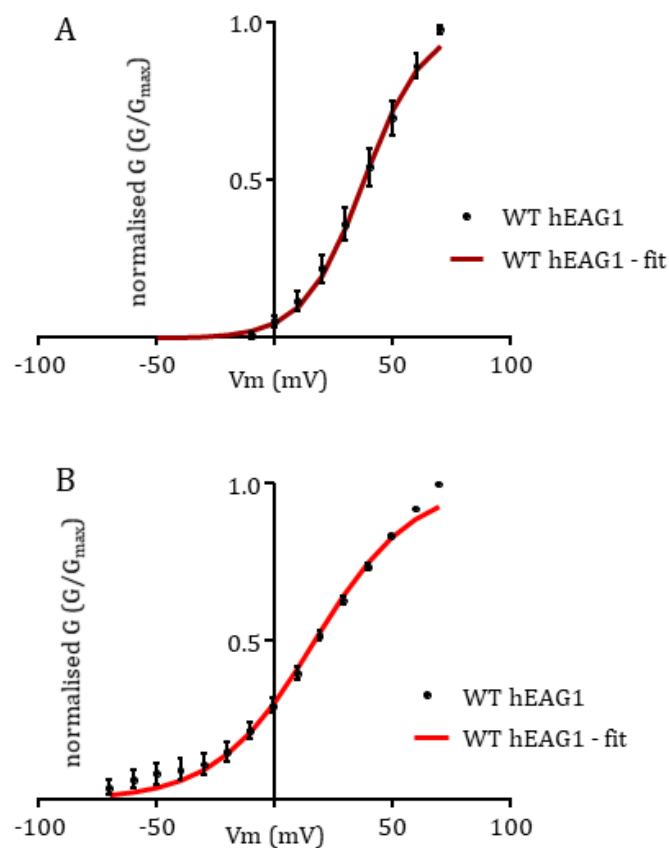


Figure 4.4. G/V graphs of WT hEAG1 showing how the conductance responds to voltage in CHO cells and oocytes.

A: this data is taken from CHO cells and shows WT hEAG1 conductance increasing with each voltage step. The Boltzmann fit is shown in dark red. The response of WT hEAG1 in CHO cells is similar to that seen in the oocytes, however the data in CHO cells appears more rightwards shifted compared to the oocytes.

B: this data is from the oocytes expressing WT hEAG1 and is shown for comparison – data described in Figure 3.2b.

Currents in CHO cells expressing WT hEAG1 were first measured in control solution in response to repetitive pulses of 700ms to a potential of +20mV and cells were then exposed to 5 μ M I&T to obtain data for noise analysis. The noise analysis protocol to +20mV was designed so that the channels would be activated but their activation kinetics wouldn't be too fast. This was so the rising phase of the current, as more channels opened in response to the voltage, was as long as possible so the analysis of the variance would be more accurate.

The maximal WT hEAG1 inhibition by 5 μ M I&T was $78.6 \pm 5.8\%$ compared to control ($p < 0.001$, $n = 16$) and not significantly different to the response seen in the oocyte system ($p > 0.05$, Table.2, Figure 4.5a). The end pulse current was normalised against control values and plotted against time. The inhibition of the current was gradual and there was no recovery of the current amplitude when recordings were measured over 300s (Figure 4.5c). Data from pXoon-expressing cells shows that there is no current produced and that the 5 μ M I&T has no effect ($n = 4$, Figure 4.5b).

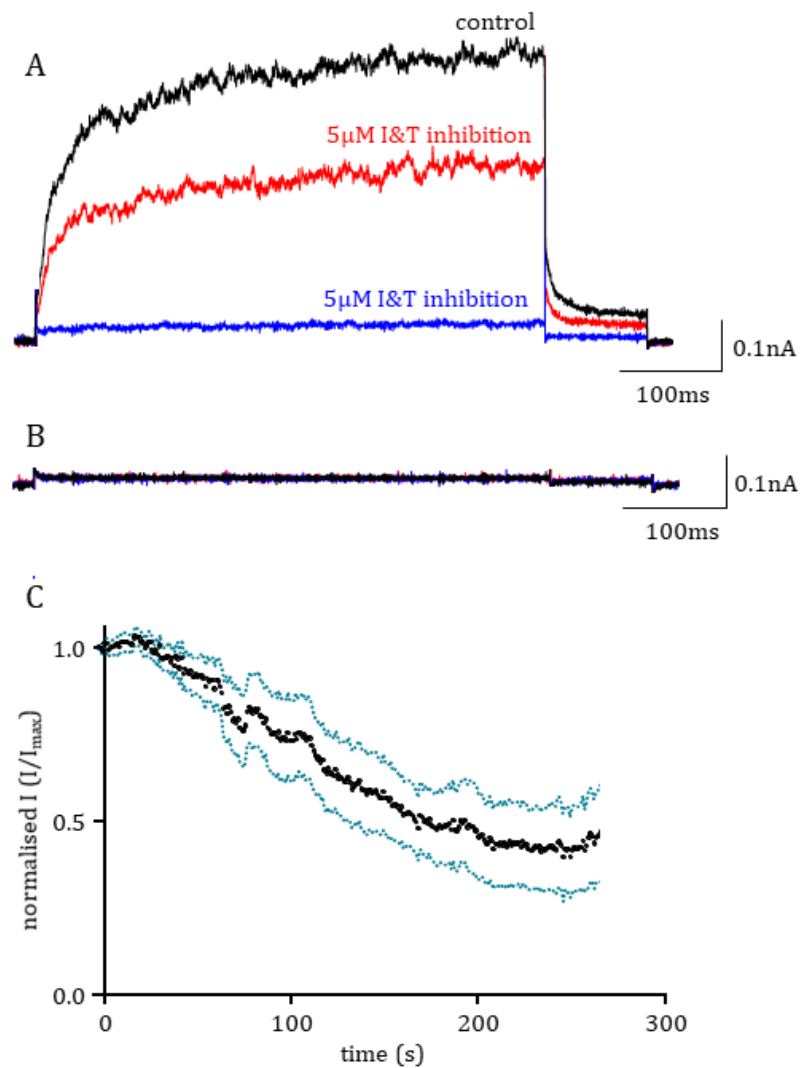


Figure 4.5. Steady pulsing data showing the response of WT hEAG1 to 5µM I&T when expressed in CHO cells.

A: current traces elicited by steps to +20mV. The traces show the current response in control (black) and in the inhibition phase (red followed by blue).

B: current traces taken from pXoon-expressing cells show that there is no current produced from this transfection.

C: a graph showing the response of the current amplitude over time when 5µM I&T was added at t=0. This graph shows a gradual decline in the current amplitude but no recovery phase as seen in the oocytes.

In oocytes, the inhibition occurs much more rapidly and recovers in amplitude over time, whereas in the CHO cells, the inhibition is much more gradual and does not recover in amplitude at time points up to 300s (Figure 4.6). Although it was not feasible to determine if the recovery of the current would occur at later time points >300s.

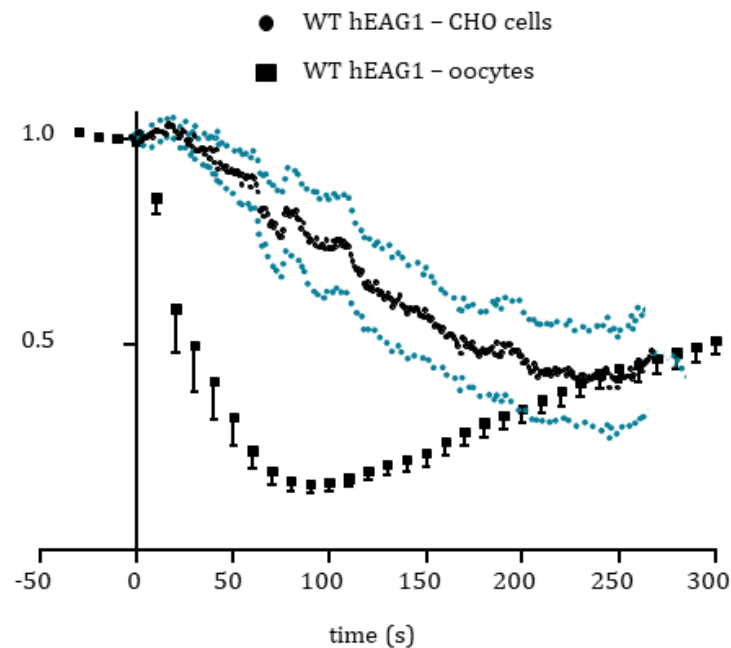


Figure 4.6. Steady pulsing data showing the difference in response of WT hEAG1 to 5 μ M I&T.

This data shows the response previously described in oocytes (Figure.3.3b) alongside the data obtained from CHO cells (black circles with dark blue SEM). The channel is inhibited in CHO cells but the rate of inhibition is much slower than in oocytes and does not show a recovery phase as it does in the oocyte system.

$\Delta 2-26$ hEAG1 currents were also characterised in CHO cells and tested against the I/V protocol shown in Figure 4.2c. The currents responded in a similar way to the I/V protocol as in oocytes. They were slow to activate and initially increased in amplitude with voltage before starting to rectify at more positive potentials (Figure 4.7). $\Delta 2-26$ hEAG1 activated with a 10-80% time course of 622.4 ± 65.2 ms at +60mV which is no different to that of the oocyte-expressed channels ($p > 0.05$, $n = 5$, Table 2.) although this may be an underestimate because a steady state activation was not reached. The currents produced in response to the I/V protocol show a component of instantaneous current at the start of the trace, this is due to a slowing of the deactivation kinetics so that channels are still open at the start of the next voltage step. The tail currents, at -30mV, do not show the current deactivating due to the kinetics being so slow (Figure 4.7).

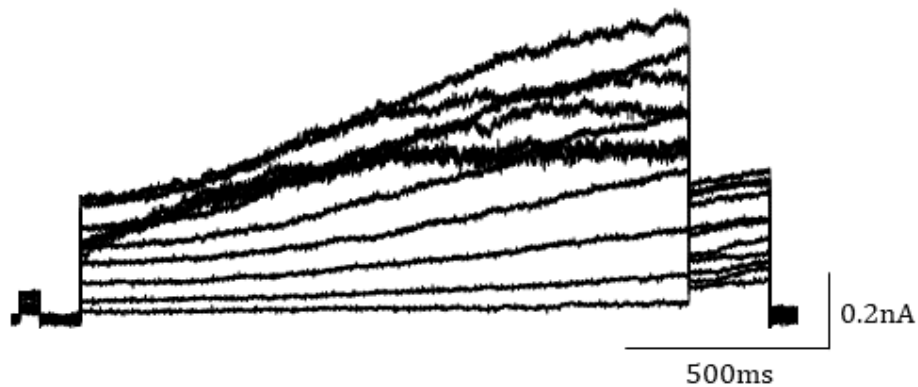


Figure 4.7. Current traces elicited from the I/V protocol of $\Delta 2-26$ hEAG1 showing how the channel responds to voltage in CHO cells.

These currents are slow to activate and rectify at more positive potentials. This behaviour is similar to that seen in the oocytes. There is also a component of instantaneous current in control in the CHO cells which is not seen in the oocytes. This may be down to an interval of 5s between protocol sweeps in CHO cells compared to 10s intervals in oocytes.

The current amplitude at the end of the pulse was measured, normalised and the mean current amplitudes were plotted against the membrane potential (Figure 4.8a). In CHO cells, the $\Delta 2-26$ hEAG1 current peak amplitude increases with membrane potential before rectifying at potentials positive to +40mV (Figure 4.8a), whereas the current rectifies at the more negative potential of +20mV in oocytes (Figure 4.8b).

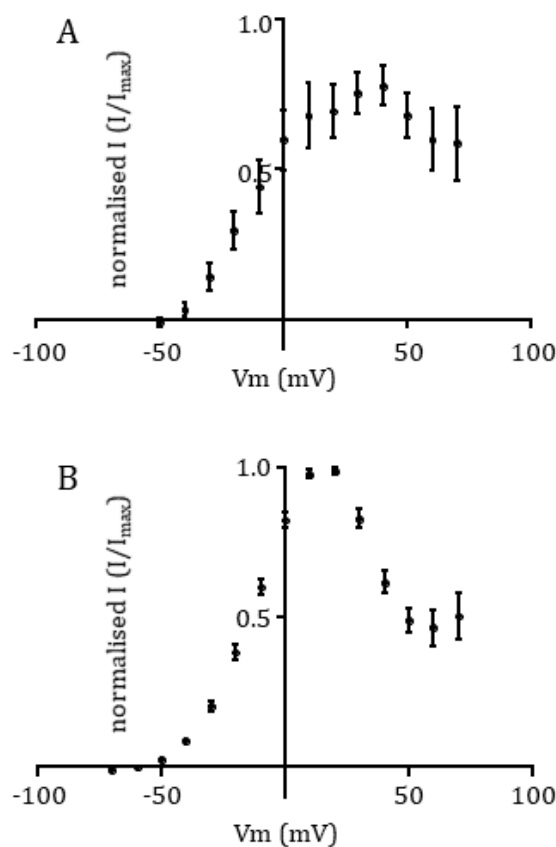


Figure 4.8. I/V graphs showing how $\Delta 2-26$ hEAG1 behaves in response to voltage in both CHO cells and oocytes.

A: this data is recorded from CHO cells using the whole cell patch clamp method. The current increases with voltage initially before peaking at +40mV. The current then rectifies with further increases in voltage.

B: this data shows the current response from oocytes. In oocytes the current begins rectifying at potentials more negative to that in the CHO cells.

The G/V curve shows that at the highest measured membrane potential, +70mV, the normalised conductance is higher in the CHO cells than it is in oocytes indicating weaker rectification (Figure 4.9). The $V_{0.5}$ value for current activation in CHO cells was $-19.1 \pm 4.3\text{mV}$ which is more negative than in oocytes albeit not significantly ($p>0.05$, $n=9$, Table 2.). The k value is $9.4 \pm 1.2\text{mV}$ in CHO cells, lower again than oocytes, but not a significant change ($p>0.05$, $n=9$, Table 2.). This data shows that $\Delta 2-26$ hEAG1 is functional in CHO cells and its biophysical properties do not differ substantially from those in the oocyte system – indicating that the biophysical parameters measured to be different for WT hEAG1 are PAS-cap mediated and not cell background dependent.

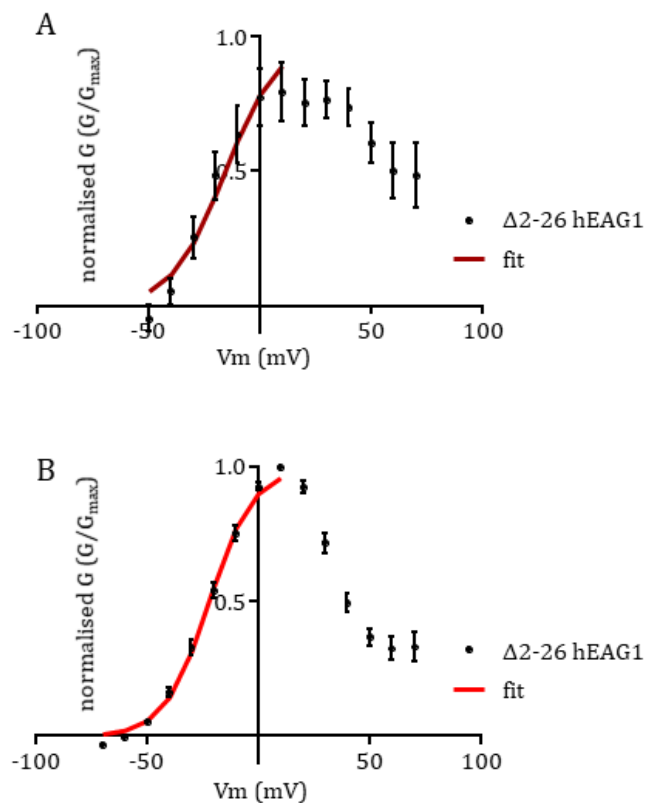


Figure 4.9. G/V graphs showing how the conductance of $\Delta 2-26$ hEAG1 behaves in response to voltage in both CHO cells and oocytes.

A: this data is recorded from CHO cells using the whole cell patch clamp method. The conductance increases with voltage initially before peaking at +10mV. The conductance then reduces with further increases in voltage.

B: this data shows the conductance response from oocytes (previously shown in Figure.3.7b). The conductance begins rectifying at the same potential in both CHO cells and oocytes.

CHO cells expressing $\Delta 2$ -26 hEAG1 were also repetitively pulsed to +20mV and exposed to 5 μ M I&T to monitor the channel's response to high $[Ca^{2+}]_i$. The current amplitude increased upon application of 5 μ M I&T before returning to control levels. A component of instantaneous current was observed, which was due to channels not fully deactivating between pulses (Figure 4.10a). The end pulse current increased by $349.4 \pm 304.9\%$ relative to control but this was incredibly variable compared to the response from the oocytes (n=4) (Figure 4.10b). The potentiated response was also to a lesser extent than the oocytes and oscillated over time before returning to control levels (Figure 4.11a).

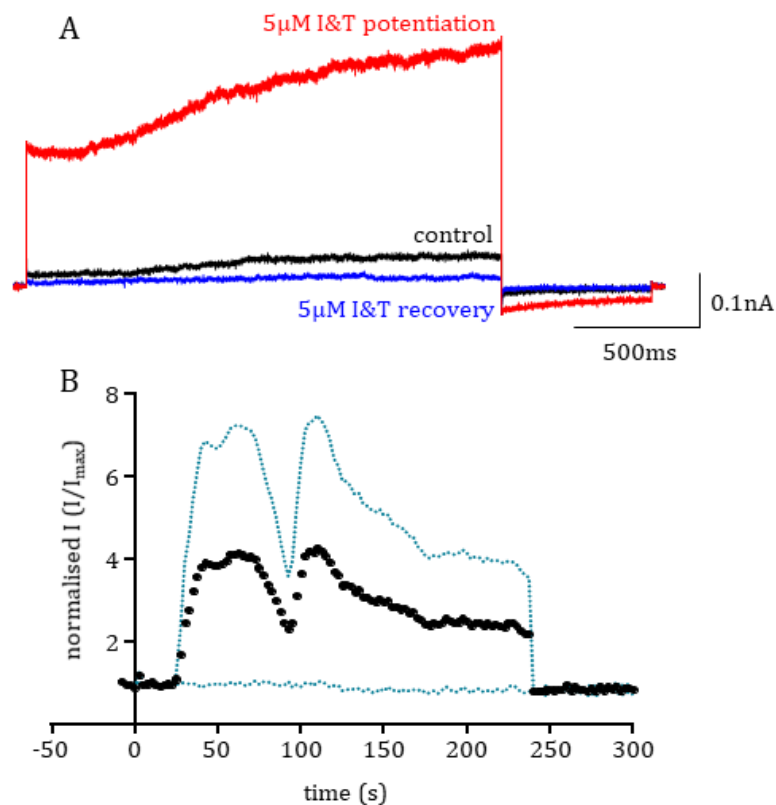


Figure 4.10. Steady pulsing data showing how $\Delta 2$ -26 hEAG1 responds to 5 μ M I&T in CHO cells.

A: these traces represent the response from a single cell. The current in control (black) is low in amplitude, following the application of 5 μ M I&T the current increases in amplitude in a similar way to the channel in oocytes (red) before recovering in amplitude back down towards control (blue).

B: this graph shows the average response of the $\Delta 2$ -26 hEAG1 current amplitude following to addition of 5 μ M I&T at t=0. The current potentiates initially before oscillating and returning towards control levels. The response of the channel varied greatly from cell to cell giving way to large error bars (blue dots).

Individual cell data are shown in Figure 4.11b. Some cells responded well to the 5 μ M I&T by increasing their current. This is shown by the black dots, which demonstrated a maximum percentage increase of 1873%. Other cells responded but on a much smaller amplitude scale increasing by 19.9% (blue dots) or 9.6% (orange dots) (Figure 4.11b).

These results indicate that the response of Δ 2-26 hEAG1 to 5 μ M I&T are more variable in CHO cells than in oocytes.

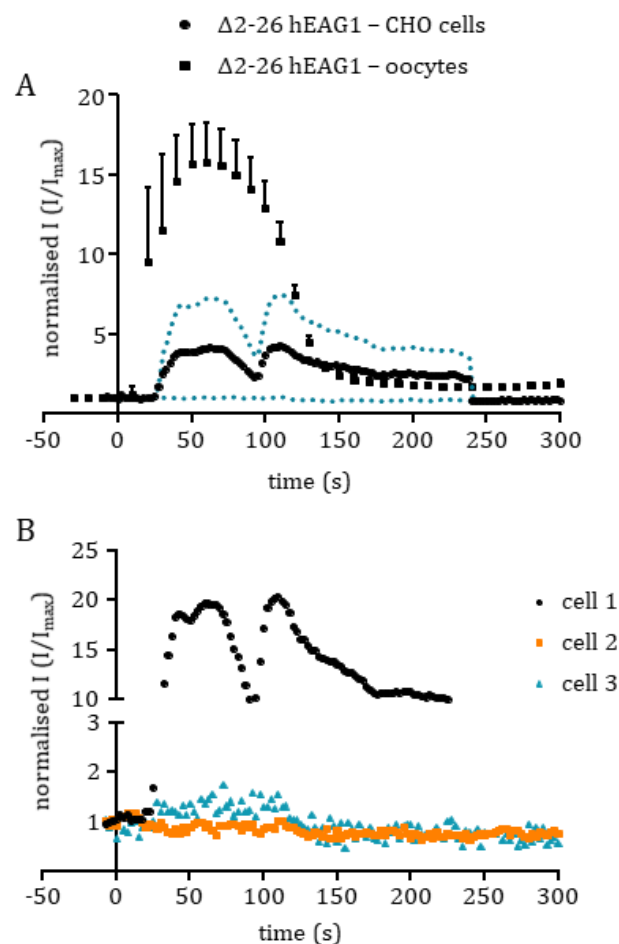


Figure 4.11. Steady pulsing data comparing Δ 2-26 hEAG1 in CHO cells and oocytes.

A: this graph compares data from oocytes (squares) to the data obtained from the CHO cells (circles). The potentiation seen in the CHO cells is not as high at that of the oocytes, nor is it as consistent, and oscillates before returning to control levels.

B: steady pulsing from individual cells demonstrating the variety of responses to 5 μ M I&T. Some cells (black) responded strongly whilst others (orange) didn't respond at all. Some cells also had a minor response (blue).

4.1.2. Simulations of hEAG1 data predict possible outcomes

Before analysing hEAG1 data, we first carried out simulations to help understand current-variance curves would be altered by changes in single channel parameters. In-house software, Tracan3, was developed to simulate voltage-gated K⁺ channel activity based on a linear scheme comprising 5 close and one open state (Figure 4.12). Simulations were accomplished by calculating the dwell time in each state and the subsequent transition step using a Markov simulation routine. The number of channels in a cell was set at 500 and the single channel current at 0.5pA. 200 pulses were given and the ensemble mean (I) and variance (σ^2) of these were calculated. Mean variance plots were generated as shown in Figure 4.13 and the equation below was fit to the data by varying i and N :

$$\text{Function 1 : } \sigma^2 = Ii - I^2/N$$

Maximum P_{open} is given by I_{max}/Ni . To alter the maximum P_{open} in the simulations the value of the rate constant γ was altered; the higher the value of γ the higher the maximum P_{open} .

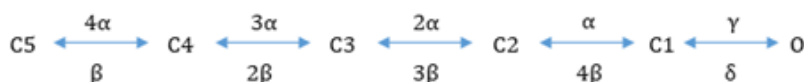


Figure 4.12 A flow chart demonstrating the closed to open state transitions of hEAG1 channels.

This flow chart shows the rates of transition between the 5 closed states of hEAG1 (4α to α). This is followed by the rate of transition to the open state (γ). Higher values of γ correspond to a higher maximum open probability.

The transition from the open to closed state 1 is also shown (δ) along with the various transition rates back through the closed states (4β to β).

Simulations for reducing the maximum P_{open} are shown in Figure 4.13, here $N = 500$, $i = 0.5\text{pA}$ and the number of sweeps was 200. The rate γ was set to 0.12ms^{-1} giving a maximum P_{open} of 0.68 as shown by the data points in blue and the fit is shown in dark blue. The result when γ was reduced to 0.04ms^{-1} , yielding an approximate P_{open} value of 0.4, is shown by the orange data points and is fit by the dark red line. Across the different simulations, the reduction in P_{open} is shown by a leftwards shift in the data. The orange data points superimpose well over the fit of the blue data points. This indicates that a reduction in P_{open} of *in vivo* WT hEAG1 recordings after application of $5\mu\text{M}$ I&T would be identified as a leftwards shift in the variance vs mean current data points.

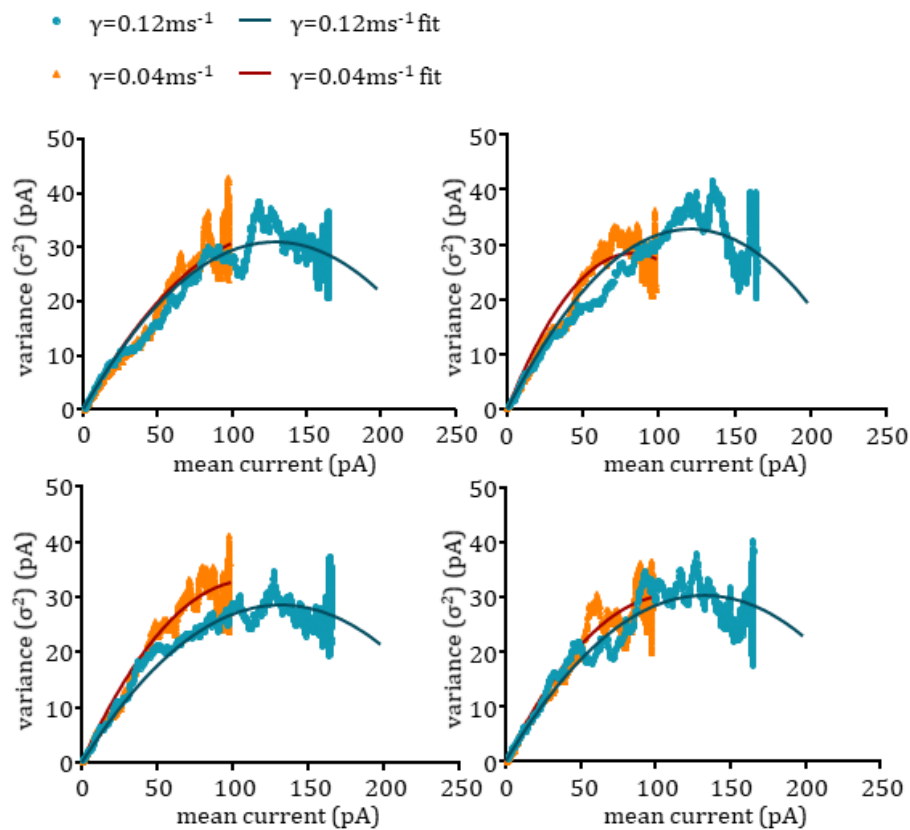


Figure 4.13. Graphs showing how the mean current and the variance change with decreasing P_{open} .

These graphs show the effect of reducing P_{open} on the variance and the mean current. $\gamma=0.12$ is shown in blue with the fit in dark blue, whilst $\gamma=0.04$ is shown in orange with the fit in dark red.

Simulations increasing γ to increase maximum P_{open} are shown in Figure 4.14 where the opposite of Figure 4.13 is seen. In Figure 4.14, the data points with γ of 0.12ms^{-1} are the same as those shown in Figure 4.13 whilst the orange data points are those returned with γ set to 0.20ms^{-1} with its fit line shown in dark red. The data here shows that by increasing the maximum P_{open} , the mean current increases relative to when γ is 0.12ms^{-1} and the orange data points again superimpose well over the dark blue fit line of the control data. This shows that the mean-variance plot is similar, but that the data continue to higher current values indicating a higher P_{open} . If a similar change in mean-variance profile was observed with $\Delta 2\text{-}26$ hEAG1 following the addition of $5\mu\text{M}$ I&T this would suggest that Ca^{2+} leads to an increase in maximum P_{open} .

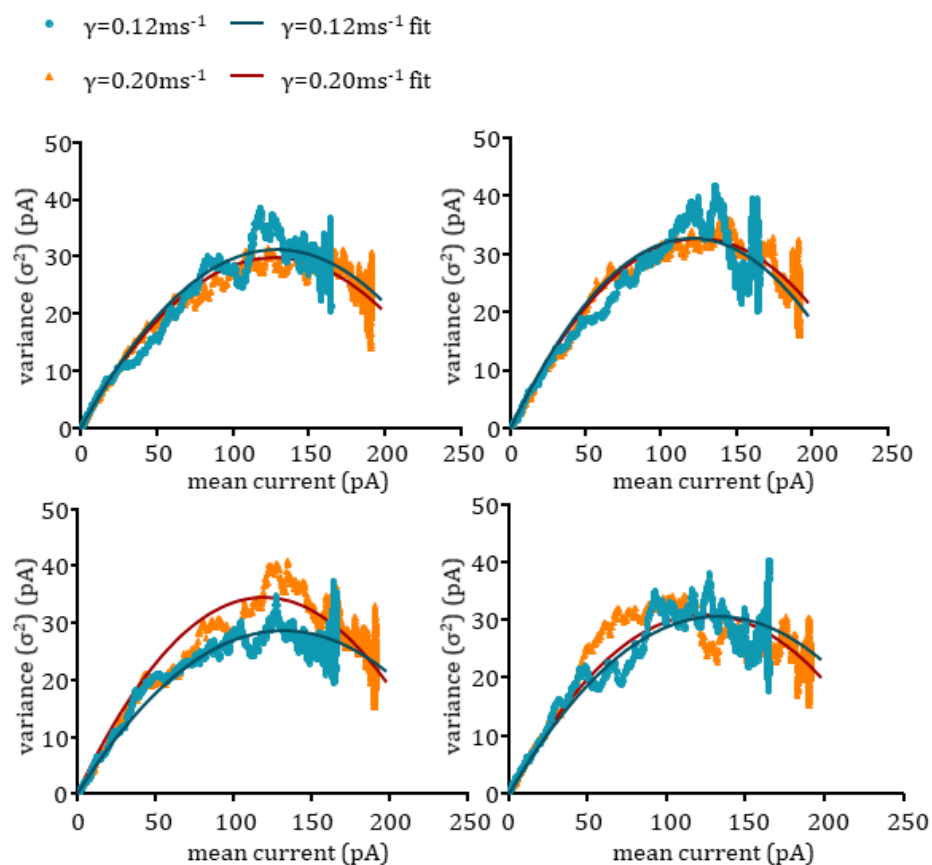


Figure 4.14. Graphs showing how the mean current and the variance change with increasing P_{open} .

These graphs show the effect of increasing P_{open} on the variance and the mean current. $\gamma = 0.12$ is shown in blue with the fit in dark blue, whilst $\gamma = 0.20$ is shown in orange with the fit in dark red.

Simulating a decrease in N was done in the same manner, N was simulated at both 500 and 50. The value of γ was maintained at 0.12ms^{-1} , i at 0.5pA and the number of sweeps at 200. A decrease in N produced a change in both the variance and the mean current (Figure 4.15). The data for $N = 50$ shows a reduced mean current and decrease in variance which is shown in the orange points and fitted with a dark red line. As expected, the control values where $N = 500$ have a much larger mean current and more variance. This simulation shows that if the reduction in current amplitude seen in the WT channel is caused by a reduction in N , the data should follow a similar trend as the simulation (Figure 4.15).

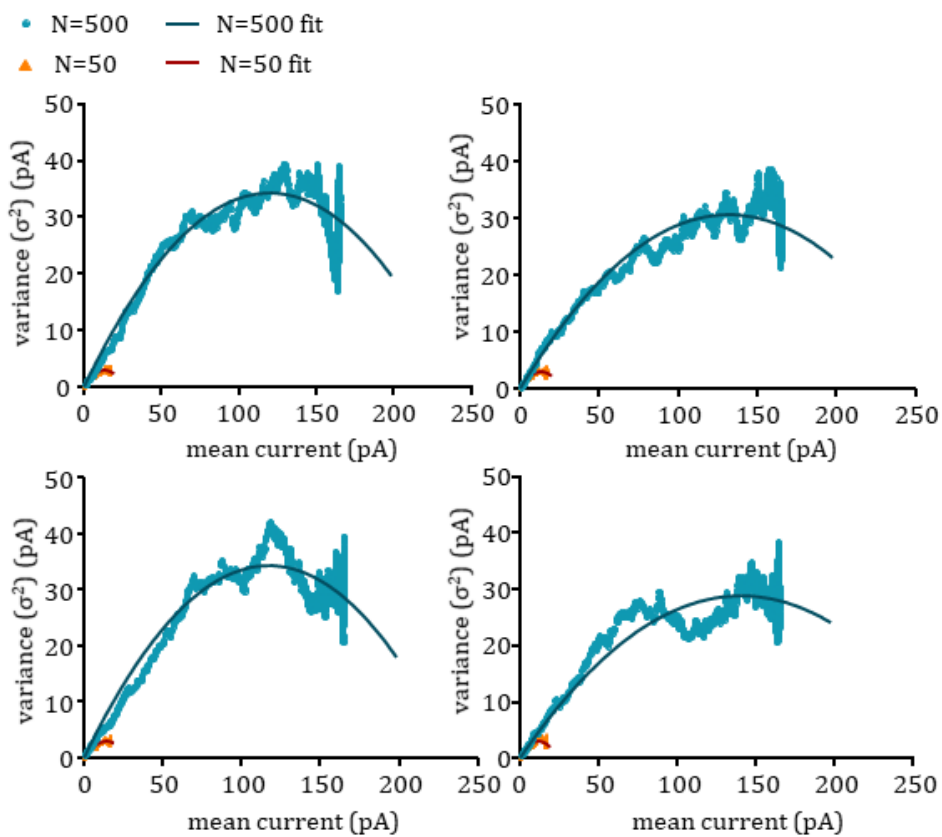


Figure 4.15. Graphs showing how variance data changes when N is reduced.

These graphs plot the mean current against the variance of simulated hEAG1 data. Here, the reduction in N is being tested, $N=500$ is shown in blue with its fit line in dark blue. $N=50$ is shown in orange and its fit line in dark red. Note how much smaller in both variance and current the line representing $N=50$ is.

Increasing N from 500 to 1000 and keeping all other variables constant showed an increase in the mean current and an increase in the variance (Figure 4.16). This would indicate that if the current potentiation seen with $\Delta 2$ -26 hEAG1 following 5 μ M I&T was down to an increase in N – perhaps via Ca²⁺ activated insertion of $\Delta 2$ -26 hEAG1 containing vesicles into the membrane – that both the variance and the mean current would be much larger than in control conditions as shown by Figure 4.16. Note that in both cases of N changing, the fit of data doesn't follow the same profile as the data produced by increasing or decreasing maximum changing P_{open}.

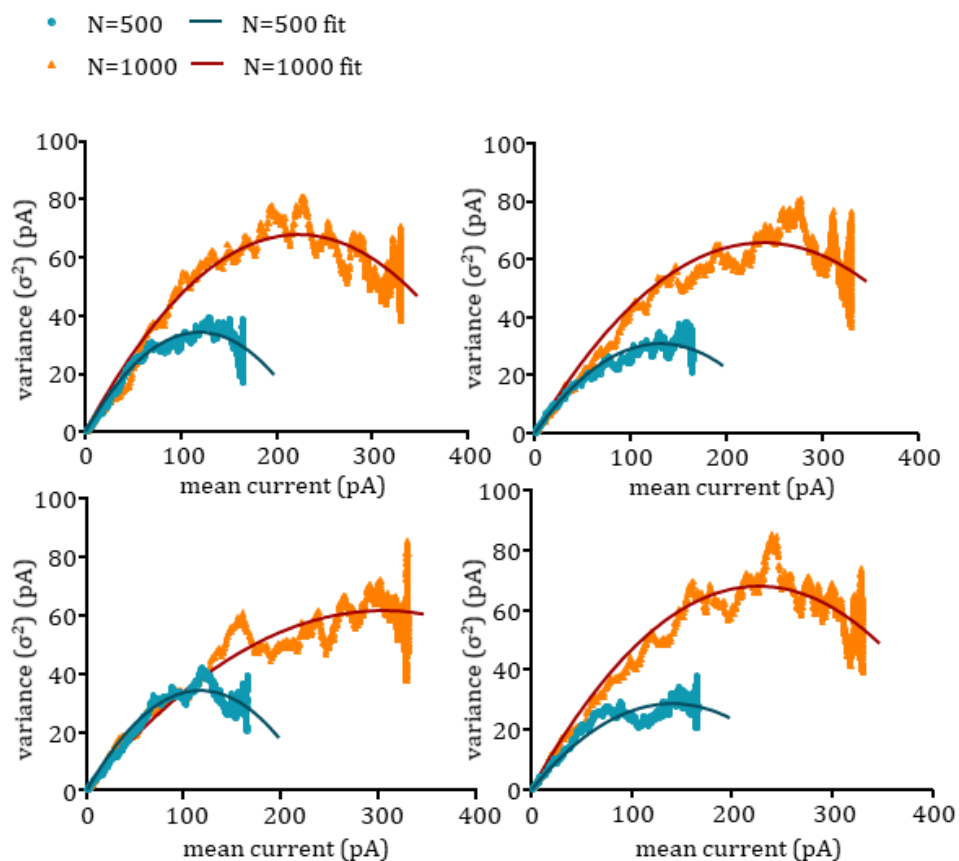


Figure 4.16. Graphs showing how variance data changes when N is increased.

These graphs plot the mean current against the variance of simulated hEAG1 data. Here, the increase in N is being tested, N=500 is shown in blue with its fit line in dark blue. N=1000 is shown in orange and its fit line in dark red. Note how much larger in both variance and current the line representing N=1000 is.

Simulations were also conducted to test the effect of changing i on the outcome of the noise analysis simulations. N was kept at 500, γ at 0.12ms^{-1} and the number of sweeps as 200. The value of i was tested at 0.5pA and either reduced to 0.25pA or increased to 0.75pA . When i was reduced from 0.5pA to 0.25pA both the variance and the mean current were reduced (Figure 4.17). The fit line for the control data does not align with the data for $i = 0.25\text{pA}$ and so differs from the reduction of P_{open} graphs (Figure 4.13). The *in silico* data provides a point of reference to compare the *in vitro* data to should the inhibition of WT hEAG1 current after application of $5\mu\text{M}$ I&T be down to a change in i .

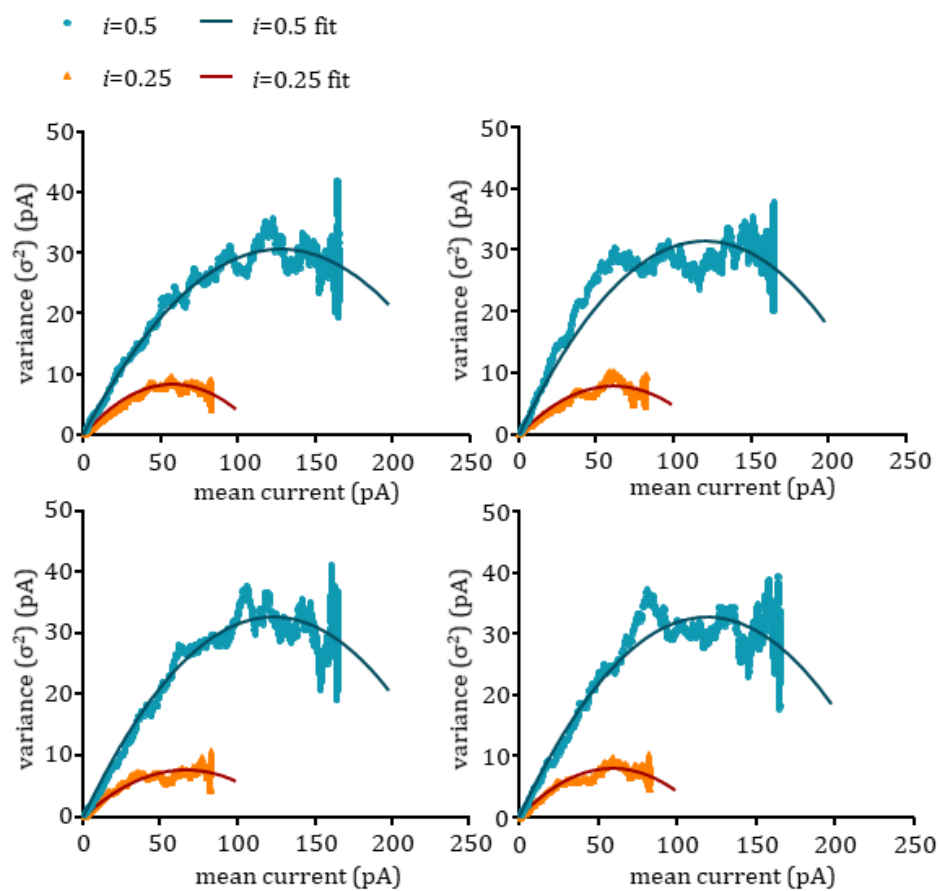


Figure 4.17. Graphs showing how the variance and mean current change upon reducing i .

These graphs demonstrate how reducing the value of i affects the mean current and the variance. The data for $i=0.5$ is shown in blue with the fit line shown in dark blue whilst the data for $i=0.25$ is shown in orange with the fit line shown in dark red.

When the value of i was increased from 0.5pA to 0.75pA, the mean current and the variance both increased with it (Figure 4.18). Similar to the simulations for decreasing i , the fit line of the control data doesn't follow the same trend as the $i = 0.75$ pA data unlike the change in P_{open} that followed the same fit line albeit right or left shifted (Figure 4.13 and Figure 4.14). This means that if the *in vivo* noise analysis data shows a change in i is behind the increase in $\Delta 2-26$ hEAG1 current that the graphs would bear similarity to those shown in Figure 4.18.

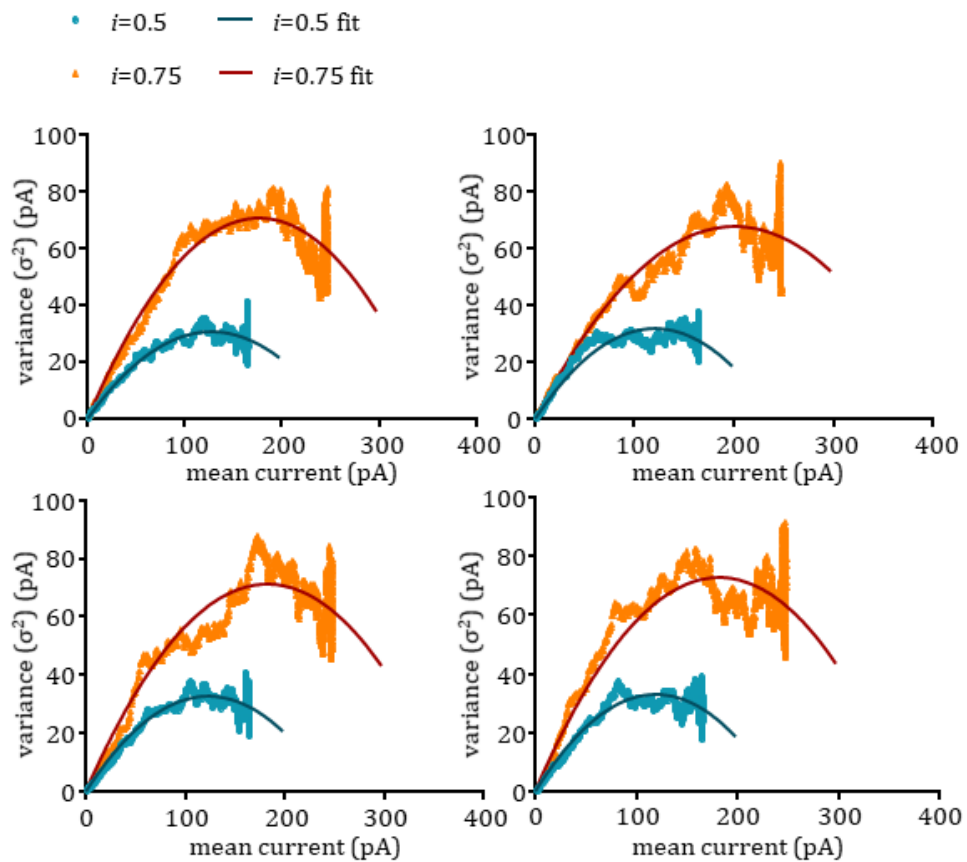


Figure 4.18. Graphs showing how the variance and mean current change upon increasing i .

These graphs demonstrate how increasing the value of i affects the mean current and the variance. The data for $i=0.5$ is shown in blue with the fit line shown in dark blue whilst the data for $i=0.75$ is shown in orange with the fit line shown in dark red.

4.1.3. Noise analysis of WT hEAG1 reveals 5 μ M I&T changes to N and P_{open}

WT hEAG1 currents measured with steady pulsing to +20mV were analysed using the Tracan3 software. Noise analysis data from 4 cells are shown plotted as mean current against variance. The maximal mean current following the addition of 5 μ M I&T is much lower than in control conditions, the maximum variance is also reduced (Figure 4.19). The data bares similarity to the simulation graphs representing a reduction in maximal P_{open} (Figure 4.13) because these too show a reduction in mean current and variance compared to the control simulation data.

The data for 5 μ M I&T sits well along the fit line for the control data, but the maximum mean current achieved is less compared to the control data (Figure 4.19). This indicates that there is a reduction in the P_{open} of the channels as the shape of the two conditions is similar to that shown by the simulation data where P_{open} was reduced (Figure 4.13). The noise analysis of WT hEAG1 currents implies that under high Ca²⁺ conditions there is a substantial reduction in P_{open}. There may also be a reduction in N, but additional experiments are needed to support this.

The software that calculates the fit of the data using Function 1 also provides estimates of the value of N and *i*. The value of N reduced by 41.7 \pm 8.6% which is a significant difference compared to control data (p<0.001, n=14). The mean value of *i* was actually increased from 0.73 \pm 0.07pA to 0.83 \pm 0.08pA, however this was not a statistically significant change (p>0.05, n=14).

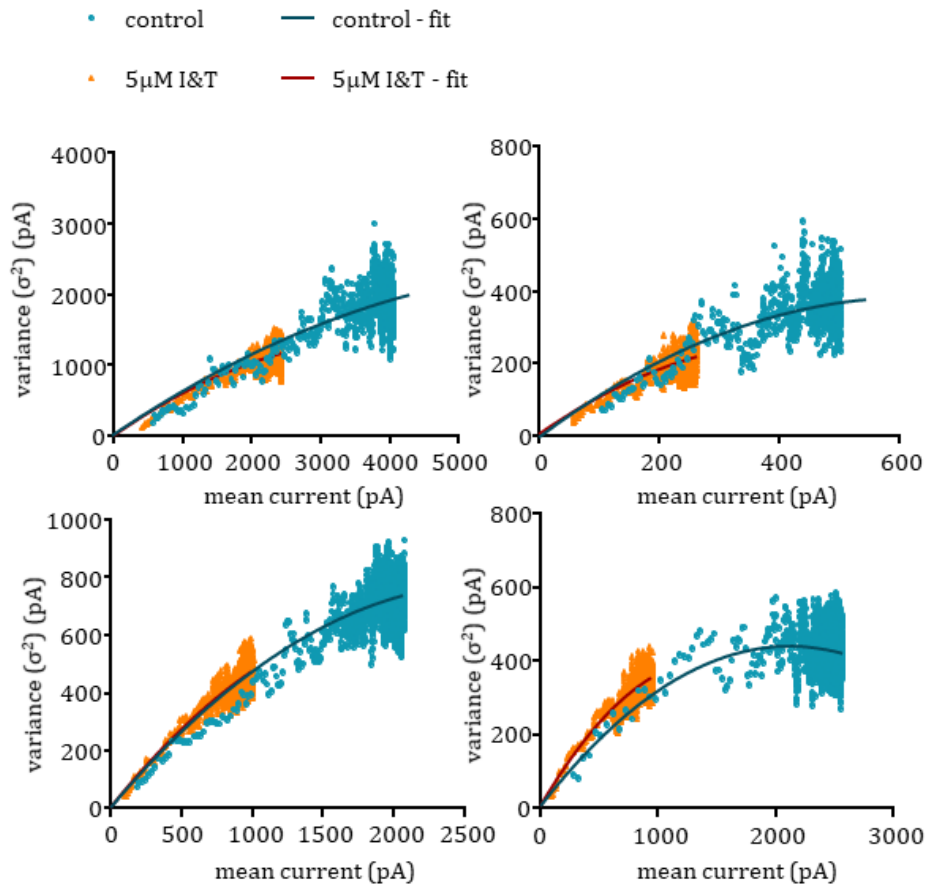


Figure 4.19. Mean-variance graphs showing how WT hEAG1 variance is affected by the addition of 5µM I&T.

These graphs show the control data (blue) against the data obtained from the same cell following the addition of 5µM I&T (orange). The mean current and the variance are both reduced in high Ca^{2+} conditions.

4.1.4. Noise analysis of $\Delta 2$ -26 hEAG1 shows that neither N or i are affected by $5\mu\text{M}$ I&T

$\Delta 2$ -26 hEAG1 currents elicited by repetitively stepping to +20mV were analysed for their variance. The mean current-variance relationship from the only quality recording of $\Delta 2$ -26 hEAG1 with $5\mu\text{M}$ I&T is shown in Figure 4.20. Here the data demonstrates a relationship similar to that of increasing P_{open} as shown in Figure 4.14.

Obtaining good quality data for the potentiation of $\Delta 2$ -26 hEAG1 proved difficult due to the component of instantaneous current that was often present during recordings once $5\mu\text{M}$ I&T was added. Due to this, more experiments are needed to draw well informed conclusions about how $5\mu\text{M}$ I&T affects current parameters.

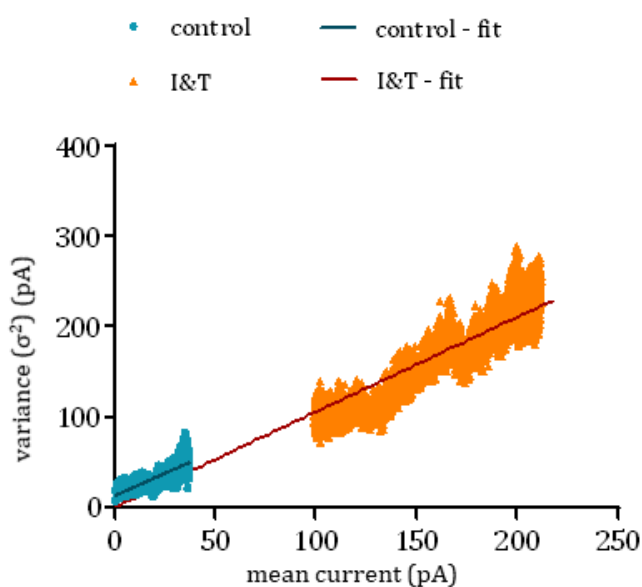


Figure 4.20. Noise analysis data of $\Delta 2$ -26 hEAG1 showing how the variance changes from control to $5\mu\text{M}$ I&T.

Variance is plotted against mean current data from a single good quality recording. Control data (blue) and $5\mu\text{M}$ I&T data (orange) were obtained by the same cell and data was fitted using function 1.

4.1.5. Surface expression assays show a reduction of WT hEAG1 expression but not of Δ 2-26 hEAG1 following 5 μ M I&T

Drawing conclusions from the noise analysis was problematic as it was difficult to distinguish between changes in N and i . As an alternative approach we investigated potential changes in N by measuring changes in the number of channels on the membrane surface. WT hEAG1 was tagged with a peptide for the α -bungarotoxin binding site (BBS). The BBS-tag was engineered between S3 and S4 on an extracellular loop and so was available to bind to extracellularly applied α -bungarotoxin (BTX) if the channel was localised to the plasma membrane. Comparison of the amount of BTX-labelled channel protein allowed measurements of channel surface expression to be made.

CHO cells transfected with WT hEAG1-BBS and Δ 2-26 hEAG1-BBS were exposed to BTX in control conditions or after application of 5 μ M I&T for 100 or 300s for WT hEAG1-BBS or 60 and 300s Δ 2-26 hEAG1-BBS. Fluorescent images of transfected CHO cells are shown in Figure 4.21. WT hEAG1-BBS surface expression is indicated by the level of BTX-conjugated to AlexaFluor-594. GFP fluorescence identifies plasmid transfected cells. DAPI fluorescence identifies the nuclei of all cells, included non-transfected cells. Only GFP expressing cells also showed AlexaFluor-594 fluorescence indicating specific BTX binding to the hEAG1-expressing cells.

The BTX fluorescence was reduced in its intensity from 8.7 ± 0.7 au to 5.6 ± 0.3 au following the 100s exposure, a reduction of $30.7 \pm 11.9\%$ ($p < 0.001$, $n=3$, no.of cells=40, Figure 4.22) compared to control cells.

The BTX fluorescent signal was also measured after 300s of exposure to 5 μ M I&T (Figure 4.22). Compared to control, the fluorescent signal had decreased from 8.7 ± 0.7 au to 6.4 ± 0.6 au, this was a reduction of $15.4 \pm 21.1\%$ and was again found to be a significant reduction from the control values ($p < 0.01$, $n=3$, no.of cells=52, Figure 4.22). There was no significant change in the fluorescent intensity between the 100s and 300s data indicating that the surface expression of WT hEAG1-BBS did not increase again following its initial decrease after 100s ($p > 0.05$).

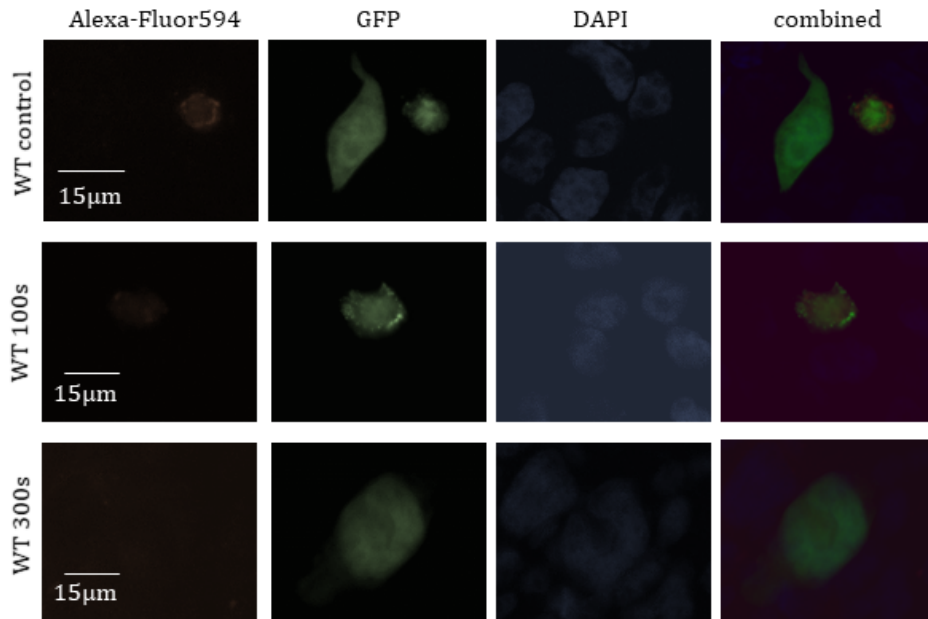


Figure 4.21. An image panel showing the change in α -BTX fluorescence following the addition of $5\mu\text{M}$ I&T for 100 and 300s.

This figure panel shows that the fluorescence of α -BTX decreases from control after 100s of $5\mu\text{M}$ I&T exposure. The fluorescence is also still reduced after 300s. The gene for GFP is present in the same plasmid as WT hEAG1 and therefore acts a marker of successfully transfected cells. DAPI was used to stain the cell nucleus.

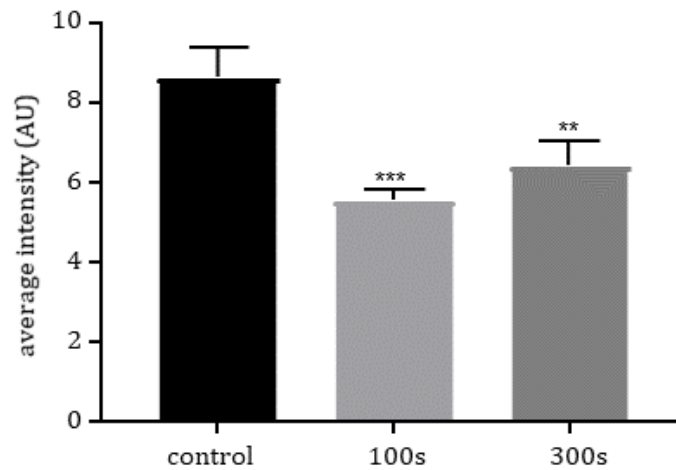


Figure 4.22. Data showing how the WT channel current and surface expression responds to $5\mu\text{M}$ I&T.

A bar chart showing how the average fluorescence intensity changed for BTX-surface labelled WT hEAG1 - BBS at 100s (peak inhibition) and 300s (peak recovery) (n=3).

A BBS-tagged version of the Δ 2-26 hEAG1 was generated for the purposes of surface expression. Fluorescent images of the transfected CHO cells are shown in Figure 4.23. BTX-AlexaFluor-594 was applied to cells in control solution and after being exposed to 5 μ M I&T for 60 and 300s (Figure 4.23).

After 60s of exposure to 5 μ M I&T the average BTX-AlexaFluor-594 fluorescent intensity had gone from 6.2 ± 0.6 au to 6.1 ± 0.4 au. This was a reduction in α -BTX fluorescence intensity of $7.3 \pm 16.3\%$ and was not statistically significant ($p > 0.05$, $n=3$, no.of cells=23, Figure 4.24). The fluorescence was also measured 300s after exposure to 5 μ M I&T, and when compared to control the fluorescence intensity had reduced to 5.7 ± 0.4 au which was a reduction of $2.3 \pm 22.4\%$. This reduction was also found to not be statistically significant ($p > 0.05$, $n=3$, no.of cells=45, Figure 4.24). These data suggest that the surface expression of Δ 2-26 hEAG1-BBS was not altered upon the application of 5 μ M I&T. This could be because there was no change in the numbers of surface located channels or there could be an alternate explanation.

It was noticed that the level of BTX-AlexaFluor-594 fluorescence was low in Δ 2-26 hEAG1-BBS transfected cells (Figure 4.23) raising the possibility that this construct was not expressed at all or expressed at low levels compared to WT hEAG1-BBS. To investigate functional expression, both constructs were characterised using whole cell patch clamp of CHO cells.

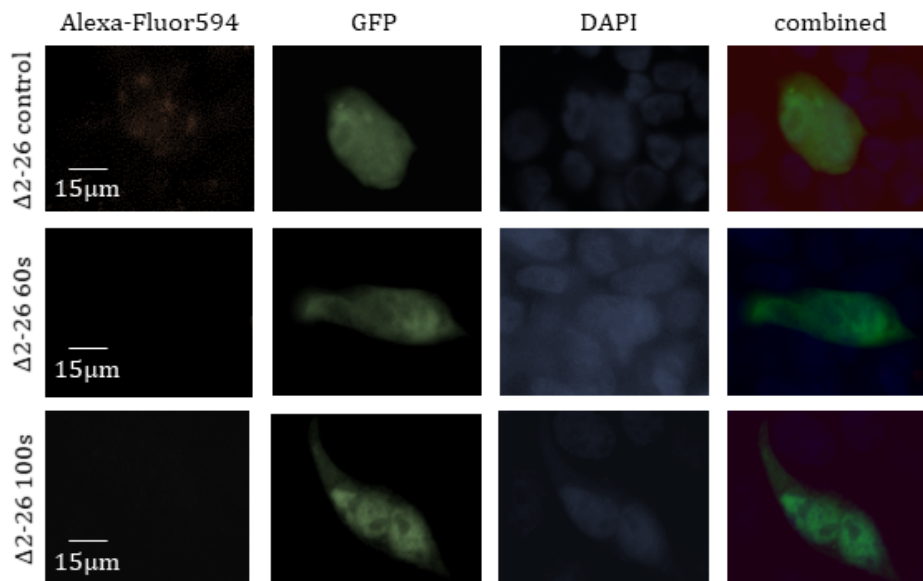


Figure 4.23. An image panel showing how the fluorescence of α -BTX changes after application of $5\mu\text{M}$ I&T for 60 and 300s to $\Delta 2$ -26 hEAG1-BBS expressing CHO cells.

This figures show how the fluorescence of bound α -BTX changes. The fluorescence is very difficult to see which may be down to low channel expression or slow rate of binding. It can still be measured using the Fiji software.

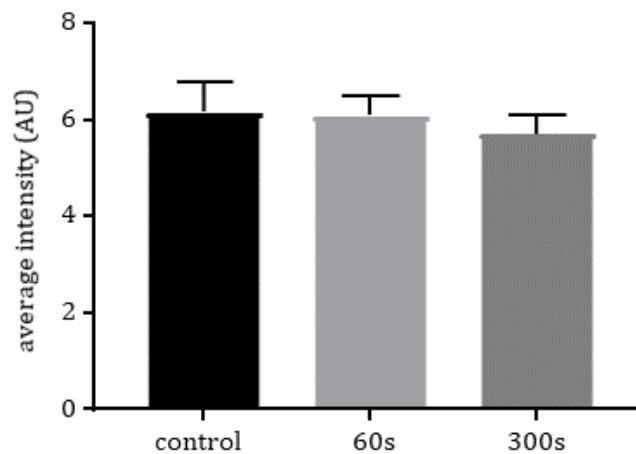


Figure 4.24. Data showing how the $\Delta 2$ -26 hEAG1 surface expression responds to $5\mu\text{M}$ I&T.

A bar chart showing how the average fluorescence intensity changed for BTX-surface labelled $\Delta 2$ -26 hEAG1 – BBS at 60s (peak potentiation) and 300s (peak recovery).

4.1.6. WT hEAG1-BBS, but not Δ 2-26 hEAG1-BBS, is expressed and functional in CHO cells

The WT hEAG1-BBS construct was expressed in CHO cells for whole cell patch clamp measurements of current to ensure the tagged channel behaves in the same as the WT channel both in control conditions and under high Ca^{2+} conditions. In control solution the currents in response to the I/V protocol were similar to that of the untagged channel. WT hEAG1-BBS current had an activation time course from 10-80% of $183.5 \pm 40.0\text{ms}$ which was not significantly slower than the untagged channel ($p > 0.05$, $n=4$, Table 2, Figure 4.25a.).

The mean normalised I/V relationships compare the response of WT hEAG1 and WT hEAG1-BBS to increasing voltage. The BBS-tagged channel current is left shifted compared to the untagged channel current (Figure 4.25c).

The G/V curves show that the BBS-tagged channel current activates at much more negative membrane potentials than the untagged channel current (Figure 4.25d). The $V_{0.5}$ value for WT hEAG1-BBS was $21.3 \pm 4.4\text{mV}$ which is significantly more negative than that of the untagged channel current which was $37.2 \pm 3.0\text{mV}$ ($p < 0.05$, $n=4$, Table 2.). The k value is $17.2 \pm 1.6\text{mV}$ which is higher than the untagged channel which was $10.3 \pm 0.6\text{mV}$ ($p < 0.001$, $n=4$, Table 2.). This data indicates that the BBS-tagged channel is well expressed responds in a voltage dependent manner, but that the voltage dependence is affected by the presence of the extracellular binding site on the voltage sensor.

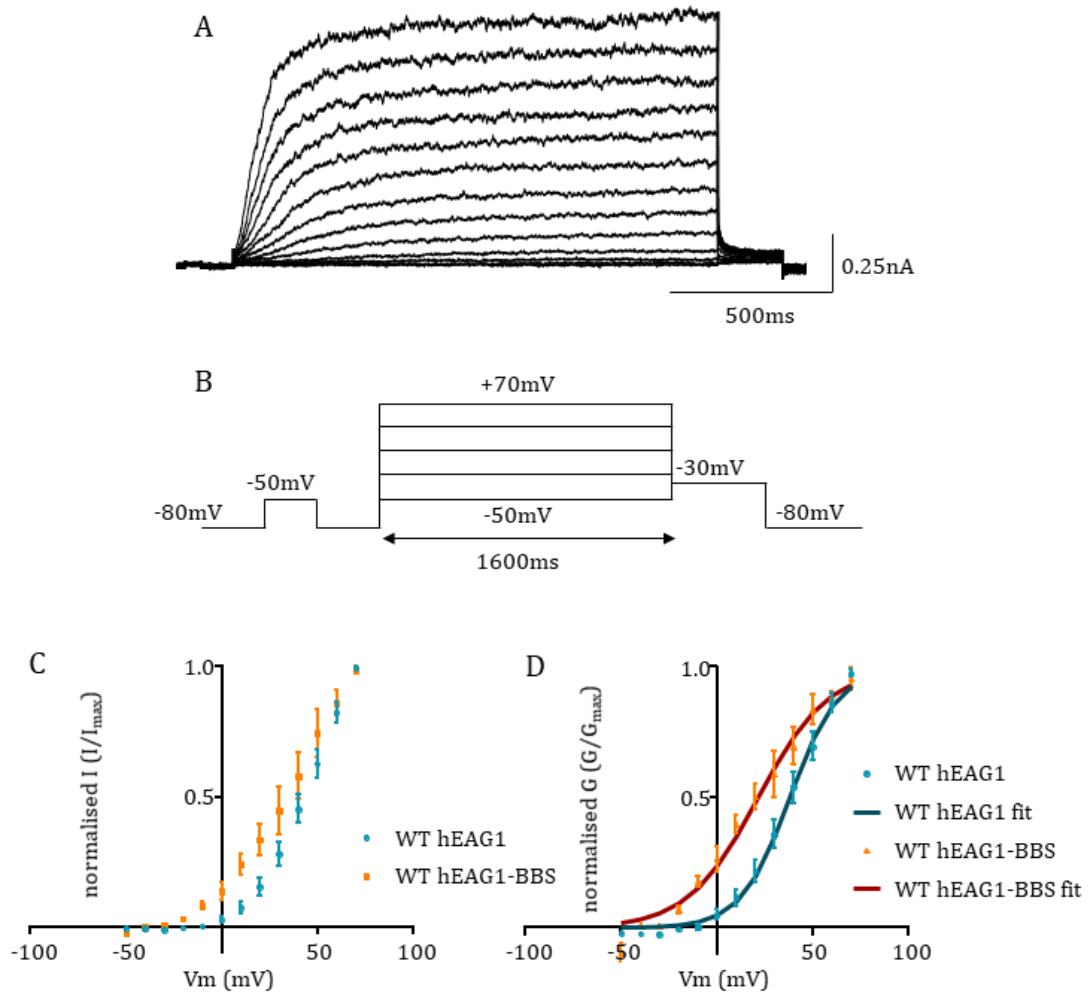


Figure 4.25. Data showing the response of WT hEAG1-BBS to the I/V protocol in control solution when expressed in CHO cells.

A: currents elicited from WT hEAG1-BBS CHO cells when using the I/V protocol shown in B. Current amplitudes reach a steady state plateau and increase in amplitude with each depolarising step.

B: the I/V protocol used in CHO cells and has been previously described in Figure 4.2.

C: I/V curves showing the relationship between current and voltage for both WT hEAG1 (blue) and WT hEAG1-BBS (orange). WT hEAG1-BBS passes more current between -20mV and +50mV than the WT channel.

D: G/V curves showing how the conductance for each channel changes with voltage. WT hEAG1-BBS (orange) activates at more negative potentials than the WT channel (blue). Data are fitted with a Boltzmann function (dark red and dark blue respectively).

WT hEAG1-BBS expressing cells were also exposed to 5 μ M I&T to measure the response of the current amplitude over time. The current gradually reduced in amplitude from control levels (Figure 4.26a). The current was inhibited by $62.6 \pm 8.1\%$ from control which was not a significant reduction ($p > 0.05$, $n = 4$). This behaviour is similar to the untagged channel, including the lack of a recovery phase (Figure 4.26b). However since the inhibition was not significant more data are needed as many of the recordings did not last the full 300s of 5 μ M I&T application.

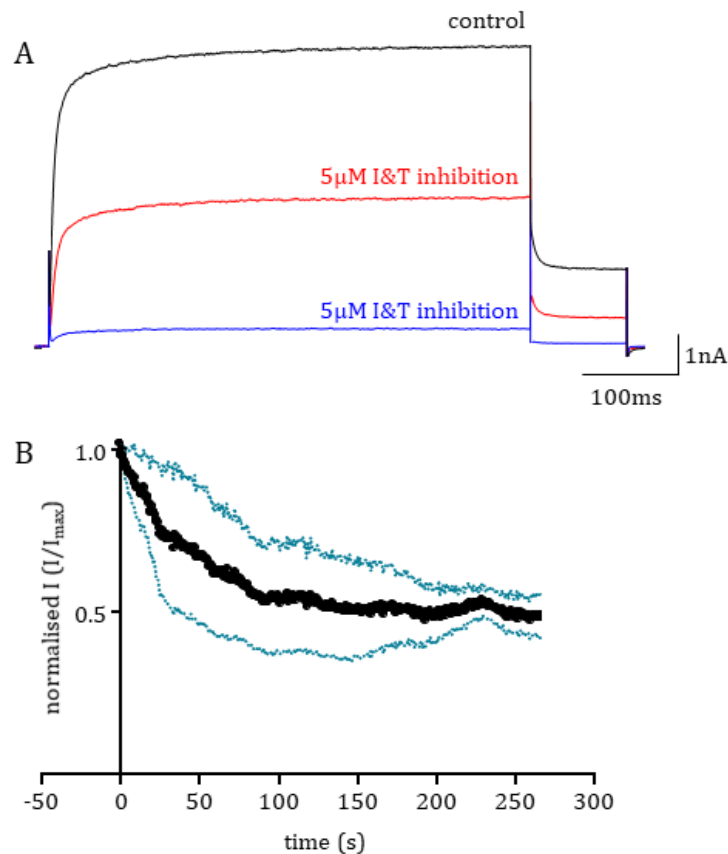


Figure 4.26. Steady pulsing data showing the response of WT hEAG1-BBS to 5 μ M I&T over time.

A: these current traces show the response of WT hEAG1-BBS to high Ca²⁺ conditions. The current is shown in control (black), 200s after exposure to 5 μ M I&T (red) and after 300s (blue). The BBS-tagged channel also doesn't show a recovery phase as the WT channel did in the oocytes.

B: this graph shows how the current amplitude changes over time following the application of 5 μ M I&T at t=0. The current gradually reduces over time. Error bars are shown as blue dots ($n = 4$).

There was a variety of responses to 5 μ M I&T in terms of current amplitude and time course of inhibition. Some cells were inhibited at a consistent rate as shown by the black dots (Figure 4.27). Others were initially inhibited more quickly but then proceeded to oscillate in amplitude over time as shown by the orange dots (Figure 4.27). Some cells, as shown by the blue dots (Figure 4.27), were inhibited quickly after the addition of 5 μ M I&T but plateaued in their current amplitude for the duration of the recording. This indicates that the BBS-tagged channel has a less reproducible response to high Ca²⁺ conditions.

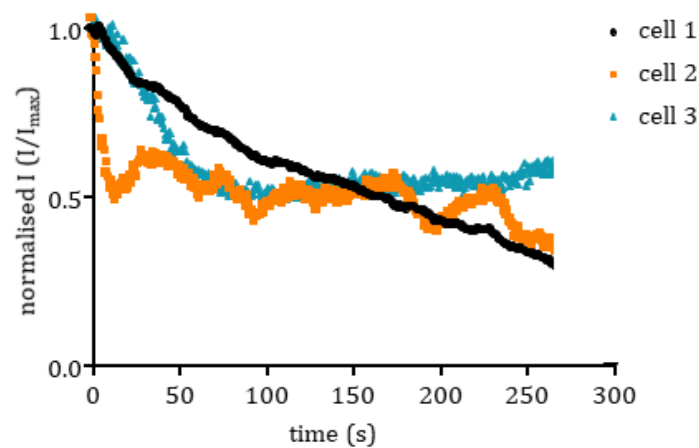


Figure 4.27. Steady pulsing data showing how some individual cells expressing WT hEAG1-BBS responded to 5 μ M I&T.

This graphs shows the variety of responses in current amplitude to 5 μ M I&T. The current in cell 1 (black) gradually decreased in amplitude for \sim 250s. Currents from cell 2 (orange) decreased quickly before oscillating for the majority of the recording. Meanwhile the current from cell 3 (blue) decreased initially before plateauing and increasing again very slightly towards the end of the recording.

The $\Delta 2-26$ hEAG1-BBS construct was also expressed in CHO cells to see how the currents responded to both voltage and $5\mu\text{M}$ I&T. The channel did express in CHO cells and produced measurable currents under the I/V protocol (Figure 4.28). The currents appear to activate slowly, but do not show any rectification at positive potentials unlike what was seen in the untagged $\Delta 2-26$ hEAG1 channel (Figure 4.28). Currents were not observed until the voltage reached -10mV (Figure 4.28c). The channels activate with a time course of $695.9 \pm 183.5\text{ms}$ at $+60\text{mV}$ which is similar to that of the untagged channel ($p > 0.05$, $n=4$, Table 2.).

The mean normalised I/V curves show that the tagged channel does not show the rectification feature and instead continues to increase its current amplitude with the increasing voltage (Figure 4.28c). The G/V curve shows that the BBS-tagged channel starts to activate at more positive membrane potentials than the untagged channel (Figure 4.28d). The $V_{0.5}$ value for $\Delta 2-26$ hEAG1-BBS was $29.2 \pm 3.5\text{mV}$ whereas the $V_{0.5}$ value for $\Delta 2-26$ hEAG1 is negative ($p < 0.0001$, $n=4$, Table 2.). The k value is $20.0 \pm 1.9\text{mV}$ which is much larger than the value of the untagged channel ($p < 0.01$, $n=4$, Table 2.). This data indicates that the addition of the BTX binding site affects the voltage dependent properties of the $\Delta 2-26$ hEAG1 channel.

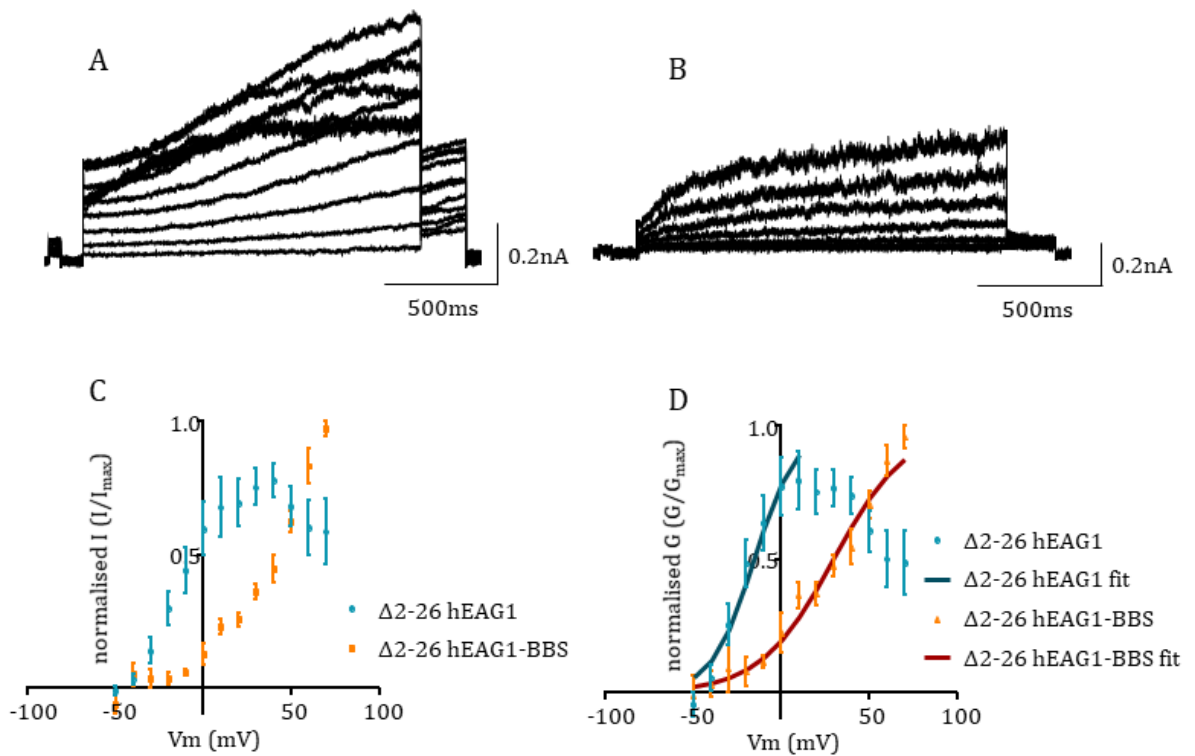


Figure 4.28. Data showing the response of $\Delta 2-26$ hEAG1-BBS to the I/V protocol.

A: current traces elicited from the untagged $\Delta 2-26$ hEAG1 channels in CHO cells. These currents have been previously described in Figure 4.7.

B: currents elicited from $\Delta 2-26$ hEAG1-BBS expressing CHO cells in response to the I/V protocol. These currents do not appear to activate at the same rate as the untagged channel shown in A. Currents from $\Delta 2-26$ hEAG1-BBS also do not rectify at positive membrane potentials as the untagged channel does (C).

C: this is an I/V graph showing the relationship each channel's current has with voltage. Whilst the untagged $\Delta 2-26$ hEAG1 channel (blue) passes more current across most potentials (-30mV to +50mV) it then reduces in amplitude with further depolarisations. $\Delta 2-26$ hEAG1-BBS (orange) passes less current but increases in amplitude with each depolarisation, a characteristic that is more similar to the WT hEAG1 channel.

D: this G/V graph shows that $\Delta 2-26$ hEAG1-BBS (orange) activates at more positive potentials than $\Delta 2-26$ hEAG1 (blue) and does not reduce in conductance at positive potentials as the $\Delta 2-26$ hEAG1 channel does. Data are fit with Boltzmann functions (dark red and dark blue respectively).

$\Delta 2-26$ hEAG1-BBS was also exposed to $5\mu\text{M}$ I&T to see how the current amplitude responds to high Ca^{2+} conditions. The mean current amplitude did not change upon addition of $5\mu\text{M}$ I&T (Figure 4.29a). Currents were measured for $>300\text{s}$ and the current amplitude varied around control and so the percentage change was not measured (Table 2.). This is a different response compared to cells expressing the untagged channel, which showed a large potentiation of the current after the application of $5\mu\text{M}$ I&T. This lack of a response to high Ca^{2+} may be why surface expression did not respond to $5\mu\text{M}$ I&T.

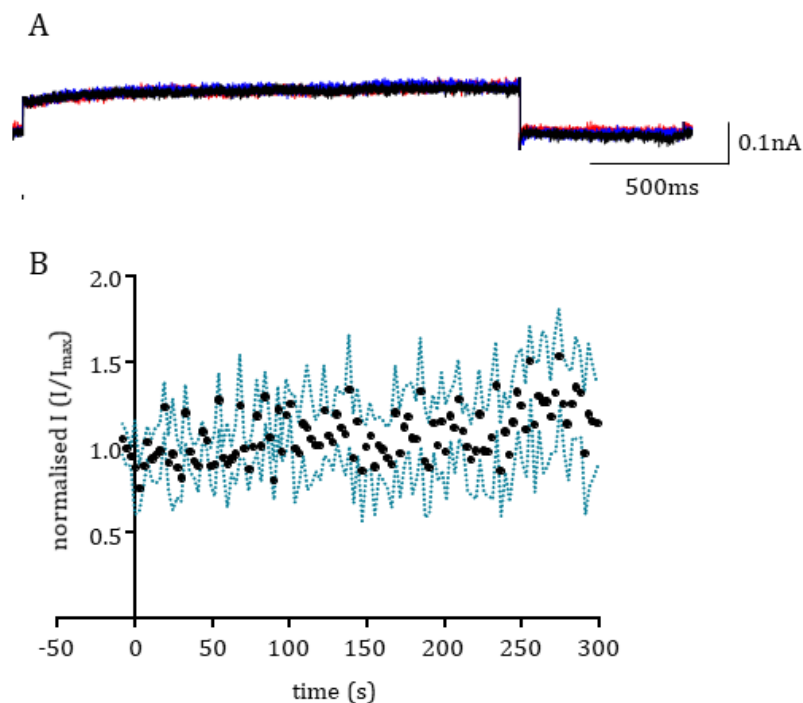


Figure 4.29. Steady pulsing data showing how $\Delta 2-26$ hEAG1-BBS responds to the addition of $5\mu\text{M}$ I&T.

A: representative current traces show that $\Delta 2-26$ hEAG1-BBS does not increase its current following the application of $5\mu\text{M}$ I&T at $+20\text{mV}$. The current in control is shown in black, and the current at two time points following the application of $5\mu\text{M}$ I&T are shown in red and blue although these are difficult to see as they are the same amplitude as control.

B: this graph shows how the current amplitude changes over time following the addition of $5\mu\text{M}$ I&T at $t=0$ ($n=3$). Current amplitudes were small giving rise to the variability seen.

The responses in single cells from the steady pulsing experiments showed that there was a variety of responses to the 5 μ M I&T. Some cells gave current that slowly increased in amplitude throughout the recording as shown by the black dots (Figure 4.30). Other cells had more of an erratic behaviour with no trend in their current amplitude but rather oscillations around their control amplitude as shown by the blue and orange dots (Figure 4.30).

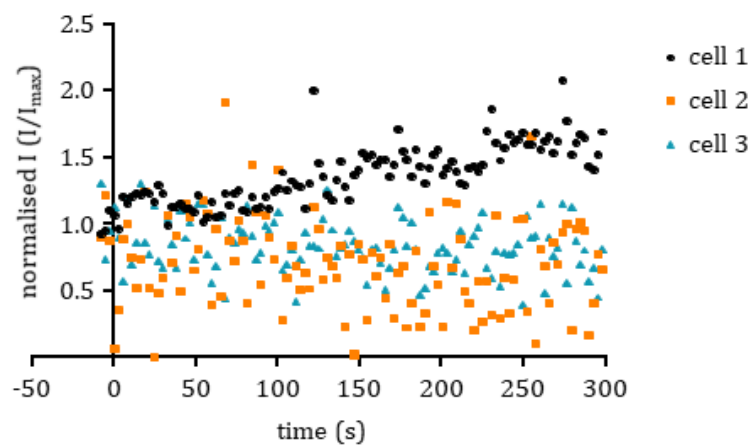


Figure 4.30. Steady pulsing data showing how different cells expressing Δ 2-26 hEAG1-BBS responds to the addition of 5 μ M I&T.

Current amplitudes plotted over time following the application of 5 μ M I&T for three different CHO cells expressing Δ 2-26 hEAG1-BBS.

Constructs	% change in I&T	V _{0.5} (mV)	k value (mV)	10-80% activation (ms)
WT hEAG1	78.6 ± 5.8 ***	37.2 ± 3.0	10.3 ± 0.6	158.5 ± 40.6
WT hEAG1-BBS	62.6 ± 8.1	21.3 ± 4.4 *	17.2 ± 1.6 ***	183.5 ± 40.0
Δ2-26 hEAG1	349.4 ± 304.9	-19.1 ± 4.3	9.4 ± 1.2	622.4 ± 65.2
Δ2-26 hEAG1-BBS	n/a	29.2 ± 3.5 ****	20.0 ± 1.9 **	695.9 ± 183.5

Table 2. A table showing the measured parameters of the WT hEAG1 channel along with 4 tested mutants using whole cell patch clamp.

This table shows the parameters measured in CHO cells from the expressed constructs. The percentage change following the addition of 5μM I&T is calculated from the steady pulsing data and were all measured at +20mV. Values highlighted in red are mutants that potentiated their current after 5μM I&T. The V_{0.5} and k values were measured from the Boltzmann fits of the G/V curves and are both expressed in mV. The 10-80% activation time course was measured at +60mV and is measured in ms. Statistical comparisons are done at WT hEAG1 vs WT hEAG1-BBS and Δ2-26 hEAG1 vs Δ2-26 hEAG1-BBS. All values are presented as mean ± SEM and significance is indicated by the asterisks (* is <0.05, ** is <0.01, *** is <0.001, **** is <0.0001).

4.2. Discussion

4.2.1. The PAS-cap likely influences the Popen of the hEAG1 channel

WT hEAG1 and the mutant Δ 2-26 hEAG1 currents have opposite responses to I&T. In oocytes, WT current is inhibited $85.5 \pm 2.9\%$ from control (n=10) whilst that of the Δ 2-26 hEAG1 is potentiated by $1272.7 \pm 197.1\%$ (n=3). As previously stated the whole cell current measured in the oocytes is comprised of single channel current (i), open probability (P_{open}) and the number of available channels (N), which means that the reduction or increase in current is caused by a change in one or more of these parameters. WT hEAG1 has a small single channel conductance of around 4.9pS which makes accurate single channel recordings challenging (Bruggemann *et al.*, 1993). Taking this into account and the fact that with the WT channel we could potentially be looking for a further reduction in single channel activity, we decided to study channel properties using non-stationary noise analysis.

Ion channel behaviour is stochastic in nature and the three variables that produce whole cell currents vary depending on the stimulus (Alvarez *et al.*, 2002). The two channels were studied in the mammalian CHO cell model as currents produced by the oocytes are too large and analysis of the noise would be more difficult. Both channels were functional in the CHO cells and gave currents that were similar to their oocyte counterparts. WT hEAG1 was inhibited by 5 μ M I&T by $78.6 \pm 5.8\%$ but this occurred with a slower time course in the CHO cells than in the oocytes which may be explained by a difference in cell background between the amphibian and mammalian systems. Studies on many ion channels have shown that they can be modulated differently between expression systems. For example the voltage dependent gating of the Na_v1.4 channel is modulated by the β 1 subunit in the mammalian system but is unaffected by the same subunit in oocytes (Lukács *et al.*, 2009). This provides evidence that ion channels are not necessarily regulated in the same way in different expression systems and may also explain why the $V_{0.5}$ and k values are different for the WT channel. One of the simplest explanation is that the intracellular Ca²⁺ responses to 5 μ M I&T are different in CHO cells and oocytes and this is investigated in the next chapter.

The $\Delta 2-26$ hEAG1 channel showed a potentiation of its current of $349.4 \pm 304.9\%$ in CHO cells which was not a significant change over control levels. This was an interesting finding but the data were variable from cell to cell. Some cells showed a large potentiation while others did not. Since the change in channel behaviour was different between cells it suggests that the Ca^{2+} responses of individual cells was variable. This will be discussed in detail in the next discussion chapter. Only cells resulting in a potentiation were considered for noise analysis.

The noise analysis programme used requires the user to input estimated values for i and N , once the data are fitted the programme then calculates values for that gave the best fit of the data. These estimates were averaged and analysed statistically to find any differences between control and $5\mu\text{M}$ I&T conditions. The WT channel data suggested that N decreases by $41.7 \pm 8.6\%$ which was found to be significant compared to control. The overlay of the mean current-variance plots show that the $5\mu\text{M}$ I&T data sits to the left of the control data, which suggests a reduction in P_{open} . Since P_{open} cannot be directly measured from noise analysis another way to analyse this would be the use of inside-out patches to obtain single channel data. As previously stated the single channel conductance of hEAG1 is small and so this would be a difficult approach requiring a cell line with minimal endogenous currents, although CHO cells are preferred over HEK293 cells for K^+ channel expression (Yu and Kerchner, 1998). It would also need ensuring there was minimal external noise input so that the small channel conductance could be seen. Test voltages furthest away from E_{K} would also encourage larger single channel currents as there would be a larger driving force for the K^+ ions.

Noise analysis from the $\Delta 2-26$ hEAG1 currents, were different in each cell investigated. There are no significant changes in N or i when $5\mu\text{M}$ I&T is applied, although only the best data was presented. However the overlay of the data indicates that there may be an increase in P_{open} and that this is what drives the large potentiation of the current. It is difficult to draw conclusions from the noise analysis of $\Delta 2-26$ hEAG1 currents because we did not obtain enough good quality data. This was in part due to the instantaneous current caused by the slowed deactivation kinetics. To try and resolve this, we used a negative tail potential between -120mV and -160mV to increase the rate of deactivation. However this came with its own

problem in that such negative potentials often caused the membrane seal to become unstable or even lost completely which impacted the amount and the quality of the data we could collect.

4.2.2. The large current inhibition caused by 5 μ M I&T can be partly explained by a reduction in surface localisation of channels

The noise analysis data suggested that the decrease in WT hEAG1 current amplitude following 5 μ M I&T could be partly explained by a decrease in surface expression. I.e. a decrease of N due to channel moving out of the plasma membrane or becoming non-functional (silent). In order to study this a specialised hEAG1 construct was used, WT hEAG1-BBS, that contained an α -bungarotoxin binding site on the S3 and S4 linker on the extracellular side of the membrane.

The surface expression assays were conducted in CHO cells. Addition of 5 μ M I&T for either 100s or 300s for the WT construct showed that there was a significant reduction in the surface expression of WT hEAG1-BBS compared to untreated control cells. This suggests that a reduction in surface expression is at least part of the mechanism behind the reduction in current amplitude. Surface expression of metabotropic glutamate receptors (mGluRs) in neurons has been shown to be regulated by Ca²⁺-calmodulin binding and that the binding of Ca²⁺-calmodulin to these receptors also influences the internalisation of associated AMPA receptors (Choi *et al.*, 2011). Another study showed that calmodulin internalised the K_{ATP} channel via activation of CaMKII and phosphorylation of the channel's pore forming subunits, resulting in internalisation in a dynamin-dependent manner (Sierra *et al.*, 2013). dEAG1 has previously been shown to activate and be regulated by CaMKII in neurons but this resulted in an increase in the current indicating that the internalisation of dEAG1 is not due to CaMKII activation (Sun *et al.*, 2004; Wang *et al.*, 2002). This shows that calmodulin regulates the surface expression of other ion channels and the internalisation of hEAG1 may be due to the interaction of calmodulin in a larger network as is the case with the AMPA receptors but not a likely direct effect from CaMKII.

4.2.3. The BBS peptide insert alters the functional properties of hEAG1 channels

Kohl *et al.* (2011) found that when expressed in oocytes, the voltage dependence of activation of the WT hEAG1-BBS currents are leftward shifted compared to the untagged WT channel current with $V_{0.5}$ values for activation of -54mV and -26mV respectively, whilst the k values were unchanged. This indicates that the voltage dependence of the channel is substantially affected by the presence of the BBS site. Our CHO cell results show a similar pattern with $V_{0.5}$ as Kohl *et al.* (2011) in the oocytes, with $V_{0.5}$ values of 21.3 ± 4.4 mV and 37.2 ± 3 mV for WT hEAG1-BBS and WT hEAG1 respectively. However we show that the k value is also significantly different between the two constructs when studied in CHO cells (10.3 ± 0.6 and 17.2 ± 1.6 for the untagged and tagged channel respectively).

However, the main interest of the patch clamp experiments was to determine whether WT hEAG1-BBS and $\Delta 2-26$ hEAG1-BBS currents in CHO cells share the same response to 5 μ M I&T as their untagged counterparts. The WT hEAG1-BBS currents in CHO cells were inhibited quickly and did not show a recovery phase. This was consistent with the surface expression assay, where there was a reduction in surface expression compared to control but no change between 100s and 300s; suggesting that there was no re-introduction of the channels back into the membrane. However, vesicles arising from plasma membrane endocytosis can be acidic and vary in pH from 4.9 to 6 in CHO cells (Yamashiro and Maxfield, 1987). The quenching of the fluorophore or dissociation from the BBS-tagged channel during the internalisation phase and re-insertion into the membrane cannot be ruled out.

The $\Delta 2-26$ hEAG1-BBS construct behaved notably differently when compared to its untagged counterpart in CHO cells. The $\Delta 2-26$ hEAG1-BBS currents showed positive shifts in the voltage dependence of activation and there was no current rectification behaviour that is such a characteristic feature of the original $\Delta 2-26$ hEAG1 mutant. More importantly, the $\Delta 2-26$ hEAG1-BBS current is not sensitive to elevated intracellular Ca^{2+} . This data indicates that the insertion of the BBS tag in the extracellular loop between S3 and S4 transmembrane domains is having an effect on the passage of current through the pore due to effects on the voltage sensor and also on Ca^{2+} -calmodulin regulation. Whilst there is no structure available of WT hEAG1 with the BBS tag it is interesting to speculate that the

addition of the BBS tag causes a structural rearrangement of the transmembrane domains themselves or that S3/S4 moves from their original positions or has altered coupling with the activation gate. There is some controversy in the hEAG/hERG field about how the PAS-cap regulates channel function. Some studies previously showed it lying between the EAG domain and the cNBHD whilst some argued it interacted with the intracellular S4-S5 linker (Lorinczi *et al.*, 2016; Haitin *et al.*, 2013; Li *et al.*, 2010). More recently the cryo-EM structure of hEAG1 shows that – at least in the calmodulin bound channel – the unstructured region of the PAS-cap may be reaching up towards the transmembrane domains (Whicher and MacKinnon, 2016). The full structure of the PAS-cap was unfortunately not resolved with residues 1-10 missing from the structure. However we can still draw some conclusions, now we have evidence that an extracellular tag between S3 and S4 causes the $\Delta 2-26$ hEAG1 channel to behave more like the WT channel in terms of its response to membrane potential. Hypothetically when the PAS-cap is present it could be interacting with the transmembrane domains in such a way as to stabilise the open conformation and prevent inactivation. When the PAS-cap is removed they are not held in the correct position anymore relative to other domains of the channel and allow inactivation to occur. The presence of the extracellular BBS tag could be acting to hold the transmembrane domains back in a position similar to that when the PAS-cap is present thus giving some insight into where the PAS-cap is acting within the structure.

The $\Delta 2-26$ hEAG1-BBS current was not potentiated by 5 μ M I&T meaning that an extracellular tag is influencing the interaction of the channel with an intracellular ligand. This suggests an interplay between the voltage sensor and the EAG/cNBHD complex, this could be mediated by the C-linker that coordinates the activation gate. Further experimentation is needed to show that the C-linker couples the voltage sensor to the binding of Ca²⁺-calmodulin.

5. Results and Discussion – Are the intracellular domains involved in hEAG1’s role in cancer?

5.1. hEAG1 is well documented as an oncogenic K⁺ channel

WT hEAG1 has been shown numerous times to be involved in the increase in proliferation of different cell types as well as reduced rates of survival of patients with hEAG1-positive tumours. Blockers of hEAG1 have also been used to show they reduce the rate of proliferation indicating that WT hEAG1 at least is involved in the proliferation side of cancer (Pardo *et al.*, 1999).

The aims of this chapter were to investigate whether the Ca²⁺-sensitivity of the channel or its intracellular domains were important for its role in proliferation. The same question was asked of the primary cilia. Sanchez *et al.* (2016) showed that the presence of WT hEAG1 induced disassembly of the primary cilia in hTERT-RPE1 cells. It is not known if the intracellular domains or the channel’s Ca²⁺ sensitivity are important for its role in this process so this was also tested.

5.1.1. ΔEAG hEAG1 and E600R hEAG1 reduce the proliferation of transfected CHO cells in a BrdU assay

There is currently no clear mechanism for how WT hEAG1 increases proliferation. hEAG1 mutants were selected to test two hypotheses. 1, the Ca²⁺ sensitivity of the channel is important and 2, specific intracellular domains (EAG domain or cNBH domain) are involved in this process. To test these hypotheses, mutants that alter the Ca²⁺ sensitivity of hEAG1 through a mechanism involving intracellular domains were expressed and their effects on proliferation measured with a BrdU incorporation assay.

8 constructs were chosen for the assay. pXoon is the vector containing the gene for GFP and the promoter sequence for expression of hEAG1 and was used as a negative control. WT hEAG1 was included as a positive control. The mutants selected were Δ2-26 hEAG1, ΔEAG hEAG1, F151N:L154N hEAG1, ΔcNBHD hEAG1, E600R hEAG1 and F714S:F717S hEAG1. Δ2-26 hEAG1 was included because it causes a large current potentiation when exposed to high intracellular Ca²⁺ conditions which is the opposite response of WT hEAG1. ΔEAG hEAG1 lacks the entire EAG domain and also shows a modest potentiation of its current when exposed to 5μM I&T. F151N:L154N hEAG1 – which will herein be referred to as BD-N1 hEAG1 – is a mutant where the residues involved in calmodulin binding to the N-

terminal binding domain have been changed to reduce calmodulin binding affinity. BD-N1 hEAG1 shows a gradual inhibition of its current when 5 μ M I&T is applied. Δ cNBHD hEAG1 is a mutant where the cNBH domain has been removed. The current of this mutant does not change in response to 5 μ M I&T and so is a good test of whether the cNBH domain alone is involved in the proliferation process. E600R hEAG1 is a charge reversal point mutation in the cNBHD. This mutant also shows a large potentiation of its current under high intracellular Ca²⁺ conditions but does not recover back to control levels. Finally, the F714S:F717S hEAG1 construct in which the residues of the second C-terminal calmodulin binding domain have been mutated to reduce calmodulin binding – herein referred to as BD-C2 hEAG1. The current of this construct shows a small transient inhibition by 5 μ M I&T but recovers back to control amplitudes quickly.

All 8 constructs were expressed in CHO cells and the number of GFP expressing cells that incorporate BrdU after a short exposure were counted to measure proliferation. Figure 5.1 shows the images taken of CHO cells expressing the 8 hEAG1 constructs and their BrdU incorporation. Proliferating cells were detected with an anti-BrdU antibody conjugated to AlexaFluor-594. The BrdU incorporation does not distinguish between transfected and non-transfected cells. GFP was used as a marker of transfected cells and was detected with an anti-GFP antibody conjugated to AlexaFluor-488. Proliferation of transfected cells was calculated from the percentage of GFP-expressing cells where BrdU was also detected in the nucleus (Figure 5.1). Figure 5.2 shows the results of the BrdU assay (n=5).

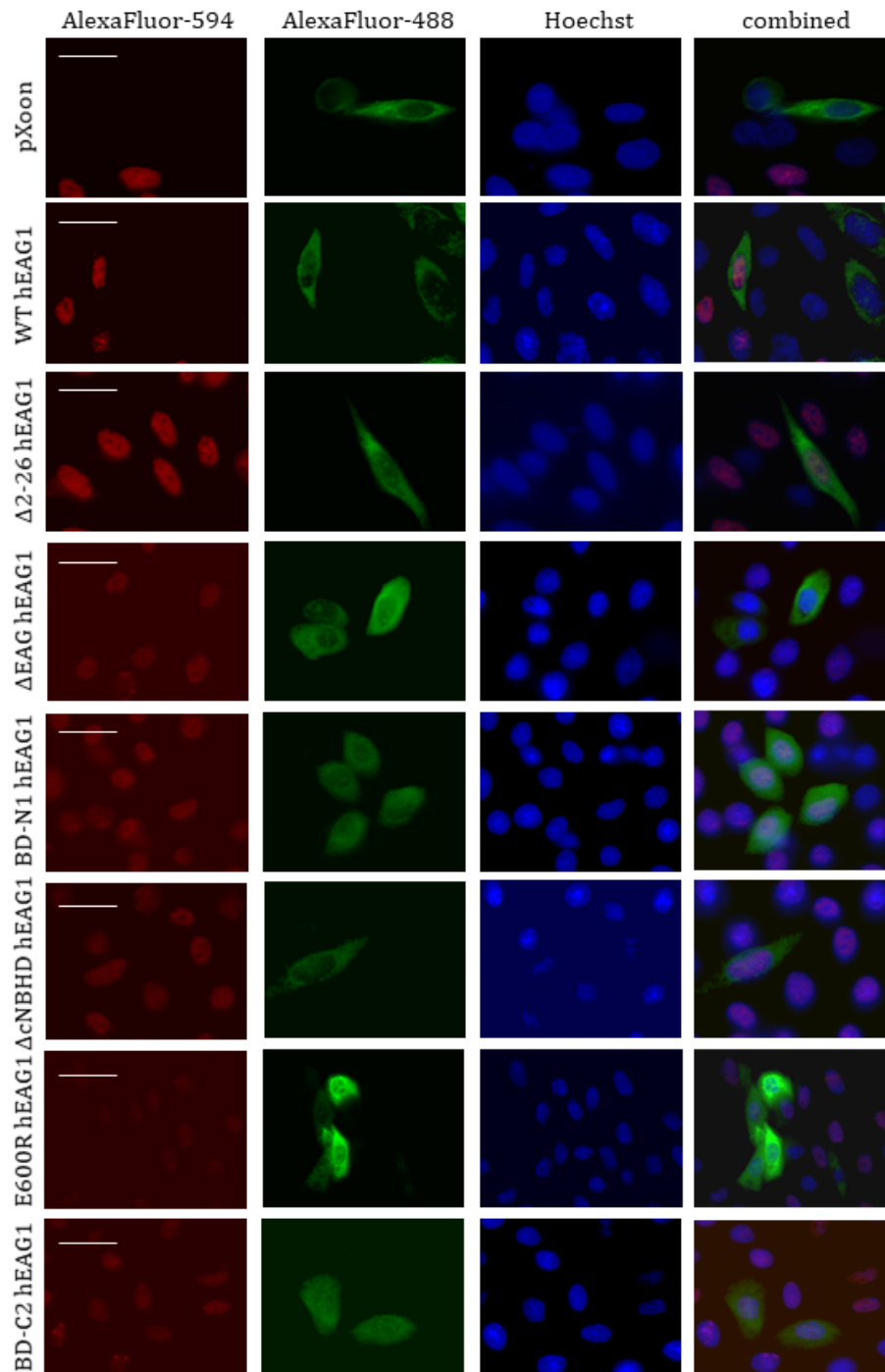


Figure 5.1. An image panel showing the BrdU incorporation, GFP expression and Hoechst staining of the nuclei of the 8 plasmid constructs used in CHO cells.

These images show the fluorescence of a BrdU antibody conjugated to AlexaFluor-594, GFP labelled with antibody conjugated to AlexaFluor-488 and the cell nucleus (Hoechst). Combined images are shown in the right most column. Scale bars represent 10 μ m.

There is a significant decrease in the percentage of BrdU-positive cells when comparing WT hEAG1-transfected to pXoon-transfected CHO cells ($p < 0.01$). All constructs are statistically compared to the WT hEAG1 values as the WT channel is being used as a positive control. $21 \pm 2.3\%$ of pXoon expressing cells were positive for BrdU staining whilst $32.7 \pm 0.4\%$ of WT hEAG1 expressing cells were BrdU positive ($n=5$). Thus WT hEAG1 expression significantly enhances rates of proliferation which agrees with previous literature (Pardo *et al.*, 1999).

The data also shows that both Δ EAG hEAG1 and E600R hEAG1 reduce the proportion of BrdU incorporating cells to $21.3 \pm 3.0\%$ and $21.8 \pm 1.4\%$ respectively (both $p < 0.05$, $n=5$, Figure 5.2) bringing rates of proliferation down to control levels. The other tested constructs, Δ 2-26 hEAG1, BD-N1 hEAG1, Δ cNBHD hEAG1 and BD-C2 hEAG1 all has BrdU incorporation percentages of $34.2 \pm 1.3\%$, $33.5 \pm 2.1\%$, $28.9 \pm 2.7\%$ and $25.6 \pm 2.8\%$ respectively, none of which were found to be statistically significant when compared to WT hEAG1 cells ($p > 0.05$, $n=5$, Figure 5.2).

This indicates that both the EAG domain and the E600 residue are involved in the mechanism of increased proliferation seen with the WT channel. Intriguingly both constructs also show potentiated current under high Ca^{2+} conditions in oocytes (Lorinczi *et al.*, 2016). Proliferation of BD-C2 hEAG1 transfected cells was also reduced but not by a statistically significant amount (Figure 5.2).

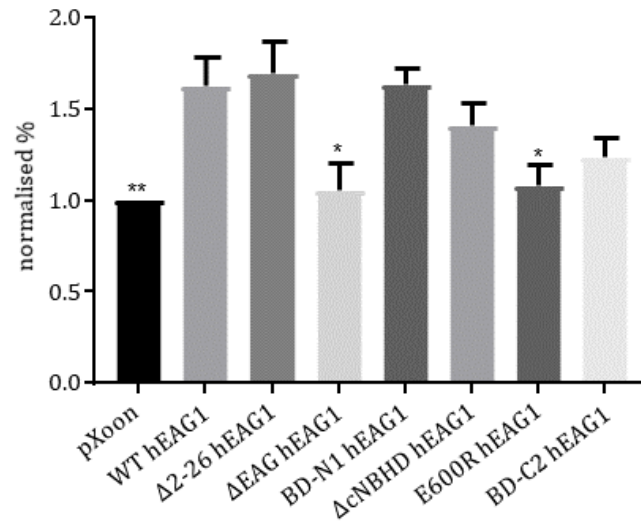


Figure 5.2. A bar chart showing the percentage of proliferating CHO cells in cultures transfected with the relevant hEAG1 construct.

Cells positive for the GFP signal were counted, then the same cells were counted for a positive BrdU signal (red fluorescence). The percentage of cells also positive for BrdU was calculated and normalised to control (pXoon). Statistics were compared against WT hEAG1 as this is a positive control and known to increase proliferation.

5.1.2. Δ EAG hEAG1 and E600R hEAG1 reduce the percentage of ciliated hTERT-RPE1 cells

The expression of WT hEAG1 has recently been suggested to reduce the number of cells with a primary cilium in hTERT-RPE1 cells (Sanchez *et al.*, 2016). The mechanism by which this happens is as yet unknown, but it is important as the retraction of the primary cilium is a prerequisite for cells to divide and increased primary cilium disassembly is linked with an increase in cell proliferation. The same constructs used in the BrdU assay were also used in immunocytochemistry experiments measuring primary cilia properties. Untransfected hTERT-RPE1 cells were studied as a second negative control as well as pXoon-transfected cells to ensure any effects seen are not caused by the transfection process itself.

The primary cilium of hTERT-RPE1 was stained for in untransfected cells as well as cells transfected with the 8 plasmid constructs shown in Figure 3.93. There was no significant difference in the percentage of cells presenting with a primary cilium from the untransfected ($93.3 \pm 1.2\%$) and the pXoon transfected ($92.5 \pm 3.1\%$) groups indicating that the transfection does not affect the cilia ($p > 0.05$, $n = 4$, Table.3, Figure 3.137).

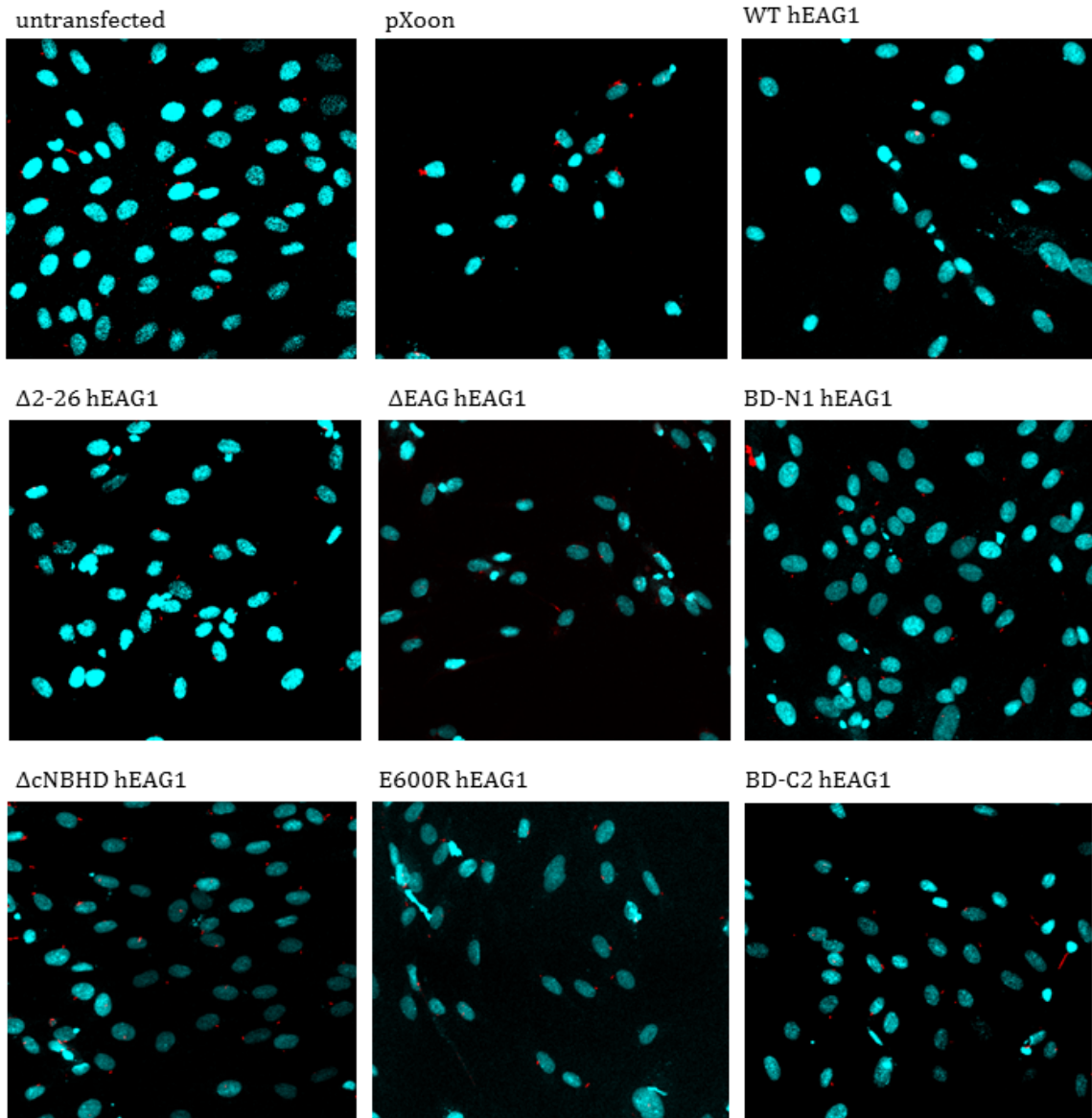


Figure 5.3. An image panel showing the acetylated-tubulin staining (AlexaFluor-594) and the nuclei staining of hTERT-RPE1 cells transfected with the 8 proliferation constructs.

Images taken of hTERT-RPE1 cells showing the primary cilia (red stain) and the nuclear staining (blue). Acetylated-tubulin is highly concentrated in the primary cilium and so acts as a marker for its presence. Untransfected and empty-vector control transfected cells show a high percentage of ciliated cells whilst WT hEAG1 transfected cells show very few cilia.

Out of the hEAG1 constructs the WT channel caused the biggest reduction in the percentage of cells presenting with a primary cilium with $47.3 \pm 2.2\%$ staining positively for the organelle (Table 3.). This was a significant reduction from the pXoon cells ($p < 0.0001$) and agrees with current data that WT hEAG1 reduces the occurrence of the primary cilium in hTERT-RPE1 cells (Figure 3.93, $n=4$) (Sanchez *et al.*, 2016). Both $\Delta 2-26$ hEAG1 and BD-C2 hEAG1 caused significant reductions to $67.1 \pm 6.8\%$ and $71.8 \pm 4.9\%$ respectively in the percentage of cells producing primary cilia (Figure 5.4, $n=4$, Table 3.). The reduction in primary cilia caused by the presence of $\Delta 2-26$ hEAG1 and BD-C2 hEAG1 was significant in both cases ($p < 0.01$ and $p < 0.001$ respectively, $n=4$).

Furthermore, the two hEAG1 constructs that significantly altered the proliferation of CHO cells also affected the percentage of hTERT-RPE1 cells with a primary cilium. Δ EAG hEAG1 and E600R hEAG1 caused reductions to $78.1 \pm 1.9\%$ and $72.5 \pm 4.8\%$ respectively ($p < 0.0001$ and $p < 0.001$, $n=4$, Table.3, Figure 5.4). Δ cNBHD hEAG1 caused a reduction to $85.9 \pm 3.6\%$ which was a significant difference when compared to that of the WT expressing cells ($p < 0.0001$, $n=4$, Table.3, Figure 5.4).

This data suggests that all of the intracellular domains of hEAG1 control its ability to retract the primary cilium and that the EAG domain and E600 residue are important for its role in proliferation – both cellular events linked to uncontrolled and rapid proliferation of cancer cells.

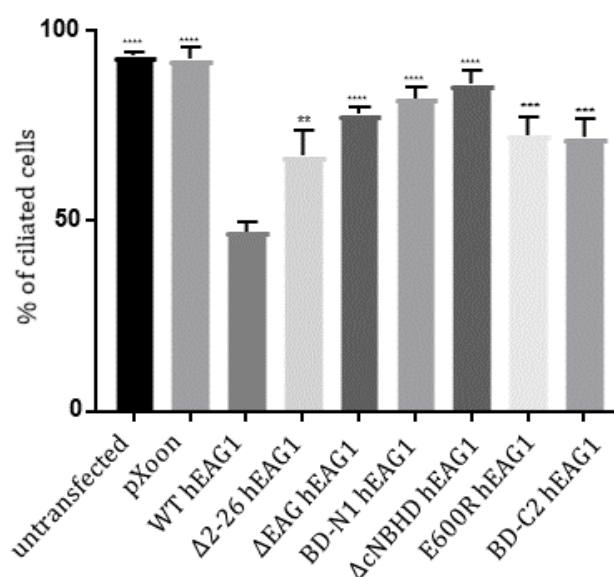


Figure 5.4. A bar chart showing how different hEAG1 constructs affect the fraction of hTERT-RPE1 cells capable of producing a primary cilium.

This bar chart shows that the WT channel drastically reduces the fraction of cells that produce a cilium. Other constructs including $\Delta 2-26$, ΔEAG , E600R and BD-C2 hEAG1 also cause a significant reduction in the number of cells that produce a cilium. Statistical analysis was performed against WT hEAG1 data as this was the positive control.

The primary cilia were also analysed for their length and width to test whether any of the hEAG1 constructs would affect these parameters. Cilia length varied from $1.68 \pm 0.06 \mu\text{m}$ to $1.99 \pm 0.03 \mu\text{m}$ (Table 3.) but none of the constructs had a significant effect when compared to the pXoon value ($p > 0.05$, Figure 5.5a). The width of the cilia were also analysed compared to pXoon, the widths varied from $0.92 \pm 0.02 \mu\text{m}$ to $1.03 \pm 0.03 \mu\text{m}$ but none of the constructs caused a significant change in cilia width ($p > 0.05$, Table.3, Figure 5.5b). Since cilia are so small it is difficult to accurately measure their length and width. Limitations of the microscope may have hindered the analysis with this data and more accurate microscopy systems would be necessary in order to accurately determine these changes.

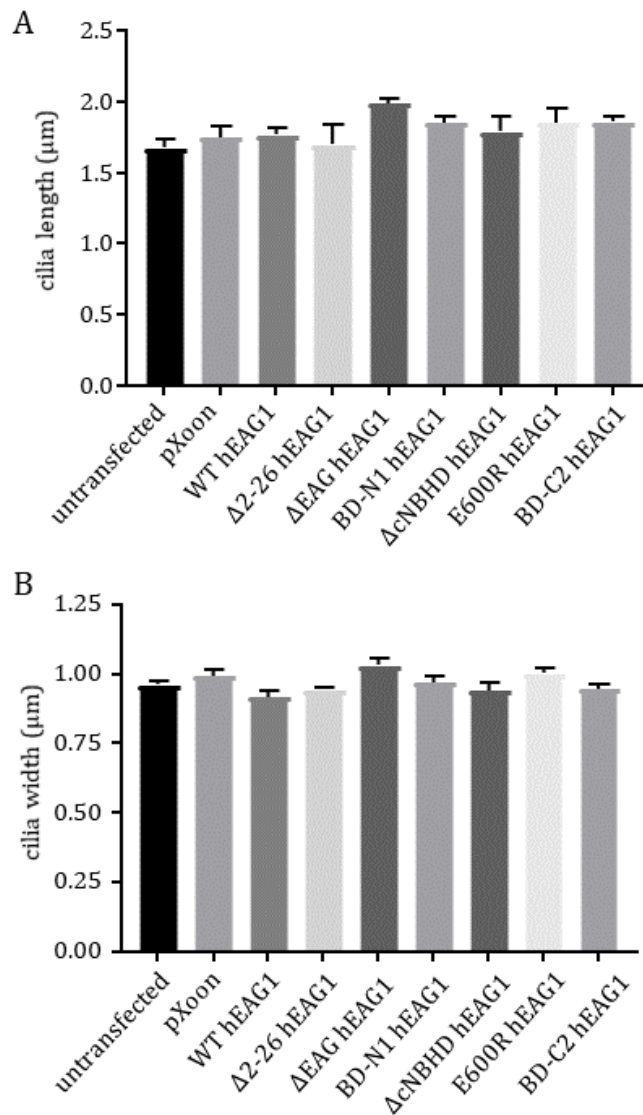


Figure 5.5. Bar charts showing how hEAG1 constructs affect the length and width of the primary cilium in hTERT-RPE1 cells.

A: this graph shows that none of the hEAG1 constructs have a significant effect on the length of the primary cilium of hTERT-RPE1 cells.

B: this graph shows that the hEAG1 constructs do not affect the width of the primary cilium of hTERT-RPE1 cells.

Additional parameters that were studied were the average cell size and circularity, both of which are markers of morphology. Changes in cell morphology have been documented in cancer (DePriest *et al.*, 1993) and because of WT hEAG1's role in proliferation and the primary cilium disassembly these parameters were also tested in hTERT-RPE1. There was no significant change in cell size or circularity between the untransfected cells and any of the transfections (Figure 5.6). Cell size varied from $225.3 \pm 14.7 \mu\text{m}^2$ down to $205.1 \pm 8.4 \mu\text{m}^2$ but was not statistically significant ($p > 0.05$, Table 3.). The circularity of the cells varied from 0.5 ± 0.1 to 0.7 ± 0.1 and these variations were also found to not be significant ($p > 0.05$, Table 3.).

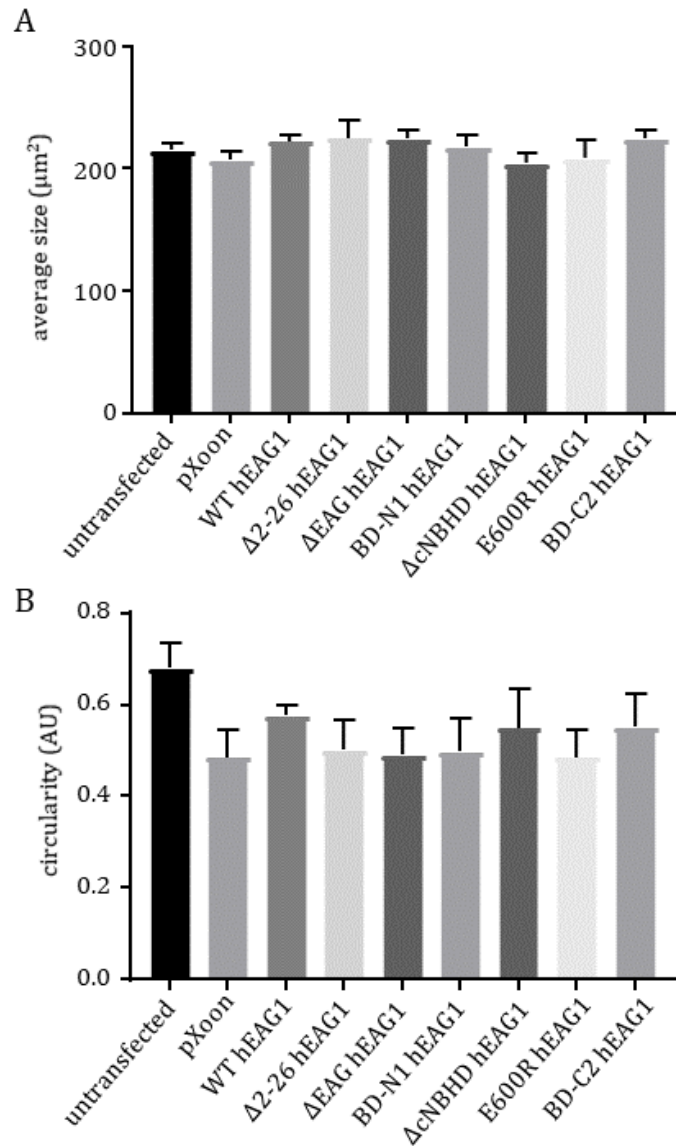


Figure 5.6. Bar charts showing how different hEAG1 constructs affect the cell size and circularity of hTERT-RPE1 cells.

A: this graph represents the change in average cell size of transfected cells. None of the hEAG1 constructs had a significant effect on the average cell size.

B: this graph represents changes in cell circularity of transfected cells. Similarly, none of the constructs used had a significant effect on the cell circularity.

5.1.3. Ca²⁺ imaging untransfected & WT hEAG1-expressing CHO cells

The constructs tested in both the BrdU proliferation assay and the primary cilia assays were transfected into CHO cells to test how the currents responded to 5 μ M I&T – the two compounds used to raise intracellular Ca²⁺. It was noted that many of the mutants had varied current responses to the 5 μ M I&T where they had previously been consistent in the oocytes.

Ca²⁺ imaging of untransfected CHO cells was carried out to test whether the response of CHO cells to 5 μ M I&T is the same as that of the oocytes which was that the Ca²⁺ level increases rapidly and stays at the same level throughout the 300s recording (Lorinczi *et al.*, 2016). CHO cells loaded with Fluo-3 were imaged every 5s for 115s prior to the addition of 5 μ M I&T. After the addition of 5 μ M I&T, the Fluo-3 signal increased (Figure 5.7) from 1 in control conditions to a maximum of 1.85 ± 0.03 which was a significant increase ($p < 0.0001$, $n = 5$, 348 cells, Figure 5.8a). The Fluo-3 signal following 5 μ M I&T was normalised to intensity values of the cells in control conditions which is shown at time points before 0 (Figure 5.8a). Following on from the rapid increase, the Ca²⁺ signal then reduced before plateauing until the end of the recording (Figure 5.8a).

Ca²⁺ signals from individual cells was also plotted to demonstrate the variety of responses to 5 μ M I&T, as shown in Figure 5.8b. Some cells showed an initially fast increase in the Ca²⁺ signal that then continued to rise with time as shown by the black and green lines whilst some cells had an increase in the Ca²⁺ signal that rapidly plateaued as shown by the blue line. Some cells (purple line) did not show an increase in Ca²⁺ signal following the addition of 5 μ M I&T (Figure 5.8b) indicating that there is an element of heterogeneity in a population of CHO cells which may go in part to explain the varied patch clamp data (shown later). The heterogeneity of the CHO cells is also shown in Figure 5.7.

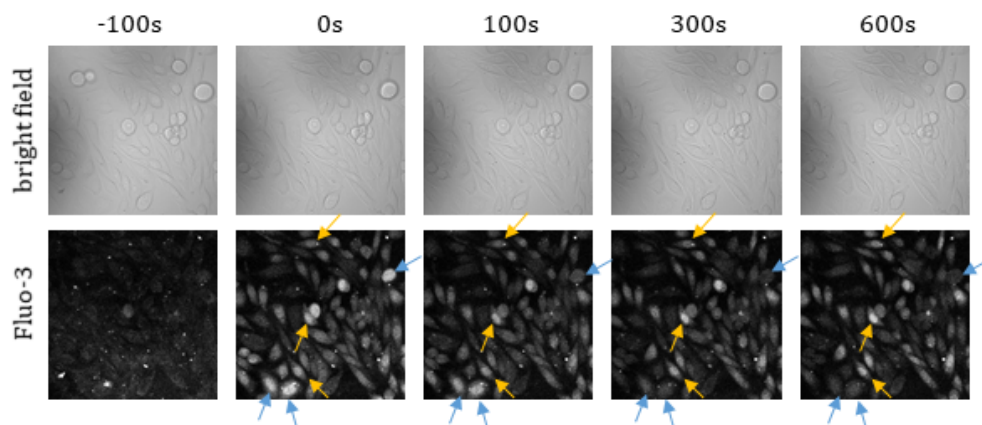


Figure 5.7. An image panel showing the changes in Ca^{2+} signal before and after the addition of $5\mu\text{M}$ I&T.

This panel shows both the bright field and fluorescent Fluo-3 images of untransfected CHO cells. $5\mu\text{M}$ I&T is added at $t=0$ and causes a rapid rise in the Ca^{2+} signal. Over time, some cells reduce their fluorescent signal – as indicated by the blue arrows – whilst others stay at a constant level – as indicated by the orange arrows. This data shows that the Ca^{2+} responses of CHO cells are heterogenous.

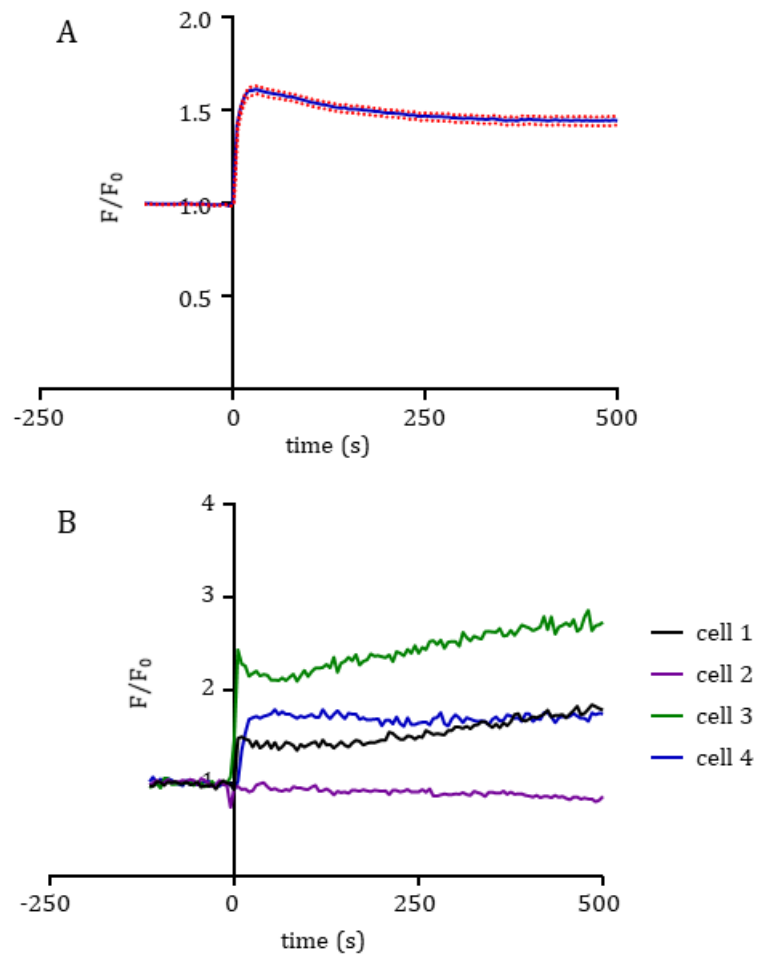


Figure 5.8. The Ca^{2+} response of untransfected CHO cells before and after $5\mu\text{M}$ I&T.

A: Fluo-3 fluorescence emissions at a wavelength of 488nm was quantified for each cell in a field and normalised to the fluorescence intensity at the beginning of the experiment to give F/F_0 . F/F_0 is plotted against time relative to application of $5\mu\text{M}$ I&T ($n=5$, cell no.=348). The Ca^{2+} signal increases rapidly following the addition of $5\mu\text{M}$ I&T at $t=0$ before reducing slightly and plateauing.

B: Fluo-3 signals (F/F_0) measured in single cells chosen to reflect a range of different responses observed. Some cells do not respond at all whilst others showing varying degrees of increase of Ca^{2+} .

A stable CHO cell line expressing WT hEAG1 was also loaded with Fluo-3 and tested for its Ca^{2+} response as there is currently no data suggesting if the presence of WT hEAG1 affects Ca^{2+} responses. $5\mu\text{M}$ I&T was added to the cells at $t=0$ after the baseline had been allowed to stabilise for 115s. After addition of $5\mu\text{M}$ I&T there was a rapid increase in the fluorescent signal (Figure 5.9 and Figure 5.10a). The signal increased from 1 to 1.91 ± 0.04 which was a significant increase in signal ($p < 0.0001$, $n=6$, 398 cells). After the peak in fluorescence the intensity declines again between the peak and 250s after $5\mu\text{M}$ I&T was first applied. After this it begins increasing again until the end of the recording. This is interesting because it implies that the presence of the channel may be affecting the Ca^{2+} response of CHO cells to $5\mu\text{M}$ I&T.

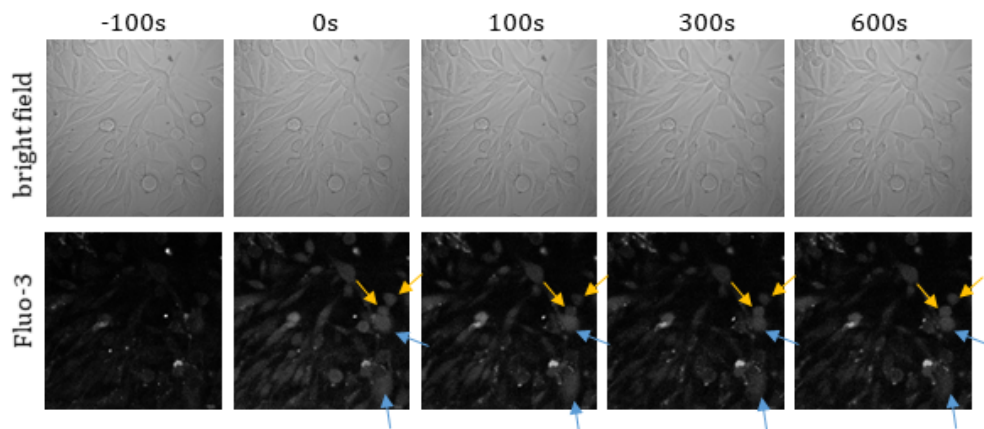


Figure 5.9. An image panel showing the changes in Ca^{2+} signal of CHO cells stably expressing WT hEAG1 before and after the application of $5\mu\text{M}$ I&T.

The image panel shows both the bright field and Fluo-3 images of WT hEAG1-CHO cells. Upon the addition of $5\mu\text{M}$ I&T at $t=0$ the Ca^{2+} signal increases from control and some cells remain at a constant level – as shown by the blue arrows – whilst other cells reduce their Ca^{2+} signal following the initial peak but then increase again over time – as shown by the orange arrows.

Individual cell data was plotted that shows once again that there is some variation in the response of the cells to 5 μ M I&T (Figure 5.10b). Some cells, with varying peaks, increase their Ca²⁺ signal rapidly which briefly plateaus before returning back down towards the control value – bearing some resemblance to a ventricular action potential. This is shown by the green, blue and purple lines (Figure 5.10b). Some cells however showed an initial rapid increase in Ca²⁺ signal that then went on to increase at a steadier rate over time as shown by the black line. Responses of individual cells are also shown in Figure 5.9.

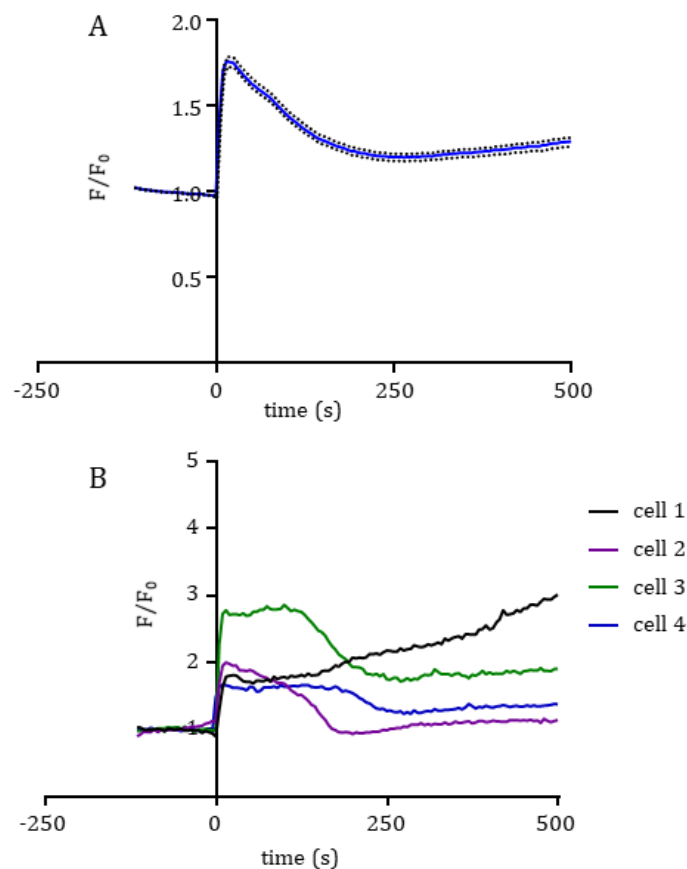


Figure 5.10. The Ca²⁺ responses of CHO cells stably expressing WT hEAG1 before and after 5 μ M I&T.

A: Fluo-3 fluorescence emissions at a wavelength of 488nm was quantified for each cell in a field and normalised to the fluorescence intensity at the beginning of the experiment to give F/F_0 . F/F_0 is plotted against time relative to application of 5 μ M I&T (n=6, cell no.=398). Similarly to the untransfected cells, there is a sharp increase in Ca²⁺ signal at $t=0$. However this reduces in intensity to a greater extent than the untransfected cells.

B: Fluo-3 signals (F/F_0) measured in single cells chosen to reflect the range of different responses observed. Some cells show a rapid increase in signal followed by an equally sized reduction in signal whilst some cells continue to increase in Ca²⁺ signal.

The responses of untransfected CHO cells and the WT hEAG1 stable CHO cell line are shown for comparison in Figure 5.11. Here the difference in response is clearer and was recorded over a longer period of time. Both cell lines increase their Ca^{2+} signal rapidly upon the addition of $5\mu\text{M}$ I&T at $t=0$ but then the cells deviate in their behaviour. The untransfected cells reduced the signal from the peak before plateauing for the duration of the recording (Figure 5.11). The stable cell line is more dynamic in response, following the peak in signal, the signal then reduces again at a faster rate than the untransfected cells. 250s from $t=0$ the signal intensity begins to increase again over time (Figure 5.11) – this bears similarity to the current amplitude of WT hEAG1 upon the addition of $5\mu\text{M}$ I&T. This indicates that not only does Ca^{2+} affect the current of hEAG1 but it seems the presence of hEAG1 affects the Ca^{2+} handling of cells expressing it, suggesting a synergistic relationship between the two which has not yet been documented

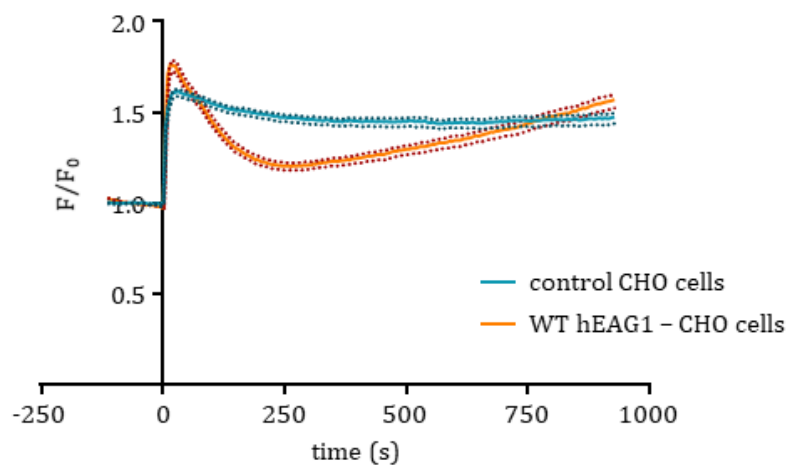


Figure 5.11. The Ca^{2+} profile of untransfected CHO cells compared to the stably transfected WT hEAG1 CHO cell line.

The response of untransfected CHO cells is shown by the blue line with the error shown in dark blue. The stably transfected cell line is shown by the orange line with the error in dark red. $5\mu\text{M}$ I&T was added at $t=0$. The CHO cells expressing WT hEAG1 show a larger reduction in Ca^{2+} signal by 250s than the untransfected cells but then begins to increase in signal again up to the same fluorescent intensity as untransfected cells.

5.1.4. Western blots show that hEAG1 protein for all constructs except Δ cNBHD hEAG1 are expressed in CHO cells.

All of the hEAG1 constructs with the exception of Δ cNBHD hEAG1 produced functional currents when expressed in CHO cells. The protein of Δ cNBHD hEAG1 may be produced by the cell but being retained in the ER where it cannot be recorded from using patch clamp.

Western blots of CHO cell lysates were conducted to stain for hEAG1 protein in transiently transfected cells. All constructs, except for the empty vector control (pXoon), produced a band at \sim 108kDa which is the predicted molecular weight for glycosylated hEAG1 (Figure 5.12). The band for Δ EAG hEAG1 sits below the other bands because the channel is missing a large portion of its structure and so runs further along the SDS-PAGE gel. No band was detected for Δ cNBHD hEAG1 indicating that the protein was not produced in CHO cells (Figure 5.12). β -actin was used as a loading control and shows even loading across all the lanes. Similar results were seen in 4 separate blots.

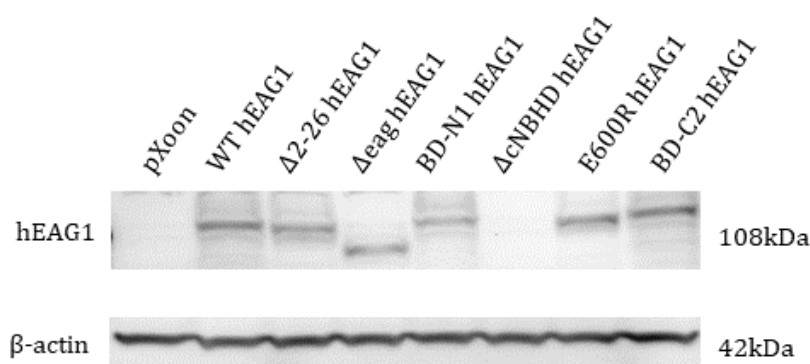


Figure 5.12. A Western blot from CHO cells transiently transfected with the hEAG1 constructs.

This Western blot shows that all hEAG1 constructs, except for Δ cNBHD hEAG1, are expressed in CHO cells. The empty vector pXoon is present as a negative control. β -actin was used as a loading control.

5.1.5. All hEAG1 constructs are functional in CHO cells except Δ cNBHD hEAG1

Some of the constructs used in the BrdU incorporation assay reduced proliferation to similar levels as the negative control cells. The functionality of all constructs in CHO cells was tested to ensure effects on proliferation were not due to differences in channel function.

All of the constructs including pXoon were transfected into CHO cells and recorded from in the whole cell patch clamp technique. The responses of WT hEAG1, Δ 2-26 hEAG1 and pXoon (vector control) have been previously shown in section 4.1. Both WT and Δ 2-26 hEAG1 produce functional currents in CHO cells that show similar responses to their oocyte counterparts in terms of voltage dependence and response to 5 μ M I&T, although responses were slower to develop.

The remaining 5 constructs were also recorded from under the I/V protocol and following the application of 5 μ M I&T. Δ EAG hEAG1 was one of two constructs that significantly reduced the number of proliferating CHO cells. It produced slowly activating currents that increased in amplitude with successive increases in membrane potential (Figure 5.13). At more positive membrane potentials, the current amplitude begins reducing. This is rectification and is a hallmark of the Δ 2-26 hEAG1 mutant. The time course of activation from 10-80% was measured to be 402.6 ± 136.2 ms at +60mV, slower than that of the WT channel in CHO cells ($p < 0.05$, $n=9$, Table 4.).

The I/V curve shows the difference in response to membrane potential of Δ EAG hEAG1 and WT hEAG1 (Figure 5.13c). The I/V data shows that Δ EAG hEAG1 activates at more negative membrane potentials than the WT channel and peaks in current amplitude at +20mV before reducing in amplitude with further increases in voltage (Figure 5.13c).

The G/V curve shows that the conductance follows the same trend as the current, increasing with voltage before peaking at +10mV and then reducing again (Figure 5.13d). The Boltzmann fit of the normalised G/V relationship provides values for $V_{0.5}$ of -13.4 ± 4.6 mV which is a significant decrease from the WT value ($p < 0.0001$, $n=9$, Table 4.). The k value was 11.0 ± 1.3 mV which is not significantly different from the WT channel ($p > 0.05$, $n=9$, Table 4.). This data shows that in CHO

cells, the removal of the EAG domain causes a negative shift in the $V_{0.5}$ value and reduces the activation kinetics of the channel which is the same as measured in oocytes.

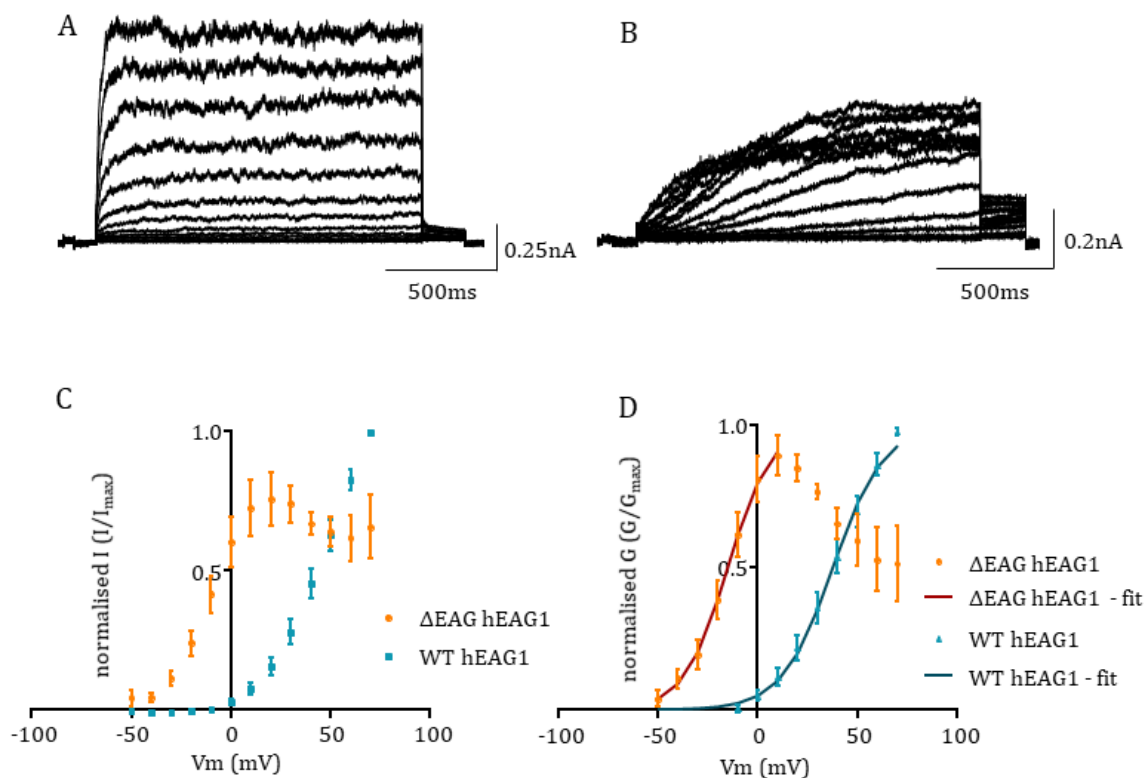


Figure 5.13. Data showing how Δ EAG hEAG1 responds to the I/V protocol when expressed in CHO cells.

A: currents elicited from the WT hEAG1 channel under the I/V protocol, currents are shown for comparison and have been previously described in Figure 4.2.

B: currents elicited from Δ EAG hEAG1 when using the I/V protocol. These are slower to activate than the WT channel and do not reach a steady state plateau during the voltage pulse. Currents from Δ EAG hEAG1 also begin reducing in amplitude with more depolarising voltages.

C: I/V curves showing how each channel's current changes with voltage. WT hEAG1 is shown for comparison (blue) and the channel passes more current with each successive depolarisation. Δ EAG hEAG1 (orange) initially passes more current at negative voltages than the WT channel and continues increasing up to +20mV. After +20mV the current amplitude reduces with depolarisation.

D: G/V curves showing the difference in conductance between WT hEAG1 (blue) and Δ EAG hEAG1 (orange). Δ EAG hEAG1 activates at more negative membrane potentials (-40mV) and peaks at +10mV. WT hEAG1 activates at 0mV and the conductance increases with each depolarisation. Data are fitted with a Boltzmann function (dark blue and dark red respectively).

The response of Δ EAG hEAG1 to 5 μ M I&T was also tested in the CHO cells since it has been previously shown to increase its current gradually over time – a more graded response than that of the Δ 2-26 hEAG1 construct (Lorinczi *et al.*, 2016). In the same way as previously shown in section 3.2, the membrane potential was pulsed to +20mV and the 5 μ M I&T was perfused directly on to the cell. The data shows an increase in the current amplitude over time and a component of instantaneous current which indicates that the channels are not all deactivating in time for the next voltage pulse (Figure 5.14a). Over time the current gradually increases by $152.1 \pm 74.2\%$, this was found to be a statistically significant increase from control ($p < 0.05$, $n = 5$, Table.2, Figure 5.14b).

Responses to 5 μ M I&T from individual cells were plotted against time to show the variety of responses recorded from Δ EAG hEAG1 expressing cells (Figure 5.14c). Some cells show a consistent increase in current following the addition of 5 μ M I&T at $t = 0$, such as the black data points (Figure 5.14c). Others show a general trend of increasing current but contains large variation within the recording – blue data points, whilst some cells barely respond at all – orange data points (Figure 5.14c). This points to variation between individual cells.

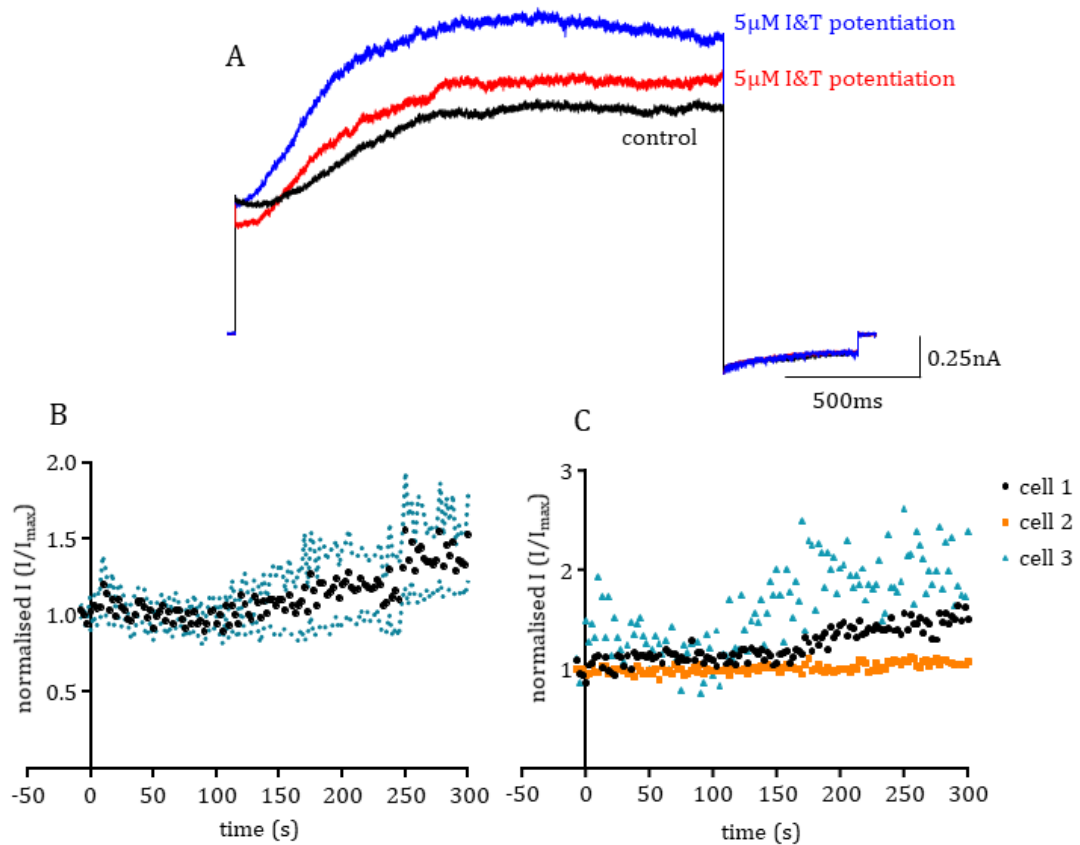


Figure 5.14. Data from Δ EAG hEAG1 expressing CHO cells showing the response of the channel to $5\mu\text{M}$ I&T.

A: representative current traces from Δ EAG hEAG1 elicited by steps to $+20\text{mV}$. The traces show the current in control (black) and after the addition of $5\mu\text{M}$ I&T (red at 160s and blue at 300s).

B: a graph showing the normalised response of the current amplitude over time when $5\mu\text{M}$ I&T was added at $t=0$. Data is normalised to control values ($n=5$). The graph shows a gradual increase in current amplitude over time. SEM is shown as blue dots.

C: this graph shows the different responses of cell expressing Δ EAG hEAG1 after addition of $5\mu\text{M}$ I&T. Amplitudes of single cell currents are plotted against time and where normalised to the amplitudes in control.

This data shows that Δ EAG hEAG1 behaves the same way in CHO cells as it does in oocytes and that its varied responses to voltage and high Ca^{2+} compared to the WT channel may be behind the reduction in proliferation seen in the BrdU incorporation assay (Figure 5.2).

The BD-N1 hEAG1 construct was expressed in CHO cells and recorded under the I/V protocol. BD-N1 hEAG1 produced currents that were similar in appearance to WT hEAG1 (Figure 5.13). The time course of activation from 10-80% was 170.4 ± 71.3 ms at +60mV which is similar to the time course of WT hEAG1 ($p > 0.05$, $n = 5$, Table 4.).

The I/V relationships shows that BD-N1 hEAG1 has a similar voltage dependence to the WT current. It shows an increase in current amplitude with each increase in membrane potential above 0mV with no rectification (Figure 5.15b). The G/V relationship shows that BD-N1 hEAG1 activates at more negative membrane potentials than the WT channel as indicated by the leftwards shift of the curve (Figure 5.15d). The $V_{0.5}$ value obtained from BD-N1 hEAG1 was 27.6 ± 6.3 mV which is not statistically different to the WT channel ($p > 0.05$, $n = 5$, Table 4.). The k value was measured to be 12.2 ± 1.0 mV which was also not significantly different from WT hEAG1 ($p > 0.05$, $n = 5$, Table 4.). This data demonstrates that in CHO cells, the mutation of the N-terminal calmodulin binding site does not affect the voltage dependence or the activation kinetics of the current.

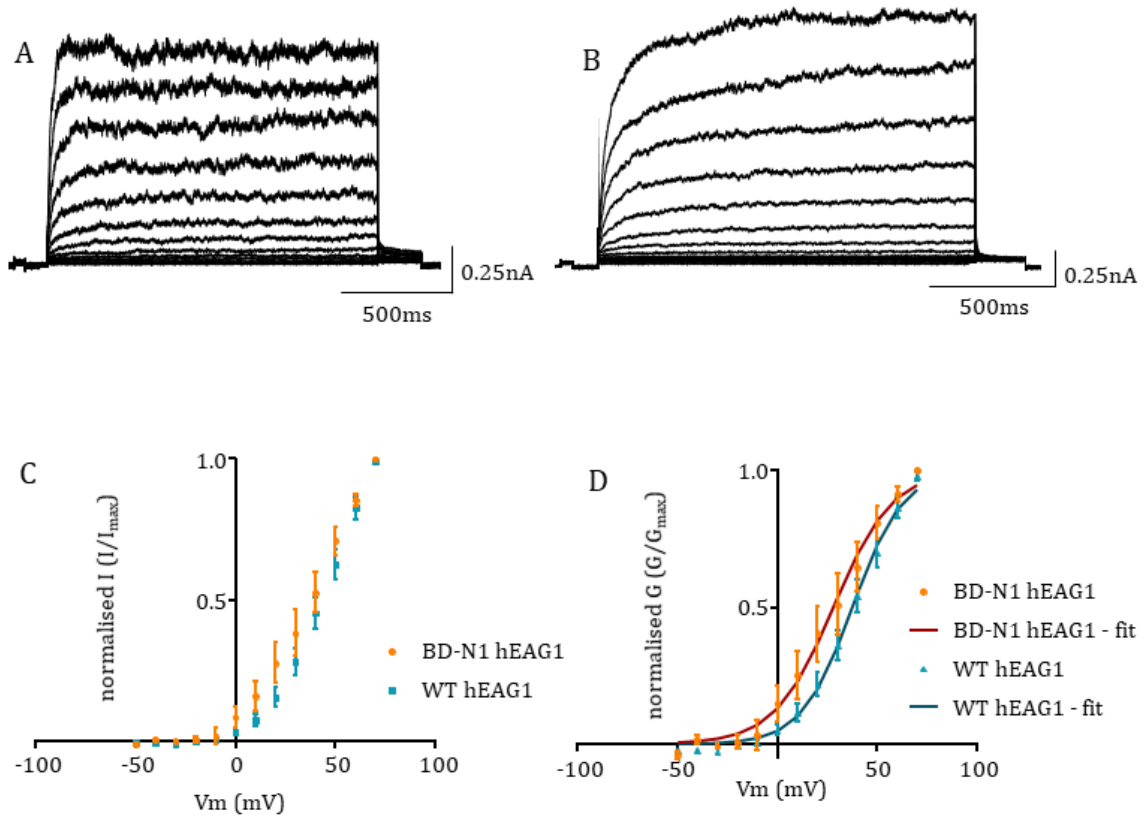


Figure 5.15. Data showing how BD-N1 hEAG1 responds to the I/V protocol when expressed in CHO cells.

A: currents elicited from the WT hEAG1 channel under the I/V protocol, currents are shown for comparison and have been previously described in Figure 4.2.

B: currents elicited from BD-N1 hEAG1 when using the I/V protocol. These are similarly quick to activate compared to the WT channel and reach a steady state plateau during the voltage pulse. Currents from BD-N1 hEAG1 do not reduce in amplitude with more depolarising voltages.

C: I/V curves showing how each channel's current changes with voltage. WT hEAG1 is shown for comparison (blue). BD-N1 hEAG1 (orange) follows a very similar trend as the WT channel and increase in current amplitude with each successive depolarisation.

D: G/V curves showing the difference in conductance between WT hEAG1 (blue) and BD-N1 hEAG1 (orange). BD-N1 hEAG1 activates at -10mV whereas WT hEAG1 activates at 0mV. Both conductances increase with each depolarisation. Data for WT hEAG1 and BD-N1 hEAG1 are fitted with a Boltzmann function (dark blue and dark red respectively).

BD-N1 hEAG1 was exposed to 5 μ M I&T to test whether the current responds in the same way in CHO cells as it did in oocytes. The current was inhibited by 57.6 \pm 13.7% from control (Figure 5.16a). This inhibition was not significant compared to control values ($p > 0.05$, $n = 4$, Table 4.). The current of BD-N1 hEAG1 reduced gradually over the course of the recording (Figure 5.16b).

Individual, normalised to control, current amplitude data from 2 cells are shown (Figure 5.16c). This shows that current from one cell was inhibited shortly after the 5 μ M I&T is perfused over the cells and that this fluctuates over the course of 300s as shown by the black data points (Figure 5.16c). Other cells, as shown by the orange data points, are inhibited slowly from the time of onset (Figure 5.16c). This variety of responses may be indicative of fluctuating Ca²⁺ in the cell.

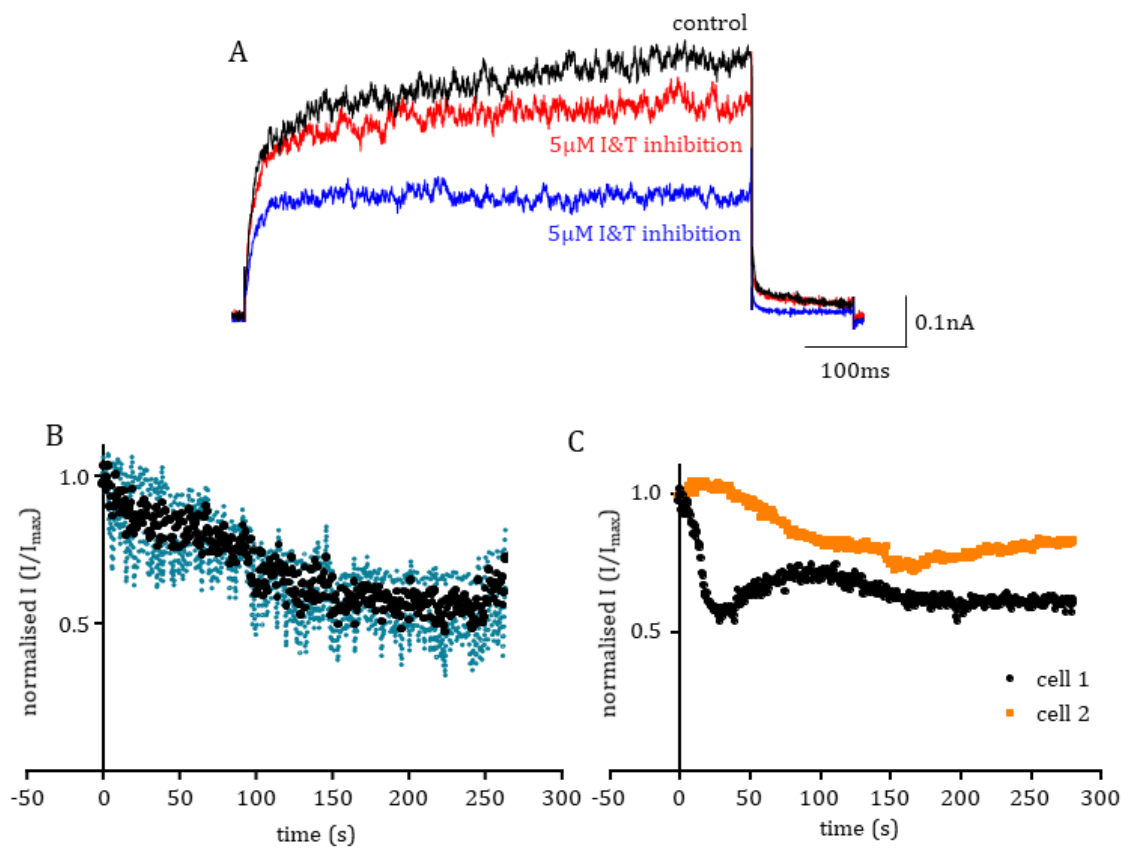


Figure 5.16. Data from BD-N1 hEAG1 expressing CHO cells showing the response of the channel to 5µM I&T.

A: representative current traces from BD-N1 hEAG1 elicited by steps to +20mV. The traces show the current in control (black) and after the addition of 5µM I&T (red at 160s and blue at 250s).

B: a graph showing the normalised response of the current amplitude over time when 5µM I&T was added at t=0. Data is normalised to control values (n=4). The graph shows a gradual decrease in current amplitude over time. SEM is shown as blue dots.

C: this graph shows the different responses of cell expressing BD-N1 hEAG1 after addition of 5µM I&T. Amplitudes of single cell currents are plotted against time and were normalised to the amplitudes in control.

Δ cNBHD hEAG1 was one of the constructs that had no significant effect on the number of proliferating CHO cells. Under the I/V protocol there were no measurable currents (Figure 5.17a) indicating that this construct was not expressed or at least not functional at the plasma membrane in CHO cells. The response of Δ cNBHD hEAG1 to the I/V protocol is shown in Figure 5.17b (n=7). Δ cNBHD hEAG1 did not respond to 5 μ M I&T in oocytes and due to the lack of measurable current 5 μ M I&T was not applied in this case.

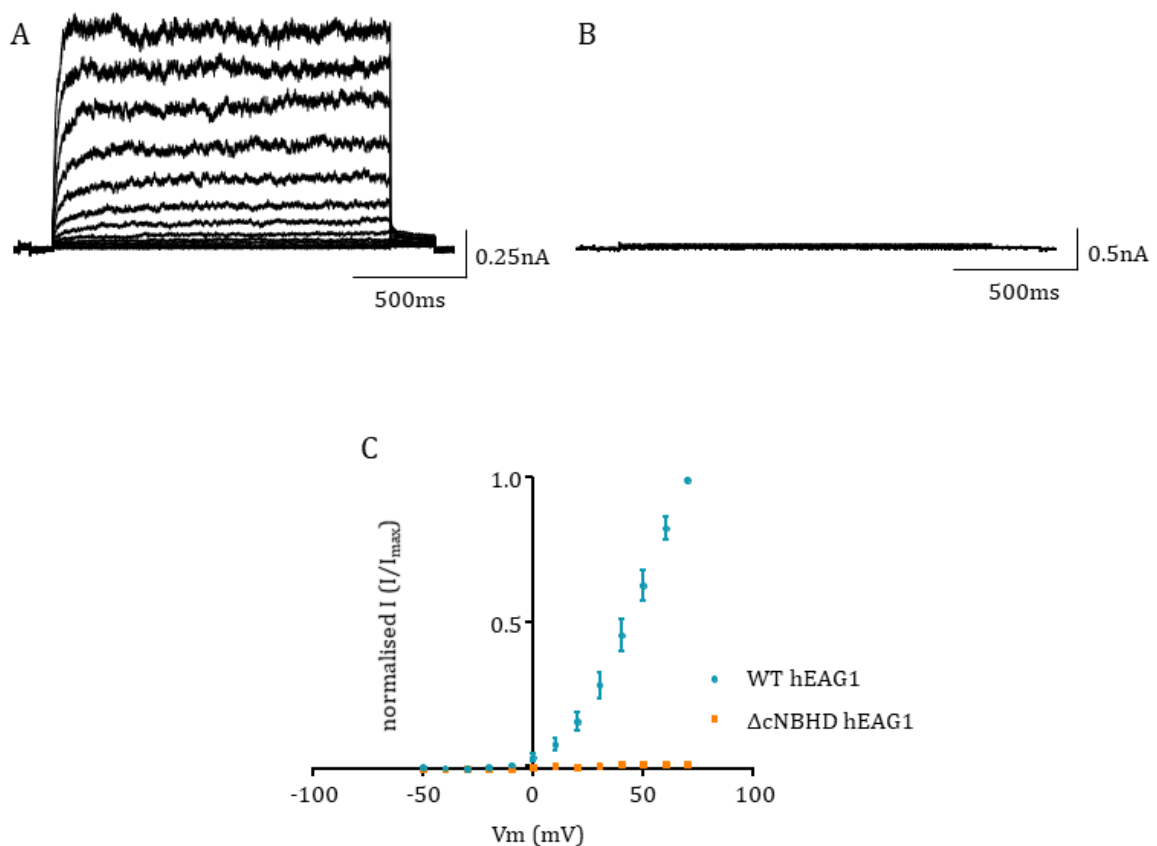


Figure 5.17. There is a loss of function of Δ cNBHD hEAG1 when expressed in CHO cells.

A: currents elicited from WT hEAG1 in response to the I/V protocol. Current amplitude increases with each depolarisation of the membrane.

B: this shows that the I/V protocol does not elicit any hEAG1 currents from Δ cNBHD hEAG1 transfected cells.

C: this I/V relationship shows the response of the WT channel (blue) to the increasing voltage of the I/V protocol. There is no current shown for Δ cNBHD hEAG1 (orange) (n=7).

E600R hEAG1 was one of the constructs that caused a reduction in the number of proliferating cells (Figure 5.2). In patch clamp recordings slowly activating currents that increased in amplitude initially before rectifying at positive potentials were observed (Figure 5.18b). These are characteristics similar to that of Δ EAG hEAG1, the other construct that affected proliferation and were similar to E600R hEAG1 currents in oocytes. The activation time course of E600R hEAG1 was 419.6 ± 71.3 ms at +60mV which was slower than that of the WT channel ($p < 0.01$, $n = 11$, Table 4.).

The mean I/V relationship shows that E600R hEAG1 passes current at more negative membrane potentials than WT hEAG1 (Figure 5.18c). The current peaks at +10mV before reducing with further increases in membrane potential. This contrasts with the WT channel that does not rectify.

The G/V graph shows the same as the I/V curve, that the conductance increases with voltage and reduces again at positive membrane potentials (Figure 5.18d). The $V_{0.5}$ value was measured as being -25.5 ± 3.2 mV which is considerably more negative than the WT current ($p < 0.0001$, $n = 11$, Table 4.). The k value was 9.3 ± 1.2 mV which is lower than the k value of WT hEAG1 but not significantly ($p > 0.05$, $n = 11$, Table 4.). This data shows that E600R hEAG1 has a negatively shifted activation voltage and activates with a slowed time course compared to the WT channel and the voltage dependence was similar in CHO cells to oocytes.

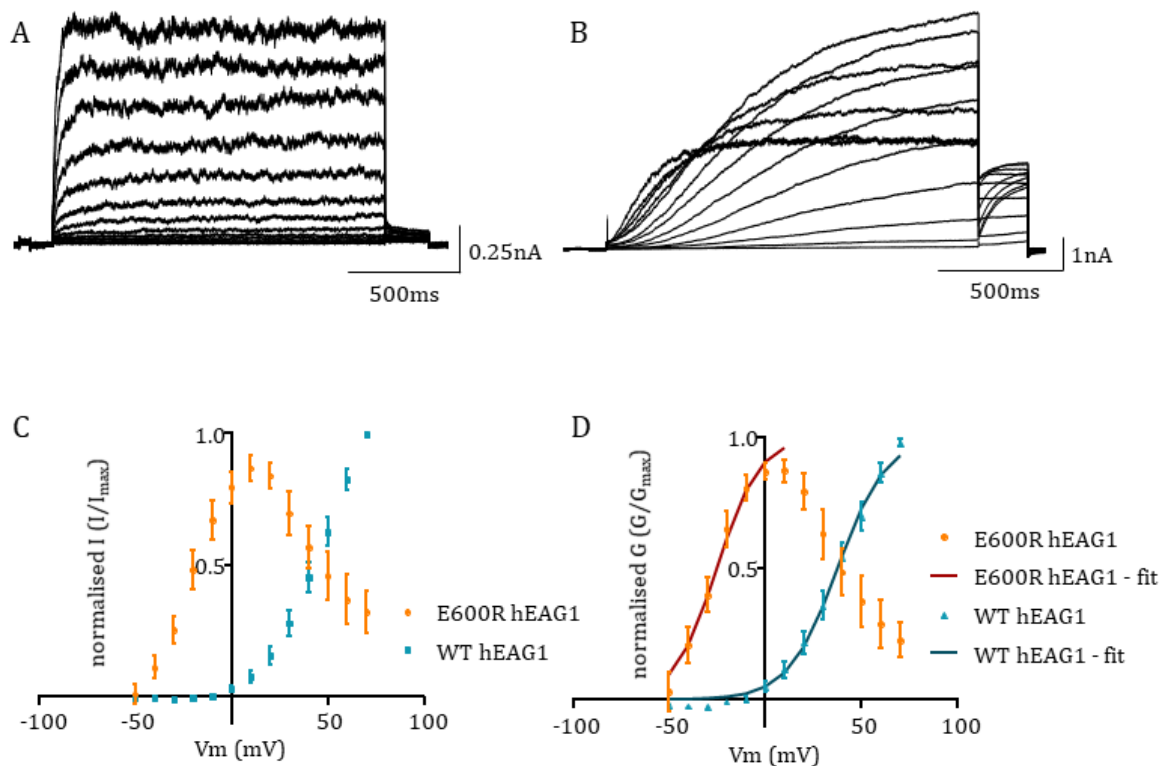


Figure 5.18. Data showing how E600R hEAG1 responds to the I/V protocol when expressed in CHO cells.

A: currents elicited from the WT hEAG1 channel under the I/V protocol, currents are shown for comparison and have been previously described in Figure 4.2.

B: currents elicited from E600R hEAG1 when using the I/V protocol. These are slower to activate than the WT channel and do not reach a steady state plateau during the voltage pulse. Currents from E600R hEAG1 also begin reducing in amplitude with more depolarising voltages.

C: I/V curves showing how each channel's current changes with voltage. WT hEAG1 is shown for comparison (blue) and the channel passes more current with each successive depolarisation. E600R hEAG1 (orange) initially passes more current at negative voltages than the WT channel and continues increasing up to +10mV. After +10mV the current amplitude reduces with depolarisation.

D: G/V curves showing the difference in conductance between WT hEAG1 (blue) and E600R hEAG1 (orange). E600R hEAG1 activates at more negative membrane potentials (-40mV) and peaks at 0mV. WT hEAG1 activates at 0mV and the conductance increases with each depolarisation. Data are fitted with a Boltzmann function (dark red and dark blue respectively).

Like Δ EAG hEAG1, E600R hEAG1 currents in oocytes have previously been shown to increase in amplitude when exposed to $5\mu\text{M}$ I&T. Cells expressing E600R hEAG1 showed an increase in the current amplitude following the application of $5\mu\text{M}$ I&T (Figure 5.19a).

In good quality recordings the current amplitude would increase after the application of $5\mu\text{M}$ I&T. Only 2 cells expressing E600R hEAG1 was of good enough quality to analyse (Figure 5.19b) hence why no mean data are presented. More recordings are needed for statistical analysis.

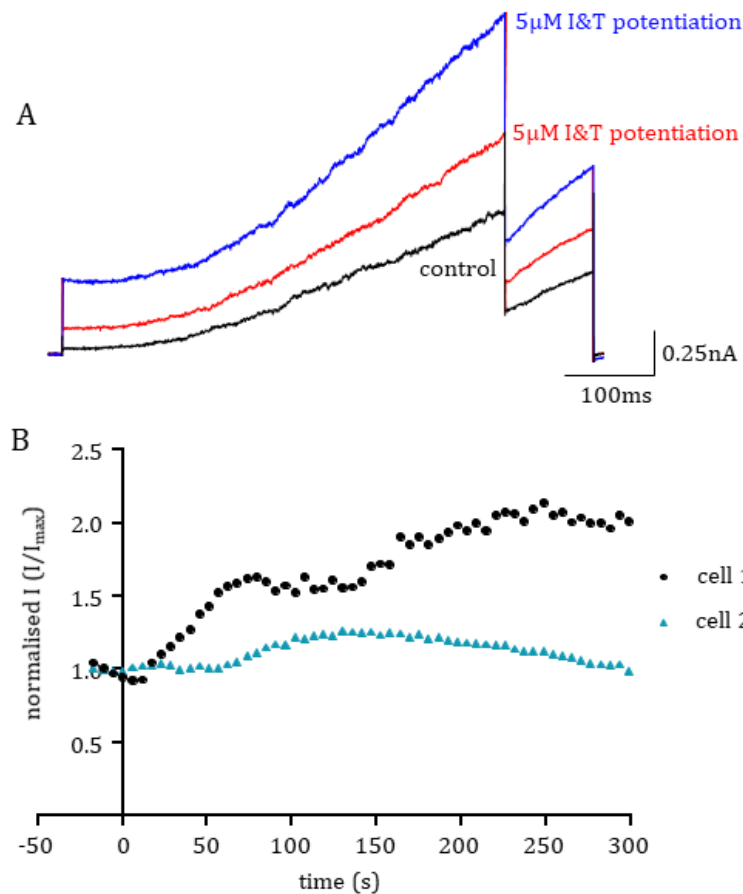


Figure 5.19. Data from E600R hEAG1 expressing CHO cells showing the response of the channel to $5\mu\text{M}$ I&T.

A: representative current traces from E600R hEAG1 elicited by steps to +20mV. The traces show the current in control (black) and after the addition of $5\mu\text{M}$ I&T (red at 160s and blue at 300s).

B: this graph shows the different responses of cell expressing E600R hEAG1 after addition of $5\mu\text{M}$ I&T. Amplitudes of single cell currents are plotted against time and where normalised to the amplitudes in control.

BD-C2 hEAG1 was the final construct to be tested under whole cell patch clamp. This channel produced currents that appeared similar to WT hEAG1 (Figure 5.20). The activation time course from 10-80% was measured to be 110.8 ± 48.8 ms at +60mV which is faster than that of WT hEAG1 albeit not significantly ($p > 0.05$, $n=5$, Table 4.).

The mean I/V relationship shows that BD-C2 hEAG1 currents have a voltage dependence that is negatively shifted relative to WT hEAG1 currents that begin to plateau at positive membrane potentials (Figure 5.20c). The mean G/V relationship for BD-C2 hEAG1 had a $V_{0.5}$ value of 16.8 ± 5.8 mV which is significantly more negative than that of WT hEAG1 ($p < 0.01$, $n=5$, Figure 5.20d, Table 4.). The k value was measured to be 10.9 ± 0.5 mV which is close to the k value of the WT channel ($p > 0.05$, $n=5$, Table 4.).

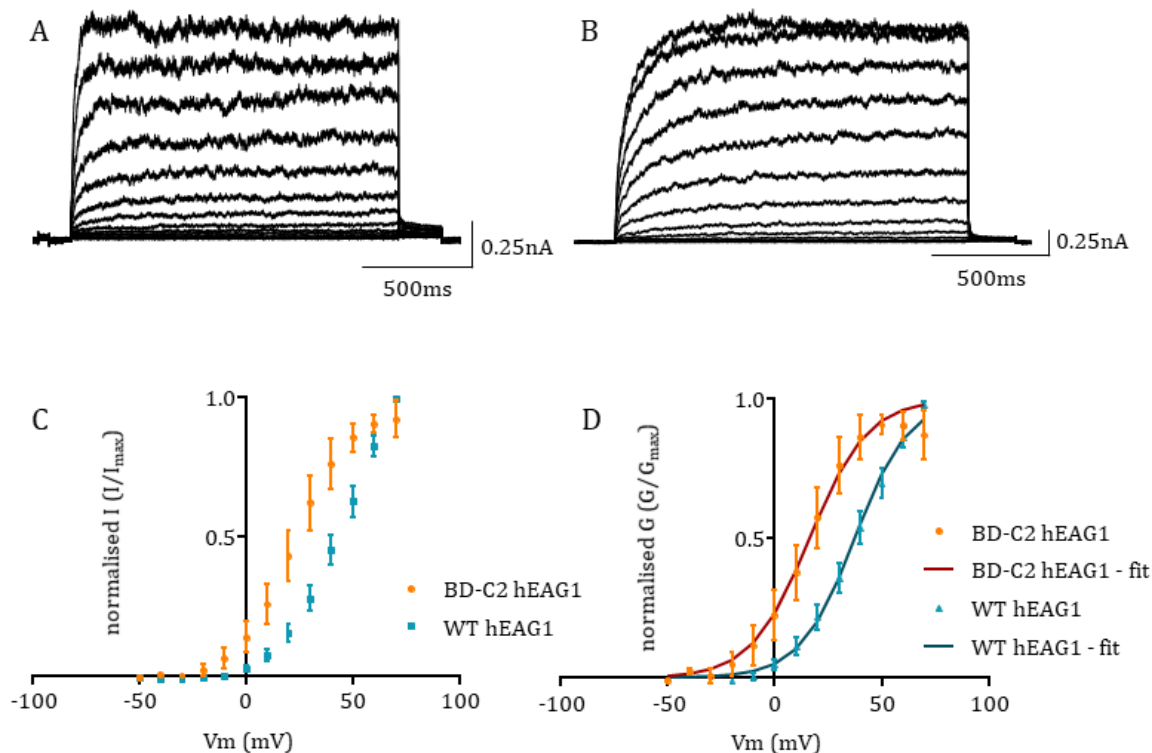


Figure 5.20. Data showing how BD-C2 hEAG1 responds to the I/V protocol when expressed in CHO cells.

A: currents elicited from the WT hEAG1 channel under the I/V protocol, currents are shown for comparison and have been previously described in Figure 4.2.

B: currents elicited from BD-C2 hEAG1 when using the I/V protocol. These are similarly quick to activate compared to the WT channel and reach a steady state plateau during the voltage pulse. Currents from BD-N1 hEAG1 do not reduce in amplitude with more depolarising voltages.

C: I/V curves showing how each channel's current changes with voltage. WT hEAG1 is shown for comparison (blue). BD-C2 hEAG1 (orange) follows a very similar trend as the WT channel and increase in current amplitude with each successive depolarisation.

D: G/V curves showing the difference in conductance between WT hEAG1 (blue) and BD-C2 hEAG1 (orange). BD-C2 hEAG1 activates at -20mV whereas WT hEAG1 activates at 0mV. Both conductances increase with each depolarisation. Data for WT hEAG1 and BD-N1 hEAG1 are fitted with a Boltzmann function (dark blue and dark red respectively).

BD-C2 hEAG1 was recorded under high Ca^{2+} conditions to make sure it followed the same pattern as in the oocytes. BD-C2 hEAG1 was inhibited gradually by the $5\mu\text{M}$ I&T with no recovery of the current amplitude following the inhibition (Figure 5.21a). The current was inhibited by $49.4 \pm 4.9\%$ compared to control but this was not a significant change ($p>0.05$, $n=5$, Table.2, Figure 5.21b). This data, including that of previous mutants, indicates that there is a difference in the response of the channels to $5\mu\text{M}$ I&T between oocytes and CHO cells.

Plotting data from individual cells is shown in Figure 5.21, it demonstrates the differences in response to the $5\mu\text{M}$ I&T. Some cells are inhibited quickly and then recover their current amplitude in a similar manner to the response in the oocytes as shown by the black data points (Figure 5.21c). Other cells were gradually inhibited following the application of $5\mu\text{M}$ I&T as shown by the blue data points (Figure 5.21c). This data indicates that there is a lot of variation in response and that this may be down to Ca^{2+} levels that vary between individual cells.

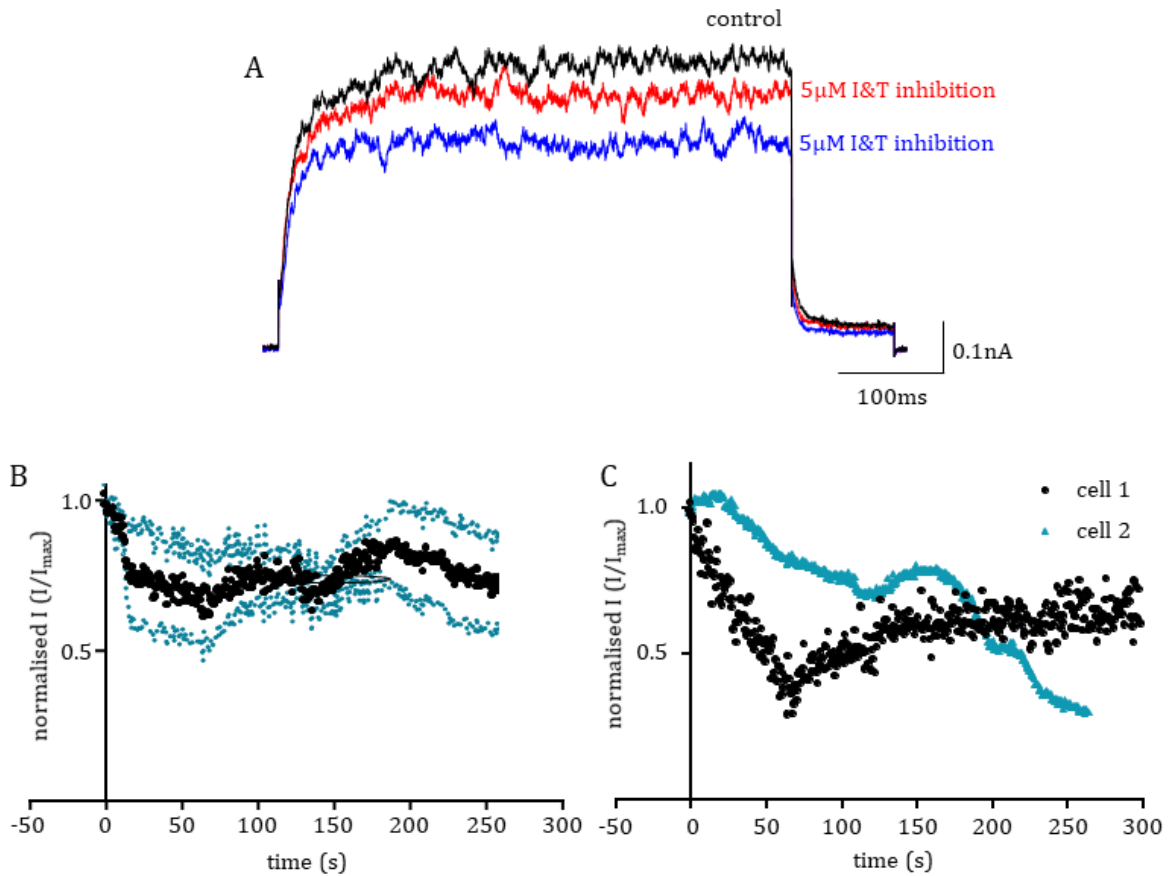


Figure 5.21. Data from BD-C2 hEAG1 expressing CHO cells showing the response of the channel to 5µM I&T.

A: representative current traces from BD-N1 hEAG1 elicited by steps to +20mV. The traces show the current in control (black) and after the addition of 5µM I&T (red at 160s and blue at 250s).

B: a graph showing the normalised response of the current amplitude over time when 5µM I&T was added at t=0. Data is normalised to control values (n=5). The graph shows a small decrease in current amplitude over time that oscillates with time. SEM is shown as blue dots.

C: this graph shows the different responses of cell expressing BD-C2 hEAG1 after addition of 5µM I&T. Amplitudes of single cell currents are plotted against time and were normalised to the amplitudes in control.

5.1.6. Addition of 140mM K⁺ causes rapid and consistent reduction in WT hEAG1 current

The patch clamp data obtained so far from the CHO cells shows that there is a lot of variation in response to the addition of 5 μ M I&T. This variation may be down to variable intrinsic factors of the cells but it may also be due to variation in the functionality of the perfusion system – since it has to be manually positioned each time. To test if this is the case, extracellular solution containing 140mM K⁺ instead of 5mM K⁺ was perfused over cells expressing WT hEAG1. If the perfusion is positioned well, the change to an 140mM K⁺ solution (equimolar with the intracellular K⁺) will result in a rapid reduction in the amount of hEAG1 current as the driving force for the ions is reduced.

Current traces of WT hEAG1 in control solution (containing 5mM K⁺) and 140mM K⁺ are shown in Figure 5.22. Figure 5.22a shows the WT channel elicited by the standard I/V protocol in 5mM K⁺. The currents are large. Following the change in extracellular K⁺ to 140mM the currents are now reduced in amplitude (Figure 5.22b). The mean I/V curve shows the large currents recorded in control conditions compared with the smaller currents recorded in 140mM K⁺. The change to 140mM K⁺ consistently reduced the amplitude of currents at every voltage in all 5 cells indicating that the perfusion is reliable (Figure 5.22c).

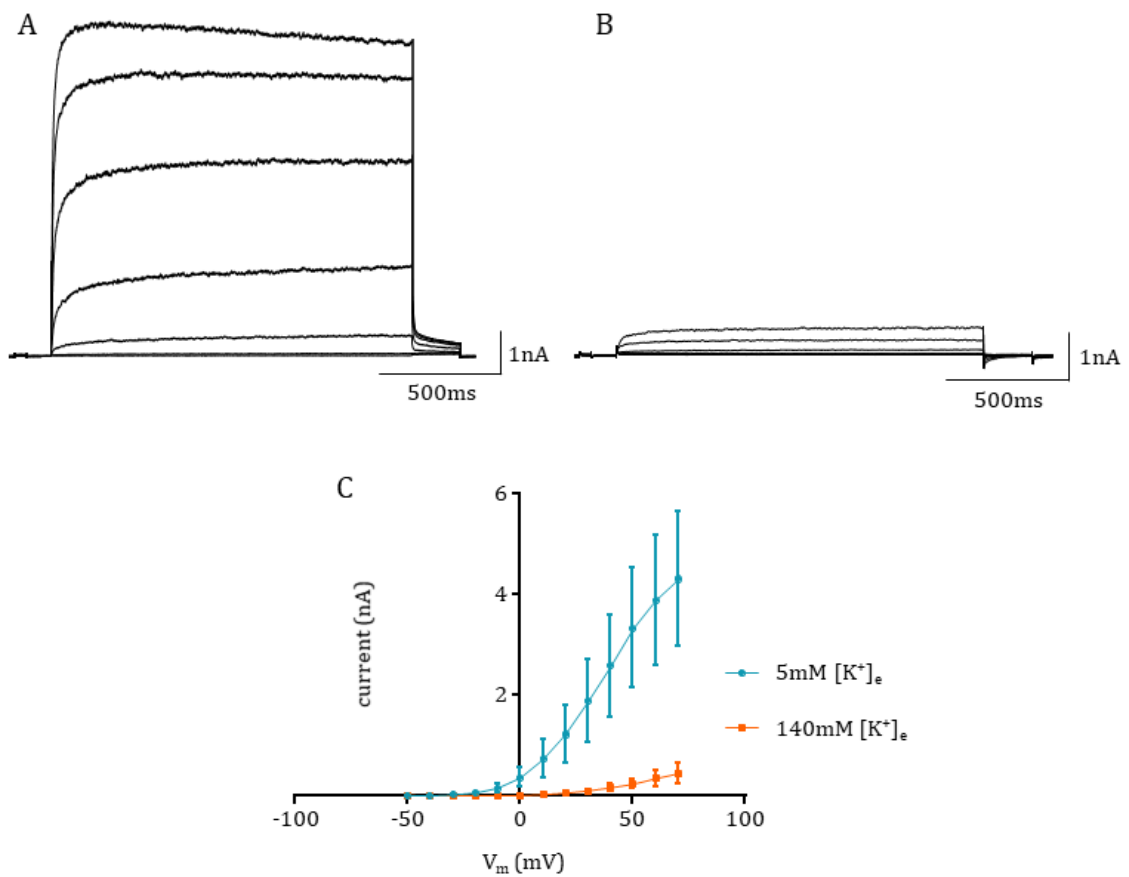


Figure 5.22. Data of WT hEAG1 showing how changing the extracellular solution from control (5mM K^+) to 140mM K^+ affects hEAG1 channel function.

A: WT hEAG1 currents in control solution which contains 5mM K^+ elicited by the I/V protocol. These currents are large in amplitude.

B: Currents from the same cell expressing WT hEAG1 following exposure to solution containing 140mM K^+ . These currents are reduced in amplitude compared to those in the control solution.

C: an I/V graph showing the differences in current amplitude between the 5mM K^+ control solution (blue) and that containing 140mM K^+ (orange). The current in 140mM K^+ is greatly reduced at all voltages measured.

The reduction in hEAG1 current after switching to 140mM K⁺ was plotted against time to measure how quickly the current responds to the change in extracellular K⁺. The current amplitude was inhibited quickly after the addition of 140mM K⁺ (Figure 5.23). It took 14.4 ± 2.4 s for the current be inhibited by 50%.

This data shows that the perfusion system is functioning well and changes in the solutions are “seen” by the cells relatively quickly after their application, this would indicate that the variation in current responses to 5 μ M I&T as seen previously are down to factors of the cells themselves and not the positioning of the perfusion system.

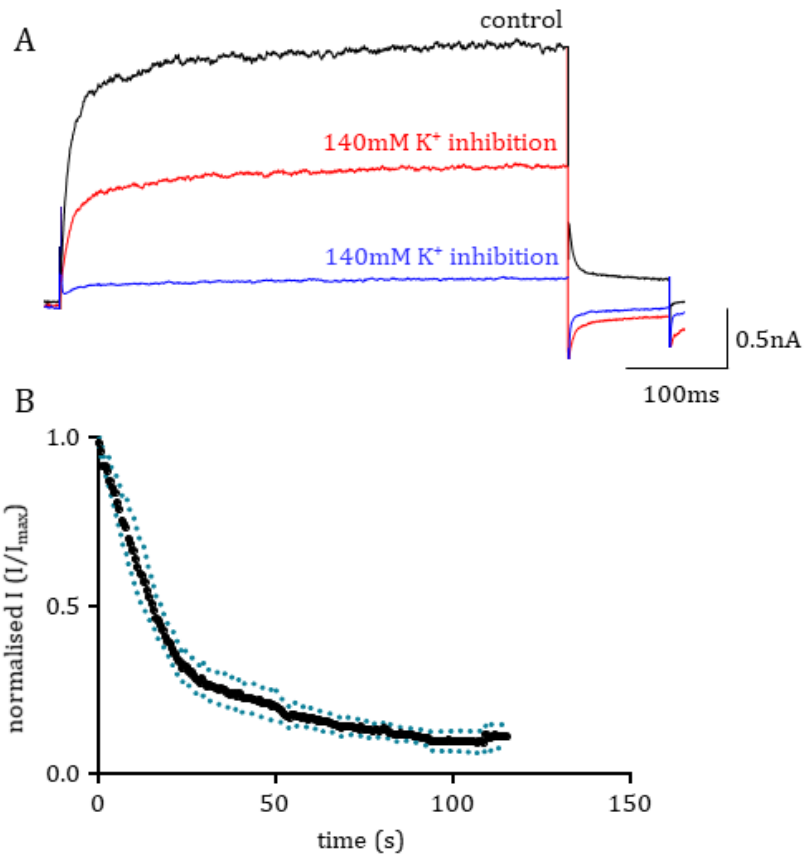


Figure 5.23. Steady pulsing data showing the change in WT hEAG1 current amplitude following the addition of 140mM $[K^+]_e$.

A: representative current traces in control (black) and following the change of extracellular K^+ to 140mM (red trace is 15s and the blue trace is 100s). Note the change in direction of the tail currents following the addition of 140mM $[K^+]_e$.

B: normalised mean end pulse current is plotted against time. Data is normalised against control current values (n=5).

5.1.7. WT hEAG1 does not affect CHO cell migration when grown in either 0.1% or 10% FBS

To date there is no data available to suggest hEAG1 has a role in the migration of cells that express it. Proliferation and migration are both considered hallmarks of cancerous cells and so the role of WT hEAG1 in various parameters of migration was tested.

CHO cells were grown in either 0.1% FBS or 10% FBS medium and transfected with pXoon or WT hEAG1. Transfected cells were imaged for 24hrs and 6 parameters were analysed which were; track displacement length which is the straight line distance from the point of origin than the cell moved in 24hrs, track length which is the overall distance travelled by the cell, track duration which is the length of time the cell was moving for, track straightness which indicates whether the cell moved back and forth (low values) or whether it moved in a direct line (high values). The last 2 parameters were measures of speed, average speed which is the mean of all the speeds travelled by a cell and maximum speed which was the fastest each cell moved between frames. Representative cell images taken at t=0 through to t=24 every 6hrs in 0.1% FBS medium are shown in Figure 5.24 and 10% FBS medium in Figure 5.25.

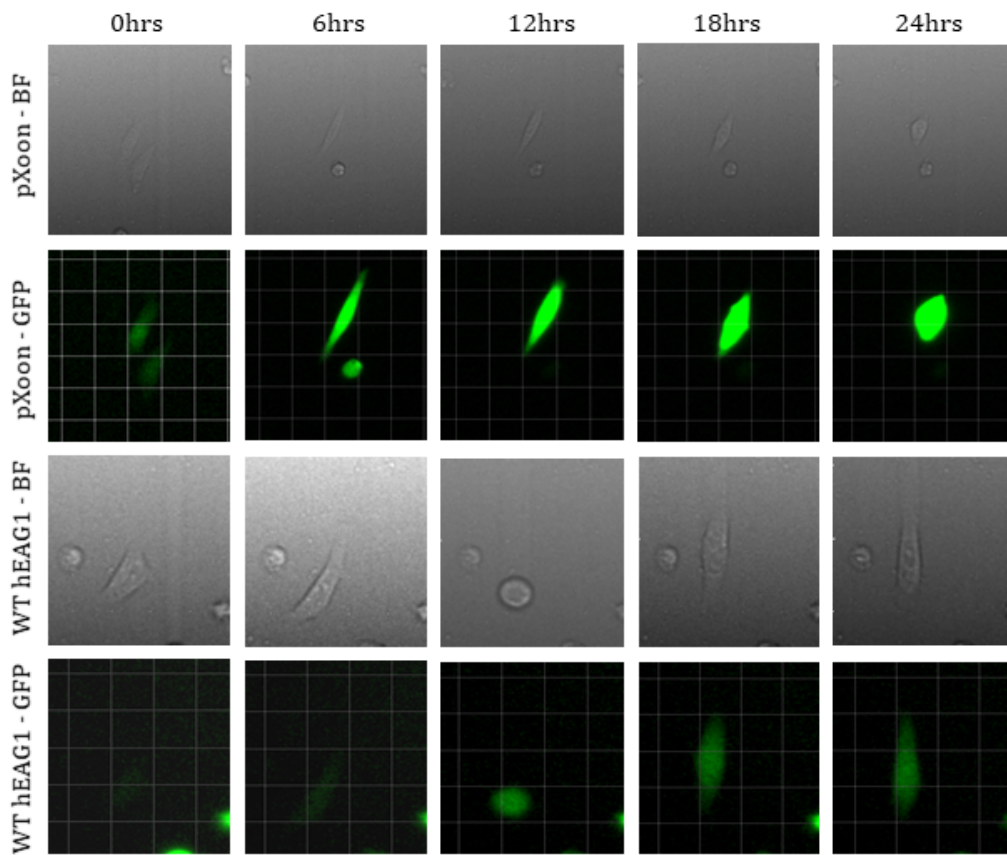


Figure 5.24. Images of pXoon and WT hEAG1 transfected CHO cells at 6hr intervals during the migration assay in 0.1% FBS.

The panel shows both the bright field (BF) and GFP images of transfected cells throughout the migration assay. Cells were tracked for 24hrs with some changing their morphology such as the example of WT hEAG1 at 12hrs. These cells were grown and tracked in media containing 0.1% FBS.

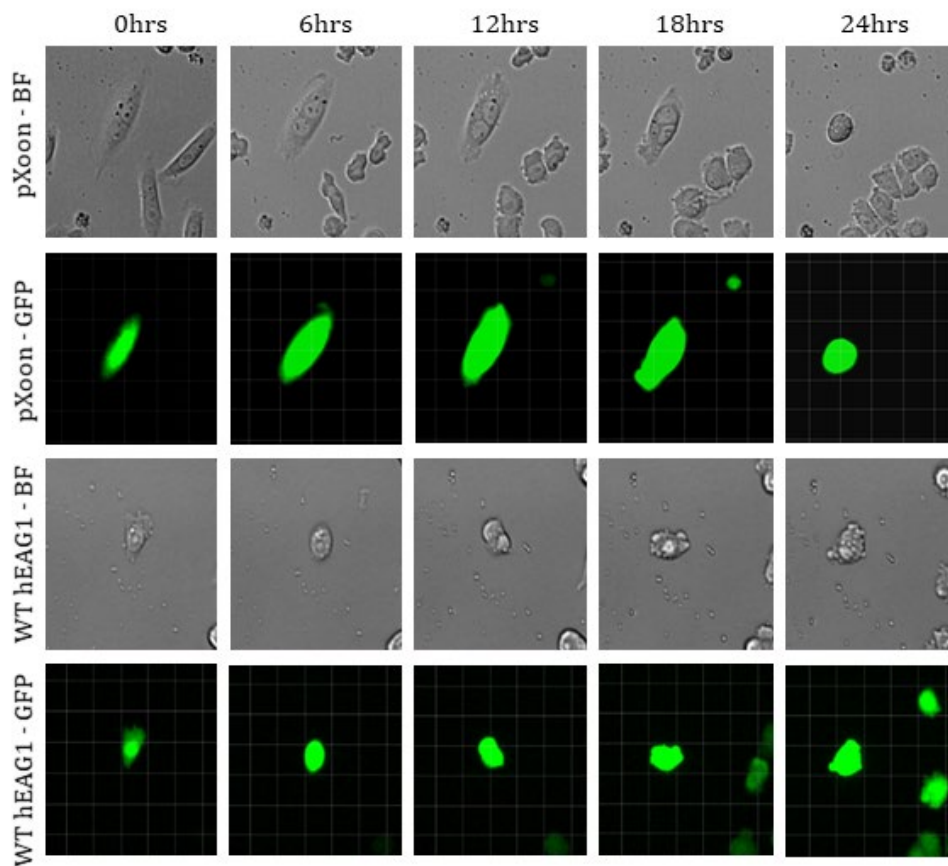


Figure 5.25. An image panel showing the migration of pXoon and WT hEAG1 expressing CHO cells in 10% FBS.

These image panels show transfected cells in both the bright field (BF) and the GFP images of CHO cells.

In cells tested in 0.1% FBS there was a decrease in the track displacement length in the WT hEAG1 cells compared to the pXoon cells (Figure 5.26a). However, there was no significant difference in the track displacement length between the pXoon control which was $20.2 \pm 6.3\mu\text{m}$ and WT hEAG1 expressing cells which was $19.6 \pm 5.4\mu\text{m}$ (both $p>0.05$, $n=3$, Table 5.). When the CHO cells were grown in 10% FBS there was an increase in the track displacement length in cells expressing WT hEAG1 compared to those expressing pXoon (Figure 5.26b). The pXoon expressing cells had a track displacement length of $9.5 \pm 1.1\mu\text{m}$ and WT hEAG1 cells had a value of $11.7 \pm 0.6\mu\text{m}$ which was again found not to be significant ($p>0.05$, $n=3$, Table 5.).

Track length was measured to be $138.8 \pm 16.5\mu\text{m}$ for pXoon cells grown in 0.1% FBS. WT hEAG1 cells grown in the same medium had a shorter track length of $121.1 \pm 13.3\mu\text{m}$ (Figure 5.26c). This reduction was found to not be a significant change from the pXoon cells ($p>0.05$, $n=3$, Table 5.). Similarly, WT hEAG1 cells grown in 10% FBS also showed a shorter track duration of $73.9 \pm 4.4\mu\text{m}$ compared to $75.2 \pm 7.2\mu\text{m}$ of pXoon cells (Figure 5.26d). There was no significant change in their track lengths ($p>0.05$, $n=3$, Table 5.).

CHO cells grown in 0.1% FBS expressing WT hEAG1 had a reduced track duration compared to CHO cells expressing pXoon (Figure 5.26e). On average, pXoon cell tracks lasted $20.5 \pm 0.7\text{hrs}$ whilst WT hEAG1 cells lasted $17.5 \pm 0.9\text{hrs}$, however this was not a significant change ($p>0.05$, $n=3$, Table 5.). Track duration was also measured in 10% FBS, cells transfected with WT hEAG1 had longer track lengths than those cells contain pXoon (Figure 5.26f). The values for track length in 10% were $12.2 \pm 0.4\text{hrs}$ and $11.4 \pm 0.8\text{hrs}$ respectively and which had no significant difference between them ($p>0.05$, $n=3$, Table 5.).

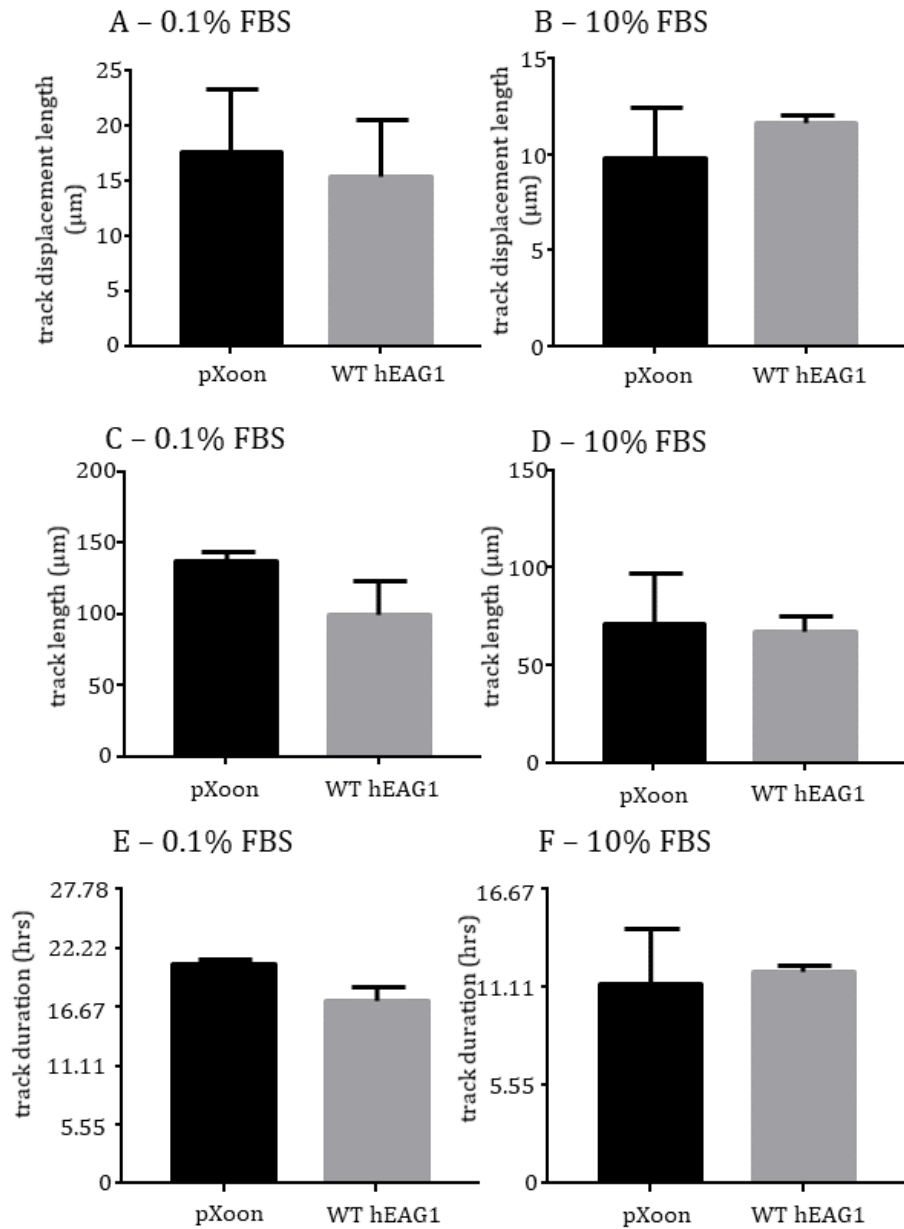


Figure 5.26. Effects of WT hEAG1 expression in CHO cells on track displacement length, track length and track duration.

A & B: the effect of pXoon and WT on track displacement length in 0.1% and 10% FBS respectively.

C & D: the effect of pXoon and WT on track length in 0.1% and 10% FBS respectively.

E & F: the effect of pXoon and WT on track duration in 0.1% and 10% FBS respectively.

The value for track straightness was higher in WT hEAG1 transfected cells than it was for pXoon transfected cells grown in 0.1% FBS. This indicates that WT hEAG1 cells moved in straighter, more direct lines than pXoon cells (Figure 5.27a). Values were measured to be 0.1 ± 0.02 and 0.2 ± 0.02 respectively which was not a significant increase ($p > 0.05$, $n=3$, Table 5.). Track straightness was also measured for cells grown in 10% FBS, here the difference between pXoon and WT hEAG1 cells was almost nothing (Figure 5.27b). The values were measured to be 0.2 ± 0.02 and 0.19 ± 0.01 for pXoon and WT hEAG1 respectively and this was not a significant difference ($p > 0.05$, $n=3$, Table 5.).

The average speed for WT hEAG1 expressing cells grown in 0.1% FBS was lower than that of pXoon expressing cells with values of $1.0 \times 10^{-3} \pm 2.7 \times 10^{-4} \mu\text{m/s}$ and $1.1 \times 10^{-3} \pm 9.4 \times 10^{-5} \mu\text{m/s}$ respectively (Figure 5.27c). This reduction in average speed was not significant and indicates that the presence of WT hEAG1 does not affect the average speed of CHO cell migration in 0.1% FBS ($p > 0.05$, $n=3$, Table 5.). The average speed was also measured in 10% FBS where it was found that the expression of WT hEAG1 caused no change in the average speed when compared to pXoon expressing CHO cells (Figure 5.27d). The values for pXoon and WT hEAG1 cells were measured to be $1.0 \times 10^{-3} \pm 7.3 \times 10^{-5} \mu\text{m/s}$ and $1.0 \times 10^{-3} \pm 5.8 \times 10^{-5} \mu\text{m/s}$ respectively which was a non-significant change ($p > 0.05$, $n=3$, Table 5.).

The final parameter measured was the maximum speed of the cells, in 0.1% FBS cells expressed WT hEAG1 showed a lower maximum speed than cells expressing pXoon (Figure 5.27e). pXoon cells had a maximum speed of $7.5 \times 10^{-3} \pm 1.9 \times 10^{-3} \mu\text{m/s}$ whilst WT hEAG1 cells had a maximum speed of $6.9 \times 10^{-3} \pm 9.6 \times 10^{-4} \mu\text{m/s}$, this was not found to be a significant change ($p > 0.05$, $n=3$, Table 5.). Maximum speed was also measured in 10% FBS where it was found that cells expressing WT hEAG1 had a reduced maximum speed than those expressing pXoon (Figure 5.27f). The values for pXoon and WT hEAG1 expressing cells are $4.4 \times 10^{-3} \pm 2.8 \times 10^{-4} \mu\text{m/s}$ and $4.3 \times 10^{-3} \pm 1.8 \times 10^{-4} \mu\text{m/s}$ respectively, however this decrease was not found to be statistically significant ($p > 0.05$, $n=3$, Table 5.).

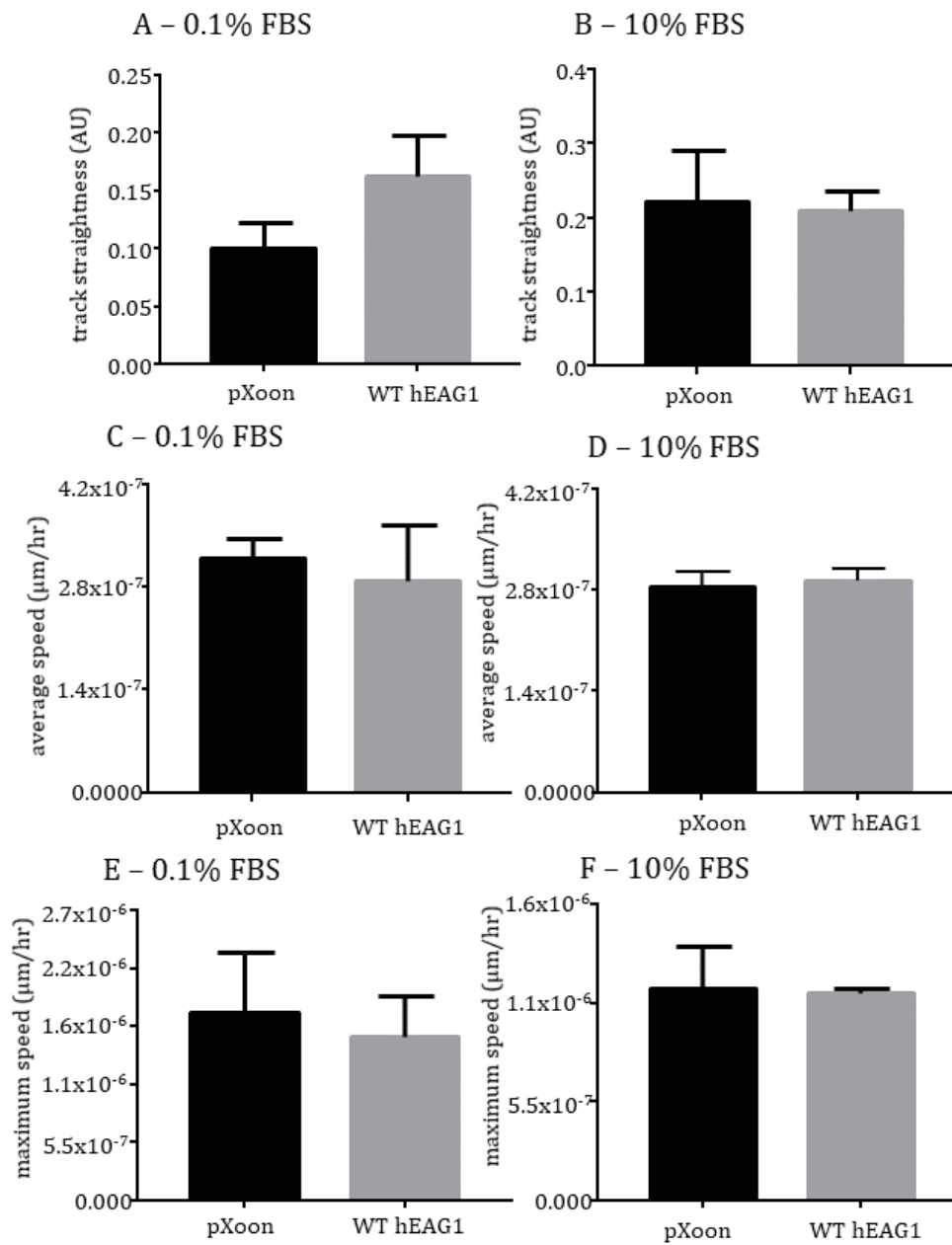


Figure 5.27. Effects of WT hEAG1 expression in CHO cells on track straightness, average speed and maximum speed.

A & B: the effect of pXoon and WT on track straightness in 0.1% and 10% FBS respectively.

C & D: the effect of pXoon and WT on average speed in 0.1% and 10% FBS respectively.

E & F: the effect of pXoon and WT on maximum speed in 0.1% and 10% FBS respectively.

Since migration parameters were measured for pXoon and WT hEAG1 expressing cells in two different FBS concentrations, the data was analysed to see if the concentration of FBS had an effect on pXoon or WT hEAG1 CHO cells. Representative images of pXoon and WT hEAG1 transfected cells in both the bright field and fluorescent filters are shown in Figure 5.25. This image panel shows that neither cell transfection survives the full 24hr time period when grown in 10% FBS medium which is different from that observed of cells grown in 0.1% FBS medium (Figure 5.24).

The track displacement length of CHO cells expressing pXoon was shorter for cells grown in 10% FBS compared to those in 0.1% FBS (Figure 5.28a). This was a reduction from $20.2 \pm 6.3\mu\text{m}$ in 0.1% FBS to $9.5 \pm 1.1\mu\text{m}$ in 10% FBS. Despite the seemingly large reduction, there was no significant change between the two medium types ($p>0.05$, $n=3$, Table 5.). WT hEAG1 expressing cells also had shorter track displacement lengths in 10% FBS compared to those in 0.1% FBS (Figure 5.28b) reducing from $19.6 \pm 5.4\mu\text{m}$ to $11.7 \pm 0.6\mu\text{m}$. This reduction was also not found to be significant ($p>0.05$, $n=3$, Table 5.).

The track length of pXoon expressing cells was shorter when cells were grown in 10% FBS than when grown in 0.1% FBS (Figure 5.28c). In 0.1% FBS, the track length was $138.8 \pm 16.5\mu\text{m}$ and it reduced to $75.2 \pm 7.2\mu\text{m}$ in 10% FBS however this was not significant ($p>0.05$, $n=3$, Table 5.). Similarly cells expressing WT hEAG1 also had shorter track lengths when grown in 10% FBS than in 0.1% FBS (Figure 5.28d). The track length reduced from $121.1 \pm 13.3\mu\text{m}$ in 0.1% FBS to $73.9 \pm 4.4\mu\text{m}$ which was not a significant reduction ($p>0.05$, $n=3$, Table 5.).

Cells expressing pXoon or WT hEAG1 both had significant reductions in their track durations in 10% FBS compared to cells in 0.1% FBS (Figure 5.28e and f). CHO cells expressing pXoon reduced from $20.5 \pm 0.7\text{hrs}$ to $11.4 \pm 0.8\text{hrs}$ ($p<0.05$, $n=3$, Table 5.) whilst cells expressing WT hEAG1 reduced from $17.5 \pm 0.9\text{hrs}$ to $12.2 \pm 0.4\text{hrs}$ ($p<0.05$, $n=3$, Table 5.). This indicates that cells grown in 10% FBS do not survive as long as cells grown in 0.1% FBS.

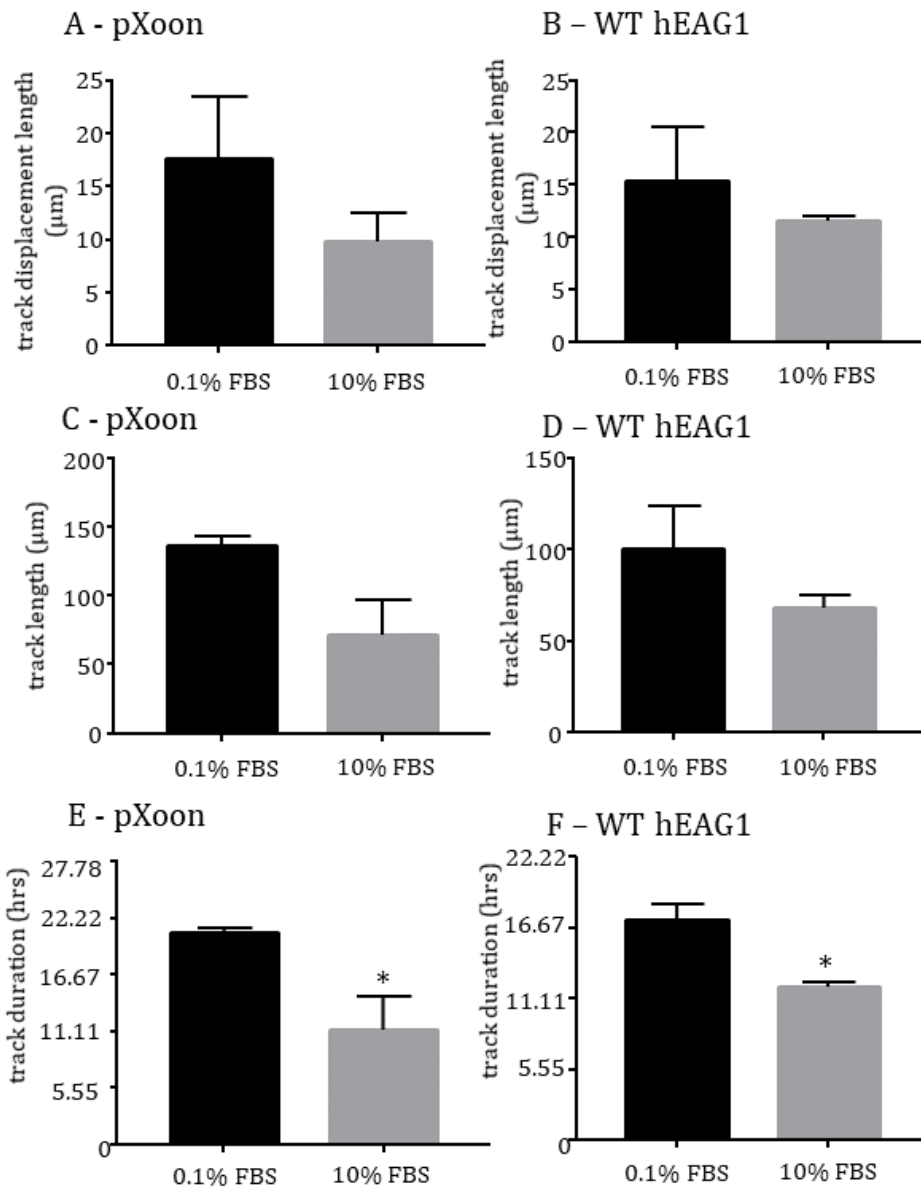


Figure 5.28. Effects of 0.1% and 10% FBS media on track displacement length, track length and track duration of pXoon and WT hEAG1 expressing CHO cells.

A & B: the effect of 0.1% and 10% FBS on track displacement length.

C & D: the effect of 0.1% and 10% FBS on track length.

E & F: the effect of pXoon and WT on track duration.

Track straightness was higher – indicating a straighter line – in pXoon cells grown in 10% FBS than those grown in 0.1% FBS (Figure 5.29a). The value rose from 0.1 ± 0.02 to 0.2 ± 0.02 , an increase that was not significant ($p > 0.05$, $n=3$, Table 5.). Cells expressing WT hEAG1 also had a higher value for track straightness when grown in 10% FBS compared with cells grown in 0.1% FBS (Figure 5.29b). In these cells the value rose from 0.15 ± 0.02 to 0.19 ± 0.01 in 0.1% FBS and 10% FBS respectively however this increase was also not significant ($p > 0.05$, $n=3$, Table 5.).

The average speed of cells expressing pXoon decreased in 10% FBS when compared to 0.1% FBS (Figure 5.29c). The speed decreased from $1.1 \times 10^{-3} \pm 9.4 \times 10^{-5}$ $\mu\text{m/s}$ to $1.0 \times 10^{-3} \pm 7.3 \times 10^{-5}$ $\mu\text{m/s}$, a decrease that was not found to be significant ($p > 0.05$, $n=3$, Table 5.). The bar chart for WT hEAG1 expressing cells indicates a increase in the average speed in cells grown in 10% FBS than those in 0.1% FBS (Figure 5.29d). The measured values were $1.0 \times 10^{-3} \pm 2.7 \times 10^{-4}$ $\mu\text{m/s}$ for 0.1% FBS and $1.0 \times 10^{-3} \pm 5.8 \times 10^{-5}$ $\mu\text{m/s}$ for 10% FBS, these values were not significantly different ($p > 0.05$, $n=3$, Table 5.).

The maximum speed of cells was also compared, the pXoon cells had a slower maximum speed in 10% FBS compared to cells in 0.1% FBS (Figure 5.29e). The maximum speed was $7.5 \times 10^{-3} \pm 1.9 \times 10^{-3}$ $\mu\text{m/s}$ in 0.1% FBS and $4.4 \times 10^{-3} \pm 2.8 \times 10^{-4}$ $\mu\text{m/s}$ for 10% FBS. Despite the large reduction in maximum speed it was not found to be significant ($p > 0.05$, $n=3$, Table 5.). The maximum speed of WT hEAG1 expressing cells was also reduced in the 10% FBS cells than in the 0.1% FBS cells (Figure 5.29f). The value decreased from $6.9 \times 10^{-3} \pm 9.6 \times 10^{-4}$ $\mu\text{m/s}$ to $4.3 \times 10^{-3} \pm 1.8 \times 10^{-4}$ $\mu\text{m/s}$, a reduction that was again not significant ($p > 0.05$, $n=3$, Table 5.).

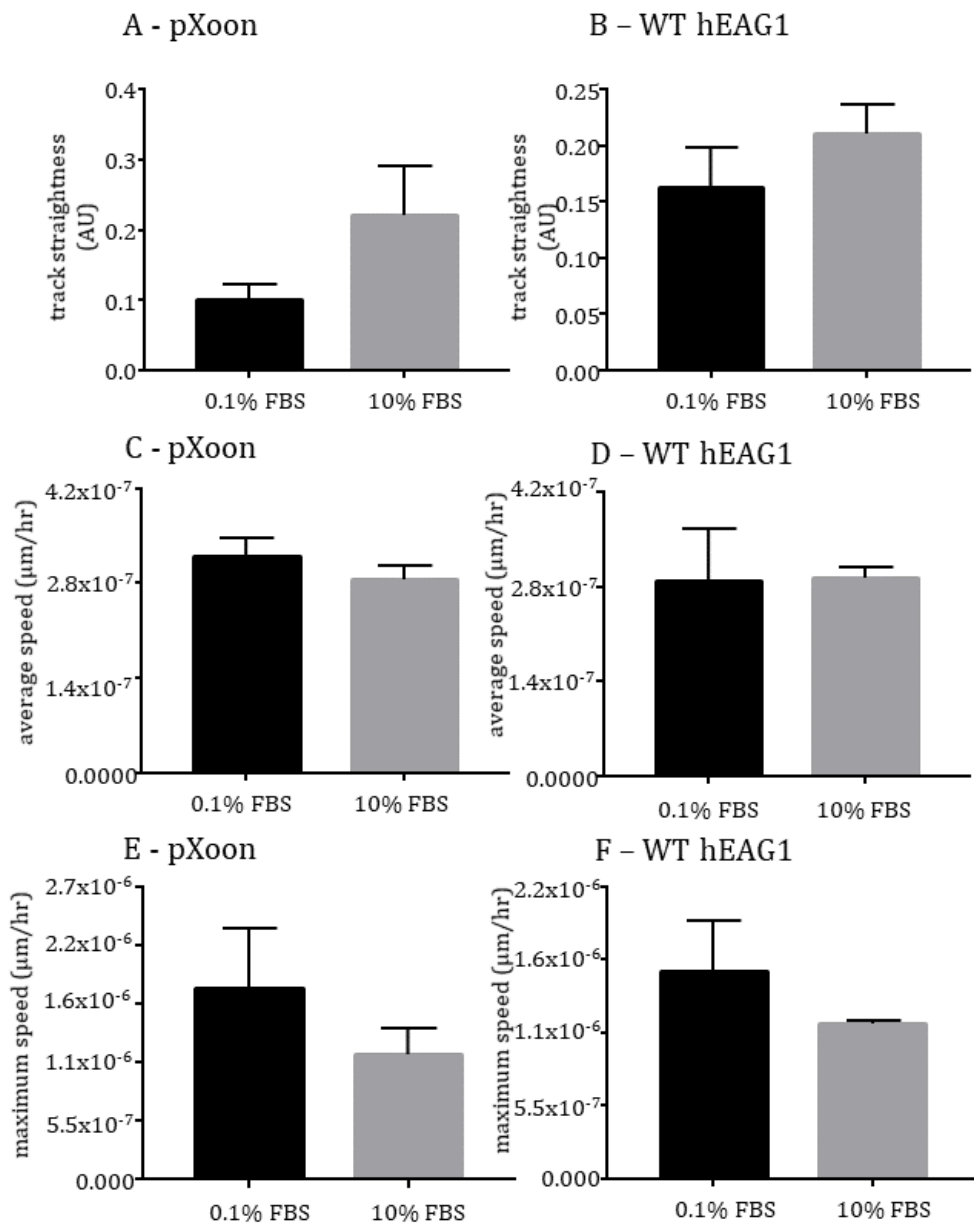


Figure 5.29. Effects of 0.1% and 10% FBS media on track straightness, average speed and maximum speed of pXoon and WT hEAG1 expressing CHO cells.

A & B: the effect of 0.1% and 10% FBS on track straightness.

C & D: the effect of 0.1% and 10% FBS on average speed.

E & F: the effect of pXoon and WT on maximum speed.

Construct	cell size (μm^2)	circularity (AU)	% of ciliated cells	cilia length (μm)	cilia width (μm)
untransfected	215.5 ± 5.1	0.7 ± 0.1	93.3 ± 1.2	1.68 ± 0.06	0.96 ± 0.02
pXoon	207.4 ± 7.1	0.5 ± 0.1	92.5 ± 3.1	1.75 ± 0.07	0.99 ± 0.02
WT hEAG1	223 ± 4.1	0.6 ± 0.02	47.3 ± 2.2	1.77 ± 0.05	0.92 ± 0.02
$\Delta 2-26$ hEAG1	225.3 ± 14.7	0.5 ± 0.1	67.1 ± 6.8	1.7 ± 0.13	0.94 ± 0.01
Δ EAG hEAG1	224.8 ± 7.3	0.5 ± 0.1	78.1 ± 1.9	1.99 ± 0.03	1.03 ± 0.03
BD-N1 hEAG1	217.7 ± 10.3	0.5 ± 0.1	82.2 ± 2.7	1.86 ± 0.04	0.97 ± 0.02
Δ cNBHD hEAG1	205.1 ± 8.4	0.5 ± 0.1	85.9 ± 3.6	1.79 ± 0.11	0.94 ± 0.03
E600R hEAG1	209.1 ± 14.2	0.5 ± 0.1	72.5 ± 4.8	1.86 ± 0.09	1.0 ± 0.02
BD-C2 hEAG1	224.3 ± 7.8	0.6 ± 0.1	71.8 ± 4.9	1.86 ± 0.03	0.95 ± 0.02

Table 3. A table displaying the parameters measured of hTERT-RPE1 cells from immunocytochemistry experiments regarding the primary cilia.

Parameters measured include cell size and circularity which are indicators of changes in cell morphology and may show whether or not the hEAG1 channel affects this. WT hEAG1 has already been shown to reduce the presence of the primary cilia and so this was tested with all mutant constructs. Cilia length and width were also measured to see if some constructs affected the structure of primary cilium itself. All values are presented as mean \pm SEM and significance is indicated by the asterisks (* is <0.05 , ** is <0.01 , *** is <0.001 , **** is <0.0001).

Constructs	% change in I&T	V _{0.5} (mV)	k value	10-80% activation (ms)
WT hEAG1	78.6 ± 5.8 ***	37.2 ± 3.0	10.3 ± 0.6	158.5 ± 40.6
ΔEAG hEAG1	152.1 ± 74.2 *	-13.4 ± 4.6 ****	11.0 ± 1.3	402.6 ± 136.2 *
BD-N1 hEAG1	57.6 ± 13.7	27.6 ± 6.3	12.2 ± 1.0	170.4 ± 71.3
ΔcNBHD hEAG1	n/a	n/a	n/a	n/a
E600R hEAG1	n/a	-25.5 ± 3.2 ****	9.3 ± 1.2	419.6 ± 71.3 **
BD-C2 hEAG1	49.4 ± 4.9	16.8 ± 5.8 **	10.9 ± 0.5	110.8 ± 48.8

Table.4. A table showing the measured parameters of the WT hEAG1 channel along with 5 tested mutants using whole cell patch clamp.

This table shows the parameters measured in CHO cells from the expressed constructs. The percentage change following the addition of 5μM I&T is calculated from the steady pulsing data and were all measured at +20mV. Values highlighted in red are mutants that potentiated their current after 5μM I&T. The V_{0.5} and k values were measured from the Boltzmann fits of the G/V curves and are both expressed in mV. The 10-80% activation time course was measured at +60mV and is measured in ms. Each mutant channel is statistically compared to the WT channel whose data is again shown for comparison. All values are presented as mean ± SEM and significance is indicated by the asterisks (* is <0.05, ** is <0.01, *** is <0.001, **** is <0.0001).

Parameter

pXoon

WT hEAG1

	0.1% FBS	10% FBS	0.1% FBS	10% FBS
Track displacement length (μm)	20.2 ± 6.3	9.5 ± 1.1	19.6 ± 5.4	11.7 ± 0.6
Track length (μm)	138.8 ± 16.5	75.2 ± 7.2	121.1 ± 13.3	73.9 ± 4.4
Track duration (hrs)	20.5 ± 0.7	11.4 ± 0.8	17.5 ± 0.9	12.2 ± 0.4
Track straightness (AU)	0.1 ± 0.02	0.2 ± 0.02	0.15 ± 0.02	0.19 ± 0.01
Average speed ($\mu\text{m/s}$)	$1.1 \times 10^{-3} \pm 9.4 \times 10^{-5}$	$1.0 \times 10^{-3} \pm 7.3 \times 10^{-5}$	$1.0 \times 10^{-3} \pm 2.7 \times 10^{-4}$	$1.0 \times 10^{-3} \pm 5.8 \times 10^{-5}$
Maximum speed ($\mu\text{m/s}$)	$7.5 \times 10^{-3} \pm 1.9 \times 10^{-3}$	$4.4 \times 10^{-3} \pm 2.8 \times 10^{-4}$	$6.9 \times 10^{-3} \pm 9.6 \times 10^{-4}$	$4.3 \times 10^{-3} \pm 1.8 \times 10^{-4}$

Table.5. A table showing the measured parameters of the migration assays conducted in both 0.1% and 10% FBS for pXoon and WT hEAG1 transfected CHO cells.

This table contains the data of six measured parameters; 1. Track displacement length which is the distance in a straight line from the point of origin. 2. Track length which is the overall distance moved by the cell. 3. Track duration which is the length of time the cell was moving. 4. Track straightness which is a measure of how straight the track is, low numbers indicate a track in which the cell changed direction multiple times. 5. Average speed which is an average of the speed between each measured position of the cells. 6. Maximum speed which is the fastest each cell moved throughout the recording period of 24hrs.

5.2. Discussion

5.2.1. Interactions between the EAG domain and the E600 residue may be behind the mechanism of increase cell proliferation but WT hEAG1 does not influence cell migration

WT hEAG1 has previously been shown to increase the proliferation of cells (Pardo *et al.*, 1998; Zhang *et al.*, 2014) and is a known regulator of the cell cycle (Borowiec *et al.*, 2011; Urrego *et al.*, 2016). Hegle *et al.* (2006) provided data that used a non-conducting mutant of hEAG1. This mutant did not increase proliferation as much as the WT channel but it did increase proliferation over control cells. This data suggests that the K⁺ conduction of hEAG1 has a role in its role in proliferation but is not the whole story. However there is no data available about how the intracellular domains or the Ca²⁺-calmodulin sensitivity of the channel contribute to this process.

We provide data that the EAG domain and the E600 residue are important in order for hEAG1 to increase the proliferation of CHO cells. It may be the case that an interaction between the EAG and cNBH domains is important and that mutation of the E600 residue disrupts this but unfortunately the Δ cNBHD hEAG1 construct was not expressed in CHO cells and so we can't say for definite how it would behave. Data gathered for the Δ EAG and E600R mutants in oocytes shows that they both have negatively shifted $V_{0.5}$ values and slowed activation kinetics in control conditions and increase their current following 5 μ M I&T. The same was also true in CHO cells. Hegle *et al.* (2006) have shown that K⁺ conductance is a factor of hEAG1 involved in proliferation. By removing the EAG domain and mutating E600 the channel is able to pass more current at resting membrane potentials than the WT channel. This may indicate that too much K⁺ conductance may be counterproductive in terms of increasing proliferation. hEAG1 has also been shown to be able to interact with and be modulated by different proteins (Piros *et al.*, 1999; Herrmann *et al.*, 2013). Removing a domain or inducing a mutation that may involve structural rearrangements of key areas may cause the potential for these protein interactions to be lost and there may be many proteins involved in proliferation that have yet to be identified as interaction partners of hEAG1.

To date there is no evidence that hEAG1 controls cell migration which is another hallmark of cancer cells (Paul *et al.*, 2017). Other K⁺ channels have been implicated in the migration of cancer cells: e.g. K_{Ca}3.1 in melanoma cells, where the K⁺ conductance appears crucial for the role (Schwab *et al.*, 1999) and hERG, the closely related channel of hEAG1, which also required K⁺ conductance in migrating MDA-MB-435S melanoma cells (Afrasiabi *et al.*, 2010). Despite this, there was no evidence of hEAG1 affecting six migration parameters either in 0.1% FBS or in 10% FBS medium. The only parameter that was significantly changed was track duration, which measures how long a cell migrates for, for both the negative control and hEAG1 when the two medium conditions were compared. It was not a hEAG1 dependent effect and can be explained as CHO cells being more likely to proliferate than migrate under higher FBS concentrations.

5.2.2. The EAG domain, cNBH domain and both calmodulin binding domains are important for the role of hEAG1 in cilia disassembly

The WT channel has been shown to be involved in the process of ciliary disassembly in hTERT-RPE1 cells (Sanchez *et al.*, 2016). Sanchez *et al.* (2016) did not provide mechanistic insight into how hEAG1 might influence deciliation, and since the disassembly of the primary cilium is an indicator of re-entry into the cell cycle we tested the same mutants used in the proliferation assay. When compared statistically to WT, all mutants increased the percentage of ciliated cells. This indicates that large portions of the intracellular domains as well as the ability to bind calmodulin at both high affinity sites may be a requirement for deciliation.

Sanchez *et al.* (2016) provided data showing that hEAG1 localises to the centrosome but do not state how this could be occurring. Should this association rely on the integrity of the intracellular domains in their entirety then mutating any of these would affect the ability to localise there and disassemble the cilia. Further experiments could utilise whether a mutant unable to bind calmodulin at both BD-N1 and BD-C2 would affect the ciliation of cells. If this mutant did affect the ciliation of cells then it would indicate that the sensitivity of hEAG1 to calmodulin is an important factor in this process.

5.2.3. The Ca²⁺ response profile of CHO cells to 5μM I&T was different when WT hEAG1 was stably expressed

Due to the variation in the response of the hEAG1 constructs used to 5μM I&T we conducted Ca²⁺ imaging in CHO cells that were untransfected. These cells showed a 1.5 fold increase in Ca²⁺ signal from control levels when 5μM I&T was applied to the cells. This agrees with data produced in oocytes where the Ca²⁺ level also increases quickly (Lorinczi *et al.*, 2016). In the CHO cells, we then observed a reduction in Ca²⁺ signal that plateaued for the duration of the recording. The design of this experiment was to test whether the Ca²⁺ concentration goes up and stays at that level for the duration of the application, which it did. However there was considerable variation between cells which may go some way to explain why some of the hEAG1 construct recordings did not respond in the same way to 5μM I&T as they did in the oocytes. Whilst thapsigargin was used to prevent uptake of Ca²⁺ into the sarco-endoplasmic reticulum we cannot guarantee that some cells have differences in efficiency of other Ca²⁺ handling mechanisms such as the mitochondria and plasma membrane Ca²⁺ ATPase (Santo-Domingo and Demaurex, 2010).

Something of particular interest was that CHO cells stably expressing WT hEAG1 had a different Ca²⁺ response to 5μM I&T than the untransfected cells. WT hEAG1 expressing CHO cells showed around 1.75 fold increase in Ca²⁺ signal, but the signal then reduced rapidly to ~1.25 fold increase over control before gradually increasing through to the end of the recording. It indicates that the presence of the hEAG1 channel affects how the Ca²⁺ is handled within the cell. Though the mechanism requires further investigation.

Our original hypothesis in terms of hEAG1's response in oocytes to 5μM I&T was that the initial binding of Ca²⁺-calmodulin inhibited the channel by inducing a conformational change that closed the pore. This was then followed by a second conformational change with Ca²⁺-calmodulin still bound in place that allowed the channel to pass current again – albeit with changed activation kinetics. In CHO cells, hEAG1 was inhibited but there was no recovery phase – at least after 5mins. Why the differences exist in the two expression systems is unclear. It may relate to differences in Ca²⁺ concentration, Ca²⁺ time courses or differences in how the hEAG1 channels respond to Ca²⁺-calmodulin. The role of Ca²⁺-calmodulin regulation of

hEAG1 in physiological processes, for example, in the pre-synaptic membranes of neurons remains to be determined.

6. Summary and conclusions

The data provided in this thesis has gone into depth in terms of studying the amphipathic helix of the PAS-cap to decipher how it functions, which residues are important for gating and voltage dependence and also for the Ca^{2+} -calmodulin sensitivity of the channel. We show that two residues in particular, N15 and F17 are critical for the stabilisation of the PAS-cap in its interaction with the EAG and cNBH domains. L18 may also be involved in the stabilisation process as its alanine mutant produced a hybrid response that was similar to the WT channel in respect to the Ca^{2+} sensitivity but was also similar to the $\Delta 2-26$ mutant in terms of voltage dependence. Additional mutagenesis also shows that N15 and E600 may be part of an interaction network as individual mutations behaved in similar ways in both control solution and high Ca^{2+} conditions, however a residue swapped mutant did not rescue a WT-like phenotype as might be expected of two residues whose interaction was highly important to proper channel function. The cryo-EM structure of the channel shows that N15 and F17 residues are on opposite sides of the helix and interact with the cNBHD and EAG domain respectively. This indicates that these residues act to keep the cNBH and EAG domains in close proximity to one another and that disruption of either residue has consequences for the stability of the intracellular domains.

Complete understanding of how N15 and F17 stabilise the helix of the PAS-cap has yet to be achieved and will become apparent given further mutagenesis studies. Cryo-EM or NMR studies of channel structure with either the N15A or F17A mutation may also provide insight in to how the intracellular domains change their interactions in the presence of these mutations. This will also help us to understand the exact role the PAS-cap plays in stabilising the intracellular domains.

We provide noise analysis evidence that the inhibition of WT hEAG1's current could be down to a reduction in open probability of the channel. We tried to understand how the $\Delta 2-26$ mutant caused such a large potentiation of the current and we believe it also to be down to a change in open probability although the data obtained proved difficult to analyse given the nature of the $\Delta 2-26$ mutant channel. A change in the number of available channels is also a possibility to be explored further. Surface expression assays showed that upon addition of $5\mu\text{M}$ I&T, the WT channel reduces the number of surface channels which adds evidence to the

argument that the decrease in WT hEAG1 current is down to not only a reduction in open probability but also a reduction in surface expressed channels. Whole cell patch clamp experiments confirmed the WT-BBS channel's functionality at the plasma membrane and showed that it was inhibited by 5 μ M I&T.

The BTX-labelled channel surface expression assay did not provide the amount of fluorescence expected and so visually analysing the slides was a challenge. The reduced amount of visible fluorescence may have been down to too short of an incubation time of BTX-594 with the samples, especially since this was performed on ice to reduce the rate of endo/exocytosis following 5 μ M I&T addition. Another way to measure whether surface expressed hEAG1 channels are being endo/exocytosed is to perform a biotinylation assay using cell-impermeable biotin analogues. This ensures labelling of surface channels only and can be performed without 5 μ M I&T and following its application at two time points. A second alternative experiment would involve the use of a hEAG1 antibody specific to the extracellular loops that tags the channels which can be pulled out using a pull down assay and a secondary antibody selective for the anti-hEAG1 primary.

We provide evidence that the EAG domain and E600 residue of the cNBHD are necessary for the WT channel to increase the number of proliferating cells. Channels either lacking the EAG domain or that contain the E600R mutant show reduced proliferation when studied in a BrdU incorporation assay. A Western blot showed that the Δ cNBHD hEAG1 construct was not expressed in CHO cells so an interaction between the EAG and cNBH domains being important for proliferation cannot be ruled out. However, we can say that the E600 residue is in itself important for hEAG1's role in proliferation. The BrdU incorporation assay was performed on transiently transfected cells and so may not be the most accurate way of monitoring the effect of these constructs on proliferation. To avoid this, stable cell lines expressing each of these constructs should be used and used again in the BrdU assay.

We show that hEAG1 does not affect six chosen parameters of migration over empty vector controls when tested in either 0.1% FBS or 10% FBS medium, this was an interesting find given that the other studies have shown the related channel, hERG1, to be involved in both the proliferation and migration of melanoma cells. This in itself provides some evidence that whilst hEAG1 and hERG1 are closely

related in terms of structure and sequence homology, they fulfil different roles in both physiology and pathophysiology. Another approach to this would be to use a chemotaxis assay in which cells are encouraged to migrate towards a stimulus. A known number of untransfected cells and WT hEAG1 stably-transfected cells would be seeded into Boyden chambers and the number of cells found to be migrating towards the stimulus would be studied using confocal microscopy. This is an improved experiment as there is a stimulus present to encourage migration whereas the assay used here had no stimulus and therefore only monitored baseline migration of the CHO cells.

Immunocytochemistry experiments of the primary cilia show that the calmodulin binding domains and the intracellular domains of hEAG1 are important for the disassembly of the primary cilia. This data indicates that completely intact intracellular domains of the channel are likely required and that loss of any domain has an effect on the primary cilium of the cell. This may also add some weight to the argument that the intracellular domains can act as a signalling scaffold for other proteins to dock at. Whilst it has not been studied here, there may be a complex cascade of interactions requiring intact hEAG1 channels in order to retract the primary cilium of cells.

Finally, we show that CHO cells have a similar Ca^{2+} response to oocytes when exposed to $5\mu\text{M}$ I&T this was that there was a rapid rise in the fluorescent signal following the addition of $5\mu\text{M}$ I&T. The exact concentration of the Ca^{2+} increase was not measured in these experiments and so direct comparisons to the oocytes cannot be made at this stage. An interesting discovery came when using CHO cells stably expressing WT hEAG1, the Ca^{2+} signal increased as expected but then proceeded to decrease again quickly. Since this was not observed in the untransfected CHO cells it indicates that the presence of the channel has an effect on how the Ca^{2+} is handled within the cell. Experiments using Ca^{2+} imaging and whole cell patch clamp would be useful here to directly correlate the changes in hEAG1 current and the cell's Ca^{2+} levels to see if the presence of hEAG1 current affects the change in intracellular Ca^{2+} over time.

7. References

- Adaixo, R. & Morais-Cabral, J. H. 2010. Crystallization and preliminary crystallographic characterization of the PAS domains of EAG and ELK potassium channels. *Acta Crystallographica Section F: Structural Biology Crystallisation Communications*, **66**(Pt 9), pp 1056-9.
- Afrasiabi, E., Hietamaki, M., Viitanen, T., Sukumaran, P., Bergelin, N. & Tornquist, K. 2010. Expression and significance of HERG (KCNH2) potassium channels in the regulation of MDA-MB-435S melanoma cell proliferation and migration. *Cellular Signalling*, **22**(1), pp 57-64.
- Akher, F. B., Ebrahimi, A. & Mostafavi, N. 2017. Characterization of π -stacking interactions between aromatic amino acids and quercetagenin. *Journal of Molecular Structure*, **1128**(13-20).
- Alvarez, O., Gonzalez, C. & Latorre, R. 2002. Counting channels: a tutorial guide on ion channel fluctuation analysis. *Advances in Physiology Education*, **26**(1-4), pp 327-41.
- Asher, V., Khan, R., Warren, A., Shaw, R., Schalkwyk, G. V., Bali, A. & Sowter, H. M. 2010. The Eag potassium channel as a new prognostic marker in ovarian cancer. *Diagnostic Pathology*, **5**(78).
- Barbato, G., Ikura, M., Kay, L. E., Pastor, R. W. & Bax, A. 1992. Backbone dynamics of calmodulin studied by ¹⁵N relaxation using inverse detected two-dimensional NMR spectroscopy: the central helix is flexible. *Biochemistry*, **31**(23), pp 5269-78.
- Baronas, V. A., Yang, R. Y. & Kurata, H. T. 2017. Extracellular redox sensitivity of Kv1.2 potassium channels. *Scientific reports*, **7**(1), pp 9142.
- Barrow, A. D. & Trowsdale, J. 2006. You say ITAM and I say ITIM, let's call the whole thing off: the ambiguity of immunoreceptor signalling. *European Journal of Immunology*, **36**(7), pp 1646-53.
- Ben-Johny, M. & Yue, D. T. 2014. Calmodulin regulation (calmodulation) of voltage-gated calcium channels. *The Journal of General Physiology*, **143**(6), pp 679-92.
- Bershteyn, M., Atwood, S. X., Woo, W. M., Li, M. & Oro, A. E. 2010. MIM and cortactin antagonism regulates ciliogenesis and hedgehog signaling. *Developmental Cell*, **19**(2), pp 270-83.
- Bian, J. S., Kagan, A. & McDonald, T. V. 2004. Molecular analysis of PIP2 regulation of HERG and IKr. *American Journal of Physiology: Heart and Circulatory Physiology*, **287**(5), pp H2154-63.
- Bijlenga, P., Occhiodoro, T., Liu, J. H., Bader, C. R., Bernheim, L. & Fischer-Lougheed, J. 1998. An ether-a-go-go K⁺ current, Ih-eag, contributes to the hyperpolarization of human fusion-competent myoblasts. *The Journal of Physiology*, **512** (Pt 2)(317-23).
- Blackiston, D. J., McLaughlin, K. A. & Levin, M. 2009. Bioelectric controls of cell proliferation: ion channels, membrane voltage and the cell cycle. *Cell Cycle*, **8**(21), pp 3527-36.

- Bock, J., Szabo, I., Gamper, N., Adams, C. & Gulbins, E. 2003. Ceramide inhibits the potassium channel Kv1.3 by the formation of membrane platforms. *Biochemical and Biophysical Research Communications*, **305**(4), pp 890-7.
- Borowiec, A. S., Hague, F., Gouilleux-Gruart, V., Lassoued, K. & Ouadid-Ahidouch, H. 2011. Regulation of IGF-1-dependent cyclin D1 and E expression by hEag1 channels in MCF-7 cells: the critical role of hEag1 channels in G1 phase progression. *Biochimica et Biophysica Acta*, **1813**(5), pp 723-30.
- Bravo-Zehnder, M., Orio, P., Norambuena, A., Wallner, M., Meera, P., Toro, L., Latorre, R. & Gonzalez, A. 2000. Apical sorting of a voltage- and Ca²⁺-activated K⁺ channel alpha -subunit in Madin-Darby canine kidney cells is independent of N-glycosylation. *Proceedings of the National Academy of Science USA*, **97**(24), pp 13114-9.
- Brelidze, T. I., Carlson, A. E., Sankaran, B. & Zagotta, W. N. 2012. Structure of the carboxy-terminal region of a KCNH channel. *Nature*, **481**(7382), pp 530-3.
- Bromstrup, T., Howard, R. J., Trudell, J. R., Harris, R. A. & Lindahl, E. 2013. Inhibition versus potentiation of ligand-gated ion channels can be altered by a single mutation that moves ligands between intra- and intersubunit sites. *Structure*, **21**(8), pp 1307-16.
- Bruggemann, A., Pardo, L. A., Stuhmer, W. & Pongs, O. 1993. Ether-a-go-go encodes a voltage-gated channel permeable to K⁺ and Ca²⁺ and modulated by cAMP. *Nature*, **365**(6445), pp 445-8.
- Camacho, J. 2006. Ether a go-go potassium channels and cancer. *Cancer Letters*, **233**(1), pp 1-9.
- Carlson, A. E., Brelidze, T. I. & Zagotta, W. N. 2013a. Flavonoid regulation of EAG1 channels. *The Journal of General Physiology*, **141**(3), pp 347-58.
- Carlson, A. E., Rosenbaum, J. C., Brelidze, T. I., Klevit, R. E. & Zagotta, W. N. 2013b. Flavonoid regulation of HCN2 channels. *The Journal of Biological Chemistry*, **288**(46), pp 33136-45.
- Chagot, B. & Chazin, W. J. 2011. Solution NMR structure of Apo-calmodulin in complex with the IQ motif of human cardiac sodium channel NaV1.5. *The Journal of Molecular Biology*, **406**(1), pp 106-19.
- Chen, Y., Sanchez, A., Rubio, M. E., Kohl, T., Pardo, L. A. & Stuhmer, W. 2011. Functional K(v)10.1 channels localize to the inner nuclear membrane. *PLoS One*, **6**(5), pp e19257.
- Choi, K. Y., Chung, S. & Roche, K. W. 2011. Differential binding of calmodulin to group I metabotropic glutamate receptors regulates receptor trafficking and signaling. *The Journal of Neuroscience*, **31**(16), pp 5921-30.
- Craven, K. B. & Zagotta, W. N. 2006. CNG and HCN channels: two peas, one pod. *Annual Review of Physiology*, **68**(375-401).

- de Guadalupe Chavez-Lopez, M., Perez-Carreón, J. I., Zuniga-Garcia, V., Diaz-Chavez, J., Herrera, L. A., Caro-Sanchez, C. H., Acuna-Macias, I., Gariglio, P., Hernandez-Gallegos, E., Chiliquinga, A. J. & Camacho, J. 2015. Astemizole-based anticancer therapy for hepatocellular carcinoma (HCC), and Eag1 channels as potential early-stage markers of HCC. *Tumour Biology*, **36**(8), pp 6149-58.
- Dechat, T., Vlcek, S. & Foisner, R. 2000. Review: lamina-associated polypeptide 2 isoforms and related proteins in cell cycle-dependent nuclear structure dynamics. *The Journal of Structural Biology*, **129**(2-3), pp 335-45.
- Delmas, P. & Brown, D. A. 2005. Pathways modulating neural KCNQ/M (Kv7) potassium channels. *Nature Reviews Neuroscience*, **6**(850).
- DePriest, P. D., Shenson, D., Fried, A., Hunter, J. E., Andrews, S. J., Gallion, H. H., Pavlik, E. J., Kryscio, R. J. & van Nagell, J. R., Jr. 1993. A Morphology Index Based on Sonographic Findings in Ovarian Cancer. *Gynecologic Oncology*, **51**(1), pp 7-11.
- Downie, B. R., Sanchez, A., Knotgen, H., Contreras-Jurado, C., Gymnopoulos, M., Weber, C., Stuhmer, W. & Pardo, L. A. 2008. Eag1 expression interferes with hypoxia homeostasis and induces angiogenesis in tumors. *The Journal of Biological Chemistry*, **283**(52), pp 36234-40.
- Downward, J., Parker, P. & Waterfield, M. D. 1984. Autophosphorylation sites on the epidermal growth factor receptor. *Nature*, **311**(5985), pp 483-5.
- Emoto, K., Masugi, Y., Yamazaki, K., Effendi, K., Tsujikawa, H., Tanabe, M., Kitagawa, Y. & Sakamoto, M. 2014. Presence of primary cilia in cancer cells correlates with prognosis of pancreatic ductal adenocarcinoma. *Human Pathology*, **45**(4), pp 817-25.
- Etxeberria, A., Aivar, P., Rodriguez-Alfaro, J. A., Alaimo, A., Villace, P., Gomez-Posada, J. C., Areso, P. & Villarroel, A. 2008. Calmodulin regulates the trafficking of KCNQ2 potassium channels. *The FASEB Journal*, **22**(4), pp 1135-43.
- Falcon-Urrutia, P., Carrasco, C. M., Lois, P., Palma, V. & Roth, A. D. 2015. Shh Signaling through the Primary Cilium Modulates Rat Oligodendrocyte Differentiation. *PLoS One*, **10**(7), pp e0133567.
- Farooqi, A. A. & Siddik, Z. H. 2015. Platelet-derived growth factor (PDGF) signalling in cancer: rapidly emerging signalling landscape. *Cell Biochemistry and Function*, **33**(5), pp 257-65.
- Feather, S. A., Winyard, P. J., Dodd, S. & Woolf, A. S. 1997. Oral-facial-digital syndrome type 1 is another dominant polycystic kidney disease: clinical, radiological and histopathological features of a new kindred. *Nephrology, Dialysis and Transplantation*, **12**(7), pp 1354-61.
- Flory, M. R., Moser, M. J., Monnat, R. J., Jr. & Davis, T. N. 2000. Identification of a human centrosomal calmodulin-binding protein that shares homology with pericentrin. *Proceedings of the National Academy of Science USA*, **97**(11), pp 5919-23.
- Foster, M. N. & Coetzee, W. A. 2016. KATP Channels in the Cardiovascular System. *Physiological Reviews*, **96**(1), pp 177-252.

- Gericke, A., Leslie, N. R., Losche, M. & Ross, A. H. 2013. PtdIns(4,5)P₂-mediated cell signaling: emerging principles and PTEN as a paradigm for regulatory mechanism. *Advances in Experimental and Medical Biology*, **991**(85-104).
- Gianulis, E. C., Liu, Q. & Trudeau, M. C. 2013. Direct interaction of eag domains and cyclic nucleotide-binding homology domains regulate deactivation gating in hERG channels. *The Journal of General Physiology*, **142**(4), pp 351-66.
- Gomez-Ospina, N., Tsuruta, F., Barreto-Chang, O., Hu, L. & Dolmetsch, R. 2006. The C terminus of the L-type voltage-gated calcium channel Ca(V)_{1.2} encodes a transcription factor. *Cell*, **127**(3), pp 591-606.
- Goncalves, J. T. & Stuhmer, W. 2010. Calmodulin interaction with hEAG1 visualized by FRET microscopy. *PLoS One*, **5**(5), pp e10873.
- Gustina, A. S. & Trudeau, M. C. 2011. hERG potassium channel gating is mediated by N- and C-terminal region interactions. *The Journal of General Physiology*, **137**(3), pp 315-25.
- Gutman, G. A., Chandy, K. G., Grissmer, S., Lazdunski, M., McKinnon, D., Pardo, L. A., Robertson, G. A., Rudy, B., Sanguinetti, M. C., Stuhmer, W. & Wang, X. 2005. International Union of Pharmacology. LIII. Nomenclature and molecular relationships of voltage-gated potassium channels. *Pharmacological Reviews*, **57**(4), pp 473-508.
- Haitin, Y., Carlson, A. E. & Zagotta, W. N. 2013. The structural mechanism of KCNH-channel regulation by the eag domain. *Nature*, **501**(7467), pp 444-8.
- Hammadi, M., Chopin, V., Matifat, F., Dhennin-Duthille, I., Chasseraud, M., Sevestre, H. & Ouadid-Ahidouch, H. 2012. Human ether à-gogo K⁺ channel 1 (hEag1) regulates MDA-MB-231 breast cancer cell migration through Orai1-dependent calcium entry. *The Journal of Cellular Physiology*, **227**(12), pp 3837-3846.
- Han, B., He, K., Cai, C., Tang, Y., Yang, L., Heinemann, S. H., Hoshi, T. & Hou, S. 2016. Human EAG channels are directly modulated by PIP₂ as revealed by electrophysiological and optical interference investigations. *Scientific Reports*, **6**(23417).
- Han, B., Zhang, M., Sun, P. & Hou, S. 2018. Capturing the Interaction Kinetics of an Ion Channel Protein with Small Molecules by the Bio-layer Interferometry Assay. *Journal of Visualised Experiments*, 133), pp.
- Harley, C. A., Starek, G., Jones, D. K., Fernandes, A. S., Robertson, G. A. & Morais-Cabral, J. H. 2016. Enhancement of hERG channel activity by scFv antibody fragments targeted to the PAS domain. *Proceedings of the National Academy of Sciences of the United States of America*, **113**(35), pp 9916-21.
- Heessen, S. & Fornerod, M. 2007. The inner nuclear envelope as a transcription factor resting place. *EMBO Reports*, **8**(10), pp 914-9.

- Hegle, A. P., Marble, D. D. & Wilson, G. F. 2006. A voltage-driven switch for ion-independent signaling by ether-a-go-go K⁺ channels. *Proceedings of the National Academy of Science USA*, **103**(8), pp 2886-91.
- Heldin, C. H., Ostman, A. & Ronnstrand, L. 1998. Signal transduction via platelet-derived growth factor receptors. *Biochimica et Biophysica Acta*, **1378**(1), pp F79-113.
- Herrmann, S., Ninkovic, M., Kohl, T., Lorinczi, E. & Pardo, L. A. 2012. Cortactin controls surface expression of the voltage-gated potassium channel K(V)10.1. *The Journal of Biological Chemistry*, **287**(53), pp 44151-63.
- Herrmann, S., Ninkovic, M., Kohl, T. & Pardo, L. A. 2013. PIST (GOPC) modulates the oncogenic voltage-gated potassium channel KV10.1. *Frontiers in Physiology*, **4**(201).
- Hsu, P. H., Ma, Y. T., Fang, Y. C., Huang, J. J., Gan, Y. L., Chang, P. T., Jow, G. M., Tang, C. Y. & Jeng, C. J. 2017. Cullin 7 mediates proteasomal and lysosomal degradations of rat Eag1 potassium channels. *Scientific Reports*, **7**(40825).
- Huang, H. & Trussell, L. O. 2011. KCNQ5 channels control resting properties and release probability of a synapse. *Nature: Neuroscience*, **14**(7), pp 840-7.
- Huang, X., Dubuc, A. M., Hashizume, R., Berg, J., He, Y., Wang, J., Chiang, C., Cooper, M. K., Northcott, P. A., Taylor, M. D., Barnes, M. J., Tihan, T., Chen, J., Hackett, C. S., Weiss, W. A., James, C. D., Rowitch, D. H., Shuman, M. A., Jan, Y. N. & Jan, L. Y. 2012. Voltage-gated potassium channel EAG2 controls mitotic entry and tumor growth in medulloblastoma via regulating cell volume dynamics. *Genes and Development*, **26**(16), pp 1780-96.
- Issy, A. C., Fonseca, J. R., Pardo, L. A., Stuhmer, W. & Del Bel, E. A. 2014. Hippocampal ether-a-go-go1 potassium channels blockade: effects in the startle reflex and prepulse inhibition. *Neuroscience Letters*, **559**(13-7).
- Jentsch, T. J. 2000. Neuronal KCNQ potassium channels: physiology and role in disease. *Nature Reviews: Neuroscience*, **1**(1), pp 21-30.
- Jimenez-Garduno, A. M., Mitkovski, M., Alexopoulos, I. K., Sanchez, A., Stuhmer, W., Pardo, L. A. & Ortega, A. 2014. KV10.1 K(+)-channel plasma membrane discrete domain partitioning and its functional correlation in neurons. *Biochimica et Biophysica Acta*, **1838**(3), pp 921-31.
- Keen, J. E., Khawaled, R., Farrens, D. L., Neelands, T., Rivard, A., Bond, C. T., Janowsky, A., Fakler, B., Adelman, J. P. & Maylie, J. 1999. Domains responsible for constitutive and Ca²⁺-dependent interactions between calmodulin and small conductance Ca²⁺-activated potassium channels. *The Journal of Neuroscience*, **19**(20), pp 8830-8.
- Kim, J., Ghosh, S., Liu, H., Tateyama, M., Kass, R. S. & Pitt, G. S. 2004. Calmodulin mediates Ca²⁺ sensitivity of sodium channels. *The Journal of Biological Chemistry*, **279**(43), pp 45004-12.
- Kobayashi, T. & Dynlacht, B. D. 2011. Regulating the transition from centriole to basal body. *The Journal of Cell Biology*, **193**(3), pp 435-44.

- Kohl, T., Lorinczi, E., Pardo, L. A. & Stuhmer, W. 2011. Rapid internalization of the oncogenic K⁺ channel K(V)10.1. *PLoS One*, **6**(10), pp e26329.
- Kortum, F., Caputo, V., Bauer, C. K., Stella, L., Ciolfi, A., Alawi, M., Bocchinfuso, G., Flex, E., Paolacci, S., Dentici, M. L., Grammatico, P., Korenke, G. C., Leuzzi, V., Mowat, D., Nair, L. D., Nguyen, T. T., Thierry, P., White, S. M., Dallapiccola, B., Pizzuti, A., Campeau, P. M., Tartaglia, M. & Kutsche, K. 2015. Mutations in KCNH1 and ATP6V1B2 cause Zimmermann-Laband syndrome. *Nature Genetics*, **47**(6), pp 661-7.
- Koshy, S., Huq, R., Tanner, M. R., Atik, M. A., Porter, P. C., Khan, F. S., Pennington, M. W., Hanania, N. A., Corry, D. B. & Beeton, C. 2014. Blocking KV1.3 channels inhibits Th2 lymphocyte function and treats a rat model of asthma. *The Journal of Biological Chemistry*, **289**(18), pp 12623-32.
- Koster, J. C., Permutt, M. A. & Nichols, C. G. 2005. Diabetes and insulin secretion: the ATP-sensitive K⁺ channel (K ATP) connection. *Diabetes*, **54**(11), pp 3065-72.
- Kovalevskaya, N. V., van de Waterbeemd, M., Bokhovchuk, F. M., Bate, N., Bindels, R. J., Hoenderop, J. G. & Vuister, G. W. 2013. Structural analysis of calmodulin binding to ion channels demonstrates the role of its plasticity in regulation. *European Journal of Physiology*, **465**(11), pp 1507-19.
- Krapivinsky, G., Krapivinsky, L., Wickman, K. & Clapham, D. E. 1995. G beta gamma binds directly to the G protein-gated K⁺ channel, IKACH. *The Journal of Biological Chemistry*, **270**(49), pp 29059-62.
- Kwon, Y., Hofmann, T. & Montell, C. 2007. Integration of phosphoinositide- and calmodulin-mediated regulation of TRPC6. *Molecular Cell*, **25**(4), pp 491-503.
- Ledoux, J., Werner, M. E., Brayden, J. E. & Nelson, M. T. 2006. Calcium-activated potassium channels and the regulation of vascular tone. *Physiology*, **21**(69-78).
- Lee, A., Wong, S. T., Gallagher, D., Li, B., Storm, D. R., Scheuer, T. & Catterall, W. A. 1999. Ca²⁺/calmodulin binds to and modulates P/Q-type calcium channels. *Nature*, **399**(6732), pp 155-9.
- Levitan, I., Fang, Y., Rosenhouse-Dantsker, A. & Romanenko, V. 2010. Cholesterol and ion channels. *Subcellular Biochemistry*, **51**(509-49).
- Li, Q., Gayen, S., Chen, A. S., Huang, Q., Raida, M. & Kang, C. 2010. NMR solution structure of the N-terminal domain of hERG and its interaction with the S4-S5 linker. *Biochemical and Biophysical Research Communications*, **403**(1), pp 126-32.
- Li, X., Anishkin, A., Liu, H., van Rossum, D. B., Chintapalli, S. V., Sassic, J. K., Gallegos, D., Pivaroff-Ward, K. & Jegla, T. 2015. Bimodal regulation of an Elk subfamily K⁺ channel by phosphatidylinositol 4,5-bisphosphate. *The Journal of General Physiology*, **146**(5), pp 357-74.

- Liu, X. B. & Murray, K. D. 2012. Neuronal excitability and calcium/calmodulin-dependent protein kinase type II: location, location, location. *Epilepsia*, **53 Suppl 1**(45-52).
- Lockwich, T. P., Liu, X., Singh, B. B., Jadlovec, J., Weiland, S. & Ambudkar, I. S. 2000. Assembly of Trp1 in a signaling complex associated with caveolin-scaffolding lipid raft domains. *The Journal of Biological Chemistry*, **275**(16), pp 11934-42.
- Logothetis, D. E., Kurachi, Y., Galper, J., Neer, E. J. & Clapham, D. E. 1987. The beta gamma subunits of GTP-binding proteins activate the muscarinic K⁺ channel in heart. *Nature*, **325**(6102), pp 321-6.
- Longin, A.-S., Mezin, P., Favier, A. & Verdeti, J. 1997. Presence of Zinc and Calcium Permeant Channels in the Inner Membrane of the Nuclear Envelope. *Biochemical and Biophysical Research Communications*, **235**(1), pp 236-241.
- Lorinczi, E., Gomez-Posada, J. C., de la Pena, P., Tomczak, A. P., Fernandez-Trillo, J., Leipscher, U., Stuhmer, W., Barros, F. & Pardo, L. A. 2015. Voltage-dependent gating of KCNH potassium channels lacking a covalent link between voltage-sensing and pore domains. *Nature Communications*, **6**(6672).
- Lorinczi, E., Helliwell, M., Finch, A., Stansfeld, P. J., Davies, N. W., Mahaut-Smith, M., Muskett, F. W. & Mitcheson, J. S. 2016. Calmodulin Regulates Human Ether a Go-Go 1 (hEAG1) Potassium Channels through Interactions of the Eag Domain with the Cyclic Nucleotide Binding Homology Domain. *The Journal of Biological Chemistry*, **291**(34), pp 17907-18.
- Lorinczi, E., Napp, J., Contreras-Jurado, C., Pardo, L. A. & Stuhmer, W. 2009. The voltage dependence of hEag currents is not determined solely by membrane-spanning domains. *European biophysics journal : EBJ*, **38**(3), pp 279-84.
- Lu, F., Chen, Y., Zhao, C., Wang, H., He, D., Xu, L., Wang, J., He, X., Deng, Y., Lu, E. E., Liu, X., Verma, R., Bu, H., Drissi, R., Fouladi, M., Stemmer-Rachamimov, A. O., Burns, D., Xin, M., Rubin, J. B., Bahassi, E. M., Canoll, P., Holland, E. C. & Lu, Q. R. 2016. Olig2-Dependent Reciprocal Shift in PDGF and EGF Receptor Signaling Regulates Tumor Phenotype and Mitotic Growth in Malignant Glioma. *Cancer Cell*, **29**(5), pp 669-683.
- Ludwig, J., Terlau, H., Wunder, F., Bruggemann, A., Pardo, L. A., Marquardt, A., Stuhmer, W. & Pongs, O. 1994. Functional expression of a rat homologue of the voltage gated ether a go-go potassium channel reveals differences in selectivity and activation kinetics between the Drosophila channel and its mammalian counterpart. *The EMBO Journal*, **13**(19), pp 4451-8.
- Lukács, P., Cervenka, R., Zarrabi, T., König, X., Hilber, K. & Todt, H. 2009. From frog oocytes to mammalian cells: substantial differences in modulation of NaV1.4 channel slow kinetic behaviour by the β 1 subunit. *BMC Pharmacology*, **9**(2), pp A24.
- MacGrath, S. M. & Koleske, A. J. 2012. Cortactin in cell migration and cancer at a glance. *The Journal of Cell Science*, **125**(Pt 7), pp 1621-6.
- Magee, A. I. & Parmryd, I. 2003. Detergent-resistant membranes and the protein composition of lipid rafts. *Genome Biology*, **4**(11), pp 234.

- Makita, N., Horie, M., Nakamura, T., Ai, T., Sasaki, K., Yokoi, H., Sakurai, M., Sakuma, I., Otani, H., Sawa, H. & Kitabatake, A. 2002. Drug-induced long-QT syndrome associated with a subclinical SCN5A mutation. *Circulation*, **106**(10), pp 1269-74.
- Marques-Carvalho, M. J., Sahoo, N., Muskett, F. W., Vieira-Pires, R. S., Gabant, G., Cadene, M., Schonherr, R. & Morais-Cabral, J. H. 2012. Structural, biochemical, and functional characterization of the cyclic nucleotide binding homology domain from the mouse EAG1 potassium channel. *The Journal of Molecular Biology*, **423**(1), pp 34-46.
- Martens, J. R., Navarro-Polanco, R., Coppock, E. A., Nishiyama, A., Parshley, L., Grobaski, T. D. & Tamkun, M. M. 2000. Differential targeting of Shaker-like potassium channels to lipid rafts. *The Journal of Biological Chemistry*, **275**(11), pp 7443-6.
- Martinez, R., Stuhmer, W., Martin, S., Schell, J., Reichmann, A., Rohde, V. & Pardo, L. 2015. Analysis of the expression of Kv10.1 potassium channel in patients with brain metastases and glioblastoma multiforme: impact on survival. *BMC Cancer*, **15**(839).
- Masi, A., Becchetti, A., Restano-Cassulini, R., Polvani, S., Hofmann, G., Buccoliero, A. M., Paglierani, M., Pollo, B., Taddei, G. L., Gallina, P., Di Lorenzo, N., Franceschetti, S., Wanke, E. & Arcangeli, A. 2005. hERG1 channels are overexpressed in glioblastoma multiforme and modulate VEGF secretion in glioblastoma cell lines. *The British Journal of Cancer*, **93**(7), pp 781-92.
- Matsukawa, H., Wolf, A. M., Matsushita, S., Joho, R. H. & Knopfel, T. 2003. Motor dysfunction and altered synaptic transmission at the parallel fiber-Purkinje cell synapse in mice lacking potassium channels Kv3.1 and Kv3.3. *The Journal of Neuroscience*, **23**(20), pp 7677-84.
- Maylie, J., Bond, C. T., Herson, P. S., Lee, W. S. & Adelman, J. P. 2004. Small conductance Ca²⁺-activated K⁺ channels and calmodulin. *The Journal of Physiology*, **554**(Pt 2), pp 255-61.
- McGaughey, G. B., Gagne, M. & Rappe, A. K. 1998. pi-Stacking interactions. Alive and well in proteins. *The Journal of Biological Chemistry*, **273**(25), pp 15458-63.
- Meiler, E., Nieto-Pelegrin, E. & Martinez-Quiles, N. 2012. Cortactin tyrosine phosphorylation promotes its deacetylation and inhibits cell spreading. *PLoS One*, **7**(3), pp e33662.
- Menendez, S. T., Villaronga, M. A., Rodrigo, J. P., Alvarez-Teijeiro, S., Garcia-Carracedo, D., Urduinguio, R. G., Fraga, M. F., Pardo, L. A., Vilorio, C. G., Suarez, C. & Garcia-Pedrero, J. M. 2012. Frequent aberrant expression of the human ether a-go-go (hEAG1) potassium channel in head and neck cancer: pathobiological mechanisms and clinical implications. *The Journal of Molecular Medicine*, **90**(10), pp 1173-84.
- Meyer, R. & Heinemann, S. H. 1998. Characterization of an eag-like potassium channel in human neuroblastoma cells. *The Journal of Physiology*, **508 (Pt 1)**(49-56).
- Michaud, E. J. & Yoder, B. K. 2006. The primary cilium in cell signaling and cancer. *Cancer Research*, **66**(13), pp 6463-7.

- Moglich, A., Ayers, R. A. & Moffat, K. 2009. Structure and signaling mechanism of Per-ARNT-Sim domains. *Structure*, **17**(10), pp 1282-94.
- Morais-Cabral, J. H. & Robertson, G. A. 2015. The enigmatic cytoplasmic regions of KCNH channels. *The Journal of Molecular Biology*, **427**(1), pp 67-76.
- Morais Cabral, J. H., Lee, A., Cohen, S. L., Chait, B. T., Li, M. & Mackinnon, R. 1998. Crystal structure and functional analysis of the HERG potassium channel N terminus: a eukaryotic PAS domain. *Cell*, **95**(5), pp 649-55.
- Mortensen, L. S., Schmidt, H., Farsi, Z., Barrantes-Freer, A., Rubio, M. E., Ufartes, R., Eilers, J., Sakaba, T., Stühmer, W. & Pardo, L. A. 2015. KV10.1 opposes activity-dependent increase in Ca²⁺-influx into the presynaptic terminal of the parallel fibre-Purkinje cell synapse. *The Journal of Physiology*, **593**(1), pp 181-196.
- Moser, J. J., Fritzler, M. J. & Rattner, J. B. 2009. Primary ciliogenesis defects are associated with human astrocytoma/glioblastoma cells. *BMC Cancer*, **9**(448).
- Muskett, F. W., Thouta, S., Thomson, S. J., Bowen, A., Stansfeld, P. J. & Mitcheson, J. S. 2011. Mechanistic insight into human ether-a-go-go-related gene (hERG) K⁺ channel deactivation gating from the solution structure of the EAG domain. *The Journal of Biological Chemistry*, **286**(8), pp 6184-91.
- Nimmrich, V. & Gross, G. 2012. P/Q-type calcium channel modulators. *British Journal of Pharmacology*, **167**(4), pp 741-59.
- Ninkovic, M., Mitkovski, M., Kohl, T., Stuhmer, W. & Pardo, L. A. 2012. Physical and functional interaction of KV10.1 with Rabaptin-5 impacts ion channel trafficking. *FEBS Letters*, **586**(19), pp 3077-84.
- O'Connell, K. M. & Tamkun, M. M. 2005. Targeting of voltage-gated potassium channel isoforms to distinct cell surface microdomains. *The Journal of Cell Science*, **118**(Pt 10), pp 2155-66.
- Oda, K., Matsuoka, Y., Funahashi, A. & Kitano, H. 2005. A comprehensive pathway map of epidermal growth factor receptor signaling. *Molecular Systems Biology*, **1**(2005.0010).
- Oser, M., Mader, C. C., Gil-Henn, H., Magalhaes, M., Bravo-Cordero, J. J., Koleske, A. J. & Condeelis, J. 2010. Specific tyrosine phosphorylation sites on cortactin regulate Nck1-dependent actin polymerization in invadopodia. *Journal of Cell Science*, **123**(Pt 21), pp 3662-73.
- Ouadid-Ahidouch, H. & Ahidouch, A. 2013. K(+) channels and cell cycle progression in tumor cells. *Frontiers in Physiology*, **4**(220).
- Ouadid-Ahidouch, H., Roudbaraki, M., Delcourt, P., Ahidouch, A., Joury, N. & Prevarskaya, N. 2004. Functional and molecular identification of intermediate-conductance Ca(2+)-activated K(+) channels in breast cancer cells: association with cell cycle progression. *American Journal of Physiology: Cell Physiology*, **287**(1), pp C125-34.

- Pannicke, T., Iandiev, I., Uckermann, O., Biedermann, B., Kutzera, F., Wiedemann, P., Wolburg, H., Reichenbach, A. & Bringmann, A. 2004. A potassium channel-linked mechanism of glial cell swelling in the postischemic retina. *Molecular and Cellular Neurosciences*, **26**(4), pp 493-502.
- Pardo, L. A., Bruggemann, A., Camacho, J. & Stuhmer, W. 1998. Cell cycle-related changes in the conducting properties of r-eag K⁺ channels. *The Journal of Cell Biology*, **143**(3), pp 767-75.
- Pardo, L. A., del Camino, D., Sanchez, A., Alves, F., Bruggemann, A., Beckh, S. & Stuhmer, W. 1999. Oncogenic potential of EAG K(+) channels. *The EMBO Journal*, **18**(20), pp 5540-7.
- Pardo, L. A. & Stuhmer, W. 2014. The roles of K(+) channels in cancer. *Nature Reviews Cancer*, **14**(1), pp 39-48.
- Paul, C. D., Mistriotis, P. & Konstantopoulos, K. 2017. Cancer cell motility: lessons from migration in confined spaces. *Nature Reviews Cancer*, **17**(2), pp 131-140.
- Pazour, G. J., Dickert, B. L., Vucica, Y., Seeley, E. S., Rosenbaum, J. L., Witman, G. B. & Cole, D. G. 2000. Chlamydomonas IFT88 and its mouse homologue, polycystic kidney disease gene tg737, are required for assembly of cilia and flagella. *The Journal of Cell Biology*, **151**(3), pp 709-18.
- Piros, E. T., Shen, L. & Huang, X. Y. 1999. Purification of an EH domain-binding protein from rat brain that modulates the gating of the rat ether-a-go-go channel. *The Journal of Biological Chemistry*, **274**(47), pp 33677-83.
- Rousseau, E., Michaud, C., Lefebvre, D., Proteau, S. & Decrouy, A. 1996. Reconstitution of ionic channels from inner and outer membranes of mammalian cardiac nuclei. *Biophysical Journal*, **70**(2), pp 703-714.
- Sale, H., Wang, J., O'Hara, T. J., Tester, D. J., Phartiyal, P., He, J. Q., Rudy, Y., Ackerman, M. J. & Robertson, G. A. 2008. Physiological properties of hERG 1a/1b heteromeric currents and a hERG 1b-specific mutation associated with Long-QT syndrome. *Circulation Research*, **103**(7), pp e81-95.
- Sanchez, A., Urrego, D. & Pardo, L. A. 2016. Cyclic expression of the voltage-gated potassium channel KV10.1 promotes disassembly of the primary cilium. *EMBO Reports*, **17**(5), pp 708-23.
- Santo-Domingo, J. & Demareux, N. 2010. Calcium uptake mechanisms of mitochondria. *Biochimica et Biophysica Acta*, **1797**(6-7), pp 907-12.
- Sarkisian, M. R., Siebzehnruhl, D., Hoang-Minh, L., Deleyrolle, L., Silver, D. J., Siebzehnruhl, F. A., Guadiana, S. M., Srivinasan, G., Semple-Rowland, S., Harrison, J. K., Steindler, D. A. & Reynolds, B. A. 2014. Detection of primary cilia in human glioblastoma. *The Journal of Neurooncology*, **117**(1), pp 15-24.
- Satir, P., Pedersen, L. B. & Christensen, S. T. 2010. The primary cilium at a glance. *The Journal of Cell Science*, **123**(Pt 4), pp 499-503.

- Schirmer, E. C. & Gerace, L. 2005. The nuclear membrane proteome: extending the envelope. *Trends in Biochemical Science*, **30**(10), pp 551-8.
- Schlichter, L. C., Jiang, J., Wang, J., Newell, E. W., Tsui, F. W. & Lam, D. 2014. Regulation of hERG and hEAG channels by Src and by SHP-1 tyrosine phosphatase via an ITIM region in the cyclic nucleotide binding domain. *PLoS One*, **9**(2), pp e90024.
- Schmitt, N., Grunnet, M. & Olesen, S. P. 2014. Cardiac potassium channel subtypes: new roles in repolarization and arrhythmia. *Physiological Reviews*, **94**(2), pp 609-53.
- Schönherr, R., Löber, K. & Heinemann, S. H. 2000. Inhibition of human ether à go-go potassium channels by Ca²⁺/calmodulin. *The EMBO journal*, **19**(13), pp 3263-3271.
- Schwab, A., Reinhardt, J., Schneider, S. W., Gassner, B. & Schuricht, B. 1999. K(+) channel-dependent migration of fibroblasts and human melanoma cells. *Cellular Physiology and Biochemistry*, **9**(3), pp 126-32.
- Sierra, A., Zhu, Z., Sapay, N., Sharotri, V., Kline, C. F., Luczak, E. D., Subbotina, E., Sivaprasadarao, A., Snyder, P. M., Mohler, P. J., Anderson, M. E., Vivaudou, M., Zingman, L. V. & Hodgson-Zingman, D. M. 2013. Regulation of cardiac ATP-sensitive potassium channel surface expression by calcium/calmodulin-dependent protein kinase II. *The Journal of Biological Chemistry*, **288**(3), pp 1568-81.
- Simms, B. A., Souza, I. A. & Zamponi, G. W. 2014. A novel calmodulin site in the Cav1.2 N-terminus regulates calcium-dependent inactivation. *European Journal of Physiology*, **466**(9), pp 1793-803.
- Simons, C., Rash, L. D., Crawford, J., Ma, L., Cristofori-Armstrong, B., Miller, D., Ru, K., Baillie, G. J., Alanay, Y., Jacquinet, A., Debray, F. G., Verloes, A., Shen, J., Yesil, G., Guler, S., Yuksel, A., Cleary, J. G., Grimmond, S. M., McGaughan, J., King, G. F., Gabbett, M. T. & Taft, R. J. 2015. Mutations in the voltage-gated potassium channel gene KCNH1 cause Temple-Baraitser syndrome and epilepsy. *Nature Genetics*, **47**(1), pp 73-7.
- Simons, K. & Toomre, D. 2000. Lipid rafts and signal transduction. *Nature Reviews: Molecular and Cellular Biology*, **1**(1), pp 31-9.
- Skoda, A. M., Simovic, D., Karin, V., Kardum, V., Vranic, S. & Serman, L. 2018. The role of the Hedgehog signaling pathway in cancer: A comprehensive review. *The Bosnian Journal of Basic Medical Sciences*, **18**(1), pp 8-20.
- Smith, K. E., Browne, L., Selwood, D. L., McAlpine, D. & Jagger, D. J. 2015. Phosphoinositide Modulation of Heteromeric Kv1 Channels Adjusts Output of Spiral Ganglion Neurons from Hearing Mice. *The Journal of Neuroscience*, **35**(32), pp 11221-32.
- Sorensen, A. B., Sondergaard, M. T. & Overgaard, M. T. 2013. Calmodulin in a heartbeat. *The FEBS Journal*, **280**(21), pp 5511-32.
- Stansfeld, C. E., Roper, J., Ludwig, J., Weseloh, R. M., Marsh, S. J., Brown, D. A. & Pongs, O. 1996. Elevation of intracellular calcium by muscarinic receptor activation induces a block of

voltage-activated rat ether-a-go-go channels in a stably transfected cell line. *Proceedings of the National Academy of Science USA*, **93**(18), pp 9910-4.

- Stengel, R., Rivera-Milla, E., Sahoo, N., Ebert, C., Bollig, F., Heinemann, S. H., Schonherr, R. & Englert, C. 2012. Kcnh1 voltage-gated potassium channels are essential for early zebrafish development. *The Journal of Biological Chemistry*, **287**(42), pp 35565-75.
- Suh, B. C. & Hille, B. 2008. PIP2 is a necessary cofactor for ion channel function: how and why? *Annual Review of Biophysics*, **37**(175-95).
- Sun, X. X., Hodge, J. J., Zhou, Y., Nguyen, M. & Griffith, L. C. 2004. The eag potassium channel binds and locally activates calcium/calmodulin-dependent protein kinase II. *The Journal of Biological Chemistry*, **279**(11), pp 10206-14.
- Tateishi-Karimata, H., Kawauchi, K. & Sugimoto, N. 2018. Destabilization of DNA G-Quadruplexes by Chemical Environment Changes during Tumor Progression Facilitates Transcription. *The Journal of the American Chemical Society*, **140**(2), pp 642-651.
- Taylor, B. L. & Zhulin, I. B. 1999. PAS domains: internal sensors of oxygen, redox potential, and light. *Microbiology and Molecular Biology Reviews*, **63**(2), pp 479-506.
- Terlau, H., Heinemann, S. H., Stuhmer, W., Pongs, O. & Ludwig, J. 1997. Amino terminal-dependent gating of the potassium channel rat eag is compensated by a mutation in the S4 segment. *The Journal of Physiology*, **502 (Pt 3)**(537-43).
- Tian, H., Feng, J., Li, J., Ho, T. V., Yuan, Y., Liu, Y., Brindopke, F., Figueiredo, J. C., Magee, W., 3rd, Sanchez-Lara, P. A. & Chai, Y. 2017. Intraflagellar transport 88 (IFT88) is crucial for craniofacial development in mice and is a candidate gene for human cleft lip and palate. *Human Molecular Genetics*, **26**(5), pp 860-872.
- Trimmer, J. S. 2015. Subcellular localization of K⁺ channels in mammalian brain neurons: remarkable precision in the midst of extraordinary complexity. *Neuron*, **85**(2), pp 238-56.
- Ufartes, R., Schneider, T., Mortensen, L. S., de Juan Romero, C., Hentrich, K., Knoetgen, H., Beilinson, V., Moebius, W., Tarabykin, V., Alves, F., Pardo, L. A., Rawlins, J. N. & Stuehmer, W. 2013. Behavioural and functional characterization of Kv10.1 (Eag1) knockout mice. *Human Molecular Genetics*, **22**(11), pp 2247-62.
- Urrego, D., Movsisyan, N., Ufartes, R. & Pardo, L. A. 2016. Periodic expression of Kv10.1 driven by pRb/E2F1 contributes to G2/M progression of cancer and non-transformed cells. *Cell Cycle*, **15**(6), pp 799-811.
- Valenzuela, S. M., Mazzanti, M., Tonini, R., Qiu, M. R., Warton, K., Musgrove, E. A., Campbell, T. J. & Breit, S. N. 2000. The nuclear chloride ion channel NCC27 is involved in regulation of the cell cycle. *The Journal of Physiology*, **529 Pt 3**(541-52).
- Vianna-Jorge, R. & Suarez-Kurtz, G. 2004. Potassium channels in T lymphocytes: therapeutic targets for autoimmune disorders? *BioDrugs*, **18**(5), pp 329-41.

- Wang, J., Myers, C. D. & Robertson, G. A. 2000. Dynamic control of deactivation gating by a soluble amino-terminal domain in HERG K(+) channels. *The Journal of General Physiology*, **115**(6), pp 749-58.
- Wang, Z., Wilson, G. F. & Griffith, L. C. 2002. Calcium/calmodulin-dependent protein kinase II phosphorylates and regulates the *Drosophila* eag potassium channel. *The Journal of Biological Chemistry*, **277**(27), pp 24022-9.
- Waters, A. M. & Beales, P. L. 2011. Ciliopathies: an expanding disease spectrum. *Pediatric Nephrology*, **26**(7), pp 1039-56.
- Webb, B. A., Zhou, S., Eves, R., Shen, L., Jia, L. & Mak, A. S. 2006. Phosphorylation of cortactin by p21-activated kinase. *Archives of Biochemistry and Biophysics*, **456**(2), pp 183-93.
- Weber, W. 1999. Ion currents of *Xenopus laevis* oocytes: state of the art. *Biochimica et Biophysica Acta*, **1421**(2), pp 213-33.
- Weiss, L. A., Escayg, A., Kearney, J. A., Trudeau, M., MacDonald, B. T., Mori, M., Reichert, J., Buxbaum, J. D. & Meisler, M. H. 2003. Sodium channels SCN1A, SCN2A and SCN3A in familial autism. *Molecular Psychiatry*, **8**(2), pp 186-94.
- Weiss, S., Oz, S., Benmocha, A. & Dascal, N. 2013. Regulation of cardiac L-type Ca(2)(+) channel CaV1.2 via the beta-adrenergic-cAMP-protein kinase A pathway: old dogmas, advances, and new uncertainties. *Circulation Research*, **113**(5), pp 617-31.
- Wheway, G., Nazlamova, L. & Hancock, J. T. 2018. Signaling through the Primary Cilium. *Frontiers in Cell and Developmental Biology*, **6**(8), pp.
- Whicher, J. R. & MacKinnon, R. 2016. Structure of the voltage-gated K(+) channel Eag1 reveals an alternative voltage sensing mechanism. *Science*, **353**(6300), pp 664-9.
- Wu, J., Wu, X., Lian, K., Lin, B., Guo, L. & Ding, Z. 2012a. Overexpression of potassium channel ether à go-go in human osteosarcoma. *Neoplasma*, **59**(02), pp 207-215.
- Wu, W., Dong, M. Q., Wu, X. G., Sun, H. Y., Tse, H. F., Lau, C. P. & Li, G. R. 2012b. Human ether-a-go-go gene potassium channels are regulated by EGFR tyrosine kinase. *Biochimica et Biophysica Acta*, **1823**(2), pp 282-9.
- Xia, F., Leung, Y. M., Gaisano, G., Gao, X., Chen, Y., Fox, J. E., Bhattacharjee, A., Wheeler, M. B., Gaisano, H. Y. & Tsushima, R. G. 2007. Targeting of voltage-gated K⁺ and Ca²⁺ channels and soluble N-ethylmaleimide-sensitive factor attachment protein receptor proteins to cholesterol-rich lipid rafts in pancreatic alpha-cells: effects on glucagon stimulus-secretion coupling. *Endocrinology*, **148**(5), pp 2157-67.
- Xia, X. M., Fakler, B., Rivard, A., Wayman, G., Johnson-Pais, T., Keen, J. E., Ishii, T., Hirschberg, B., Bond, C. T., Lutsenko, S., Maylie, J. & Adelman, J. P. 1998. Mechanism of calcium gating in small-conductance calcium-activated potassium channels. *Nature*, **395**(6701), pp 503-7.

- Yamashiro, D. J. & Maxfield, F. R. 1987. Acidification of morphologically distinct endosomes in mutant and wild-type Chinese hamster ovary cells. *The Journal of Cell Biology*, **105**(6 Pt 1), pp 2723-33.
- Yang, M. & Brackenbury, W. J. 2013. Membrane potential and cancer progression. *Frontiers in Physiology*, **4**(185).
- Yu, S. P. & Kerchner, G. A. 1998. Endogenous voltage-gated potassium channels in human embryonic kidney (HEK293) cells. *The Journal of Neuroscience Research*, **52**(5), pp 612-7.
- Zhang, D. Y., Wang, Y., Lau, C. P., Tse, H. F. & Li, G. R. 2008. Both EGFR kinase and Src-related tyrosine kinases regulate human ether-a-go-go-related gene potassium channels. *Cell Signal*, **20**(10), pp 1815-21.
- Zhang, J., Chan, Y. C., Ho, J. C., Siu, C. W., Lian, Q. & Tse, H. F. 2012. Regulation of cell proliferation of human induced pluripotent stem cell-derived mesenchymal stem cells via ether-a-go-go 1 (hEAG1) potassium channel. *American Journal of Physiology: Cell Physiology*, **303**(2), pp C115-25.
- Zhang, Y.-Y., Yue, J., Che, H., Sun, H.-Y., Tse, H.-F. & Li, G.-R. 2014. BKCa and hEag1 Channels Regulate Cell Proliferation and Differentiation in Human Bone Marrow-Derived Mesenchymal Stem Cells. *The Journal of Cellular Physiology*, **229**(2), pp 202-212.
- Ziechner, U., Schonherr, R., Born, A. K., Gavrilova-Ruch, O., Glaser, R. W., Malesevic, M., Kullertz, G. & Heinemann, S. H. 2006. Inhibition of human ether a go-go potassium channels by Ca²⁺/calmodulin binding to the cytosolic N- and C-termini. *The FEBS Journal*, **273**(5), pp 1074-86.

